Probing the Vicinity of Compact Sources: Galactic Black Holes and X-ray Pulsars

Dissertation
der Mathematisch-Naturwissenschaftlichen Fakultät
der Eberhard Karls Universität Tübingen
zur Erlangung des Grades eines
Doktors der Naturwissenschaften
(Dr. rer. nat.)

vorgelegt von
Menglei Zhou, M.Sc.
aus Wuxi/China

Tübingen
2025

Gedruckt mit Genehmigung der Mathematisch-Naturwissenschaftlichen Fakultät der Eberhard Karls Universität Tübingen.

Tag der mündlichen Qualifikation:	22.07.2025
Dekan:	Prof. Dr. Thilo Stehle
1. Berichterstatter:	Prof. Dr. Andrea Santangelo
2. Berichterstatter:	Prof. Dr. Klaus Werner

Ich erkläre, dass ich die zur Promotion eingereichte Arbeit mit dem Titel "Probing the Vicinity of Compact Sources: Galactic Black Holes and X-ray Pulsars" selbstständig verfasst, nur die angegebenen Quellen und Hilfsmittel benutzt und wörtlich oder inhaltlich übernommene Stellen als solche gekennzeichnet habe. Ich versichere an Eides statt, dass diese Angaben wahr sind und dass ich nichts verschwiegen habe. Mir ist bekannt, dass die falsche Abgabe einer Versicherung an Eides statt mit Freiheitsstrafe bis zu drei Jahren oder mit Geldstrafe bestraft wird.

Ort/Place, Datum/Date	Unterschrift/Signature

Abstract

Compact objects such as black holes and neutron stars are natural laboratories for studying matter and radiation under the most extreme physical conditions, shaped by strong gravitational, magnetic, and relativistic effects. Investigating how matter accretes onto these compact objects and radiates energy is key to understanding high-energy astrophysics and testing fundamental physics in the strong-field regime. In this dissertation, I present a systematic study of the accretion and radiative behaviors of Galactic black hole binaries and X-ray pulsars, focusing on key sources including Cygnus X-1, GRS 1915+105, and 4U 1907+09. By combining broadband spectral-timing analysis with recent advances in X-ray polarimetry, this work aims to construct a comprehensive, multi-dimensional picture of the inner regions surrounding compact objects. The dissertation includes several published articles, provided in the Appendix.

The investigation begins with Cygnus X-1, the first discovered black hole binary and a cornerstone for studying accretion physics and spectral state transitions. Using observations from the X-ray mission *Insight*-HXMT, we explore how timing properties evolve across different spectral states over a broad energy range. Our findings confirm key signatures of reflection, variability, and coherence behavior associated with state changes, revealing how the physical conditions of the accretion flow and corona evolve with spectral transitions.

Building on the study of accretion dynamics, we next examine GRS 1915+105, a black hole X-ray binary known for its long-term brightness and complex variability. Through a multi-year monitoring campaign with NICER and HXMT, we trace the source's transition from a classical soft state into an obscured state. This evolution is accompanied by significant changes in the ionization properties of its disk winds, offering new insights into the link between accretion flow geometry and outflow launching mechanisms across different accretion regimes.

Extending the focus from black holes to neutron stars, we investigate the accretion-powered X-ray pulsar 4U 1907+09 using IXPE. These observations provide the first detailed measurements of the polarization properties of this source. By analyzing both phase-averaged and phase-resolved polarization behaviors, we explore the stable geometry of the magnetosphere and the effects of short-term variability on emission patterns, offering a new window into the complex magnetic structures shaping the X-ray emission from accreting neutron stars.

The results presented in this dissertation advance our understanding of the physical processes governing accretion, variability, and energy release in compact objects. By combining spectral, timing, and polarimetric techniques, this work highlights the necessity of multi-dimensional approaches to break observational degeneracies and unveil the intrinsic properties of these systems. These findings also have broader implications for measuring black hole spins, understanding jet formation, and probing

the magnetospheres of neutron stars. The methodologies developed and applied here lay important groundwork for future high-energy astrophysics missions such as *eXTP* and *Athena*, which will offer even deeper insights into the extreme environments shaped by strong gravity.

Zusammenfassung

Kompakte Objekte wie Schwarze Löcher und Neutronensterne dienen als natürliche Labore zur Erforschung von Materie und Strahlung unter den extremsten physikalischen Bedingungen, die durch starke Gravitations-, Magnetfeld- und relativistische Effekte geprägt sind. Die Untersuchung der Akkretion von Materie auf diese kompakten Objekte und der dabei emittierten Strahlung ist entscheidend für das Verständnis der Hochenergieastrophysik und für Tests grundlegender physikalischer Theorien im starken Feldregime. In dieser Dissertation präsentiere ich eine systematische Studie des Akkretions- und Strahlungsverhaltens galaktischer Schwarzer-Loch-Binärsysteme und Röntgenpulsare, mit einem besonderen Fokus auf zentrale Quellen wie Cygnus X-1, GRS 1915+105 und 4U 1907+09. Durch die Kombination von breitbandiger spektral-timing-Analyse mit aktuellen Fortschritten in der Röntgenpolarimetrie soll ein umfassendes, multidimensionales Bild der inneren Regionen kompakter Objekte gezeichnet werden. Die Dissertation enthält mehrere veröffentlichte Artikel, die im Anhang beigefügt sind.

Die Untersuchung beginnt mit Cygnus X-1, dem ersten entdeckten Schwarzen-Loch-Binärsystem und einem Meilenstein für das Studium der Akkretionsphysik und spektraler Zustandswechsel. Mithilfe von Beobachtungen der Röntgenmission *Insight*-HXMT analysieren wir die Entwicklung der zeitlichen Eigenschaften über verschiedene spektrale Zustände hinweg in einem breiten Energiebereich. Unsere Ergebnisse bestätigen zentrale Merkmale von Reflexion, Variabilität und Kohärenzverhalten im Zusammenhang mit Zustandsänderungen und zeigen, wie sich die physikalischen Bedingungen des Akkretionsflusses und der Korona im Zuge dieser Übergänge verändern.

Aufbauend auf der Untersuchung der Akkretionsdynamik analysieren wir anschließend GRS 1915+105, ein Schwarzes-Loch-Röntgendoppelsternsystem, das für seine langanhaltende Helligkeit und komplexe Variabilität bekannt ist. Im Rahmen einer mehrjährigen Beobachtungskampagne mit NICER und HXMT verfolgen wir den Übergang der Quelle von einem klassischen weichen Zustand in einen verdeckten Zustand. Dieser Übergang geht mit erheblichen Veränderungen in den Ionisationseigenschaften der Scheibenwinde einher und liefert neue Erkenntnisse über den Zusammenhang zwischen der Geometrie des Akkretionsflusses und den Mechanismen des Windausstoßes in verschiedenen Akkretionsregimen.

Mit dem Wechsel vom Schwarzen Loch zum Neutronenstern untersuchen wir schließlich den akkretionsgetriebenen Röntgenpulsar 4U 1907+09 mithilfe von IXPE. Diese Beobachtungen liefern die ersten detaillierten Messungen der Polarisationsmerkmale dieser Quelle. Durch die Analyse sowohl phasenintegrierter als auch phasenaufgelöster Polarisationsdaten erforschen wir die stabile Geometrie der Magnetosphäre und die Auswirkungen kurzfristiger Variabilität auf die Emissionsmuster. Dies eröffnet neue Einblicke in die komplexen Magnetfeldstrukturen, die die Röntgenstrahlung

akkretierender Neutronensterne formen.

Die in dieser Dissertation präsentierten Ergebnisse erweitern unser Verständnis der physikalischen Prozesse, die Akkretion, Variabilität und Energieausschüttung in kompakten Objekten steuern. Durch die Kombination spektraler, zeitlicher und polarimetrischer Techniken wird die Notwendigkeit multidimensionaler Ansätze aufgezeigt, um beobachtbare Degeneriertheiten aufzulösen und die intrinsischen Eigenschaften dieser Systeme zu enthüllen. Die gewonnenen Erkenntnisse haben zudem weiterreichende Implikationen für die Bestimmung von Spins Schwarzer Löcher, das Verständnis von Jet-Bildung und die Erforschung von Magnetosphären bei Neutronensternen. Die in dieser Arbeit entwickelten und angewandten Methoden bilden eine wichtige Grundlage für zukünftige Missionen der Hochenergieastrophysik wie *eXTP* und *Athena*, die noch tiefere Einblicke in die von starker Gravitation geprägten Extremumgebungen ermöglichen werden.

Notation

Acronyms & Abbreviations

e.g.	for example (*exempli gratia*)
etc.	and so on (*et cetera*)
i.e.	that is (*id est*)
ADAF	Advection Dominated Accretion Flow
AGN	Active Galactic Nucleus
AMXP	Accreting Millisecond X-ray Pulsar
BAT	Burst Alert Telescope (onboard *Swift*)
BeXB	Be/X-ray Binary
BH	Black Hole
BHB	Black Hole Binary
CCD	Charge-Coupled Device
CRSF	Cyclotron Resonance Scattering Feature
DFT	Discrete Fourier Transform
EoS	Equation of State
eXTP	enhanced X-ray Timing and Polarimetry Mission
FFT	Fast Fourier Transform
FRB	Fast Radio Burst
GPD	Gas Pixel Detector (onboard IXPE)
GR	General Relativity
GRB	Gamma-Ray Burst
GTI	Good Time Interval
HE	High Energy telescope (onboard HXMT)
HFQPO	High Frequency Quasi-Peridoic Oscillation
HID	Hardness-Intensity Diagram
HMXB	High-Mass X-ray Binary
HXMT	Hard X-ray Modulation Telescope
IDFT	Inverse Discrete Fourier Transform
ISCO	Innermost Stable Circular Orbit
`ISIS`	Interactive Spectral Interpretation System
ISM	InterStellar Medium
IXPE	Imaging X-ray Polarimetry Explorer
LE	Low Energy telescope (onboard HXMT)
LFQPO	Low Frequency Quasi-Peridoic Oscillation
LMXB	Low-Mass X-ray Binary
MAXI	Monitor of All-sky X-ray Image
MDP	Minimum Detectable Polarization

ME	Medium Energy telescope (onboard HXMT)
MJD	Modified Julian Date
NICER	Neutron star Interior Composition ExploreR
NS	Neutron Star
PA	Polarization Angle
PCA	Proportional Counter Array (onboard RXTE)
PD	Polarization Degree
PDF	Probability Density Function
PSD	Power Spectral Density
QED	Quantum ElectroDynamics
QPO	Quasi-Peridoic Oscillation
rms	root mean square
RXTE	Rossi X-ray Timing Explorer
SFXT	Supergiant Fast X-ray Transient
SGXB	Supergiant X-ray Binary
SSD	Silicon Drift Detector
SXT	Soft X-ray Transients
TOV	Tolman-Oppenheimer-Volkoff
WD	White Dwarf
XRB	X-Ray Binary
XRISM	X-Ray Imaging and Spectroscopy Mission
XRP	X-Ray Pulsar
XTI	X-ray Timing Instrument (onboard NICER)

Constants

$c = 2.99792458 \times 10^8\,\mathrm{m\,s^{-1}}$	the speed of light in Vacuum
$G_\mathrm{N} = 6.6738(8) \times 10^{-11}\,\mathrm{m^3\,kg^{-1}\,s^{-2}}$	Gravitational constant
$k_\mathrm{B} = 1.3806488(13) \times 10^{-23}\,\mathrm{J\,K^{-1}}$	Boltzmann constant
$\mu_0 = 4\pi \times 10^{-7}\,\mathrm{N\,A^{-2}}$	the permeability of Free Space
$\epsilon_0 = 1/(\mu_0 c^2) = 8.854187817\ldots \times 10^{-12}\,\mathrm{F\,m^{-1}}$	the permittivity of Free Space
$e = 1.602176565(35) \times 10^{-19}\,\mathrm{C}$	electron charge magnitude
$m_\mathrm{e} = 9.10938291(40) \times 10^{-31}\,\mathrm{kg}$	electron mass
$m_\mathrm{p} = 1.672621777(74) \times 10^{-27}\,\mathrm{kg}$	proton mass
$r_\mathrm{e} = e^2/(4\pi\epsilon_0 m_\mathrm{e} c^2) = 2.8179403267(27) \times 10^{-15}\,\mathrm{m}$	classical electron radius
$\sigma_\mathrm{T} = 8\pi r_\mathrm{e}^2/3 = 0.6652458734(13) \times 10^{-30}\,\mathrm{m^{-2}}$	Thomson cross section
$\mathrm{AU} = 1.49597870700 \times 10^{11}\,\mathrm{m}$	the Astronomic Unit
$\mathrm{pc} = 3.08567758149 \times 10^{16}\,\mathrm{m}$	Parsec (1 AU/1 arcsec)
$M_\odot = 1.9885(2) \times 10^{30}\,\mathrm{kg}$	solar mass
$L_\odot = 3.828 \times 10^{26}\,\mathrm{W} = 3.828 \times 10^{33}\,\mathrm{erg\,s^{-1}}$	solar luminosity
$r_\mathrm{g} = G_\mathrm{N}(M/M_\odot)c^{-2} \approx 1.4766(M/M_\odot) \times 10^3\,\mathrm{m}$	the gravitational radius

Miscellaneous

log	The natural logarithm (base e, *i.e.* $\log \mathrm{e} = 1$)

Contents

1 Overview

The study of compact astrophysical objects—namely, white dwarfs (WDs), neutron stars (NSs), and black holes (BHs)—provides profound insight into some of the most extreme physical environments in the Universe. Formed in the final stages of stellar evolution, these objects serve as natural laboratories for testing theories of strong gravity, dense matter, magnetohydrodynamics, and high-energy radiation processes. Within the Milky Way alone, hundreds of compact objects have been identified, many of them in binary systems where their presence is revealed through intense X-ray emission produced by accretion processes. In this dissertation, I will focus in particular on the latter two types: NSs and BHs.

When embedded in X-ray binaries (XRBs), compact objects can interact with a companion star, accreting material via Roche-lobe overflow or stellar winds. The infalling matter releases gravitational potential energy, heating up to millions of degrees and emitting in the X-ray regime. These X-ray binaries are categorized into various sub-classes, such as low-mass X-ray binaries (LMXBs) and high-mass X-ray binaries (HMXBs), each offering insights into different physical scenarios. Furthermore, certain black hole binaries (BHBs) can exhibit relativistic jets, drawing parallels to active galactic nuclei (AGNs) but on smaller mass and spatial scales, hence the term "microquasars".

In this chapter, we lay the foundational astrophysics necessary for interpreting high-energy observations of compact sources, particularly those studied in this dissertation: BHBs Cygnus X-1 and GRS 1915+105, as well as an accretion-powered pulsar 4U 1907+09. We begin with a comprehensive discussion of stellar evolution leading to compact remnants, followed by an exploration of their physical properties, accretion dynamics, and observational manifestations. Special attention is given to X-ray spectroscopy, timing analysis, and polarimetry, which together enable a multi-dimensional probe into the inner workings of these enigmatic systems.

1.1 Introduction

1.1.1 Stellar Evolution and the Formation of Compact Objects

This subsection is primarily based on the textbooks by Karttunen et al. [97] and Longair [118].

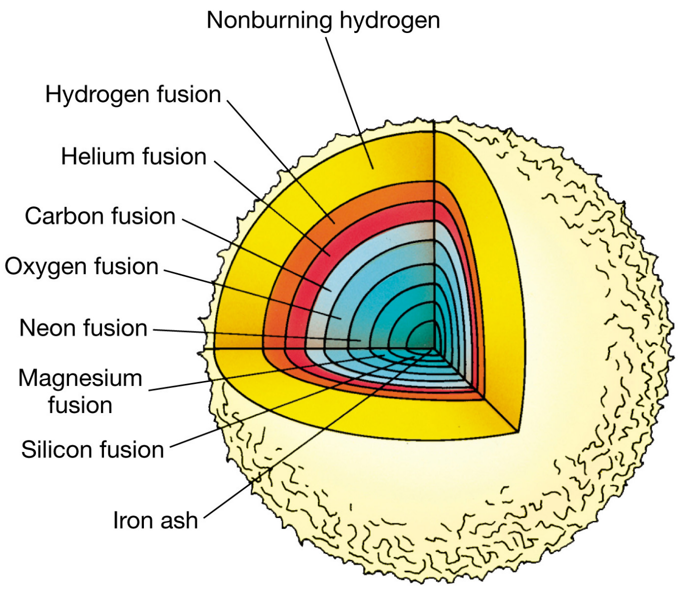

Figure 1.1: The internal structure of a massive star. The most metallic layers are in the most internal part of the stars, like the layers of an onion. (Figure from `https://www.cosmos.esa.int/web/cesar/the-hertzsprung-russell-diagram`)

Massive Star Evolution

Stars are gravitationally bound plasma spheres sustained by the thermonuclear fusion of lighter elements into heavier ones. Stellar evolution is governed primarily by the initial mass of the star. While low-mass stars (e.g., like the Sun) end their lives as white dwarfs, massive stars ($M \gtrsim 8\,M_\odot$) undergo a more violent demise.

During the main sequence phase, massive stars fuse hydrogen into helium via the CNO cycle. As the hydrogen in the core depletes, fusion continues in successively heavier elements: helium to carbon and oxygen, then neon, magnesium, silicon, and finally iron (see Fig. 1.1). However, iron fusion is endothermic and cannot generate energy to support the star against gravitational collapse.

Once an iron core forms and exceeds the Chandrasekhar limit ($\sim 1.4\,M_\odot$), it becomes unstable and collapses under its own gravity. The outcome of this collapse depends critically on the mass of the progenitor and the dynamics of the explosion.

Core-Collapse Supernovae

The core-collapse triggers a supernova explosion (Type II, Ib, or Ic), where the outer layers of the star are violently expelled (see the review by Woosley & Janka [213]). The collapsing core may reach nuclear densities ($\sim 10^{14}$ g cm^{-3}), at which point the repulsive component of the strong nuclear force and neutron degeneracy pressure can temporarily halt the collapse.

In some cases, a rebounding shock wave leads to successful ejection of the envelope. In others, the shock may stall and require neutrino heating or other mechanisms to revive the explosion. Regardless of the mechanism, the remnant left behind is either a NS or, if the mass is too great, a BH (Fig. 1.2).

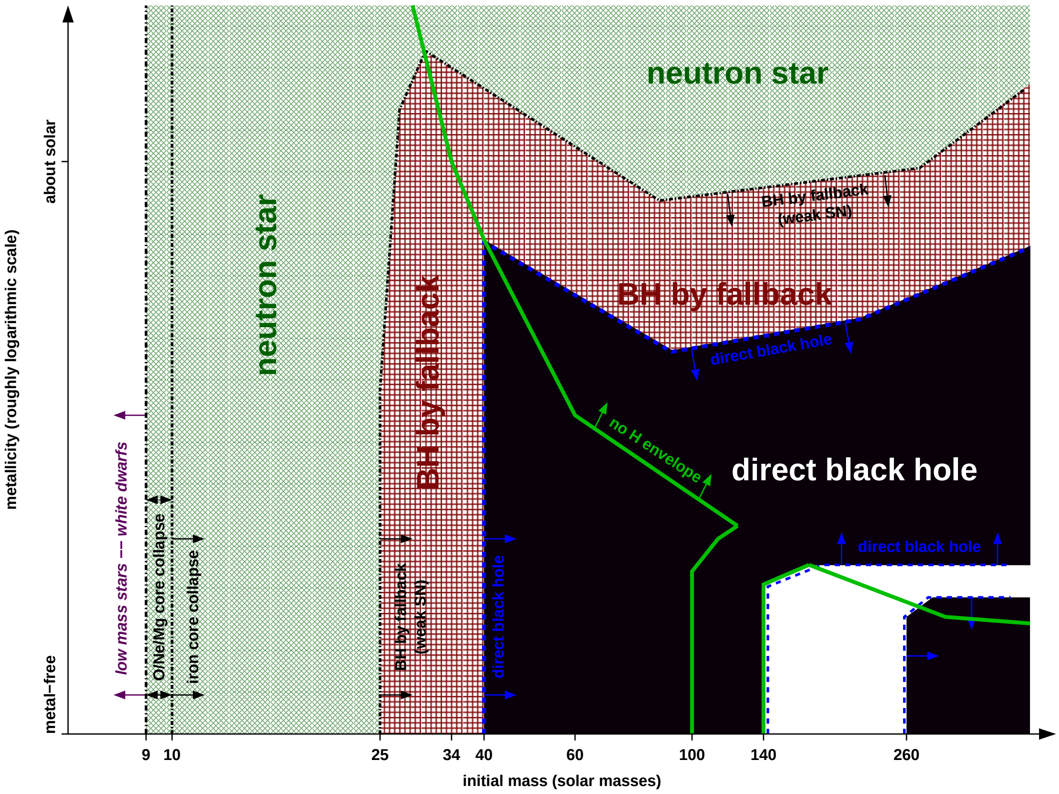

Figure 1.2: The endpoints of massive single stars as a function of initial metallicity and inital mass. (Adopted from Heger et al. [79])

Formation of Neutron Stars

When the collapsing core mass is in the range $\sim$1.4–2.2 $M_\odot$, neutron degeneracy pressure halts the collapse, forming a NS. These are incredibly compact objects with typical radii of 10–12 km and densities exceeding nuclear saturation density. Their magnetic fields are among the strongest in the Universe, reaching up to 10^{15} G in magnetars.

Newly formed NSs are often born spinning rapidly due to angular momentum conservation and may manifest as radio or X-ray pulsars (XRPs). They cool via neutrino emission and thermal X-ray radiation. If in a binary system, accretion can spin them up and change their emission properties, producing accretion-powered pulsars detectable in the X-ray band.

Formation of Black Holes

If the collapsing stellar core exceeds the Tolman-Oppenheimer-Volkoff (TOV) limit, no known pressure can prevent collapse into a singularity. A BH is then formed, characterized by the presence of an event horizon—a boundary beyond which nothing can escape. For stellar-mass BHs, the threshold is thought to be $\gtrsim$ 2.2–3 $M_\odot$ depending on the equation of state (EoS) [96].

The exact process of BH formation remains an area of active research. In some cases, the BH may form via fallback accretion: even if the initial explosion is successful, some of the ejected material may fall back onto the NS and push it over the mass limit. Alternatively, very massive stars ($M \gtrsim 40\,M_\odot$) may undergo "failed supernovae" or direct collapse, forming BHs with little or no associated electromagnetic emission.

Accretion and Emission Mechanisms

Accretion is a fundamental process through which compact objects, such as BHs and NSs, acquire mass and radiate energy. In these systems, material from a companion star or the interstellar medium (ISM) loses angular momentum and spirals inward, forming an accretion disk. Viscous dissipation within the disk converts gravitational potential energy into thermal energy, which is subsequently radiated across a broad range of wavelengths, from radio to X-rays. The detailed structure and radiative properties of the accretion flow depend on factors such as the mass accretion rate, the geometry of the disk, and the strength of magnetic fields. In BH systems, a significant fraction of the energy may also be released in the form of relativistic jets. For accreting NSs, additional emission arises from the solid surface and magnetic poles, where material is funneled by strong magnetic fields, leading to pulsations and complex spectral features. Understanding accretion and emission mechanisms is essential for interpreting observational signatures and probing the physical conditions in the extreme environments near compact objects.

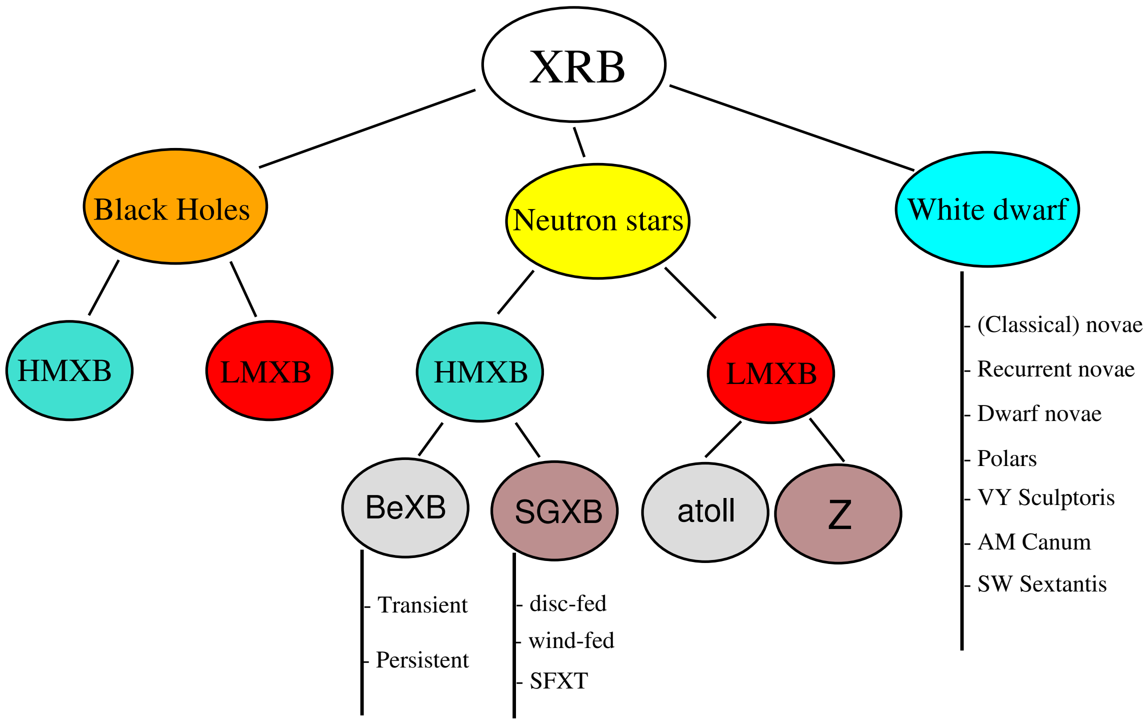

Figure 1.3: The classification of XRBs. (Figure from Reig [171])

Eddington Limit

The Eddington limit defines the maximum luminosity that a spherically symmetric, steady-state object can achieve when there is a balance between outward radiation pressure and inward gravitational force. Beyond this limit, radiation pressure would exceed gravity, leading to the expulsion of accreting material or the disruption of the star's outer layers. Mathematically, the Eddington luminosity depends on the mass of the object and the opacity of the surrounding material, and is given by

$$L_{\mathrm{Edd}} = \frac{4\pi G_{\mathrm{N}} M m_{\mathrm{p}} c}{\sigma_{\mathrm{T}}} \approx 1.26 \times 10^{38} \left(\frac{M}{M_{\odot}}\right) \mathrm{erg\,s^{-1}}\,, \tag{1.1}$$

where m_{p} is the proton mass, G_{N} is the gravitational constant, c is the speed of light, and σ_{T} denotes the cross section for Thomson scattering. The Eddington limit plays a critical role in the evolution of massive stars, the behavior of accreting BHs, and the dynamics of AGNs.

1.1.2 Classification of X-ray Binaries

This subsection is primarily based on the review by van den Heuvel [197] and Chapters 105 & 106 in the handbook edited by Bambi & Santangelo [12].

XRBs are systems in which a compact object—either a NS or a BH—accretes matter from a companion star, producing X-rays. These systems are broadly classified based on the mass of the donor star and the nature of the accretion mechanism. This classification is not only taxonomic but also reflects different physical processes, timescales, and observational signatures (see an example in Fig. 1.3).

High-Mass X-ray Binaries (HMXBs)

HMXBs are systems in which the donor star is an O or B-type star, typically with a mass $\gtrsim 10\,M_\odot$. These stars are young, massive, and luminous, and often possess strong stellar winds or decretion disks.

Sub-classes include:

- **Be/X-ray binaries (BeXBs)**: The donor is a rapidly rotating B-type star surrounded by a circumstellar decretion disk. The NS companion is usually in an eccentric orbit, accreting material as it passes through the disk near periastron. These systems are often transient, producing Type I outbursts (periastron passages) and occasional giant Type II outbursts.
- **Supergiant X-ray binaries (SGXBs)**: The donor is a supergiant star with a dense stellar wind. The compact object accretes via wind capture, resulting in persistent or quasi-persistent X-ray emission. Orbital periods are typically shorter and more circular than in BeXBs.
- **Supergiant Fast X-ray Transients (SFXTs)**: A subclass of SGXBs characterized by brief, bright flares lasting hours, followed by long periods of quiescence. The origin of the flaring is debated, with models invoking clumpy winds, magnetic gating, or centrifugal barriers.

HMXBs are generally young systems (ages $\sim 10^6$–10^7 years), located in star-forming regions and near the Galactic plane. Their high X-ray luminosities and short evolutionary timescales make them key probes of massive star evolution and accretion physics.

Low-Mass X-ray Binaries (LMXBs)

In contrast, LMXBs consist of an old, low-mass ($\lesssim 1\,M_\odot$) donor star and a compact object. Mass transfer occurs via Roche-lobe overflow and is typically stable, forming an accretion disk around the compact object.

LMXBs are generally older systems ($\gtrsim 1$ Gyr), found in the Galactic bulge, globular clusters, and elliptical galaxies. Subtypes include:

- **Persistent LMXBs**: These systems maintain a high mass transfer rate, leading to continuous X-ray emission. Many show thermonuclear bursts (Type I) if the accretor is a NS.
- **Transient LMXBs**: These systems exhibit episodic outbursts due to accretion disk instabilities. They are further categorized into:
  - *Soft X-ray transients (SXTs)*: Typically associated with BHs or weakly magnetized NSs.
  - *Accreting millisecond XRPs (AMXPs)*: NSs that show coherent pulsations and are likely progenitors of recycled radio pulsars.

Many LMXBs are known to harbor BHs, such as GX 339−4 [see e.g., 218] and V404 Cygni [178], making them important targets for studying accretion states, jet formation, and BH spin.

Persistent vs. Transient Sources

A key observational dichotomy in XRBs is whether they are persistent or transient. This classification depends largely on the stability of the accretion disk and the mass transfer rate.

- **Persistent sources**: Accrete at a high enough rate to keep the accretion disk ionized and stable. These systems exhibit continuous X-ray emission and are often used to study steady-state accretion.
- **Transient sources**: Exhibit large outbursts separated by long periods of quiescence. Outbursts can last weeks to months and are believed to be caused by thermal-viscous instabilities in the accretion disk.

Transient behavior is particularly common in LMXBs, especially those with BH accretors. During outbursts, these systems often undergo state transitions, disk-jet coupling, and strong variability, offering a valuable laboratory for time-domain astrophysics.

Microquasars and Relativistic Jets

Some X-ray binaries, particularly those containing BHs, exhibit relativistic jets similar to those in AGN. These systems are referred to as *microquasars* due to their scaled-down analogy with quasars. These microquasars represent one of the central topics explored in this thesis.

Key features of microquasars include:

- **Relativistic jets**: Observed in the radio and infrared, often with superluminal motion. Jets can be steady (in the hard state) or transient (during state transitions).
- **Disk-jet connection**: The launch of jets is closely tied to changes in the accretion flow, with transient jets occurring when the inner disk moves inward or the corona changes structure.
- **Multi-wavelength behavior**: These systems exhibit correlated variability across X-ray, optical, infrared, and radio bands.

Notable microquasars include:

- **GRS 1915+105**: Exhibits super-Eddington accretion, rapid variability, and powerful jets. It displays over a dozen different variability classes with complex timing and spectral behavior [see e.g., 20, 84, 138].

- **Cygnus X-1**: One of the earliest BH candidates and a persistent radio emitter with a compact jet (see Jiang [93] nad the references therein).

- **GRO J1655−40**: Known for producing superluminal jet ejections and a well-measured BH spin [215].

Studying microquasars provides insights into jet launching mechanisms, energy extraction from spinning BHs (e.g., via the Blandford-Znajek process, Blandford & Znajek [22]), and accretion-ejection coupling.

1.1.3 Neutron Stars and Pulsars

This subsection is based on the book edited by Rezzolla et al. [175] and the review by Mushtukov & Tsygankov [148].

Basic Properties of Neutron Stars

NSs are the densest observable stellar remnants, typically possessing masses in the range of 1.2–2.1 $M_\odot$ and radii around 10–12 km. Their central densities can exceed $5 \times 10^{14}\,\mathrm{g\,cm^{-3}}$, surpassing that of atomic nuclei. Due to their compactness, they have intense surface gravity:

$$g \approx \frac{G_\mathrm{N} M}{R^2} \sim 10^{14}\,\mathrm{cm\,s^{-2}}\,, \tag{1.2}$$

which dramatically affects both their internal physics and observational signatures.

NSs are primarily composed of neutrons, surrounded by a thin crust of heavy nuclei, and may contain exotic phases such as quark-gluon plasma or hyperons in their cores. Their exact internal composition remains uncertain, making NSs key objects for constraining the EoS of ultra-dense matter. Investigating the EoS of NSs is one of the central topics in contemporary X-ray astrophysics.

Magnetic Fields and Magnetospheres

A subset of NSs exhibit powerful magnetic fields that significantly influence their physical properties. At birth, these can reach values of 10^{12}–10^{13} G, and in the case of magnetars, up to 10^{15} G. These fields are likely inherited from the progenitor star and amplified via flux conservation during the collapse:

$$B_\mathrm{NS} \approx B_\mathrm{prog} \left(\frac{R_\mathrm{prog}}{R_\mathrm{NS}} \right)^2 . \tag{1.3}$$

The magnetic field governs the NS's magnetosphere—a region dominated by the magnetic pressure and populated by charged particles. Rotation of the NS induces electric fields, which accelerate particles and generate coherent radio emission in pulsars or high-energy radiation in X-rays (Fig. 1.4).

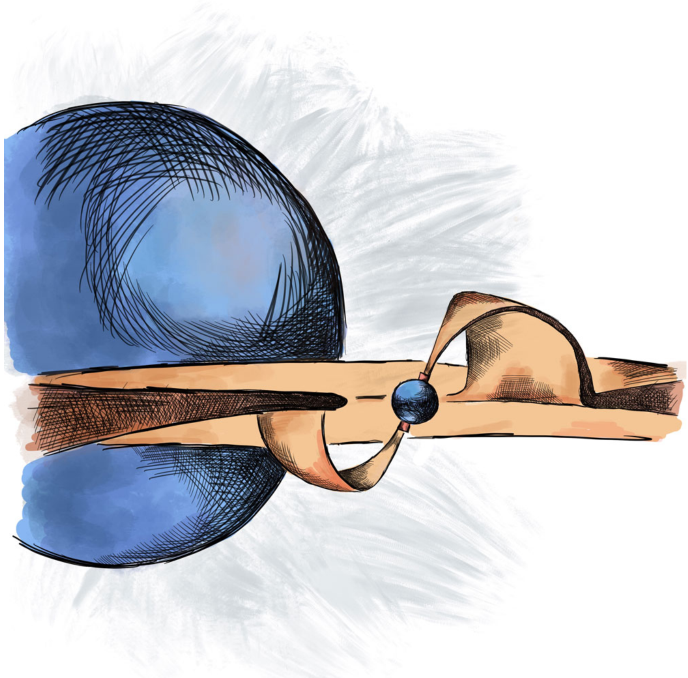

Figure 1.4: Schematic of accretion in XRPs: material from the companion star feeds an accretion disk or stellar wind. At the magnetospheric radius, the NS's magnetic field halts the flow's radial motion, forcing it to channel along magnetic field lines. Guided to the magnetic poles, the material impacts the surface, releasing energy primarily as X-rays. (Figure from Mushtukov & Tsygankov [148])

Rotation and Pulsar Phenomenology

Newly formed NSs spin rapidly due to angular momentum conservation. Observed spin periods range from milliseconds (in millisecond pulsars) to several seconds. Rotational kinetic energy is often radiated via magnetic dipole radiation, leading to a gradual spin-down over time.

Pulsars are NSs with a misalignment between the magnetic and rotational axes, producing lighthouse-like beams that sweep across the sky. When these beams cross Earth's line of sight, periodic pulses are observed. Most known pulsars emit in radio frequencies, but some are visible in X-rays and gamma-rays, particularly young or accreting systems.

The spin period P and its derivative $\dot{P}$ yield insights into a pulsar's magnetic field B and age τ via the magnetic dipole model [124]:

$$B \approx 3.2 \times 10^{19} \sqrt{P\dot{P}}\,\mathrm{G}\,, \quad \tau = \frac{P}{2\dot{P}}\,. \tag{1.4}$$

Measurements of P and $\dot{P}$ allow us to estimate key physical parameters of isolated NSs, which form distinct populations in the P-$\dot{P}$ diagram, as illustrated in Fig. (1.5). In binary systems, NSs may accrete matter from a companion star, leading to powerful X-ray emission. If the accreted matter is funneled onto the magnetic poles, hot spots form and rotate with the star, generating modulated X-ray emission known as X-ray pulsations.

These accretion-powered XRPs can be broadly categorized based on the nature of the

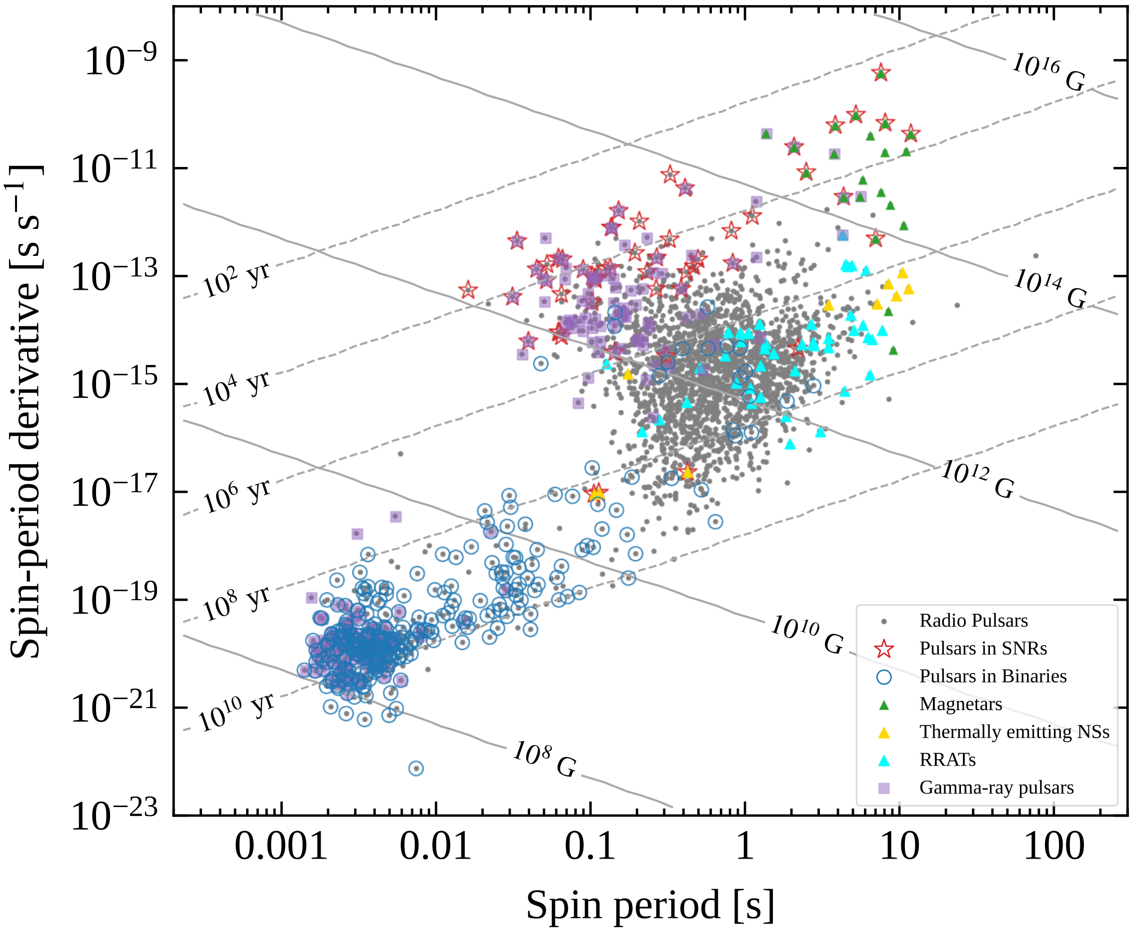

Figure 1.5: The P-$\dot{P}$ diagram includes all non-accreting NSs from the ATNF pulsar catalogue (v1.66). Green triangles, grey dots, light blue triangles, green triangles, and yellow triangles represent magnetars, rotation-powered pulsars, rotating radio transients (RRATs), X-ray dim isolated neutron stars (XDINSs), and central compact objects (CCOs), respectively. Solid and dashed lines denote constant dipolar magnetic field and characteristic age, as derived from the equations in Eq. (1.4). (Figure from Borghese & Coti Zelati [26])

mass transfer:

- **Wind-fed systems**: Typically involve high-mass companions (e.g., O or B stars). Matter is captured from the stellar wind and channeled onto the NS (e.g., Vela X-1, 4U 1907+09).
- **Disk-fed systems**: Often seen in LMXBs, where matter from the Roche-lobe-filling donor forms an accretion disk before reaching the NS surface.

Accreting X-ray Pulsars

Strong magnetic fields ($B \sim 10^{12}$ G) truncate the accretion disk at the magnetospheric radius:

$$R_{\rm m} \approx \left(\frac{\mu^4}{2G_{\rm N} M \dot{M}^2} \right)^{1/7} , \tag{1.5}$$

where $\mu = BR^3$ is the magnetic dipole moment and $\dot{M}$ is the accretion rate. Accreting material follows field lines, leading to cyclotron line features in the X-ray spectrum that directly measure magnetic field strength.

XRPs provide unique probes of magnetized accretion physics, emission geometries, and plasma behavior in extreme fields. Their pulse profiles and energy-dependent timing behavior are used to infer the structure of the accretion column, scattering regions, and magnetic topology.

1.1.4 Stellar-Mass Black Holes in the Galaxy

This subsection is based on the monograph by Bambi [10] and extends the discussion to include cases and nuances not fully addressed in the original text.

Evidence for Black Holes

BHs are defined by the presence of an event horizon—a boundary beyond which no information can escape. Since this makes them intrinsically dark, their detection relies on indirect observational signatures, particularly in binary systems where they interact with a stellar companion. The existence of supermassive black holes is strongly supported by observations of stellar orbits around the galactic center (see Fig. 1.6).

The primary evidence for the existence of stellar-mass BHs comes from:

1. **Dynamical mass measurements** in X-ray binaries where the compact object's mass exceeds the maximum allowed for a NS ($\sim 3\,M_\odot$).
2. **Spectral and timing behavior**, such as the absence of pulsations or Type I X-ray bursts (which are indicative of a NS surface), and the presence of relativistic reflection and broad iron lines.
3. **Event horizon indicators**, such as the presence of a hard spectral cutoff and lack of surface thermal emission even in quiescence.

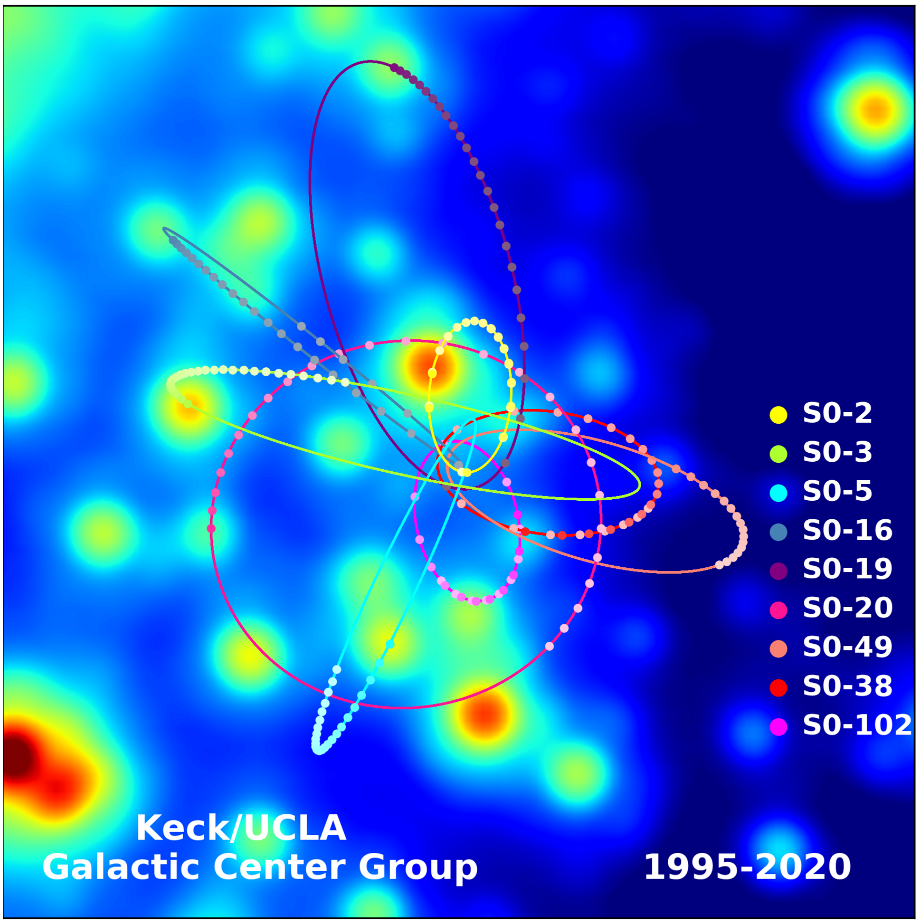

Figure 1.6: Strong evidence for the presence of a supermassive BH at the Galactic center. The points represent stellar orbits, from which a central mass of approximately $\sim 4 \times 10^6\, M_\odot$ is inferred. This updated version of Ghez et al. [69] includes observations up to 2020 (Figure from `https://galacticcenter.astro.ucla.edu/images.html`)

Some well-known Galactic BH candidates include Cygnus X-1 [137], GRS 1915+105 [170], and GRO J1655−40 [16], with masses typically in the range 5–20 $M_{\odot}$. These systems have enabled in-depth studies of accretion physics in strong gravity regimes.

Black Hole Accretion States

Stellar-mass BHs in binaries exhibit a range of spectral states driven by changes in the accretion rate and the structure of the accretion flow (see the review by Remillard & McClintock [173]). The canonical states include:

- **Hard State**: Dominated by hard, power-law-like emission from a hot, optically thin corona. The accretion disk is thought to be truncated at large radii. Variability is strong and characterized by low-frequency quasi-periodic oscillations (LFQPOs). Typically, no disk winds are observed in high-inclination BHBs (see e.g., Ponti et al. [163], but we have exceptions, see Chapter 6).
- **Soft State**: Dominated by thermal emission from a geometrically thin, optically thick disk extending close to the innermost stable circular orbit (ISCO). Variability is low, and the power-law component is weaker. Disk winds can be detected in high-inclination BHBs (see Fig. 1.7).
- **Intermediate and Very High States**: Transitional states with complex timing behavior, strong disk-corona coupling, and jet activity. These states are particularly valuable for studying disk-jet connections and BH spin.

State transitions are typically traced via hardness-intensity diagrams (HIDs, see Fig. 1.8) [19, 54], and the timing evolution often shows hysteresis patterns (see an example in Fig. 1.8). GRS 1915+105 is a notable outlier, displaying unique limit-cycle variability across dozens of complex variability classes [20].

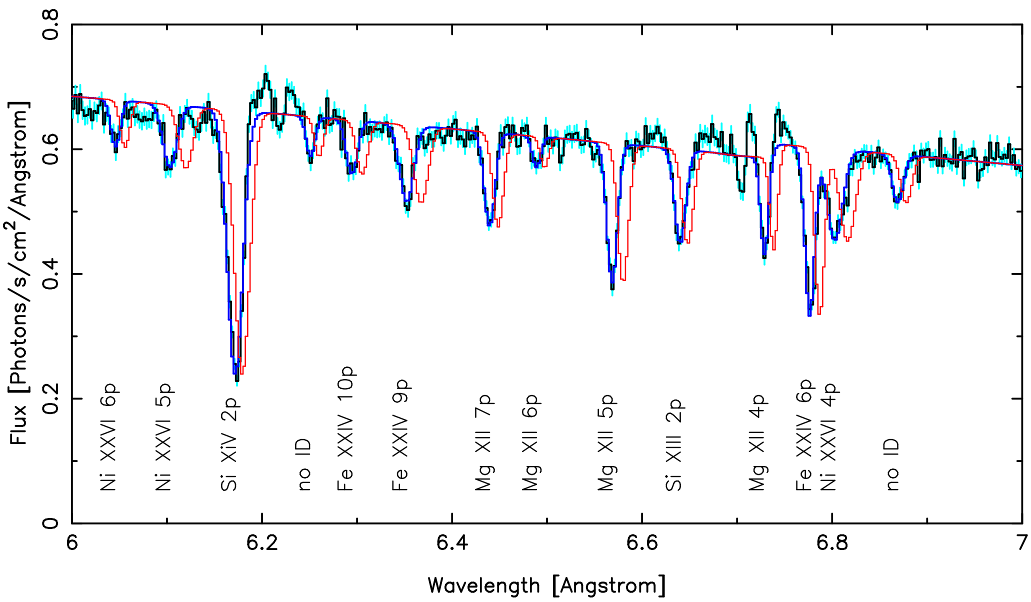

Figure 1.7: The presence of disk winds are typically presented as blue-shifted absorption lines. In this figure, the black curve with blue error bars is the *Chandra* spectrum of LMXB GRO J1655−40, while the red curve is the best-fit model adjusted to zero Doppler shift. (Adopted from Miller et al. [134])

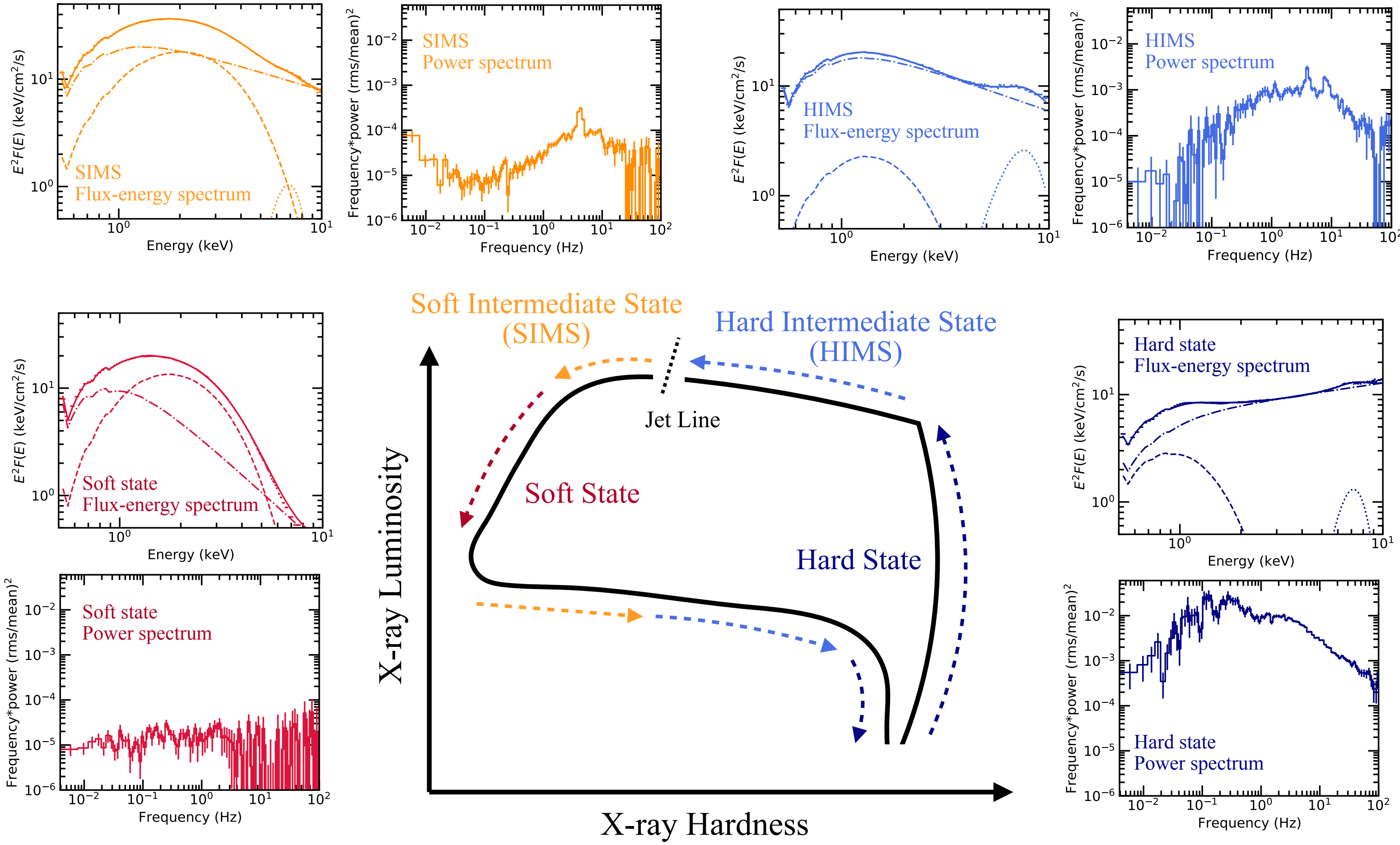

Figure 1.8: A typical hardness-intensity diagram (HID) of the outburst of the black hole binary MAXI J1820+070 is shown. This figure also illustrates the typical spectra, including their components, as well as the power spectral densities (PSDs) corresponding to each state. (Figure from Wang et al. [205])

Measuring Black Hole Spin

The spin of a BH is a fundamental parameter affecting the ISCO and efficiency of accretion. Several observational methods have been developed to estimate the dimensionless spin parameter $a_* = Jc/G_\mathrm{N}M^2$ (see a recent review by Reynolds [174]):

1. **Continuum-fitting method**: Models the thermal emission from a thin accretion disk, assuming the inner edge corresponds to the ISCO[1] (see Fig. 1.9). Requires independent measurements of mass, inclination, and distance [220].

2. **Relativistic reflection spectroscopy**: Analyzes the shape of fluorescent iron lines and Compton reflection components, which are broadened and skewed due to relativistic effects near the BH [52].

3. **Gravitational Waves**: The spin parameter can be estimated from gravitational wave signals during the inspiral phase of a binary BH merger, when the two BHs are still well separated and orbiting their common center of mass.

Some of these methods have yielded high-spin estimates ($a_* \gtrsim 0.95$) for systems like Cygnus X-1 (Fabian et al. [53], Parker et al. [160], Zhao et al. [224], but see also e.g., Walton et al. [204]) and GRS 1915+105 [133, 170], though debates continue regarding systematic uncertainties and model dependencies.

Disk-Corona Geometry and Spectral Modeling

A key open question in BH astrophysics concerns the geometry of the X-ray emitting regions. The standard picture involves a geometrically thin, optically thick accretion disk, coupled with a hot, optically thin corona responsible for inverse-Compton upscattering of soft disk photons into hard X-rays.

Various geometrical models have been proposed:

- **Lamp-post model**: A compact corona located above the BH's rotation axis. It produces both direct emission and irradiation of the inner disk, leading to reflection features.

- **Extended slab/sandwich models**: The corona envelops the disk, allowing for a more distributed reflection and scattering geometry.

- **Truncated disk with inner hot flow**: The thin disk is truncated at a radius $r > r_\mathrm{ISCO}$, with the inner region filled by a hot advection-dominated accretion flow (ADAF) [151, 152].

The geometry of the corona can strongly influence the slopes of both the Comptonized spectrum generated by the corona and the reflection spectrum from the accretion disk.

[1]The ISCO is conceptually defined by the condition $\partial_r^2 V_\mathrm{eff} = 0$ or $\partial_\theta^2 V_\mathrm{eff} = 0$ in spherical coordinates within the framework of general relativity, where V_eff is the effective potential. Its radius evolves from $9\,r_\mathrm{g}$ to $6\,r_\mathrm{g}$ to $1\,r_\mathrm{g}$ as the spin parameter a_* increases from -1 (maximally counter-rotating) to 0 (non-rotating) to 1 (maximally co-rotating) in Kerr spacetime [14].

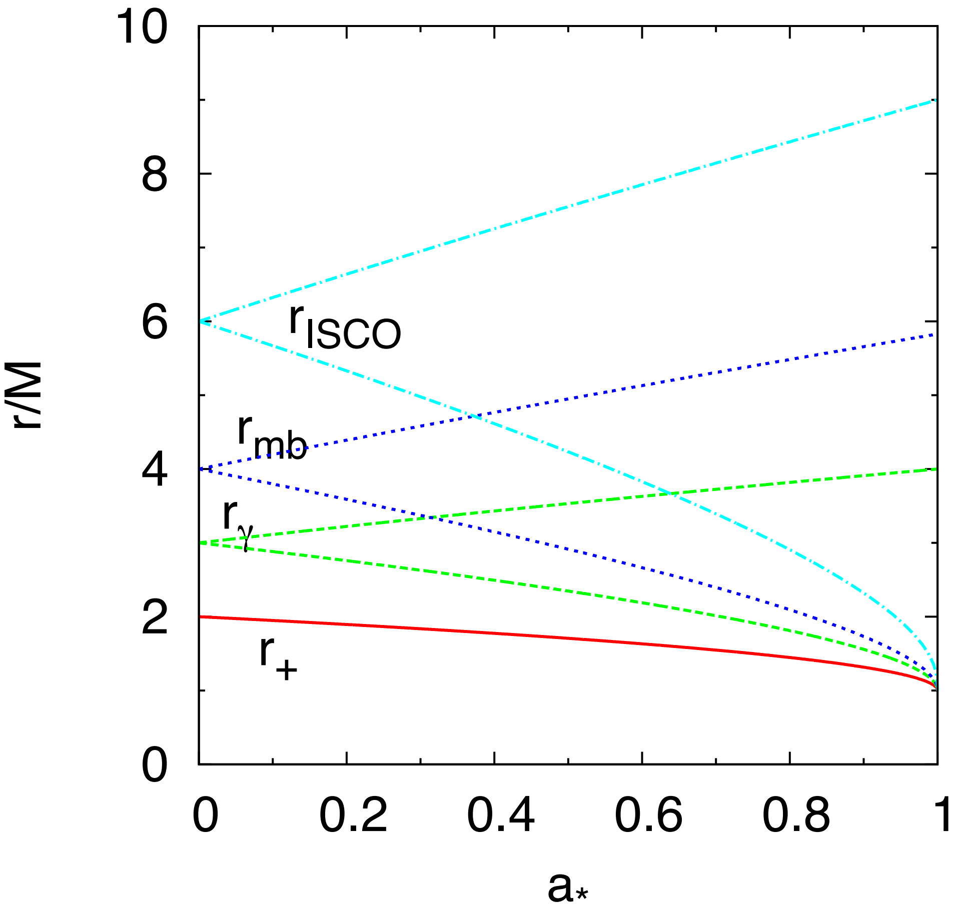

Figure 1.9: Radial coordinates of the event horizon (r_+), photon circular orbit (r_γ), marginally bound orbit ($r_{\rm mb}$), and ISCO ($r_{\rm ISCO}$) in the Kerr metric as functions of the spin parameter (a_*). For each radius, the upper curve corresponds to counterrotating orbits, and the lower curve to corotating orbits. (Figure from Bambi [11])

X-ray spectral modeling combines multiple components: multicolor disk blackbody, Comptonization, reflection, and sometimes a jet. Advanced models like `relxill` [45, 64] or `Nthcomp` [217] enable fitting relativistically blurred reflection spectra and continuum emission.

Jets and Disk-Jet Coupling

Many BHBs produce relativistic jets—collimated outflows detectable in the radio and infrared (Fig. 1.10). Jet production is strongly state-dependent [see e.g., 40, 54, 56]:

- **Steady, compact jets** are observed in the hard state.
- **Transient, ballistic jets** are launched during state transitions.
- **Jet quenching** occurs in the soft state.

This behavior suggests a coupling between the inner disk, corona, and jet-launching regions. Observational campaigns across the electromagnetic spectrum (e.g., RXTE, *Chandra*, VLA) have been crucial in tracking this interplay in real time.

Observational Diagnostics

Several tools are employed to probe the nature of BHBs:

1. **Spectroscopy**: Tracks continuum shape, iron line profiles, and reflection features. Useful for measuring accretion rates, inner disk radius, and spin.
2. **Timing analysis**: Power spectral densities (PSDs), time lags, and QPOs reveal information about variability mechanisms, disk-corona dynamics, and potential relativistic precession.
3. **Polarimetry**: Measures the orientation and degree of X-ray polarization, which constrains the geometry and scattering mechanisms. The advent of missions like IXPE has opened a new window in this domain.

Together, these methods allow astronomers to construct a coherent picture of accretion physics around stellar-mass BHs and provide tests of general relativity (GR) in the strong-field regime.

1.1.5 Observational Techniques for Compact Objects

This subsection is chiefly based on the handbooks edited by Arnaud et al. [3] and Bambi & Santangelo [12].

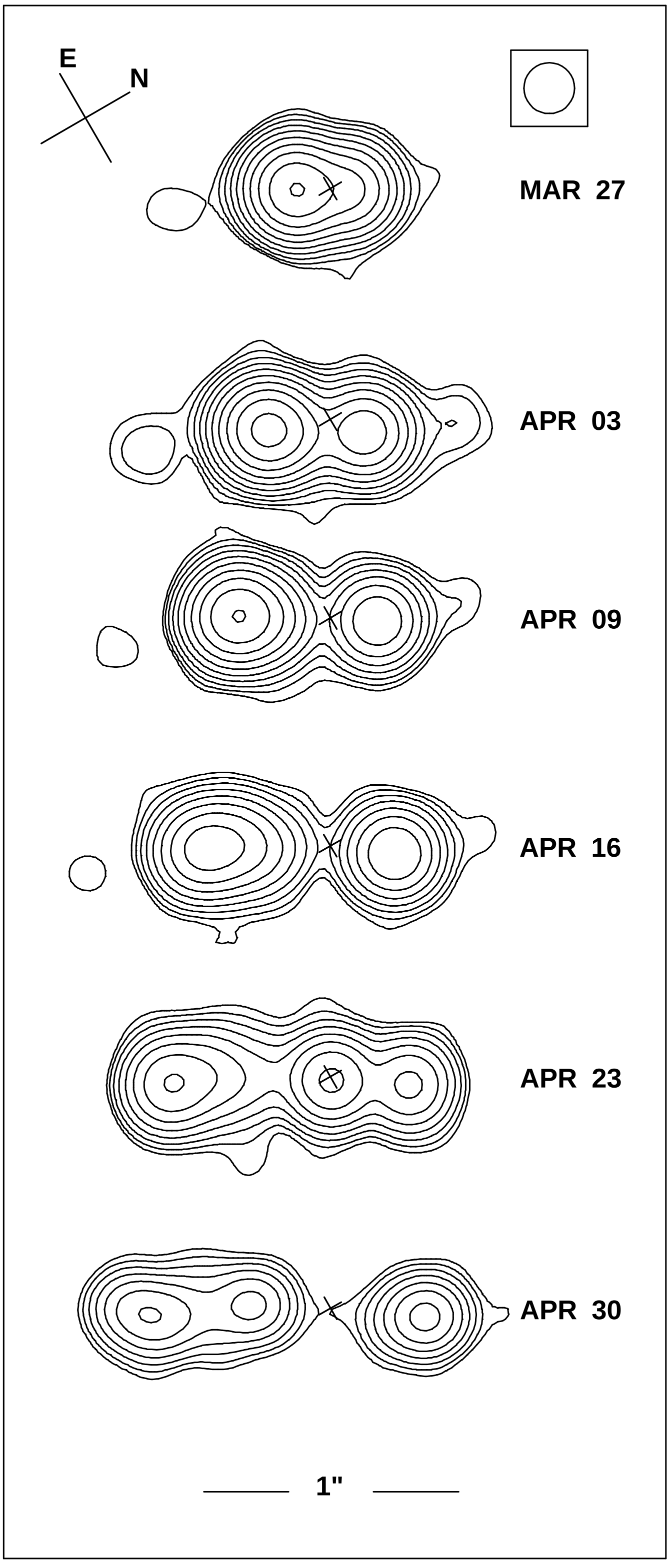

Figure 1.10: The evolution of radio condensations (jets) propagating away from GRS 1915+105, positioned with a cross (×) at the center. (Adopted from Mirabel & Rodríguez [138])

X-ray Spectroscopy for BHBs

X-ray spectroscopy provides a wealth of information about the physical processes and environments near compact objects. The observed spectra of accreting BHs are often composed of multiple components, including thermal emission from the accretion disk, non-thermal coronal emission, and reflection features.

Key spectral components include:

- **Thermal disk emission**: Modeled as a multicolor blackbody (`diskbb`, Makishima et al. [122], Mitsuda et al. [139]; `kerrbb`, Li et al. [111]) originating from the optically thick, geometrically thin accretion disk.
- **Comptonized corona**: A hot, optically thin plasma that up-scatters soft photons into a hard power-law tail. Modeled with `cutoffpl`, `Nthcomp` [217], or similar.
- **Reflection spectrum**: Features such as the Fe Kα line ($\sim$6.4–6.9 keV) [52] and Compton hump ($\sim$20–40 keV) [115], caused by hard X-rays reprocessed in the disk.

Relativistic effects near compact objects cause significant broadening and skewing of the reflection features. Advanced models like `relxill` and `reflionx` [177] incorporate general relativistic ray-tracing to interpret these signatures. Spectral fitting enables measurement of the inner disk radius, inclination, ionization state, and potentially the BH spin.

X-ray Spectroscopy for XRPs

The X-ray spectra of accreting XRPs reflect the complex interplay between strong magnetic fields, accretion dynamics, and radiation processes. Unlike black hole binaries, the accretion flow in XRPs is channeled by the NS's magnetic field onto the magnetic poles, forming accretion columns where the observed X-ray emission originates.

Common spectral components include:

- **Hard X-ray continuum**: Typically modeled with a power law modified by a high-energy cutoff, representing Comptonized emission from the accretion column. Empirical models like `cutoffpl`, `highecut`, or physical models such as `compTT` are often used [15].
- **Cyclotron resonant scattering features (CRSFs)**: Broad absorption-like features caused by resonant scattering of X-rays off electrons in quantized magnetic fields. These features, usually found between 10–70 keV, provide direct measurements of the magnetic field strength [39].
- **Fluorescent iron line**: A narrow Fe Kα line at around 6.4 keV, produced when hard X-rays are reprocessed by relatively cold material in the stellar wind or accretion environment [193].

- **Photoelectric absorption**: Significant absorption at low energies due to dense local material, especially in wind-fed systems. Partial covering models (e.g. `pcfabs`) are frequently used to account for inhomogeneous obscuration.

Phase-averaged spectroscopy provides an overview of the average emission properties, while phase-resolved analysis is essential to capture variations linked to the NS's rotation. These studies offer insights into the structure of the accretion column, the geometry of the magnetic field, and the interaction between the inflowing matter and the stellar surface.

X-ray Timing

Timing analysis is critical for probing dynamical processes on short timescales. Compact objects vary rapidly due to changes in the accretion flow, magnetic field interactions, and relativistic motion.

Key timing tools include:

- **Power spectral densities (PSDs)**: Show the distribution of variability power across frequencies. Often reveals broad-band noise, QPOs, and harmonic structures.
- **Quasi-periodic oscillations (QPOs)**: Narrow peaks in the PSDs associated with disk oscillations, relativistic precession, or magnetospheric interactions. Frequencies can range from $\sim$0.01 Hz to kHz (see a recent review by Ingram & Motta [92]).
- **Lag-energy and lag-frequency spectra**: Measure time delays between energy bands, providing insight into the geometry and causal connections between emission regions [159].

In NSs, coherent pulsations trace the spin of the magnetic field, while burst oscillations reflect surface thermonuclear processes. In BHs, QPOs may encode information about the ISCO, Lense-Thirring precession [13], or accretion instabilities [188].

X-ray Polarimetry

X-ray polarimetry offers a new dimension for studying compact objects, providing geometric and magnetic field information inaccessible through spectroscopy or timing alone.

Polarization in X-rays arises through:

- **Thomson scattering**: In optically thick disks or magnetospheres, this introduces a polarization angle tied to the geometry.
- **Synchrotron or cyclotron emission**: In magnetized plasmas, these mechanisms can produce high degrees of polarization.
- **General relativistic effects**: Near compact objects, strong gravitational lensing and light bending modify the observed polarization degree and angle.

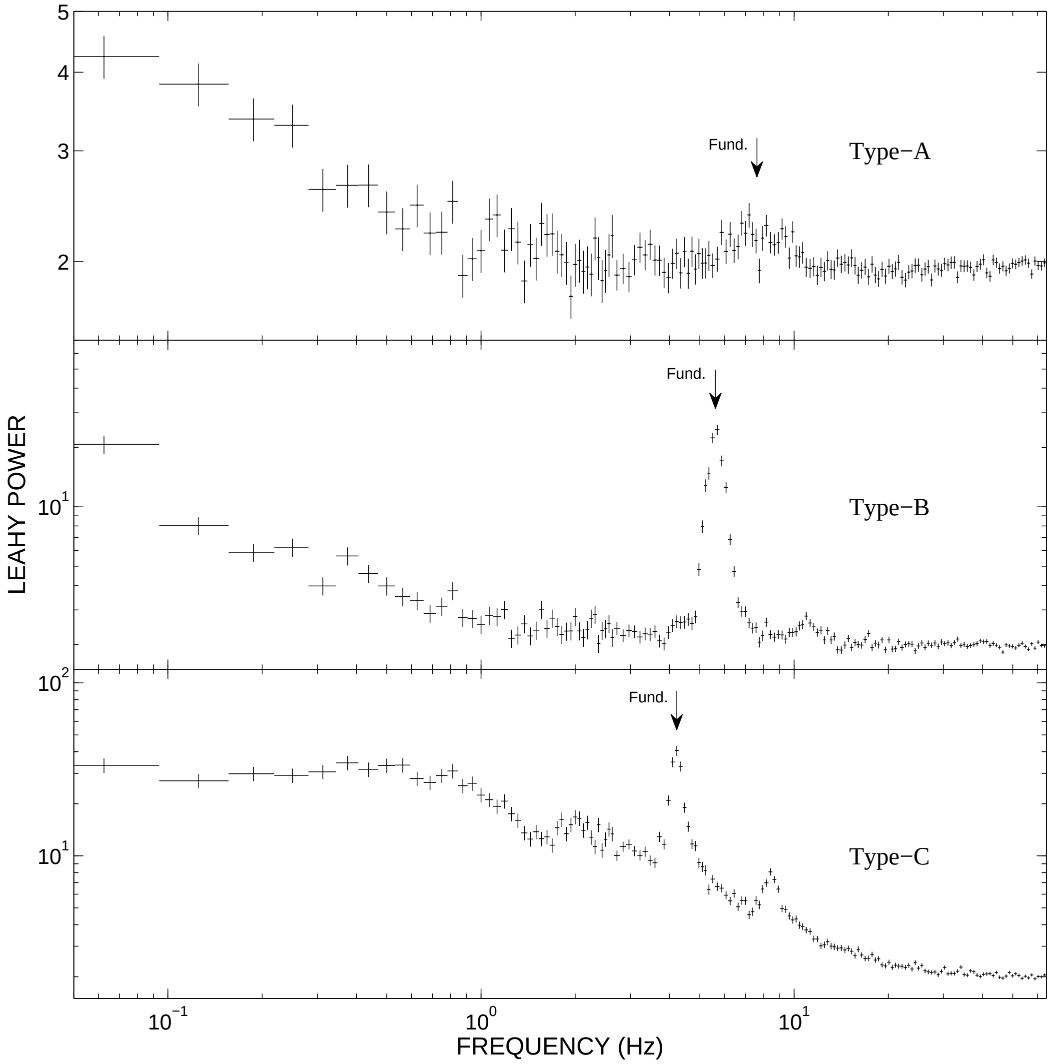

Figure 1.11: The classification of LFQPOs, based on their frequency range, coherence (Q-factor), and amplitude. Type-C QPOs are the most common, characterized by high coherence and strong variability, often associated with the hard and intermediate states. Type-B and type-A QPOs appear at higher accretion rates and show lower amplitude and coherence. (Adopted from Motta et al. [143])

The **Imaging X-ray Polarimetry Explorer (IXPE)** has opened the soft X-ray (2–8 keV) band for polarimetric studies. Its gas pixel detector measures photoelectron directions, enabling determination of the polarization vector.

Polarimetric measurements constrain:

- Disk inclination and corona geometry in BH systems.
- Magnetic field topology in NSs.
- Emission mechanisms in jets and magnetospheres.

Instrumentation and Detector Technologies

Modern X-ray observatories are equipped with specialized instruments designed for imaging, spectroscopy, timing, and polarimetry:

- **Wolter-type optics**: X-rays can only be focused using grazing-incidence mirrors, typically in configurations combining a paraboloid and a hyperboloid. These optics enable high angular resolution, down to sub-arcsecond levels (e.g., *Chandra*).
- **Charge-Coupled Device (CCD) detectors**: Provide imaging capabilities and moderate spectral resolution. CCDs are sensitive to both the energy and arrival time of incoming X-ray photons (e.g., *XMM-Newton*, *Suzaku*).
- **Microcalorimeters**: Enable high-resolution X-ray spectroscopy by precisely measuring the tiny temperature rise caused by the absorption of individual photons (e.g., the Resolve instrument onboard *XRISM*).
- **Gas Pixel Detectors (GPDs)**: Employed in X-ray polarimetry missions such as *IXPE*, GPDs determine the polarization of incoming photons by tracking the initial direction of photoelectron emission.
- **Timing detectors**: Fast detectors such as silicon drift detectors (SDDs), used onboard *NICER*, provide high time resolution down to the microsecond level, crucial for studying fast variability in compact objects.

Each instrument must be calibrated to understand its response, effective area, and background characteristics. Calibration is especially critical for high-resolution and polarimetric measurements, where systematic uncertainties can dominate the signal.

1.2 Outline

The remainder of this dissertation is organized as follows. Chapter 2 provides an overview of the instrumentation used, while Chapter 3 outlines the methods employed for observational data analysis. A summary of the original publications is presented in Chapter 4. Chapters 5–7 contain brief results and discussions for each project. Finally, Chapter 8 concludes the dissertation and offers an outlook for future work.

2 Instrumentations

In the current era of high-energy astrophysics, space-based observatories play a pivotal role in probing the extreme environments surrounding compact objects such as NSs and BHs. The observatories we utilize in this thesis are the Hard X-ray Modulation Telescope (HXMT), the Neutron Star Interior Composition Explorer (NICER), and the Imaging X-ray Polarimetry Explorer (IXPE). Each of these missions is optimized for a particular diagnostic—spectroscopy, timing, or polarimetry—and together they represent a complementary suite of observational tools for studying the physics of strong gravity, dense matter, and relativistic jets.

2.1 Hard X-ray Modulation Telescope (HXMT)

Hard X-ray Modulation Telescope, also dubbed as *Insight*-HXMT or HXMT, is China's first X-ray space observatory, launched on June 15, 2017 by the China National Space Administration [219, 221]. It has three collimated telescopes onboard: the Low Energy (LE) telescope, covering the 1–15 keV band [37]; the Medium Energy (ME) telescope, covering 5–30 keV [34]; and the High Energy (HE) telescope, covering the 25–250 keV band [116], promising simultanous observations with a broad energy band of 1–250 keV. These three telescopes are all aligned to one direction and are designed to observe the same source simultaneously. HXMT runs in a low earth orbit with an inclination angle of 43°.

HXMT combines wide-field monitoring and pointed observation capabilities, enabling both all-sky surveys and targeted studies. It plays a critical role in detecting transient events and monitoring the long-term variability of BH candidates, accreting X-ray binaries, and magnetars. Its high-energy coverage enables observations of spectral state transitions, hard X-ray tails, and Compton reflection in accreting systems. With microsecond-level timing precision in the HE band, HXMT is also suitable for probing fast variability phenomena such as pulsations and QPOs. The mission contributes to

Table 2.1: The main charateristics of the three payloads onborad *Insight*-HXMT.

	LE	ME	HE
Detectors	SCD	Si-PIN	NaI/CsI
Geometrical area	384 cm^2	952 cm^2	5000 cm^2
Energy range (keV)	1–15	5–30	20–250
Time resolution	1 ms	180 μs	25 μs
Energy resolution	2.5% at 6 keV	14% at 20 keV	19% at 60 keV
Data handling capability	$\leq$ 3 Mbp/s	$\leq$ 3 Mbp/s	$\leq$ 300 kbp/s

Figure 2.1: An artist's illustration of Insight-HXMT in space. (Figure from IHE [1])

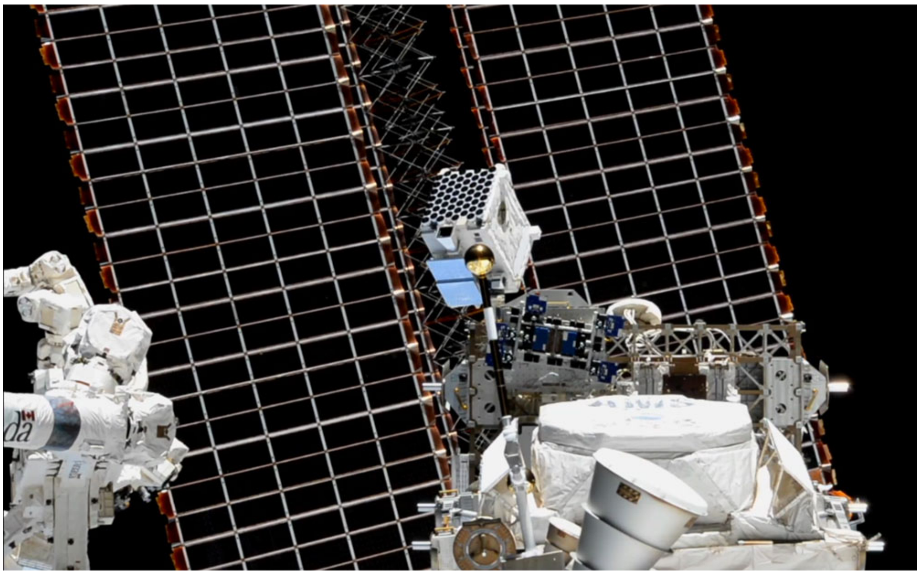

Figure 2.2: NASA NICER Telescope on top of International Space Station. (Figure from `https://svs.gsfc.nasa.gov/13031/`)

multi-messenger astronomy by supporting electromagnetic follow-up of Gamma-ray bursts or gravitational wave events [see e.g., 31].

2.2 Neutron Star Interior Composition Explorer (NICER)

The Neutron Star Interior Composition Explorer (NICER) is a NASA X-ray Explorer Mission that was launched on 3rd June, 2017, and as a commercial resupply mission mounted aboard the International Space Station on the ExPRESS Logistics Carrier-2. It is optimized for soft X-ray observations in the 0.2–12 keV range, with a primary focus on high-precision timing and spectroscopy of NSs [68]. The main instrument of NICER is the X-ray Timing Instrument (XTI).

The XTI comprises a collection of 56 co-aligned X-ray concentrator optics with

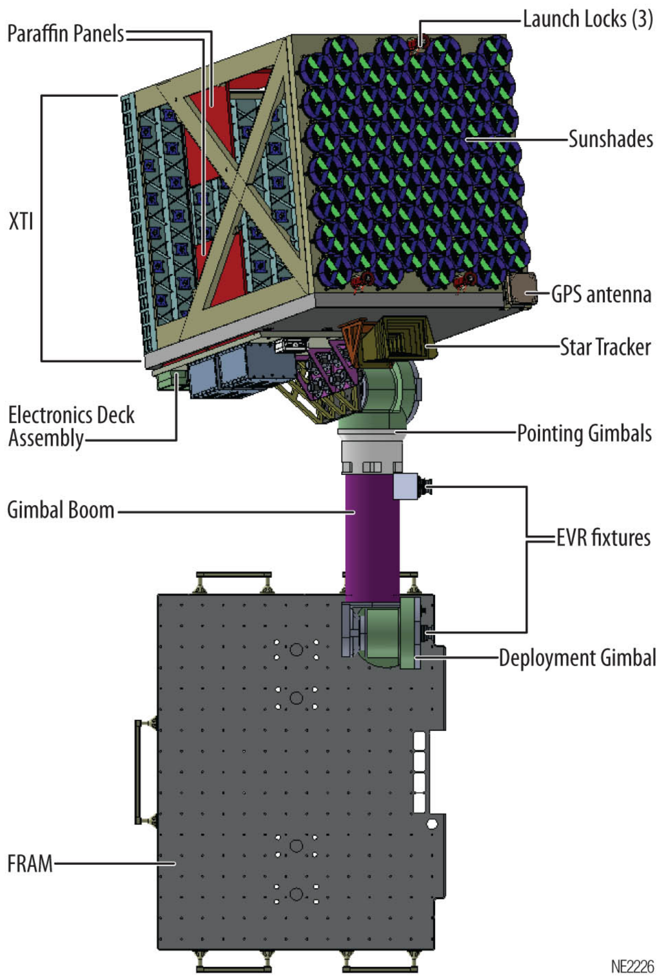

Figure 2.3: Structural overview of the NICER instrument. (Figure from `https://heasarc.gsfc.nasa.gov/docs/nicer/nicer_tech_desc.html`)

matching focal plane modules containing silicon drift detectors, and among them there are 52 function in orbit, extending to a soft X-ray band with a time-tagging resolution of ∼100 nanoseconds, synchronized to GPS-based time references. The energy resolution is ∼85 eV at 1 keV. The X-ray concentrators use grazing incident reflections to focus X-rays.

The mission's core objective is to constrain the EoS of the NSs through precise measurements of mass and radius, obtained via pulse-profile modeling of thermally emitting millisecond pulsars [24]. NICER also observes a wide variety of phenomena including X-ray bursts, accretion-powered millisecond pulsars, and fast variability in BH binaries. The instrument's exceptional timing resolution facilitates the study of strong-gravity effects, such as relativistic precession and frame dragging near the ISCO.

2.3 Imaging X-ray Polarimetry Explorer (IXPE)

The Imaging X-ray Polarimetry Explorer (IXPE), launched by a Falcon 9 rocket on 9th December, 2021, is a joint mission of NASA and the Italian Space Agency. It is

Figure 2.4: Artist's illustration of the IXPE observatory in orbit. (Figure from `https://ixpe.msfc.nasa.gov/multimedia/images/`)

the first dedicated X-ray polarimetry mission, operating in the 2–8 keV range. The payload consists of three identical mirror-detector units employing GPDs, capable of measuring the degree and angle of X-ray polarization while simultaneously collecting imaging, spectral, and timing data [207, 208].

Key capabilities include:

- **Angular resolution**: ~ 30 arcsec (half-power diameter).
- **Effective area**: $\sim 120\,\mathrm{cm}^2$ per telescope at 2 keV.
- **Minimum detectable polarization (MDP)**: a few percent for bright sources.

IXPE enables direct investigation of the magnetic field structure and geometry in X-ray sources, including pulsars, magnetars, supernova remnants, and active galactic nuclei. Polarimetric data help discriminate between emission mechanisms (e.g., synchrotron, Comptonization) and test predictions of quantum electrodynamics (QEDs) such as vacuum birefringence. Early IXPE results have revealed the coronal geometry in Cygnus X-1 [106] and polarization patterns in the Crab Nebula [29], providing new insights into compact object astrophysics.

2.4 Complementarity and Scientific Synergy

HXMT, NICER, and IXPE provide a complementary set of tools for probing high-energy processes in the universe. HXMT offers broad energy coverage and extensive monitoring capability; NICER provides unmatched soft X-ray timing precision and spectral throughput; IXPE introduces a new observational dimension through polarization. Together, these missions allow for multifaceted studies that correlate spectral, timing, and polarimetric data.

Joint observations have the potential to transform our understanding of relativistic accretion, jet formation, NS interiors, and magnetospheric physics. As a coordinated observational framework, these instruments exemplify the increasing role of time-domain and multi-messenger astrophysics in the exploration of extreme cosmic phenomena.

3 Methods: Spectral, Timing and Polarimetric Analyses

3.1 Spectral Analysis

The spectrum represents the energy distribution of photons emitted from the observed source. By fitting the observed spectrum with either phenomenological or physically motivated models, we can quantitatively infer the intrinsic properties of the source. Typically, X-ray detectors measure photon counts in discrete energy channels. The relationship between the observed count spectrum, $C(I)$, and the intrinsic source spectrum, $S(E)$, is given by

$$C(I) = \int S(E) \cdot R(I, E) \cdot A(E) \mathrm{d}E + B(I) \,, \tag{3.1}$$

in which $R(I, E)$ is the normalized instrumental response matrix, $A(E)$ is the effective area of the instrument, and $B(I)$ represents the background spectrum.

In general, the response matrix $R(I, E)$ is not guaranteed to be invertible. As a result, directly inverting the observed count spectrum $C(I)$ to recover the intrinsic source spectrum $S(E)$ can lead to large uncertainties. To avoid this, the standard approach is to assume a spectral model for $S(E)$, fold it through the response matrix to obtain the expected counts, and then compare these to the observed data in count space rather than flux space.

3.1.1 Models in Spectral Fitting

Below is a brief summary of commonly used models in X-ray spectral fitting, with a focus on those adopted in this thesis.

Phenomenologial Models

Analytical models are often employed to phenomenologically describe the spectral continuum. These include `powerlaw`, `cutoffpl`, `bknpower`, `highecut`, and `edge`. The models `powerlaw`, `cutoffpl`, `bknpower`, and `highecut` are particularly useful for approximating the Comptonized continuum, depending on the energy range of interest and often in conjunction with physical models. The key parameters and mathematical formulations of these models are outlined below. Please note that additive models are represented by $A(E)$ and multiplicative models are represented by $M(E)$.

`powerlaw`:

$$A(E) = K \cdot E^{-\Gamma}\,, \tag{3.2}$$

where Γ is the photon index.

`cutoffpl`:

$$A(E) = K \cdot E^{-\Gamma} \exp\left(-\frac{E}{E_{\rm fold}}\right)\,, \tag{3.3}$$

with Γ being the photon index and $E_{\rm fold}$ the folding enenrgy.

`bknpower`:

$$A(E) = \begin{cases} K \cdot E^{-\Gamma_1}\,, & \text{if } E \leq E_{\rm break}\,, \\ K \cdot {E_{\rm break}}^{-\Gamma_1+\Gamma_2} \cdot E^{-\Gamma_2}\,, & \text{if } E > E_{\rm break}\,, \end{cases} \tag{3.4}$$

where Γ_1 and Γ_2 are the two photon indeces for the energy bands below and above the breaking energy $E_{\rm break}$, respectively.

`highecut`:

$$M(E) = \begin{cases} 1\,, & \text{if } E \leq E_{\rm cut}\,, \\ \exp\left(-\frac{E-E_{\rm cut}}{E_{\rm fold}}\right)\,, & \text{if } E > E_{\rm cut}\,. \end{cases} \tag{3.5}$$

A high-energy cutoff model with two parameters: the cutoff energy $E_{\rm cut}$ and the folding energy $E_{\rm fold}$.

`edge`:

$$M(E) = \begin{cases} 1\,, & \text{if } E \leq E_{\rm threshold}\,, \\ \exp\left[-D \cdot \left(\frac{E}{E_{\rm threshold}}\right)^{-3}\right]\,, & \text{if } E > E_{\rm threshold}\,. \end{cases} \tag{3.6}$$

a model used to characterize photoelectric absorption edges, where D represents the edge depth and $E_{\rm threshold}$ the edge energy.

`Nthcomp` [217]

`Nthcomp` provides a more physically accurate representation of thermal Comptonization compared to the `cutoffpl` model. The high-energy rollover is sharper and characterized by the electron temperature $kT_{\rm e}$. A significant feature, especially relevant for XRBs, is the model's inclusion of the low-energy turnover due to seed photon upscattering. Below the typical seed photon energy, the Comptonized spectrum significantly deviates from a power law.

The seed photons are typically described by a blackbody or disk blackbody spectrum, parameterized by a seed photon temperature $kT_{\rm bb}$. The spectral shape between the low- and high-energy turnovers is determined by the electron temperature and the optical depth of the scattering medium, often approximated by an asymptotic photon index Γ.

`TBabs` [210]

Tübingen-Boulder ISM absorption model. It computes X-ray absorption cross sections through contributions from gas-phase, grain-phase, and molecular components of the ISM. The model accounts for shielding by interstellar grains (a minor effect), and includes only molecular hydrogen among molecular species.

The gas-phase cross section includes the sum of photoionization cross sections of elements weighted by updated interstellar abundances, which are selectable via the "`abund wilm`" command in `Xspec`. For further details on the updated photoionization cross sections and abundances, refer to Verner et al. [202], Wilms et al. [210].

`diskbb` [122, 139]

`diskbb` models the thermal emission from a geometrically thin, optically thick accretion disk composed of multiple blackbody components. The temperature profile follows $T(r) \propto r^{-\frac{3}{4}}$, leading to a multicolor blackbody spectrum representative of a standard accretion disk.

`xillverCp` & `relxillCp`

`xillverCp` is a physically motivated reflection model that computes the angle-dependent reflection spectrum from an optically thick, plane-parallel accretion disk illuminated by a power-law X-ray source (described by `Nthcomp`). The model includes photoelectric absorption, fluorescence emission lines (most notably the iron Kα line), and Compton scattering in a self-consistent manner. It incorporates detailed atomic data and solves the radiative transfer equations through the illuminated atmosphere, making it particularly well-suited for modeling the reflection features observed in the hard X-ray band. Key parameters include the ionization parameter $(\log \xi)$[1], iron abundance (A_{Fe}), and the photon index (Γ) of the incident spectrum. A comprehensive description is provided by García & Kallman [65] and García et al. [64].

`relxillCp` extends the model `xillverCp` by convolving it with relativistic effects expected in the strong gravity regime near a BH, using the relativistic blurring kernel `relline` [45]. It simulates the observed spectrum from an accretion disk extending down to a few gravitational radii, accounting for Doppler boosting, gravitational redshift, and light bending. These features make `relxillCp` particularly powerful for constraining the geometry of the corona (modeled here with a broken power-law emissivity profile characterized by indices q_{in} and q_{out}, and a break radius r_{br}), as well as the disk inclination (i) and the BH spin (a_*).

These models are among the most widely used tools in X-ray spectral analysis of AGNs and XRBs, where reflection features are prominent and affected by strong gravity near compact objects.

[1]The ionization parameter ξ is defined as $\xi = L_{\mathrm{X}} / \left(N_{\mathrm{e}} \cdot r^2\right)$, where L_{X} is the X-ray luminosity of the source, N_{e} is the electron number density of the plasma, and r is the distance between the plasma and the emitting source. See Tarter et al. [190].

3.2 Timing Analysis

In this section, I will introduce the commonly-used methods in X-ray timing analysis. The formulae and calculations are followed. For more details of the Fourier-related analysis, please refer to van der Klis [198] and Nowak et al. [159].

3.2.1 Fourier Techniques

Photon arrivals at an X-ray detector are typically recorded based on their arrival time, energy, and position on the observer plane. Using these data, we can construct a time series with uniformly spaced timestamps, each representing the flux within the corresponding time interval:

$$x(t) = [x(t_0), x(t_1), x(t_2), x(t_3), ..., x(t_{N-1})] \,, \tag{3.7}$$

This is the so-called light curve.

The discrete Fourier transform (DFT) is often regarded as the initial approach to uncovering potential periodicity hidden within a time-dependent series. The formula reads

$$X_j = \sum_{k=0}^{N-1} x_k \exp\left(-\frac{2\pi \mathbf{i} jk}{N}\right) , \tag{3.8}$$

where x_k denotes the $(k+1)$-th component $x(t_k)$.

The corresponding Fourier frequencies are given by

$$f_j = \frac{j}{T} = \frac{j}{N \cdot \Delta t} \,, \tag{3.9}$$

where $j \in [0, N-1]$, and $T = N \cdot \Delta t$ is the length of the light curve. Consequently, the flux decomposition as a function of frequency can be expressed as

$$\begin{aligned} x_k &= \frac{1}{N} \sum_{j=0}^{N-1} X_j \exp\left(\frac{2\pi \mathbf{i} jk}{N}\right) \\ &= \frac{1}{N} \sum_{j=0}^{N-1} X_j \exp\left(2\pi \mathbf{i} \cdot f_j \cdot \Delta t \cdot k\right) , \end{aligned} \tag{3.10}$$

which defines the inverse discrete Fourier transform (IDFT).

We notice that $\exp\left(\frac{2\pi \mathbf{i} jk}{N}\right) = \exp\left[-\frac{2\pi \mathbf{i}(N-j)k}{N}\right]$, which implies that frequencies corresponding to indices $j > N/2$ are typically considered negative frequencies[2]

[2]The Fourier frequencies are

$$\left[0, \frac{1}{N \cdot \Delta t}, \dots, \frac{N/2-1}{N \cdot \Delta t}, \frac{N/2}{N \cdot \Delta t}, -\frac{N/2-1}{N \cdot \Delta t}, \dots, -\frac{1}{N \cdot \Delta t}\right]$$

if N is even, or

$$\left[0, \frac{1}{N \cdot \Delta t}, \dots, \frac{(N-1)/2}{N \cdot \Delta t}, -\frac{(N-1)/2}{N \cdot \Delta t}, \dots, -\frac{1}{N \cdot \Delta t}\right]$$

if N is odd. Negative frequencies are denoted by red.

Since each pair of positive and negative frequencies results in DFT components that are complex conjugates when x_k is real, we discard the negative frequencies and focus solely on the positive ones.

In some literatures we can also see another definition of DFT by

$$X_j = \sum_{k=0}^{N-1} x_k \exp\left(\frac{2\pi \mathbf{i} jk}{N}\right). \tag{3.11}$$

This definition is identical to the previous one, as the corresponding frequencies follow the formulas below:

$$j = \begin{cases} -\frac{N}{2}, \ldots, \frac{N}{2} - 1 & \text{if } N \text{ is even,} \\ -\frac{N-1}{2}, \ldots, \frac{N-1}{2} & \text{if } N \text{ is odd.} \end{cases} \tag{3.12}$$

In fact, this alternative definition swaps the left and right halves of the transform's result and reverses the output, ultimately preserving the bijection between the DFT and the corresponding frequencies.

Practically, we prefer to set N as a power of 2 to enable the Fast Fourier Transform (FFT). In this case, N is even. The minimum nonzero frequency is given by $f_{\rm min} = 1/T = 1/(N\Delta t)$, while the highest physical frequency, known as the *Nyquist frequency*, is $f_{\rm max} = 1/(2\Delta t)$.

3.2.2 Power Spectral Density and Cross Spectrum

The power spectral density (PSD) is a real quantity to represent the squared magnitude of the complex products of DFT of a time series:

$$P(\nu_j) = X_j^* X_j = |X_j|^2 \,. \tag{3.13}$$

The uncertainties of the PSD are on the same order of magnitude as the PSD values themselves. However, these uncertainties can be reduced by averaging over more samples (as the mean value of the power scales with $1/\sqrt{N}$, in which N is the sample number). We can average the PSDs not only across multiple segments of a long light curve but also within different frequency bins to reduce the uncertainties of the PSD.

The Normalization of the PSDs

The normalization of PSDs is considered to facilitate the comparison of light curve PSDs from different sources with varying flux levels. Here, I introduce two normalization methods: the Leahy normalization [109] and the fractional rms-squared normalization, also known as rms normalization or Miyamoto normalization [18, 141]. Both methods are designed to scale the Poisson noise in a real PSD to its expected value.

$$P_{\rm Normalized}(\nu_j) = \begin{cases} 1 \cdot X_j^* X_j \,, & \text{unnormalized}\,, \\ \frac{2}{R \cdot T} \cdot X_j^* X_j \,, & \text{Leahy norm}\,, \\ \frac{2}{R^2 \cdot T} \cdot X_j^* X_j \,, & \text{fractional rms norm}\,, \end{cases} \tag{3.14}$$

where R is the mean count rate and T denotes the length of each segment.

The expectation value of the Poisson noise under each normalization[3] is

$$\langle N_{\text{Poisson}} \rangle = \begin{cases} R \cdot T\,, & \text{unnormalized}\,, \\ 2\,, & \text{Leahy norm}\,, \\ \frac{2}{R}\,, & \text{fractional rms norm}\,, \end{cases} \tag{3.15}$$

Leahy normalization and fractional rms normalization each offer distinct advantages. Leahy normalization allows for straightforward estimation and subtraction of Poisson noise. In contrast, fractional rms normalization makes the PSDs independent of the source's mean count rate, enabling direct comparison of timing properties across sources with different luminosities, masses, or spectral states.

3.2.3 The Cross Spectrum and Lag Spectrum

Let x_k and y_k be two light curves with identical time resolution (Δt) and total duration (T). The cross spectrum between the two light curves is defined as

$$C(\nu_j) = X_j^* Y_j\,, \tag{3.16}$$

where X_j and Y_j are the DFTs of x_k and y_k, respectively. Unlike the PSDs, the cross spectrum is generally a complex quantity. When multiple segments of equal length are available, the cross spectrum can be averaged across segments to improve statistical robustness.

In practice, the real and imaginary components of the cross spectrum do not have straightforward physical interpretations on their own. Therefore, any physical conclusions drawn from either component should be made with caution.

However, the phase lag between two light curves can be defined using the argument of the cross spectrum:

$$\phi(\nu_j) = \arg\left[C\left(\nu_j\right)\right]\,. \tag{3.17}$$

This phase lag $\phi(\nu_j)$ can be related to its corresponding Fourier frequency ν_j to yield the time lag:

$$\delta t(\nu_j) = \frac{\phi(\nu_j)}{2\pi\nu_j}\,, \tag{3.18}$$

which represents the time delay, at each frequency band ν_j, between the two light curves x_k and y_k.

It is important to note that phase lags are inherently limited to the range $(-\pi, \pi]$ due to their periodic nature. Consequently, the corresponding time lags $\delta t(\nu_j)$ also have a bounded absolute value, especially at low frequencies where small changes in phase

[3]The following results rely on Parseval's theorem for the DFT, which states:

$$\sum_{k=0}^{N-1} |x_k|^2 = \frac{1}{N}\sum_{j=0}^{N-1} |X_j|^2\,.$$

We present the results below without providing the detailed derivations.

can result in large variations in δt. As a result, it is not always straightforward to connect measured phase or time lags directly to specific physical processes.

Nevertheless, the phenomenological behavior of phase and time lags—such as their energy or frequency dependence—can still provide valuable insights into the geometry and dynamics of the emitting regions.

3.2.4 The Coherence Function

The *coherence function* quantifies the linear correlation between variations in two light curves as a function of Fourier frequency. In X-ray astronomy, it is commonly used to measure how strongly variability in one energy band is related to that in another, providing insights into the coupling between different emission components such as the accretion disk and corona.

The squared coherence function is defined as:

$$\gamma^2(\nu_j) = \frac{|\langle C(\nu_j)\rangle|^2}{\langle|X(\nu_j)|^2\rangle \, \langle|Y(\nu_j)|^2\rangle} \,, \tag{3.19}$$

where $C(\nu_j)$ is the cross spectrum between the two light curves x_k and y_k, and $X(\nu_j)$, $Y(\nu_j)$ are their respective DFTs. The angle brackets $\langle\cdot\rangle$ denote averaging over multiple segments to improve statistical reliability.

The coherence function takes values between 0 and 1: $\gamma^2(\nu) = 1$ indicates perfect linear correlation at frequency ν; $\gamma^2(\nu) \ll 1$ indicates weak or no correlation, possibly due to intrinsic non-linearities or uncorrelated noise.

In practice, coherence estimates must be corrected for Poisson noise and other biases to avoid overestimating correlation strength, especially at high frequencies or low signal-to-noise ratios. High coherence across a wide frequency range suggests a stable and tightly coupled system, while dips in coherence may reflect changes in spectral state, physical disconnection between emission regions, or the presence of incoherent variability components. Here we adopt the intrinsic coherence function that is proposed by Vaughan & Nowak [201]:

$$\gamma^2(\nu_j) = \frac{|\langle C_{XY}(\nu_j)\rangle|^2 - n^2}{\langle P_X(\nu_j)\rangle \cdot \langle P_Y(\nu_j)\rangle} \,, \tag{3.20}$$

in which

$$n^2 = \frac{1}{KM}\left[(\langle P_X(\nu_j)\rangle - N_X) \cdot N_Y + (\langle P_Y(\nu_j)\rangle - N_Y) \cdot N_X + N_X \cdot N_Y\right] . \tag{3.21}$$

Here the noise components of the light curves x_k and y_k are denoted by N_X and N_Y, respectively.

3.3 Polarimetric Analysis

Polarization describes the orientation and coherence properties of the electric field vector of an electromagnetic wave. In astrophysics, polarization measurements provide valuable diagnostic information about the geometry, magnetic fields, and emission mechanisms of radiation sources, especially when combined with spectral and timing observations. For instance, X-ray polarization can reveal the structure of relativistic jets, probe the geometry of accretion disks around compact objects, and test predictions of strong gravity and quantum electrodynamics in extreme environments.

The polarization state of electromagnetic radiation is completely described by the four *Stokes parameters*: I, Q, U, and V. These parameters encode the total intensity, the degree and orientation of linear polarization, and the presence of circular polarization. Mathematically, they are defined as follows:

$$I = \langle E_x^2 + E_y^2 \rangle \,, \tag{3.22}$$

$$Q = \langle E_x^2 - E_y^2 \rangle \,, \tag{3.23}$$

$$U = \langle 2E_x^2 E_y^2 \cos\delta \rangle \,, \tag{3.24}$$

$$V = \langle 2E_x^2 E_y^2 \sin\delta \rangle \,. \tag{3.25}$$

- $I = \sqrt{Q^2 + U^2 + V^2}$: the total intensity of the radiation beam.
- Q: the difference in intensity between linearly polarized components aligned with the horizontal (0°) and vertical (90°) axes.
- U: the difference in intensity between linear polarizations at +45° and −45° to the reference axis.
- V: the difference in intensity between right-handed and left-handed circularly polarized components.

Together, these parameters form a vector representation of the polarization state:

$$\mathbf{S} = \begin{pmatrix} I & Q & U & V \end{pmatrix} \,. \tag{3.26}$$

In most astrophysical X-ray sources, circular polarization (V) is negligible, and the analysis focuses on linear polarization described by Q and U. From these components, the degree of linear polarization P and the polarization angle ψ can be derived as:

$$P = \frac{\sqrt{Q^2 + U^2}}{I} \,, \qquad \psi = \frac{1}{2} \arctan\left(\frac{U}{Q}\right) \,. \tag{3.27}$$

Here, P quantifies the fraction of the total light that is linearly polarized, while ψ gives the orientation of the polarization vector projected onto the plane of the sky. For a more comprehensive discussion, we refer the reader to Kislat et al. [99], upon which the following analysis is based, along with the references therein.

3.3.1 Polarization Measurements in X-rays

The measurement of X-ray polarization is technically challenging due to the inherently low degree of polarization and the limited photon statistics typically available. Modern X-ray polarimeters, such as those onboard IXPE, utilize the photoelectric effect to infer polarization properties. When an X-ray photon is absorbed in a gas pixel detector,

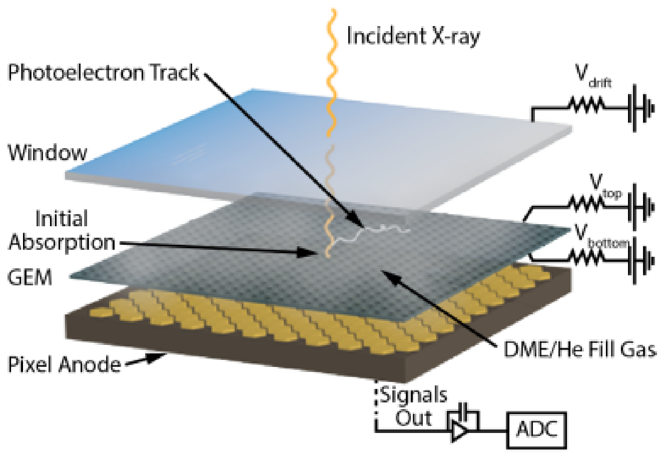

Figure 3.1: Schematic diagram of the polarization-sensitive GPD onboard the IXPE mission. (Figure from Weisskopf et al. [207])

it ejects a photoelectron preferentially in the direction of the electric field vector of the incident photon (see Fig. 3.1). By measuring the azimuthal angle distribution of photoelectron tracks, one can reconstruct the polarization degree and angle of the incoming radiation.

The observed modulation curve, i.e., the histogram of azimuthal angles, can be modeled as:

$$N(\phi) \propto \frac{1}{2\pi} \left(1 + P\mu \cos\left(2\left(\phi - \psi\right)\right)\right) , \tag{3.28}$$

where $N(\phi)$ is the count rate as a function of azimuthal angle ϕ, P is the polarization degree, μ is the modulation factor (a measure of the instrument's sensitivity to polarization), and ψ is the polarization angle. The modulation factor depends on the energy of the incident photons and the detector properties, and must be calibrated for accurate polarization measurement.

For an X-ray polarimeter, it records photons with the most probable value of ψ_k, the measured polarization angle for each photon event, and sum the Stokes parameters for N photons. We can introduce the normalized Stokes parameters: i_k, q_k and u_k as follows:

$$i_k = 1 , \qquad q_k = \cos 2\psi_k , \qquad u_k = \sin 2\psi_k . \tag{3.29}$$

The Stokes parameters of the entire observation are given by:

$$I = \sum_k i_k = N , \tag{3.30}$$

$$Q = \sum_k q_k , \tag{3.31}$$

$$U = \sum_k u_k , \tag{3.32}$$

The normalized Stokes parameters are then defined as:

$$\mathcal{Q} = Q/I , \tag{3.33}$$

$$\mathcal{U} = U/I , \tag{3.34}$$

and they follow a bivariate normal distribution:

$$P(\mathcal{Q},\mathcal{U}) = \frac{1}{2\pi\sigma^2} \exp\left[-\frac{(\mathcal{Q}-\langle\mathcal{Q}\rangle)^2 + (\mathcal{U}-\langle\mathcal{U}\rangle)^2}{2\sigma^2}\right] . \tag{3.35}$$

The uncertainties in the normalized Stokes parameters $\mathcal{Q}$ and $\mathcal{U}$ are derived from the observational data, and those of the polarization degree and angle are inferred from their respective statistical distributions.

Practically, polarimetric measurements must account for both the effective area and the modulation factor of the instrument when registering photons across different energies. In this section, I introduce two algorithms for determining the normalized Stokes parameters, each incorporating the energy-dependent instrument response, including the effective area and modulation factor.

`pcube` method

The `pcube` method ignores the full energy response matrix but accounts for energy dependence by weighting individual photon contributions. All photons detected within the selected time interval and energy band are used to compute the Stokes parameters via weighted summation:

$$I = \sum_k \frac{1}{A\left(E_k\right)} , \tag{3.36}$$

$$Q = \sum_k \frac{q_k}{\mu\left(E_k\right) \cdot A\left(E_k\right)} , \tag{3.37}$$

$$U = \sum_k \frac{u_k}{\mu\left(E_k\right) \cdot A\left(E_k\right)} , \tag{3.38}$$

where $A\left(E_k\right)$ is the instrumental effective area and $\mu\left(E_k\right)$ is the modulation factor of the instrument at the energy of the k-th photon.

The normalized Stokes parameters can be simply derived by

$$\mathcal{Q} = Q/I\,, \qquad \mathcal{U} = U/I\,.$$

This method enables a straightforward estimation of polarization parameters without requiring an *a priori* spectral model, while fully accounting for the instrument's energy-dependent sensitivity and modulation efficiency.

XSPEC method

In contrast to the `pcube` method, the XSPEC method incorporates the full energy response of the instrument. It generates three spectra by summing the Stokes parameters into their respective energy channels. Additionally, it produces a response matrix file (one `.rmf` file) and two auxiliary response files (one `.arf` file and one `.mrf` file), which contain information about the instrument's effective area and modulation factor.

For photon events recorded by a single detector, this approach yields three separate spectra—corresponding to the Stokes I, Q, and U components—which can be loaded into `Xspec` for spectral fitting. Compared to the `pcube` method, this approach requires both a spectral model to describe the I spectrum and an energy-dependent polarization model to characterize the Q and U spectra. A variety of polarization-sensitive models can be applied, with the most commonly used being `polconst`, which assumes a constant polarization degree and polarization angle across all energies.

4 Summary of the Original Publications

In this chapter, I outline the contexts, objectives and main methods presented in Zhou et al. [226], Zhou et al. [227] and Zhou et al. [225], which are provided in the Appendix. The main results will be discussed in Chapters 5–7. For further details, readers are encouraged to refer to the original publications.

4.1 Spectral-Timing Analysis of Cygnus X-1 [226]

4.1.1 Background and Motivation

BHBs are binary systems where a stellar-mass BH accretes matter from a companion star, producing X-ray emission as gravitational energy is converted into radiation. This emission is often highly variable and offers a window into the dynamics of accretion and the geometry of the innermost regions around BHs. A hallmark of transient BHBs is their dramatic outbursts, during which they follow a well-defined sequence of spectral states, typically represented as a q-shaped track in the HID [57, 85]. These transitions—from a faint quiescent state to a luminous soft state via intermediate and hard states—are accompanied by changes in timing properties, jet activity, and accretion flow geometry [46, 173].

Cygnus X-1 stands out among BHBs as a rare example of a persistent source. Unlike the majority of transient systems, it does not trace the canonical q-track but remains in either the hard or soft state for extended periods [25, 27, 206]. Spectral state transitions in Cygnus X-1 occur irregularly and are often subtler, yet are thought to be associated with major shifts in the accretion geometry, sometimes coinciding with the emergence of compact jets [189]. In the hard state, the X-ray spectrum exhibits a power-law with photon index $\Gamma \lesssim 2.0$, while in the soft state, thermal disk emission dominates, often accompanied by a steep power-law tail ($\Gamma \gtrsim 2.7$) [192].

The physical mechanism behind these transitions continues to be a central topic of debate. The truncated disk model has emerged as a leading framework: in this picture, the accretion disk is truncated at some radius, with a hot, optically thin inner flow or corona filling the gap [90, 151, 152]. This model explains many observed spectral-timing correlations and has gained support from numerical simulations and observational studies [71, 161, 185]. However, alternative interpretations focusing on the evolution of the inner disk and reflection features, such as the iron Kα line, suggest a more complex interplay of components [66, 67, 184].

Spectral-timing analysis provides a powerful means of probing these processes, particularly at energies where the reflection component becomes significant. Previous

Table 4.1: Start dates and end dates of the HXMT observations.

Proposal ID	Start Date (MJD)	End Date (MJD)
P0101315	2017-08-24 (57989)	2019-06-12 (58646)
P0201012	2019-07-11 (58675)	2020-04-27 (58966)
P0305079	2020-08-08 (59069)	2020-09-25 (59117)

studies using *RXTE*/PCA have revealed correlations between timing features and spectral properties in Cygnus X-1 [6, 164, 179]. The *Insight*-HXMT mission now enables spectral-timing investigations at higher energies (above 15 keV), providing new constraints on the behavior of the corona and the reflection region. This work aims to extend our understanding of the mechanisms governing state transitions and accretion physics in this uniquely persistent source.

The aim of this research is to investigate the spectral characteristics and energy-resolved timing properties of Cygnus X-1 at higher energies, as previously identified by, e.g., Böck et al. [23], Grinberg et al. [76].

4.1.2 Methods

In this study, we employ spectral-timing analysis to examine the spectral and temporal behavior of the BH binary Cygnus X-1, using data from Insight-HXMT satellite. The satellite is equipped with three telescopes: LE (1–15 keV), ME (5–30 keV), and HE (25–250 keV). These instruments provide a comprehensive view of the X-ray emission from Cygnus X-1, allowing us to explore both its spectral and timing properties in greater detail than previous missions.

The data from three separate observation proposals were used in this study (see Table 4.1), which cover different spectral states of Cygnus X-1. The observations were processed using the HXMT Data Analysis Software (HXMTDAS) and the corresponding calibration database, with good time intervals (GTIs) selected based on specific criteria, including elevation angle, cut-off rigidity, and offset angle [77, 113, 114]. The light curves were generated for the timing analysis, and energy spectra were extracted using tools such as `ISIS` and `Xspec` for spectral fitting. The energy ranges selected for the spectral analysis are 2–10 keV for LE, 10–30 keV for ME, and 28–120 keV for HE. For timing analysis, the light curves were binned with a time resolution of approximately 2 ms, and the corresponding PSDs were calculated, correcting for Poisson noise and dead-time effects [222].

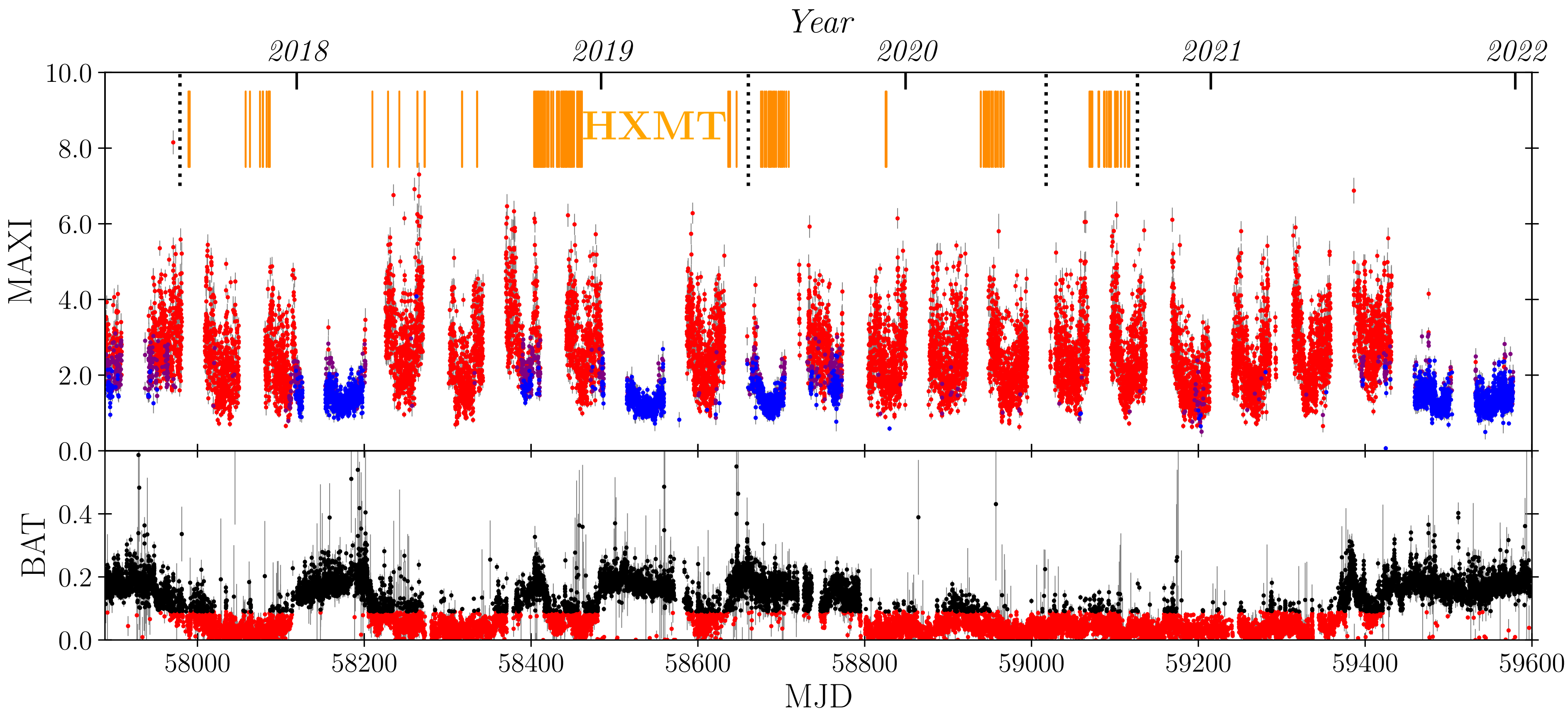

Figure 4.1: Long-term behavior of Cygnus X-1 measured by all-sky monitors MAXI and *Swift*-BAT. We follow the same approaches of state definition proposed by Grinberg et al. [75]. In the *upper panel*, the hard, intermediate, and soft states are denoted by blue, purple, and red points, respectively. In the *lower panel*, the unclassified and soft states are plotted with black and red points, respectively. The duration of HXMT observations on Cygnus X-1 is shown in dark orange stripes at the top. (Adopted from Zhou et al. [226])

The energy-dependent timing properties were studied by dividing the energy bands for each telescope into multiple proper sub-bands. The timing analysis aimed to explore the variability across these energy ranges, particularly the low-frequency quasi-periodic oscillations (LFQPOs) observed in the hard and intermediate states of BHBs [92, 209]. Furthermore, the power spectrum of the source was examined to assess the evolution of the spectral features and time-lags between different energy bands, which can provide crucial insights into the geometry and physics of the accretion flow.

In addition to the spectral and timing analysis, the long-term behavior of the source was examined by generating an HID based on the LE data. The HID provides a clear view of the source's state transitions and allows for comparison across different spectral states, from the hard state to the soft state, which are most stable in Cygnus X-1 [75, 131]. By analyzing the timing properties of Cygnus X-1 across these states, we aim to deepen our understanding of the accretion processes and the nature of the state transitions in BHB systems.

4.2 The Dimming GRS 1915+105 [227]

4.2.1 Background and Motivation

BHBs, consisting of a stellar-mass BH accreting material from a companion star, serve as cosmic laboratories for studying high-energy astrophysical phenomena. Among these, GRS 1915+105 is a particularly remarkable case. Discovered in 1992 by the GRANAT/WATCH experiment [35, 36], it has captivated the astrophysics community with its complex and extreme behaviors. This system exhibits a remarkable array of phenomena: superluminal radio jets [138], high-frequency quasi-periodic oscillations (HFQPOs) [142], and highly ionized disk winds [110, 196]. Its light curves are so distinctive that they have been empirically classified into at least 14 variability classes [5, 20, 78, 100, 181, 228], offering unique insights into accretion physics, disk-jet coupling, and wind formation.

For over two decades following its discovery, GRS 1915+105 maintained a persistently high luminosity, an unusually long outburst duration among BHBs. In 2018, however, its flux began to decline, possibly signaling the end of this prolonged active phase [153]. This dimming was accompanied by evolving timing signatures, including strong low-frequency QPOs [102], and was punctuated by transient radio and X-ray flares [101, 144, 145]. Despite the dramatic decrease in luminosity, evidence of continued accretion activity persisted, suggesting a more complex transition into quiescence than seen in typical transients. Notably, in 2021, the detection of extremely low-frequency QPOs ($\simeq$0.2 Hz) marked a new regime in its variability behavior [104].

The physical interpretation of such behavior remains challenging. As in other BHBs, the standard HID framework captures the gross evolution of spectral states [57, 85]. In the hard state, power-law emission dominates, and jets are prominent; in the soft state, thermal disk emission and ionized winds become more pronounced. GRS 1915+105, however, complicates this narrative. Its LFQPOs exhibit a negative correlation with spectral hardness up to at least 90 keV [183, 216, 226], and its highly ionized winds—evident in features such as Fe XXV Heα and Fe XXVI Lyα—are indicative of powerful outflows during soft states [135, 154, 196].

The drivers of these winds remain uncertain. Potential mechanisms include radiation pressure at high Eddington ratios [84, 168], thermal heating of the disk atmosphere [17, 47, 212], and magnetic acceleration [63]. Furthermore, the presence of clumpy, rapidly varying absorption structures—observed in both BHBs and AGNs—adds complexity to the picture [9, 103, 146, 147]. Understanding these mechanisms in GRS 1915+105 may provide broader insights into the nature of accretion and feedback processes across BH mass scales [129].

The goal of this work is to investigate the properties of the rarely observed disk winds with moderate ionization ($3 \leq \log \xi \leq 4$) in the hard state, and to compare them with the more commonly detected winds in the soft state of the same source. We also examine whether the disk winds in the hard state are related to the observed dimming of the source.

4.2.2 Methods

In this study, we focus on the period just before GRS 1915+105 entered its obscured state, using all public data observed between MJD 57932 (June 8, 2017) and MJD 58608 (May 5, 2019). The data were obtained from the XTI of NICER and Insight-HXMT. These instruments provide simultaneous broadband X-ray coverage that allows for detailed spectral-timing analysis. The analysis was performed by tracing the evolution of key parameters and probing their correlations using the data from both instruments, which offer complementary energy coverage.

The spectral-timing analysis used joint data from NICER and HXMT, leveraging the broadband coverage provided by both instruments. This combined approach enabled a more comprehensive understanding of the source's behavior during its transition into a quiescent state. The NICER data were processed using the standard `HEASOFT` tools, with stringent screening criteria to minimize background contamination. The HXMT data were processed using the Insight-HXMT Data Analysis Software (`HXMTDAS`) and the calibration database, with additional criteria applied to ensure high-quality photon events. For the spectral analyses, energy bands of 0.4–10 keV were used for NICER, and 2–10 keV for the LE telescope, 10–30 keV for the ME telescope, and 28–90 keV for the HE telescope of HXMT. Background estimation was performed using dedicated tools provided by the HXMT team [77, 113, 114].

The joint fitting of NICER and HXMT spectra allowed for the extension of the spectral analysis to higher energies, particularly during observations before 2018, where the coverage from HXMT's higher energy ranges provided additional leverage. This joint fitting approach helped to better constrain various spectral models and improved our understanding of the accretion process in GRS 1915+105. By combining data from both instruments, we could optimize the spectral-timing analysis and obtain more reliable results, particularly for the phase of the source's decay prior to its entry into the obscured state. This method also enabled a more accurate characterization of the spectral properties of the source across a wide range of energies.

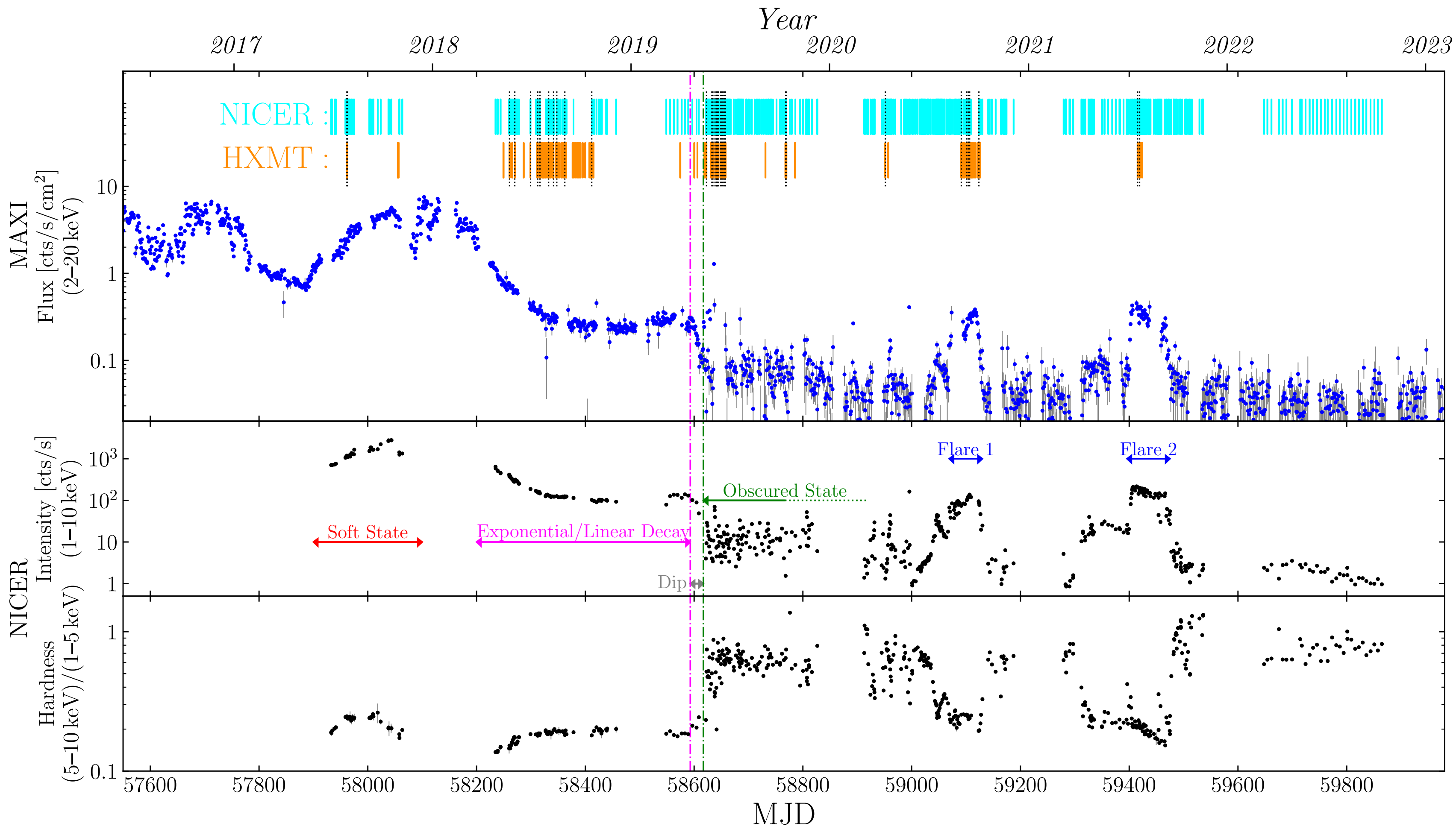

Figure 4.2: Top: Daily 2–20 keV flux from MAXI, with NICER and *Insight*–HXMT coverage marked by cyan and dark orange bars. Dotted lines indicate quasi-simultaneous observations. Middle: NICER 1–10 keV raw count rate, with spectral states indicated by arrows (see text for classification criteria). Bottom: Hardness ratio from NICER, defined as the 5–10 keV to 1–5 keV count rate. Dash-dotted magenta and green lines (MJD 58593 and 58617) mark the onset of the pre-flare dip and transition into the obscured state, respectively. (Adopted from Zhou et al. 227)

4.3 Polarimetric Measurements of 4U 1907+09 [225]

4.3.1 Background and Motivation

HMXBs consist of a compact object, such as a NS, that accretes matter from a massive companion star. In systems with strongly magnetized NSs, the accretion flow is interrupted by the NS's magnetosphere at a distance of approximately 10^8–10^9 cm [50, 107]. The matter is then channeled along magnetic field lines onto the NS's surface, where its gravitational potential energy is released. Depending on the accretion rate, this process can create hot spots or extended accretion columns at the magnetic poles. Due to the misalignment between the magnetic poles and the spin axis, these systems emit pulsed X-rays, producing what is known as an XRP [see, e.g., 148]. XRPs serve as natural laboratories for studying the extreme conditions where matter, light, and magnetic fields interact in ways that are not possible in terrestrial labs.

The phase-dependent characteristics of pulsed X-ray emission in XRPs are determined by the geometry of the emission region, the orientation of the pulsar relative to the observer, and the complexities of radiative transfer in the presence of an intense magnetic field. However, a comprehensive theoretical framework that fully explains these properties is still lacking. One of the primary challenges is the uncertainty surrounding the fundamental geometric configuration of XRPs.

Polarimetric observations offer a way to address this uncertainty by allowing the determination of key geometric parameters, such as the inclination of the pulsar's spin axis relative to the line of sight and the magnetic obliquity. Additionally, they can distinguish between different emission region geometries. The NS's extreme magnetic field significantly influences X-ray emission polarization from XRPs by altering the Compton scattering cross-sections. Under favorable orientations, photon scattering in such a highly magnetized plasma can lead to significant polarization, with theoretical predictions suggesting a degree of polarization up to 80% [32, 130]. As shown by Meszaros et al. [130], the linear polarization of X-rays is highly sensitive to the geometry of the emission region, with variability observed in both energy and pulse phase. Consequently, phase-resolved polarimetry is a critical tool for constraining the system's viewing geometry and differentiating among competing radiation models.

The X-ray mission IXPE enables the detection of linear X-ray polarization in a variety of astrophysical X-ray sources, including XRPs [see 167, for a review][1]. Most studied pulsars show no significant energy dependence of polarization angle (PA), with Vela X-1 and 4U 1538−52 being the only known exceptions [60, 117]. These sources, however, exhibit polarization degrees (PD) that are significantly lower than theoretical predictions.

The source studied in this paper, 4U1907+09, was first detected in the third Uhuru survey [59, 70], and confirmed as an HMXB with an O-type supergiant companion [41, 157, 199]. It hosts a pulsar with a spin period of ~ 437.5 s [121], orbiting an eccentric ($e \simeq 0.28$) orbit with a period of $\simeq 8.3753$ d [91, 126]. The broadband

[1]Polarimetric measurements have also been conducted for other XRPs, including Her X-1 [49, 82, 223], Cen X-3 [195], X Persei [149], 4U 1626−67 [125], Vela X-1 [60, 62], GRO J1008−57 [194], EXO 2030+375 [123], LS V +44 17 [48], GX 301−2 [187], Swift J0243.6+6124 [166], SMC X-1 [61], and 4U 1538−52 [117].

X-ray spectrum of 4U1907+09 can be well modeled by an absorbed power law with a high-energy cut-off [58]. Additionally, cyclotron resonance scattering features (CRSFs) at 17–19 keV and their harmonic around 38 keV have been reported [43, 132, 191], with an estimated magnetic field strength of 2×10^{12} G [81, 200].

The aim of this work is to measure the polarimetric properties of the X-ray pulsar 4U 1907+09, which has not been previously observed by IXPE. This source is slightly fainter than other X-ray pulsars targeted by IXPE, and its relatively low luminosity may reveal intriguing polarimetric behavior.

4.3.2 Methods

IXPE observed 4U 1907+09 twice, in November 2024, during the bright periods near the periastron. The total effective exposures for the two observations were 117.9 ks and 118.0 ks, respectively. The data were processed using the IXPEOBSSIM package with the latest calibration files. The photon extraction regions were defined to minimize background, and the data were corrected for position offset and energy calibration. The pulse period and its first derivative were determined independently from the data using Z^2 statistics. These results ensure the alignment of the pulse profiles over the extended observation period.

Polarimetric data were analyzed by extracting Stokes I, Q, and U spectra from the three IXPE detectors, applying consistent energy binning across all instruments. The spectra were then jointly fitted using the XSPEC package along with the IXPE response matrices. The fitting procedure employed χ^2 statistics, and uncertainties were quoted at the 68.3% confidence level (1σ). In addition, we applied the model-independent `pcube` algorithm to facilitate comparison with the XSPEC-based results. Together, these complementary approaches provided a comprehensive analysis of the polarization properties of 4U 1907+09 during its bright phase.

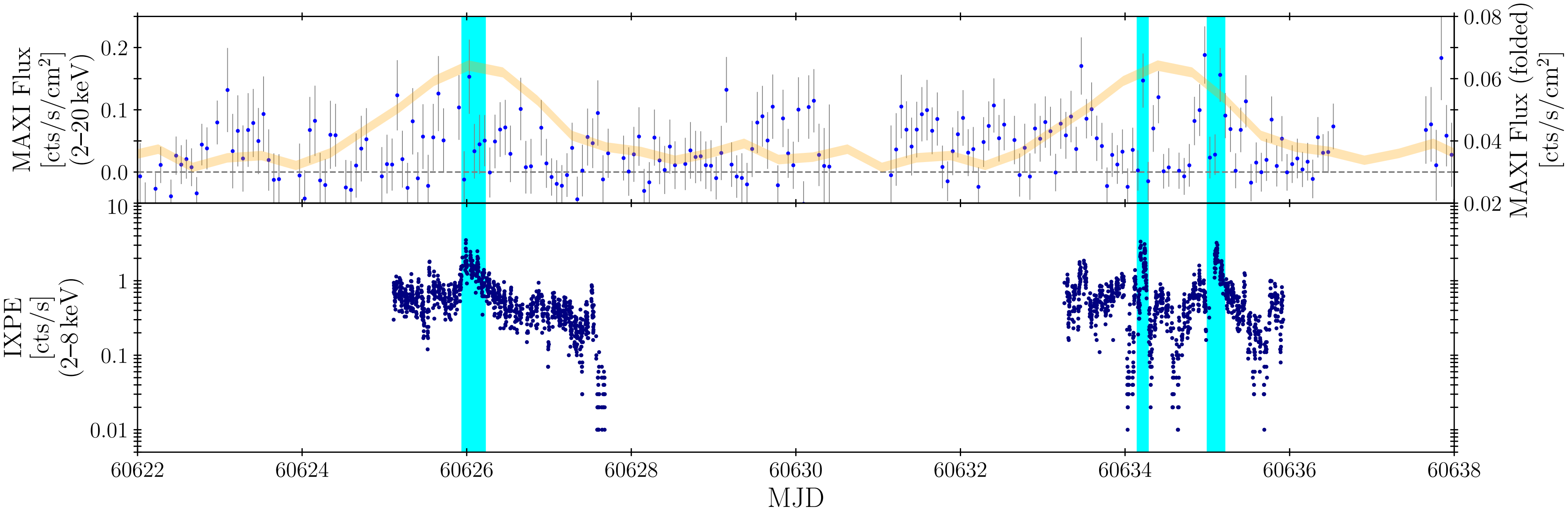

Figure 4.3: X-ray light curve of 4U 1907+09. Upper panel: the light curve in the 2–20 keV band as observed by MAXI near the IXPE observations. In the same panel, we also present the folded orbital light curve for MAXI data after MJD 59000 based on the ephemerides from in 't Zand et al. [91], displayed in light orange, with its width representing flux uncertainties. Note that the folded orbital light curve uses the right-hand axis to emphasize its shape. Lower panel: the combined light curve of 4U 1907+09 from all 3 DUs of IXPE, with the time resolution of 100 s. The duration of the three flares observed by IXPE is indicated by cyan stripes. (Adopted from Zhou et al. [225])

Table 4.2: Orbital parameters for 4U 1907+09 (adopted from in 't Zand et al. [91]).

Parameter	Value	Unit
Orbital period	$8.3753^{+0.0003}_{-0.0002}$	d
$T_{\pi/2}$	$50134.76^{+0.16}_{-0.20}$	MJD
$a_{\mathrm{X}} \sin i$	83 ± 4	light-sec
Longitude of periastron	330 ± 20	deg
Eccentricity	$0.28^{+0.10}_{-0.14}$	

Table 4.3: Pulsar ephemerides for Obs. 1 & 2 of 4U 1907+09 with IXPE.

Parameter	Obs. 1	Obs. 2
Start [MJD]	60625.1	60633.3
End [MJD]	60627.7	60635.9
Exposure [ks]	117.9	118.0
t_0 [MJD]	60625.1139919	
Pulse period [s]	$443.73^{+0.03}_{-0.01}$	
Pulse period derivative [10^{-8}s s^{-1}]	5^{+3}_{-6}	

Notes. The reported reference time t_0 defines the zero phases of the pulse profiles (see Fig. 7.1).

5 Spectral-Timing Analysis of Cygnus X-1 [226]

5.1 Results

5.1.1 Spectral Analysis

For spectral-timing analysis, we use a simple phenomenological model, commonly applied in prior studies of Cygnus X-1, consisting of a broken power law with a high-energy cut-off and a disk component:

$$\texttt{const} \times \texttt{TBabs} \times (\texttt{bknpower} \times \texttt{highecut} + \texttt{gaussian} + \texttt{diskbb}) \,,$$

where `TBabs` represents interstellar absorption [202, 210], and `bknpower` × `highecut` models the hard X-ray continuum. The Gaussian line models the iron Kα emission at 6.4 keV, and `diskbb` fits the thermal emission from the accretion disk [122, 139]. In the hard state, the disk component is insignificant, but it dominates in the soft state. Typical spectra for Cygnus X-1 are shown in Fig. (5.1).

We use a minimal signal-to-noise ratio of 10 for the data, with systematic errors of 0.5%, 0.5%, and 1.0% for LE, ME, and HE, respectively [105, 112]. The peak of the Gaussian line is fixed at 6.4 keV, and the column density $N_{\rm H}$ is fixed at $7.1 \times 10^{21} {\rm cm}^{-2}$ [83]. Other parameters remain free. Overall, we achieve good spectral fits.

5.1.2 Energy-Resolved Timing Properties

Power Spectra and the Fractional rms

Power spectra (PSDs) are calculated using the discrete Fourier transform, with results normalized to rms fluctuations relative to the mean count rate [18, 140]. The fractional rms is the integral of the PSD over frequencies from 0.0625 to 256 Hz. A background correction is applied to the rms, as background photons contribute significantly, especially in the soft state. The corrected rms is given by:

$$\text{rms} = \sqrt{\sum P \cdot \Delta f} \, \left(\frac{S+B}{S} \right) \,, \tag{5.1}$$

where P is the noise-subtracted power, and S and B are the source and background photon count rates, respectively. This correction factor ensures that the background noise, which has its own intrinsic variability, does not overestimate the fractional rms.

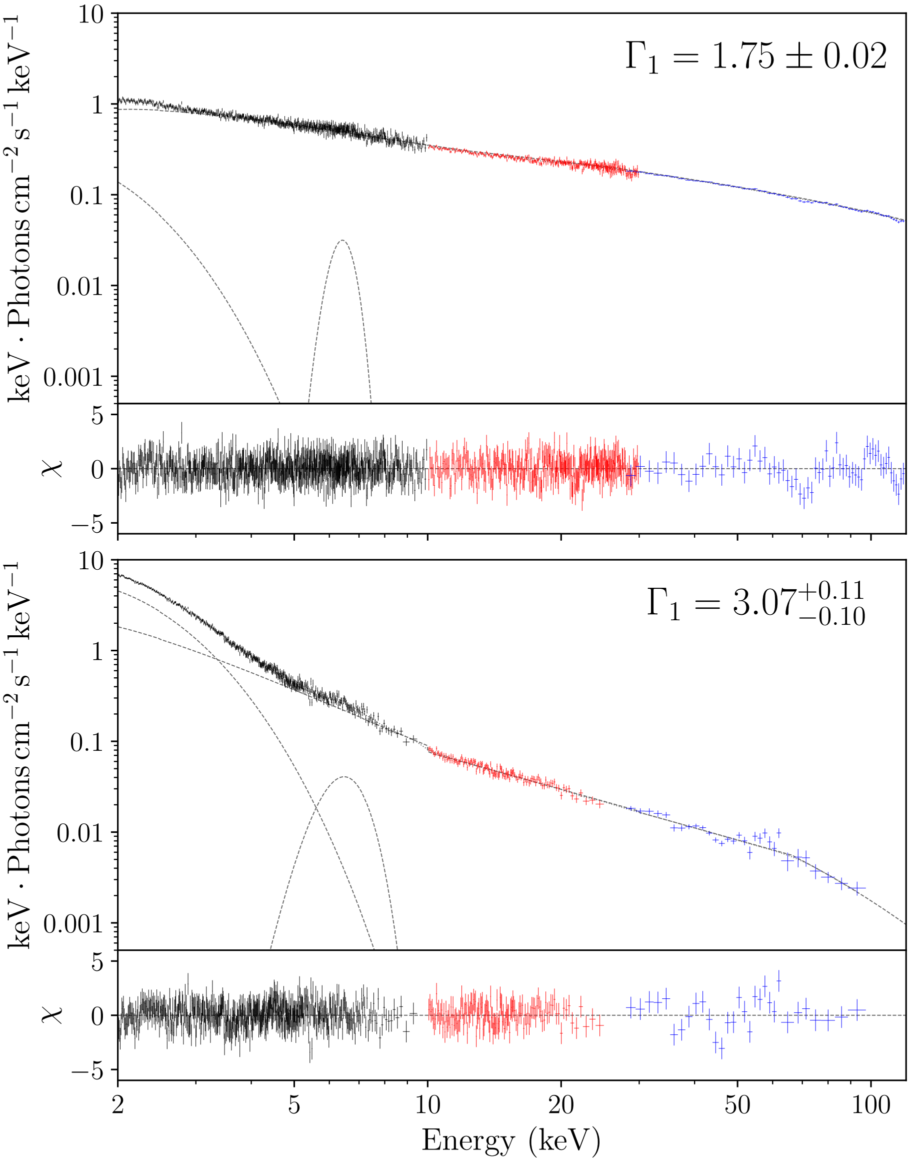

Figure 5.1: Typical spectra of Cygnus X-1 with HXMT observations. The *upper panel* shows a spectrum in the hard state (obs ID: P0201012171). The spectrum in the *lower panel* is in the soft state (obs ID: P0101315057). Data from LE/ME/HE telescope are denoted with black/red/blue crosses. The powerlaw continuum, the thermal component, and the iron line emission are indicated with dashed lines. (Adopted from Zhou et al. [226])

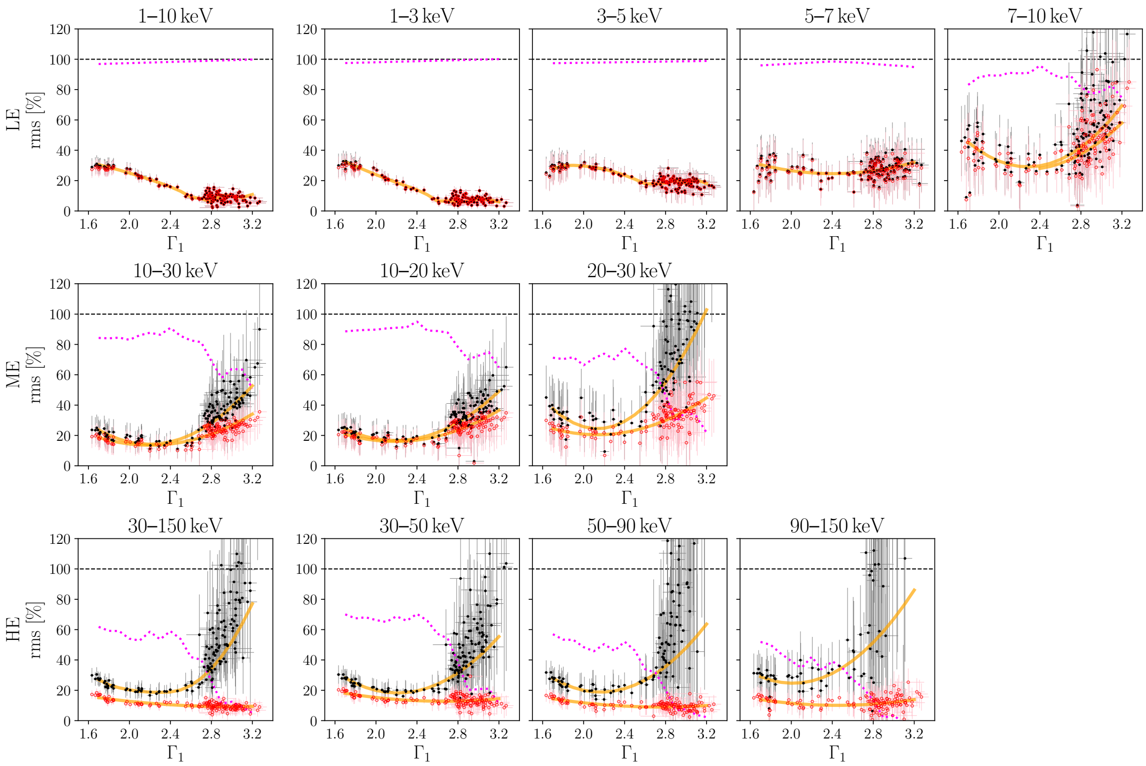

Figure 5.2: The correlations between the soft photon index Γ_1 and the fractional rms from all the instruments on HXMT. The red circles are the raw rms without the correction of Eq. (5.1), and the black dots are the corrected total rms according to Eq. (5.1). The magenta dotted lines denote the signal-background ratio $S/(S+B)$. The orange solid lines show the trends of the corrected/uncorrected total rms when varying Γ_1. (Adopted from Zhou et al. [226])

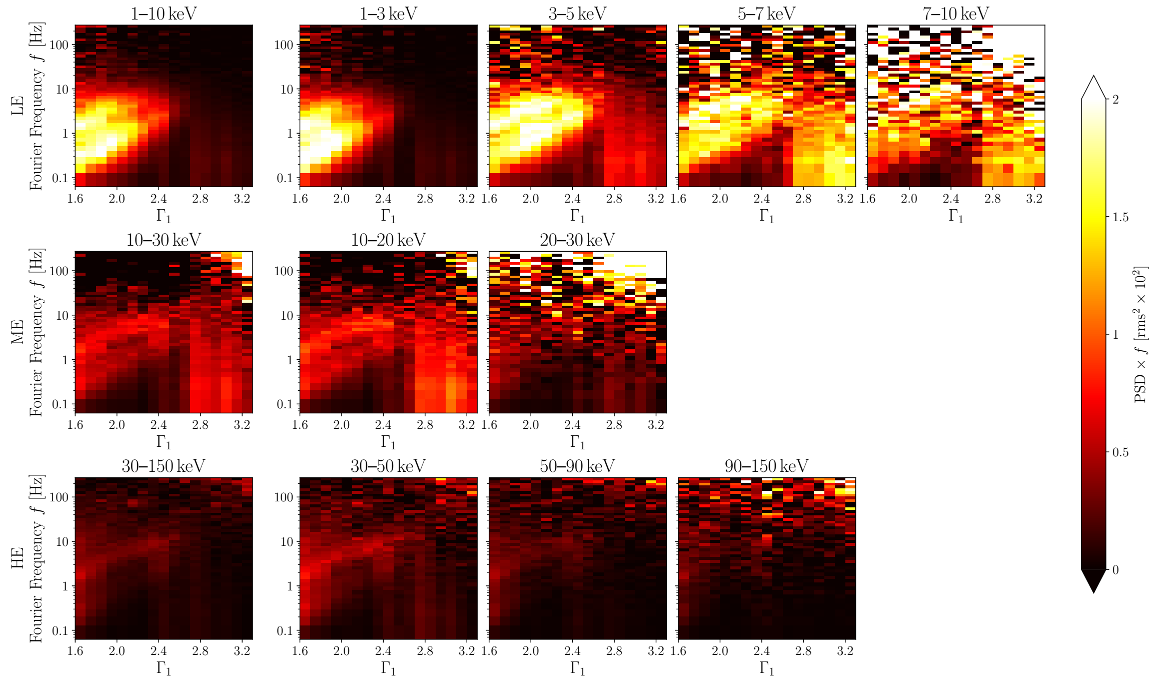

Figure 5.3: The evolution of PSDs versus the soft photon index Γ_1 from different energy bands provided by all instruments on HXMT. The color scale represents the averaged value of $\mathrm{PSD}(f_i) \times f_i$ at individual frequencies f_i. Please note that the PSD values in these plots have not been corrected by Eq. (5.1) in order to avoid the covering effect due to high signal-background ratio. (Adopted from Zhou et al. [226])

Figure (5.2) shows rms correlations with Γ_1 for various instruments. The effect of background correction is illustrated with the ratio $S/(S+B)$, showing that corrected rms exceeds raw rms when background contamination is higher. Smooth curves are used to highlight trends, especially in noisy data.

Evolution of the PSDs with Spectral Shape

We follow Böck et al. [23] and Grinberg et al. [76] to visualize PSD evolution in Γ_1-f_i-space[1]. PSDs are averaged within Γ_1 bins, with frequency rebinning in logarithmic scale between 0.0625 Hz and 256 Hz. The evolution of PSDs across energy bands is shown in Fig. (5.3), where variability strength in HE bands is lower due to background photons affecting harder X-ray ranges. To highlight variability above 30 keV, the HE bands are rescaled (Fig. 5.4).

Coherence Function and Phase-lags

Coherence functions and phase-lags are calculated from Fourier transforms of simultaneous light curves. The coherence $\gamma^2(f)$ measures the linear correlation between two time series, ranging from 0 (no coherence) to 1 (perfect coherence). Negative coherence values are ignored, as they result from noise-dominated spectra. A coherence greater

[1]The Γ_1-f_i-space refers to the parameter space defined by the soft photon index Γ_1 and the individual Fourier frequency f_i. Each spectrum is assigned to a specific Γ_1 bin, and the PSDs within each bin are averaged to reduce statistical uncertainties.

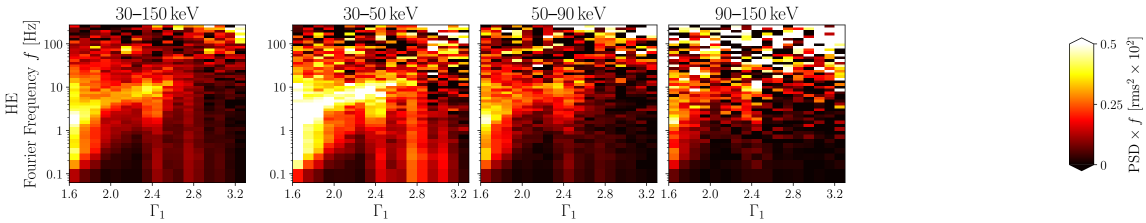

Figure 5.4: Same as the last row of Fig. (5.3), but with a different color scale, in order to illustrate the evolution of the variability component more clearly. (Adopted from Zhou et al. [226])

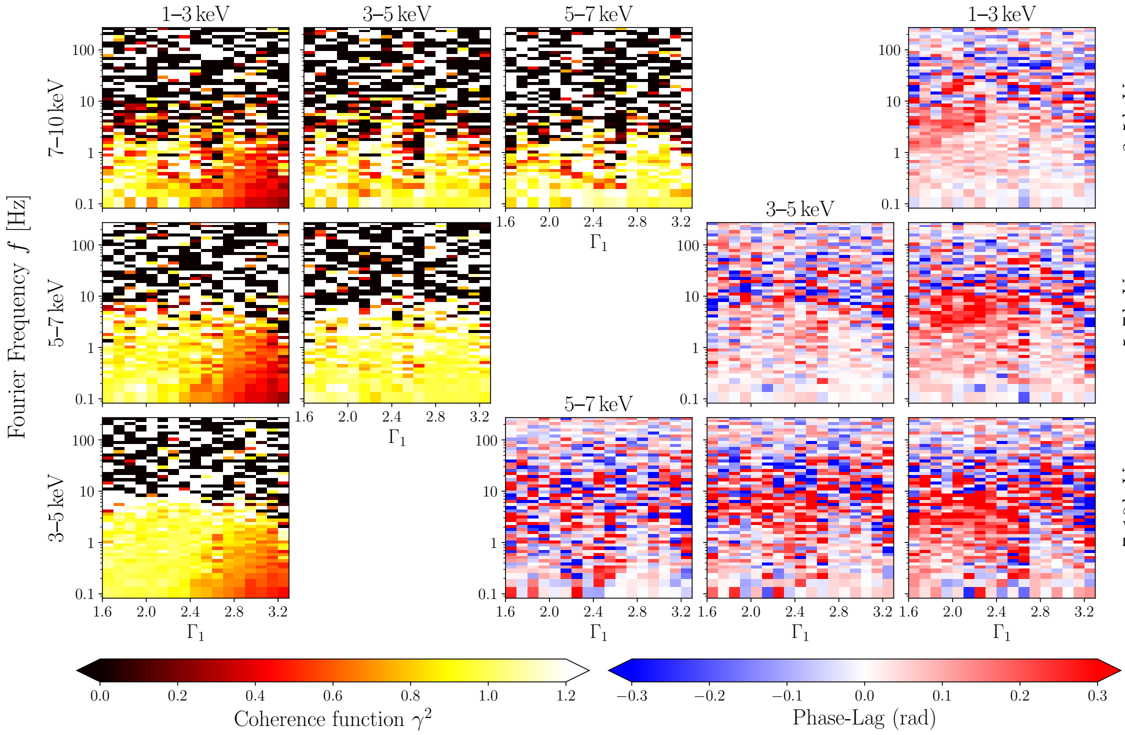

Figure 5.5: Evolution of the coherence function γ^2 and the phase-lags versus the soft photon index Γ_1 between different energy bands of the LE telescope. (Adopted from Zhou et al. [226])

than 1 is acceptable in cases of strong correlation.

Coherence is presented in Γ_1-f_i-space for different energy bands in Fig. (5.5). Loss of coherence is observed in the soft state, especially between the 1–3 keV and higher energy bands, as the dominant emission origin shifts from power-law to thermal. The phase-lags are shown with red for hard lags and blue for soft lags. For ME and HE data, due to noise, averaged coherence and phase-lag are used (see Fig. 5.6 and Fig. 5.7).

5.2 Discussion

5.2.1 Discussion on the Spectral Analysis

We verify the validity of our spectral modeling by checking correlations between spectral hardness, soft photon index Γ_1, and the ratio of unabsorbed energy flux from

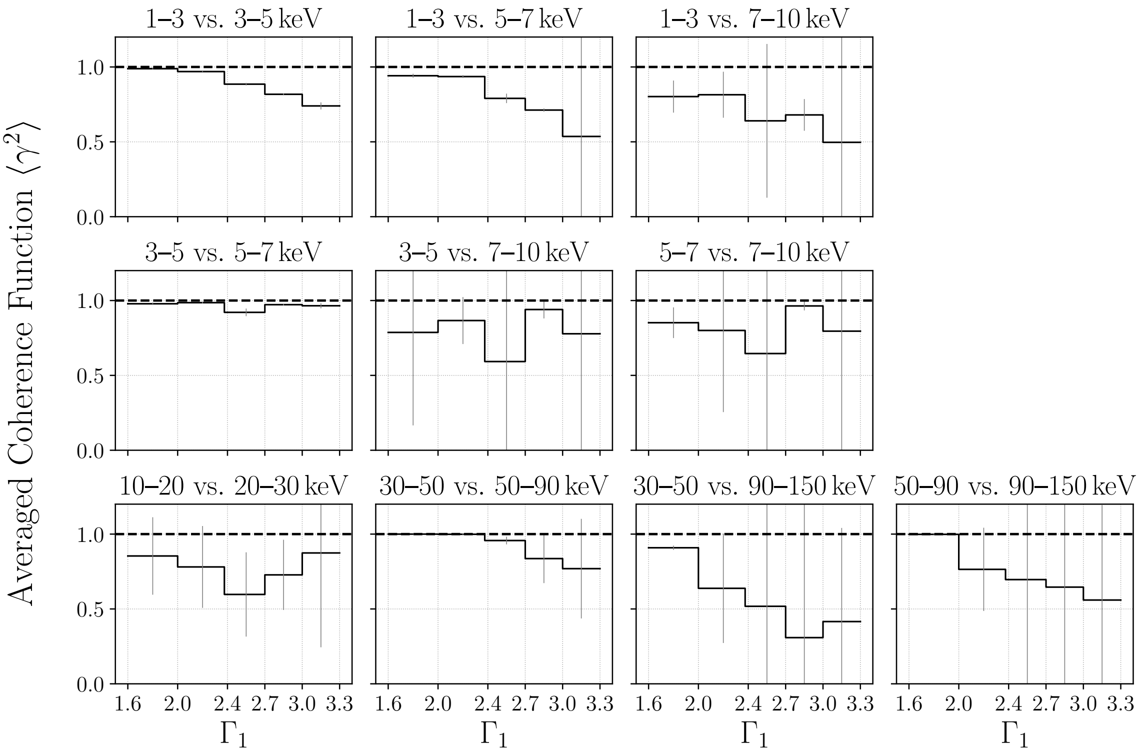

Figure 5.6: The evolution of the coherence $\langle\gamma^2\rangle$ averaged in 0.0625–6 Hz frequency range versus the states (classified by the soft photon index Γ_1) between different energy bands. (Adopted from Zhou et al. [226])

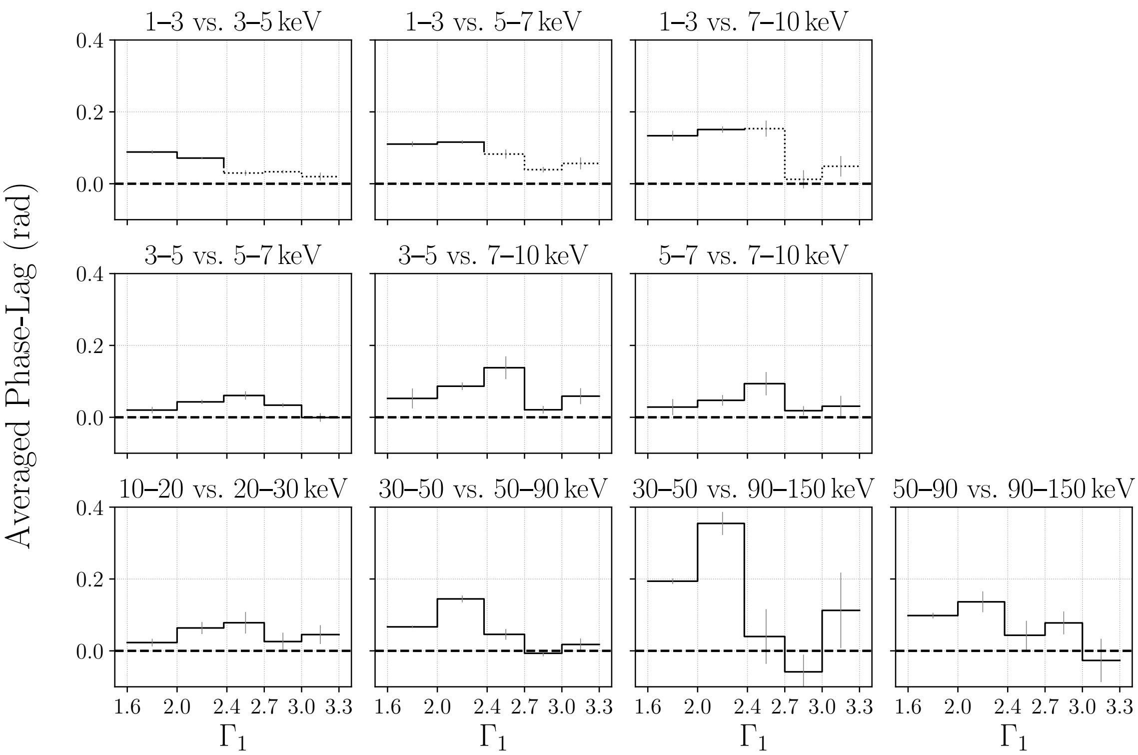

Figure 5.7: Similar to Fig. (5.6), but with the evolution of the averaged phase-lag versus the states (classified by the soft photon index Γ_1). In the first three panels, the averaged phase-lags with $\Gamma_1 \geq 2.4$ are denoted by dotted lines, as we know that the loss of coherence is due to the different emission origins. (Adopted from Zhou et al. [226])

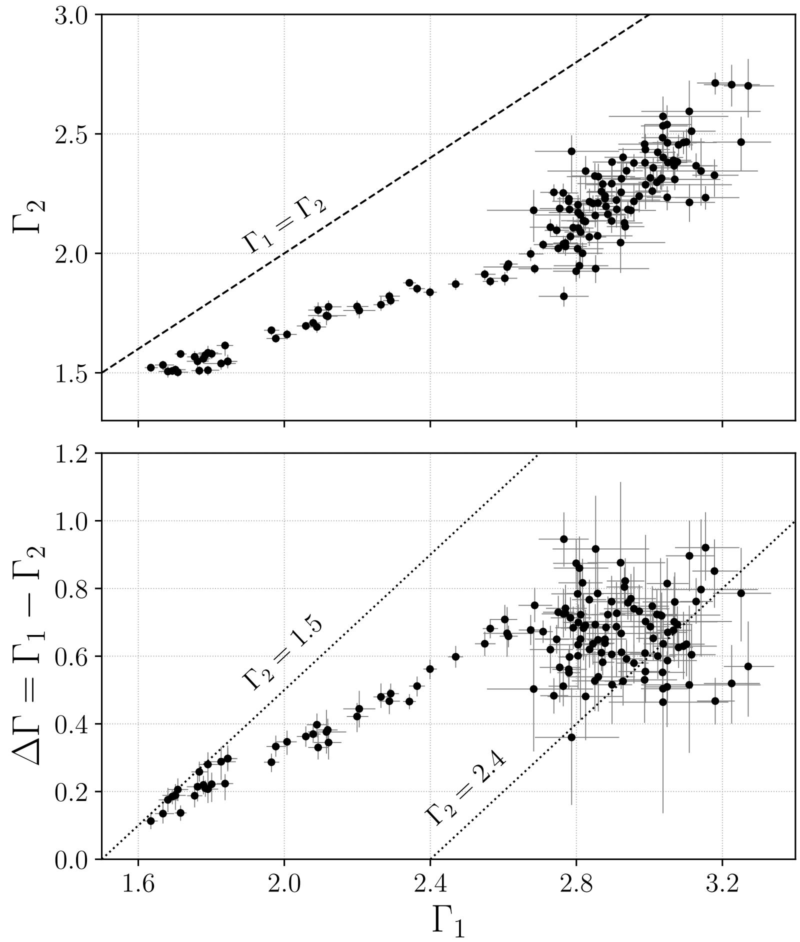

Figure 5.8: The *upper panel* shows the soft photon index Γ_1 versus the hard photon index Γ_2 in model `bknpower`. The dashed line indicates that $\Gamma_1 = \Gamma_2$. In the *lower panel*, the correlations between Γ_1 and the difference of two photon indices, defined by $\Delta\Gamma = \Gamma_1 - \Gamma_2$, are shown. The lines that are parallel to the dotted lines indicate a constant Γ_2. (Adopted from Zhou et al. [226])

thermal radiation to total energy flux in the 2–5 keV range (Fig. 5.9). Both correlations show expected trends for hard-to-soft transitions, helping define the source state based on Γ_1: the hard state ($\Gamma_1 \leq 2.0$), the hard intermediate state ($2.0 < \Gamma_1 \leq 2.4$), the soft intermediate state ($2.4 < \Gamma_1 \leq 2.7$), and the soft state ($\Gamma_1 > 2.7$). This choice aligns with the PSD shape change in the 3–5 keV band and coherence between 1–3 and 3–5 keV bands.

The positive correlation between reflection intensity (iron Kα line equivalent width) and Γ_1 is consistent with previous studies [72, 186]. Shaposhnikov & Titarchuk [179] and Steiner et al. [186] suggest that the corona shrinks in intermediate and soft states, and Petrucci et al. [162] explains the Comptonization effect in the hard state, where the iron line is diluted due to the higher optical depth of the corona.

The Γ_1 versus Γ_2 correlation shows a "bend" at $\Gamma_1 \approx 2.7$, coincident with the soft state onset (Fig. 5.8). This deviation appears even with a free N_{H}, suggesting the bend is not an artifact of our model's parameter choices. We also quantify reflection intensity via photon index differences ($\Delta\Gamma$) using the `bknpower` $\times$ `highecut` model. We find a clear positive trend between $\Delta\Gamma$ and Γ_1, confirming that reflection is stronger in the soft state.

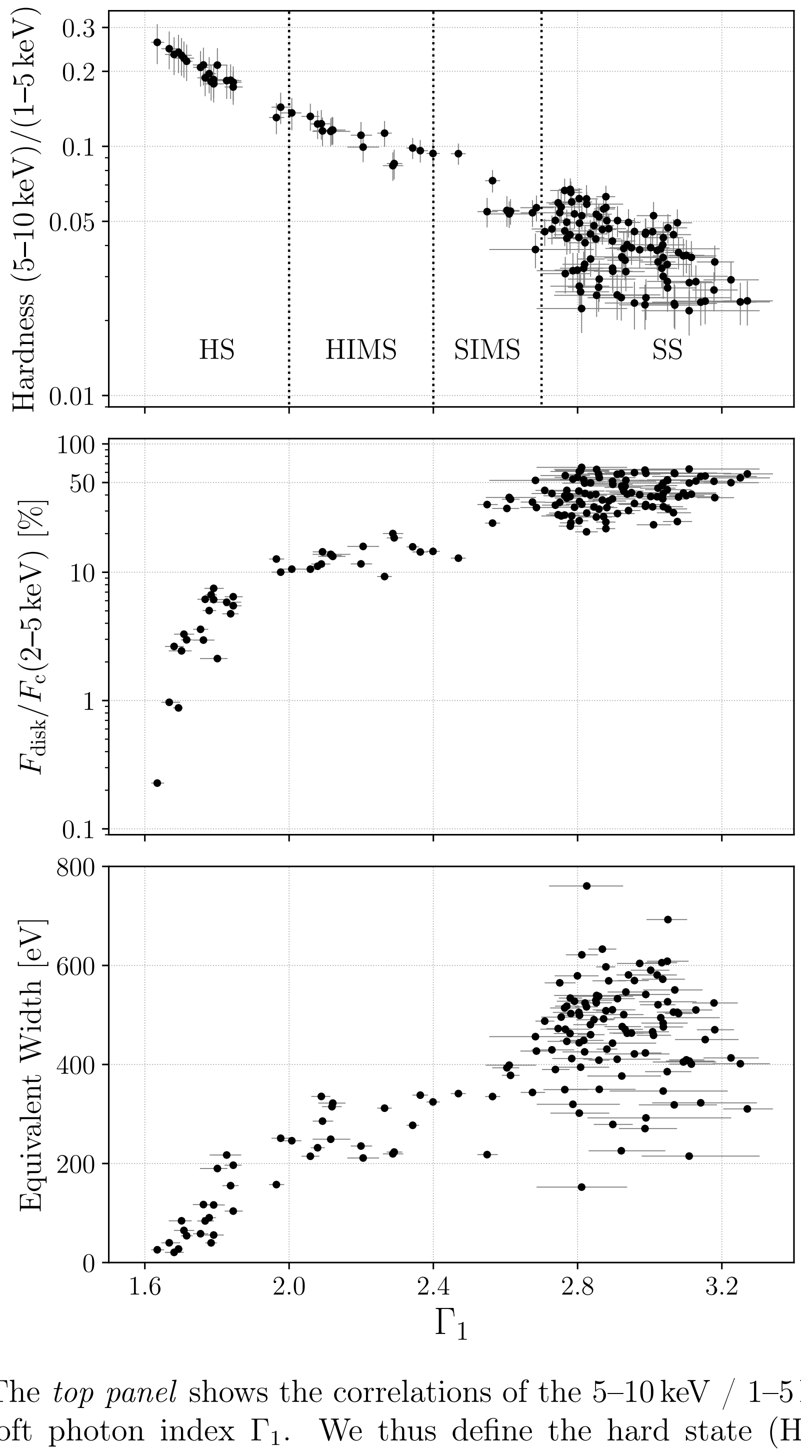

Figure 5.9: The *top panel* shows the correlations of the 5–10 keV / 1–5 keV hardness versus the soft photon index Γ_1. We thus define the hard state (HS), the hard intermediate state (HIMS), the soft intermediate state (SIMS), and the soft state (SS) with Γ_1 values. The *middle panel* shows the ratio of unabsorbed energy flux of the disk components over the total energy flux versus Γ_1. The *bottom panel* shows the intensity of reflection that is denoted by the equivalent widths of the iron Kα lines, is stronger in the soft state than in the harder state. (Adopted from Zhou et al. [226])

5.2.2 Discussion on the Timing Properties

The Total Fractional rms

We present both corrected and uncorrected rms in Fig. (5.2). When background contribution increases, it smears the power spectrum and rms. To recover the intrinsic rms trends, we consider: (1) raw rms is valid if background varies like the source; (2) corrected rms is valid if background is constant; and (3) the true value lies between these extremes, as source variability dominates in all cases. Thus, the true total rms should fall between the two orange curves in Fig. (5.2). With better data quality, the curves converge, narrowing the uncertainty range.

Fig. (5.2) also shows positive trends between total rms and Γ_1 in hard X-ray bands during the soft state, challenging the common notion that rms is always lower in the soft state due to thermal dominance[e.g., 19, 80]. This holds only when soft bands (e.g., 1–3 keV or 1–10 keV) are included. In harder bands, dominated by Comptonized photons even in the soft state, we observe a slightly negative trend for $\Gamma_1 \lesssim 2.7$ and a positive trend for $\Gamma_1 \gtrsim 2.7$.

Total rms integrates the PSD over all frequencies. Different rms values imply distinct radiation properties. Even with a flat rms-Γ_1 relation, as in the 5.0–7.0 keV band, the timing behaviors in soft and hard states differ, as shown by the PSD evolution discussed in Sects. 5.1.2 and 5.2.2.

Evolution of the PSDs

We extend previous *RXTE*-based studies (2.1–15 keV; Böck et al. [23], Grinberg et al. [76]) to lower and higher energies, enabling better tracking of disk and high-energy power-law variability.

Figure (5.3) shows a transition at $\Gamma_1 \simeq 2.7$. Below this, two broad variability components appear in the 1–10,Hz range, shifting to higher frequencies as the source softens. Their central frequencies are nearly energy-independent [120]. Although previously identified as QPOs [72, 179], their broad shape is inconsistent with LFQPOs [92].

Following Grinberg et al. [76], we label these as Component 1 (lower frequency) and Component 2 (higher frequency). Component 2 strengthens and dominates above ~10 keV, while Component 1 fades. We trace Component 2 up to 50–90 keV (Fig. 5.4).

The 90–150 keV band shows no clear structure, despite averaging PSDs over four Γ_1-defined states (Fig. 5.10). Still, variability decreases, consistent with *INTEGRAL*/SPI results[30]. This band is of interest due to the ~150 keV spectral cutoff [211] and polarized hard tail [33, 94, 108, 176].

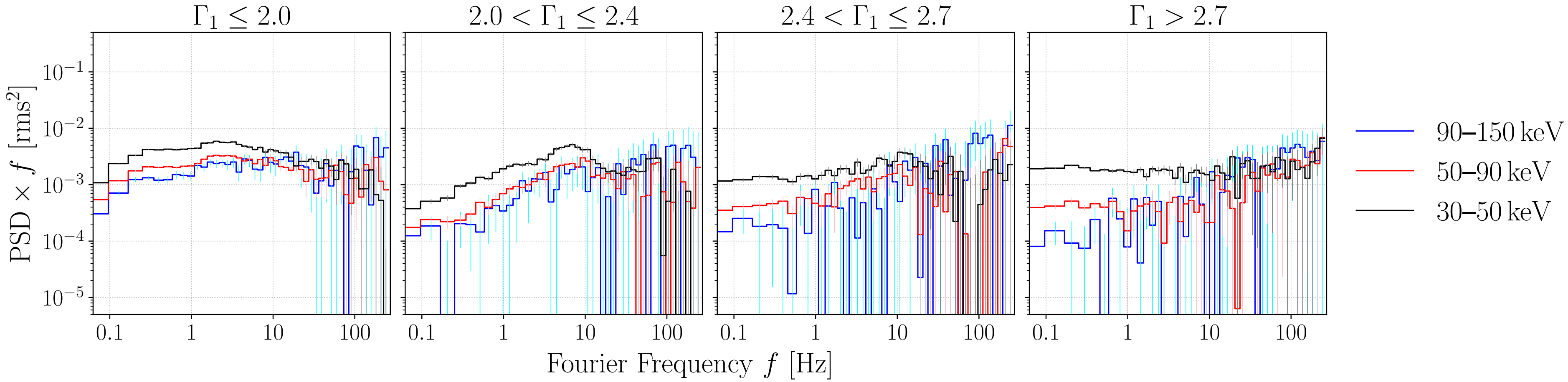

Figure 5.10: Average power spectra calculated from light curves obtained from the HE instrument in different energy bands in four different Γ_1 ranges. The PSDs for the 30–50 keV band, 50–90 keV band, and 90–150 keV band are denoted with black/red/blue lines, respectively. The PSDs are rebinned to $\mathrm{d}f/f = 0.15$. (Adopted from Zhou et al. [226])

Previous studies modeled these components with Lorentzians whose frequencies increase with softening [e.g., 23, 158, 164]. These components shape the total rms in Fig. (5.2). In bands above 3 keV, rms drops slightly across $1.6 \lesssim \Gamma_1 \lesssim 2.7$, while in 1–3 keV, thermal disk photons introduce red-noise variability that fades more rapidly, explaining the continuous rms decrease.

At $\Gamma_1 \gtrsim 2.7$, PSDs switch to a red-noise f^{-1} shape below 10 Hz, now observed up to high energies where the power law dominates [76]. This transition causes the positive rms tail in hard bands (Fig. 5.2). In the soft state, red-noise variability strengthens with energy [38, 42], consistent with the PSD brightness and corrected rms trends.

The Coherence Function and the Phase-lags

Figure (5.6) shows reduced coherence in the soft state ($\Gamma_1 \geq 2.7$), particularly between HE ($\geq$ 30 keV) and LE (1–3 keV) bands. The LE loss is due to dominant thermal disk photons, while the HE loss stems from a poor signal-to-background ratio. Unlike Grinberg et al. [76], who used a 2.1 keV lower bound, our data include softer energies. Recomputing coherence for a 2.1–4.5 keV band confirms no loss, indicating thermal dominance only below 2.1 keV.

A coherence dip is also seen in $2.4 \lesssim \Gamma_1 \lesssim 2.7$, consistent with Grinberg et al. [76]. This may be linked to jet instability in the soft intermediate state [e.g., 23, 40, 54]. Due to low coherence, phase-lags for $\Gamma_1 \geq 2.4$ are shown as dotted lines in Fig. (5.7) and not discussed further.

Figure (5.5) shows dominant hard lags in the 1–10,Hz range in the intermediate state, and at slightly lower frequencies in the hard state, aligning with the variability components. In the soft state, phase-lags fluctuate around zero, leading to a drop in average lags for $\Gamma_1 > 2.7$ (Fig. 5.7).

Average phase-lags are mostly positive, indicating that hard photons lag soft ones [e.g., 23, 42, 76, 159, 164]. We focus on adjacent bands (e.g., 3–5 vs. 5–7 keV), as phase-lags between distant bands can be summed if coherence is high.

From 1.6 to 2.7 in Γ_1, average lags increase, peaking in the soft intermediate state ($2.4 \lesssim \Gamma_1 \lesssim 2.7$), consistent with Grinberg et al. [76]. This trend likely reflects changes in corona geometry, as also suggested by PSD transitions.

However, in the 1–3 vs. 3–5 keV band, this trend reverses in the hard and hard intermediate states ($1.6 \lesssim \Gamma_1 \lesssim 2.4$). Here, lags slightly decrease with increasing Γ_1, possibly due to the 1–3 keV band being more influenced by seed photons from the disk or jet base, while the 3–5 keV band is dominated by Comptonized emission.

5.2.3 Variability Properties of Cygnus X-1 in a Larger Context

We have discussed the variability properties of Cygnus X-1 and now consider the context of state transition mechanisms, the disk-corona model, and accretion scenarios in BHBs.

Comparison with the Behaviors of Other BHBs

Cygnus X-1, a persistent BHB fed by wind, shows similar accretion behavior to other BHBs, although most are transient. The total rms decreases as the state softens [19], as seen in both transient and persistent BHBs [e.g., 173]. However, energy band choice affects the trends. LFQPOs are common in transient BHBs, with their central frequencies rising during hard-to-soft transitions [203]. Cygnus X-1, however, shows higher variability in the soft state compared to transients [e.g., 80]. Hard lags grow during transitions to intermediate states [172], and a decrease in phase-lag occurs during the soft state transition [2, 76].

Current Models to Describe Timing Properties

The variability components are strongly linked to state transitions, crucial for understanding the accretion scenario. Cygnus X-1's state transition is fast [23], but the PSDs do not show a shift from variability components to a red-noise spectrum. The variability components in the PSD are smooth, incompatible with models like Lense-Thirring precession [13] or accretion-ejection instability [188]. Many models, assuming truncated disks and hot flows, suggest the transition happens when the truncation radius decreases, which increases characteristic frequencies (see Ingram & Motta [92] for a recent review). However, some results challenge this, indicating the inner disk radius may remain close to the ISCO [e.g., 66]. Therefore, we lean toward considering the variability components as geometrical effects originating from the corona.

In the soft state, the power spectrum is dominated by red noise, with PSD shapes similar across energy bands. This can be explained by Comptonization of thermal photons, indicating a destroyed corona structure, causing the disappearance of variability components [119].

The Geometry of the Corona during the State Transitions

The intensity of the reflection component is stronger in the soft state. Petrucci et al. [162] and Shaposhnikov & Titarchuk [179] suggest that as the state softens, the corona shrinks and moves closer to the accretion center, aligning with the dominance of disk components in soft X-ray bands. The corona in the hard state has a higher optical depth, absorbing and Comptonizing seed photons. As the state softens, the corona shrinks, allowing thermal photons to escape, while only a few are Comptonized. The sudden change in the PSD and phase-lag may support the idea of the corona splitting into smaller pieces as it shrinks [51]. Variations in the reflection strength could indicate this scenario, though uncertainties prevent firm conclusions.

6 The Dimming GRS 1915+105 [227]

6.1 Spectral-Timing Analysis

We used `ISIS` v1.6.2 [86] for spectral-timing fitting, accessing `Xspec` models [4].

6.1.1 Timing Analysis

NICER and HXMT light curves were extracted from screened event files and processed with `Stingray` [7, 88, 89]. For NICER/XTI (1–10 keV), light curves used a time resolution of 2^{-9} s ($\sim$2 ms). Power spectra were calculated from 32 s segments (2^{14} bins), yielding a frequency range of 0.03125–256 Hz. Frequencies were logarithmically rebinned with $\mathrm{d}f/f = 0.03$, and white noise was corrected using Zhang et al. [222]. Data above 30 Hz were excluded due to Poisson noise dominance.

GRS 1915+105's spectral states are reflected in its timing properties. Before 2018, it was in a soft state (class λ), showing only flicker noise. From April 2018 to April 2019, distinct LFQPOs emerged in the 1–10 Hz band. After MJD 58621 (May 18, 2019), Poisson noise dominated, marking the obscured state. HXMT data from this period show consistent QPO frequencies between LE and ME detectors (Fig. 6.1), despite stronger background noise, confirming that QPOs extend above 10 keV into the non-disk-dominated continuum.

We modeled NICER PSDs, which are less noisy, using two zero-centered Lorentzians for noise and three free-centered ones for QPOs [158]. Fig. (6.2) shows typical fits. The lowest-frequency QPO is the main component; the next higher one is the first harmonic. The central frequencies and uncertainties from all available observations are shown in Fig. (6.5), with a 2:1 ratio confirmed . A third QPO occasionally appears but lacks consistent correlation with the main features.

6.1.2 Spectral Analysis

We adopted systematic errors of 0.5% (HXMT/ME), 1.0% (HXMT/HE; Li et al. [112]), and 1.5% (NICER/XTI[1]). Spectra were grouped with the optimal binning method from Kaastra & Bleeker [95], ensuring at least 30 counts per bin.

[1] `https://heasarc.gsfc.nasa.gov/docs/nicer/analysis_threads/cal-recommend/`

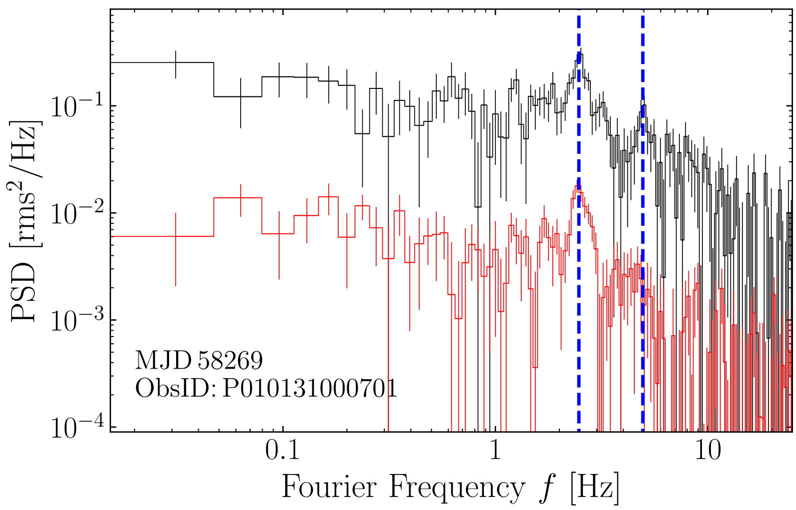

Figure 6.1: Typical PSDs simultaneously observed with HXMT/LE (in black) and HXMT/ME (in red). The PSDs of LE are multiplied by a constant of 20 to avoid overlapping in the figure. The central frequencies of the main QPO and its first harmonic are 2.47 Hz and 4.94 Hz, respectively, as indicated by two dashed blue lines. (Adopted from Zhou et al. [227])

Preliminary Modeling for NICER only

We initially modeled NICER spectra using `TBabs` × `Nthcomp`, adding a `diskbb` component in the soft state. Cross-sections and abundances followed Verner et al. [202] and Wilms et al. [210]. Though the fits yielded high χ^2, we obtained well-constrained photon indices. The QPO frequency-Γ correlation is shown in Fig. (6.5).

The panels *a*–*c* of Fig. (6.3) displays typical residuals. We detected a broadened Fe Kα line and absorption near 7 keV (Fe XXVI Lyα). In the decay phase, a narrow line below 7 keV emerged, inconsistent with a single relativistic reflection model unless an unphysical inclination ($< 30°$) is assumed. Fixing $i = 60°$ [55, 170] revealed the need for a distant reflector. We also included a fixed 1.84 keV Si edge (`edge`) to address residuals-likely instrumental [102, 110, 127].

An Improved Physical Model for a Simultaneous Fit

We jointly fit NICER+HXMT data pre- and post-2018. Building on the initial model, we added `xillverCp` for distant reflection and `relxillCp` for disk reflection. Model parameters were fixed as follows: $a_* = 0.98$, $i = 60°$, $R_{\rm in}$ at ISCO, outer radius $400\,r_{\rm g}$, $q_{\rm in} = q_{\rm out} = 3$. Reflection components shared Γ and $kT_{\rm e}$ with `Nthcomp`, and $A_{\rm Fe}$ was tied and varied between 0.5–2. $\log N$ and $\log \xi$ were initially free. We used `nthratio` to correct low-energy slopes.

We included `zxipcf` for ionized absorption, with fixed covering fraction and redshift. Although based on `XSTAR`, and calibrated for $\Gamma = 2$, it was still suitable for fast modeling across plasma states. The final XSPEC model was:

$$\texttt{TBabs} \times \texttt{edge} \times \texttt{zxipcf} \times (\texttt{Nthcomp} + \texttt{diskbb} + \texttt{nthratio} \times (\texttt{relxillCp} + \texttt{xillverCp}))\,. \tag{6.1}$$

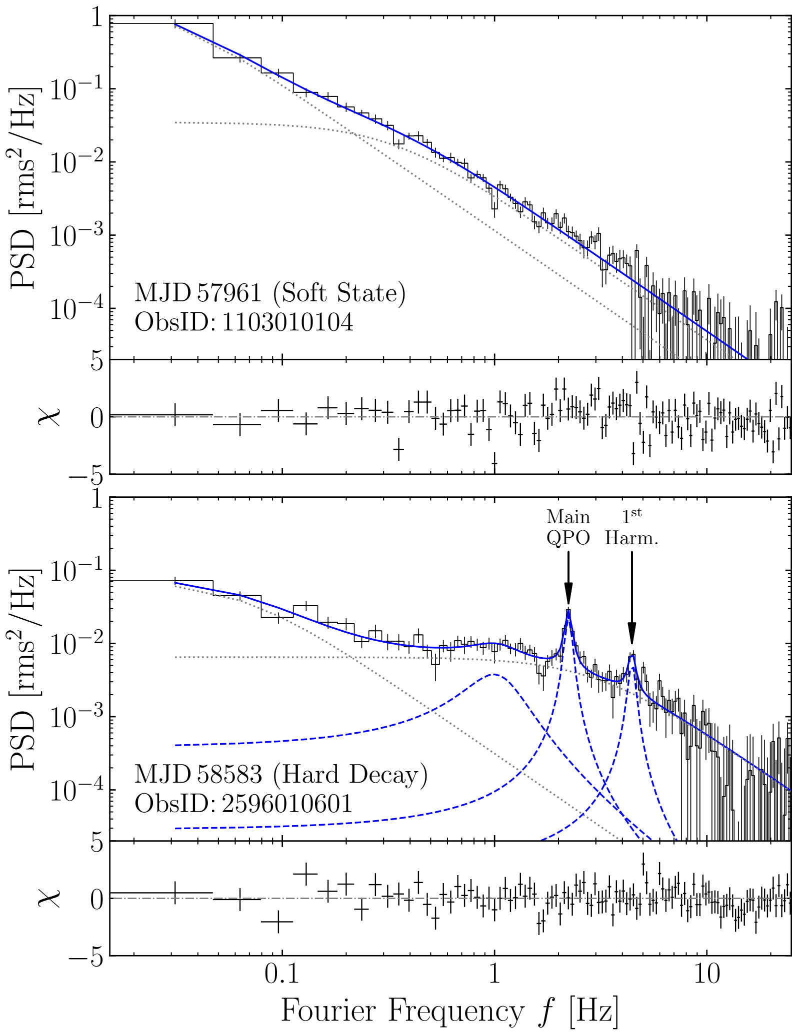

Figure 6.2: Two typical power spectra produced by NICER data in the soft (*upper panel*) and hard state during the decay phase (*lower panel*) with their best-fit models. The Lorentzians with a central frequency at zero are indicated with dotted gray lines, and the Lorentzians with a nonvanishing central frequency are indicated with dashed blue lines. As the best-fit model, the sums of all the Lorentzians are denoted with solid blue lines. The measured central frequencies of the main QPO and the first harmonic in the hard state are $2.23^{+0.18}_{-0.19}$ Hz and $4.44^{+0.05}_{-0.06}$ Hz, respectively. (Adopted from Zhou et al. [227])

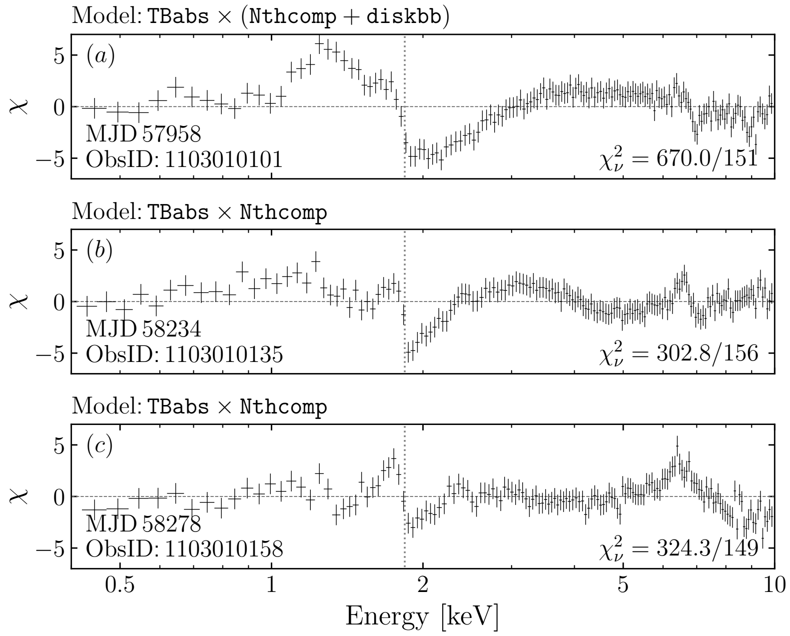

Figure 6.3: Residuals for different states. (*a*-*c*) show NICER-only preliminary fit residuals; dotted lines mark the Si edge (1.84 keV) and narrow Fe Kα line. (Adopted from Zhou et al. [227])

`zxipcf` was omitted in the decay phase due to weak absorption features. Compared to Koljonen & Hovatta [102], our model better constrained the continuum above 10 keV, used `TBabs`+`edge`, added distant and ionized reflection (`xillverCp`) and ionized absorption (`zxipcf`), and corrected slope mismatches via `nthratio`.

Panels (*d*) and (*e*) in Fig. (6.4) show improved residuals. We fixed $A_{\rm Fe} = 1$, $\log N = 15$, and $\log \xi = 0$ in model `xillverCp` in later fits.

NICER-only Modeling

In the decay phase, $kT_{\rm e}$ reached its upper limit (150 keV), and could not be constrained in the soft state. We allowed $kT_{\rm e}$ to vary before 2018. The `diskbb` and `zxipcf` components were excluded during the decay, retained only for the soft state and late decay (post-2019).

For NICER-only data (majority), we fixed $kT_{\rm e} = 150$ keV in the decay phase. $A_{\rm Fe} = 1$, $\log N = 15$, and $\log \xi = 0$ were assumed in model `xillverCp`. Results are shown in Fig. (6.6).

6.2 Results

6.2.1 Before 2018

GRS 1915+105 was in the soft state, dominated by thermal emission. The ISM absorption column density was steady at $(5.7 \pm 0.1) \times 10^{22}$ cm^{-2}. The Comptonization showed steep photon indices ($\Gamma \simeq 3.4$), and disk temperatures $T_{\rm in} \sim 1$ keV, which is

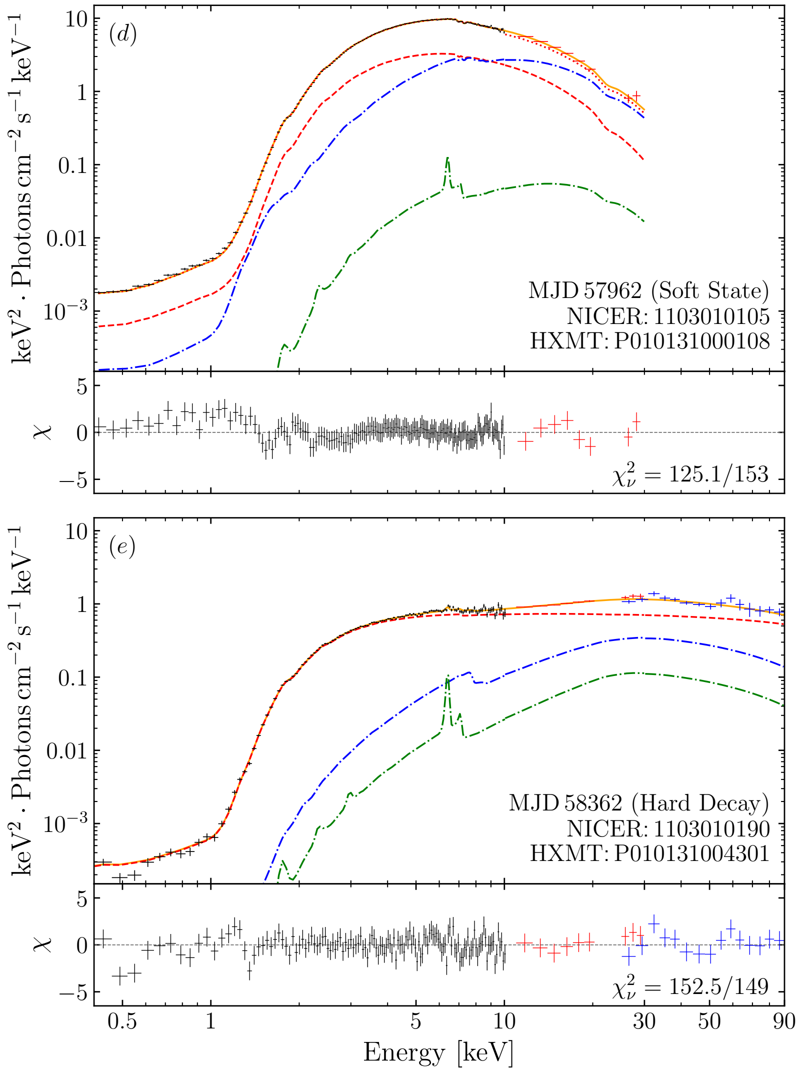

Figure 6.4: Spectral compositions for different states. (*d*-*e*) display typical broadband spectra from joint NICER and HXMT data fit by the model in Eq. (6.1). Components: power-law (dashed red), relativistic (dash-dotted blue), and distant reflection (dash-dotted black). (Adopted from Zhou et al. [227])

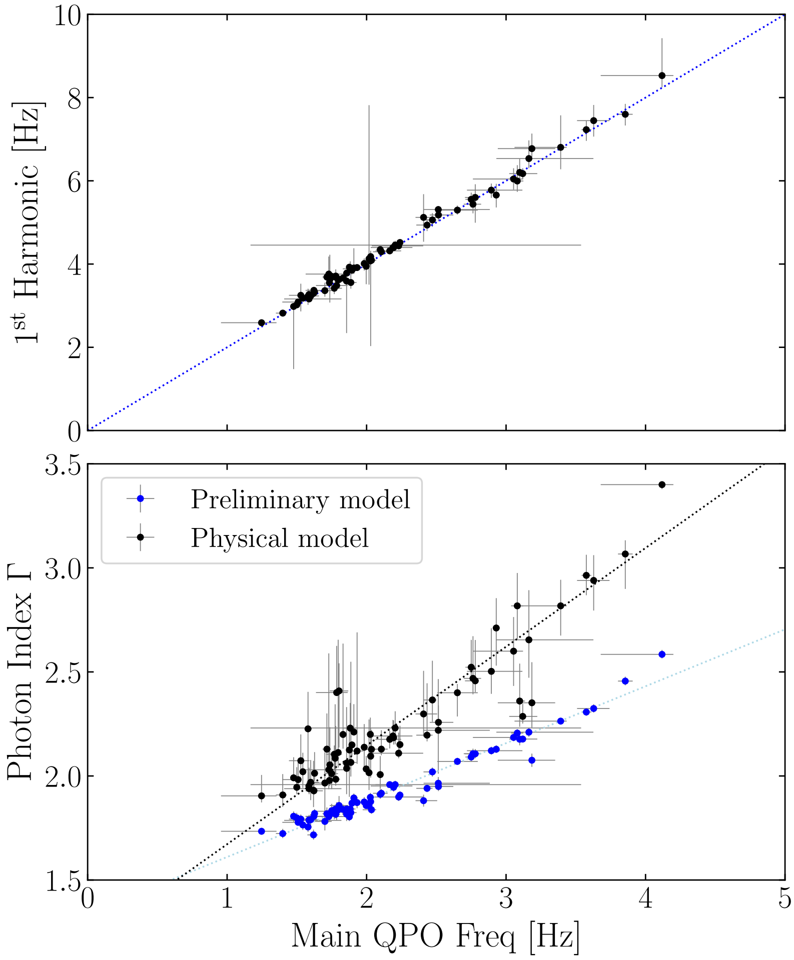

Figure 6.5: *Upper panel*: Correlation between the main QPO frequency and the first harmonic. The dotted blue line indicates the double relation. *Lower panel*: Correlation between the main QPO frequency and the measured photon index Γ with the preliminary model and an improved physical model described in Sect. 6.1.2. The dotted lines show the best fits assuming a linear model. (Adopted from Zhou et al. [227])

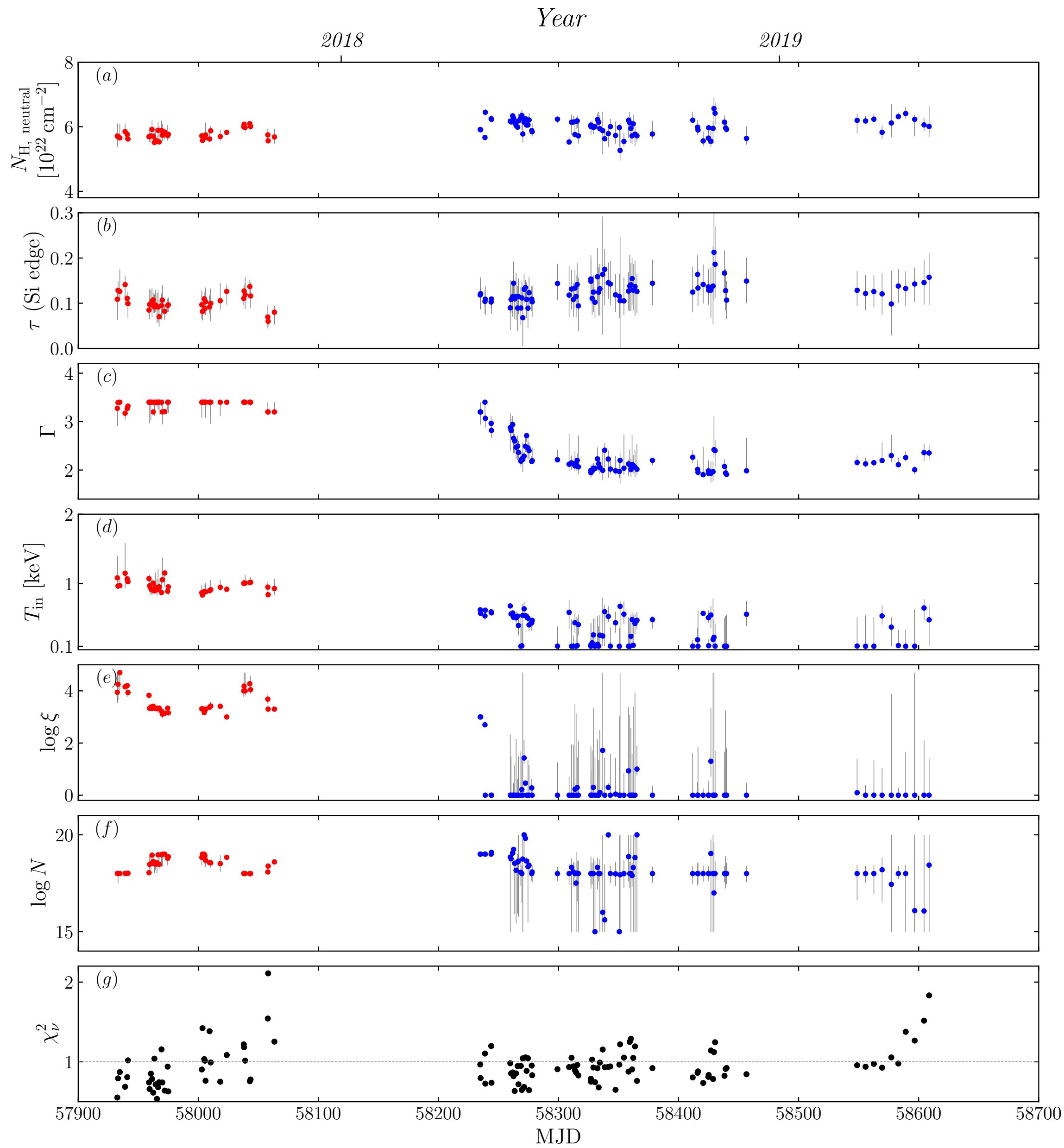

Figure 6.6: Evolution of key spectral parameters over time: (*a*) N_{H}, (*b*) Si edge optical depth τ, (*c*) photon index Γ, (*d*) disk temperature T_{in}, (*e*) ionization degree $\log \xi$, (*f*) electron density $\log N$, and (*g*) reduced χ^2. Red/blue points: soft/hard states. (Adopted from Zhou et al. [227])

higher than during the decay phase (see panel *a*, *c*, *d* of Fig. 6.6). Electron temperatures kT_e were unconstrained, with a lower bound of 5 keV. The disk remained highly ionized, with $\log \xi > 3$.

Our T_{in} estimates are lower than previous studies (e.g., 1.65–2.15 keV in Neilsen et al. [154]), likely due to a lower ISM N_H adopted in our model.

Ionized absorption was present in all NICER data before 2018, with $\log \xi > 4$, mainly from Fe XXVI Lyα at 7 keV (see Fig. 6.3, panel *a*). Column densities were poorly constrained due to the high ionization.

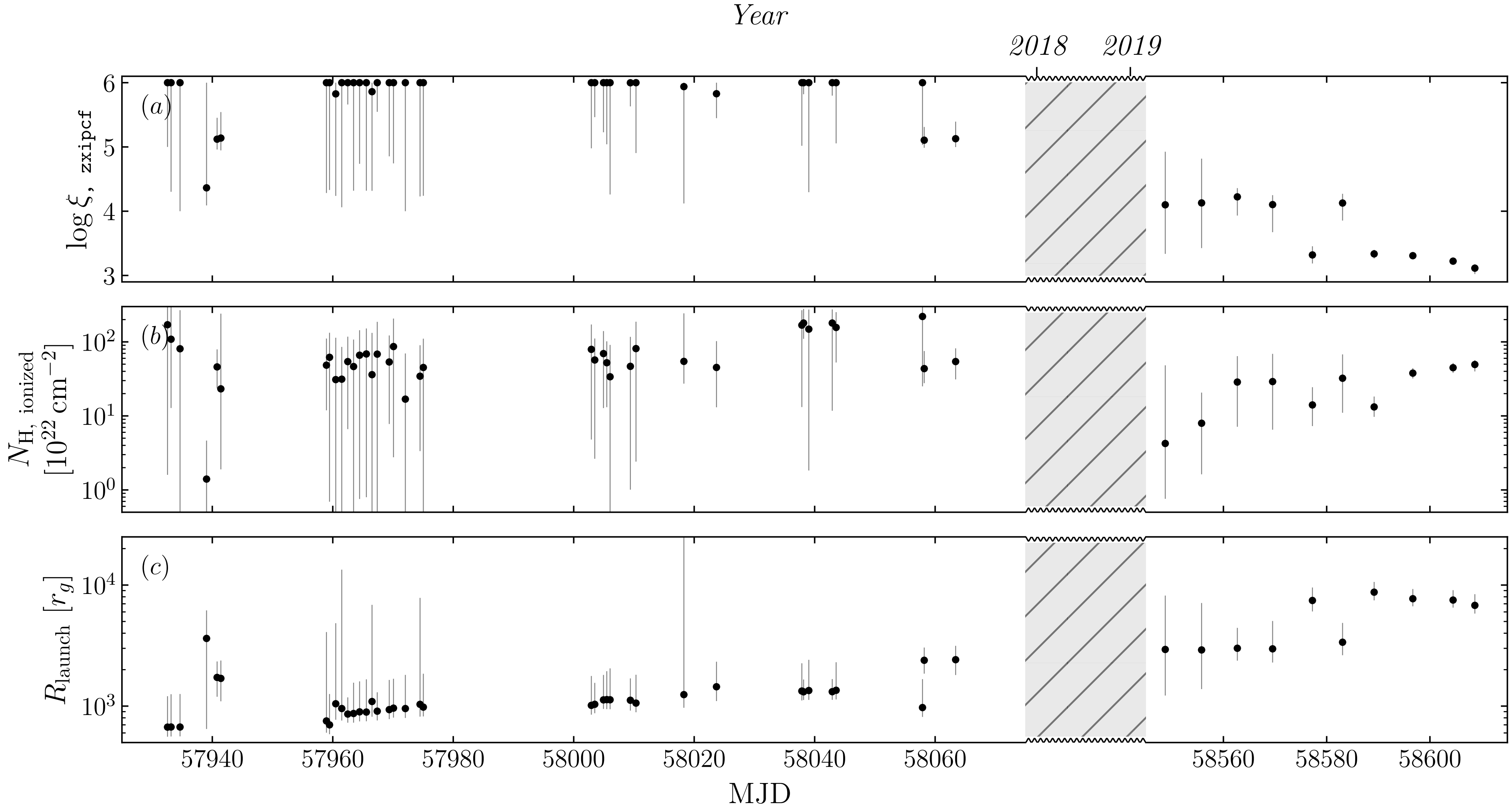

Figure 6.7: Evolution of ionized wind absorption in the soft state and end of the decay phase. Data from MJD 58075–58545 are excluded due to the absence of strong features. (a) Ionization degree, (b) column density, (c) inferred wind launching radius assuming $N_{\mathrm{e}} = 10^{14}\,\mathrm{cm}^{-3}$. (Adopted from Zhou et al. [227])

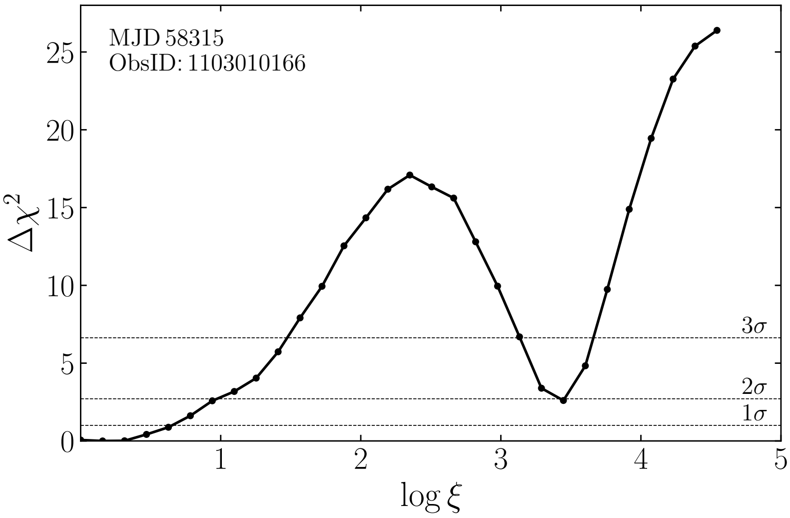

Figure 6.8: $\Delta\chi^2$ fitting statistics of an example spectrum in the decay phase, plotted vs. different values of the ionization degree $\log\xi$ of the relativistic reflection component `relxillCp`. The sample points are shown as black dots and are connected by solid lines. There are two local minima in this plot, with distinct ionization degrees. We discarded the solution with higher $\log\xi$ because it resulted in a vanishing primary emission originating from the corona. (Adopted from Zhou et al. [227])

We estimated the wind launching radius via $R_{\rm launch} \leq \sqrt{L/(N_{\rm e}\cdot\xi)}$ [190], with $L \approx (18 \pm 8)\%, L_{\rm Edd}$ and $N_{\rm e} = 10^{14}\,{\rm cm}^{-3}$ [155]. This yielded $R_{\rm launch} \sim 10^3$–$10^4\,r_{\rm g}$, anti-correlated with $\log\xi$ but not with $T_{\rm in}$ (Fig. 6.7, panel *c*).

6.2.2 During the Decay Phase

Using the model in Sect. 6.1.2, we analyzed the spectral evolution during the exponential/linear decay phase.

The QPO-Γ Correlation

Figure (6.5) shows a quasi-linear correlation between LFQPO frequency and photon index Γ, even with the improved model (Eq. 6.1), though the added complexity increases Γ uncertainties. The steeper Γ arises from modeling the iron line as a reflection feature, not an isolated emission.

The timing analysis suggests that GRS 1915+105 evolves from an intermediate state to a hard state after MJD 58200, and back to a hard-intermediate state. The Γ evolution supports this classification. Despite ionized winds near the end of the decay, the QPO-Γ relation holds, indicating the corona evolves independently of the winds.

Such correlations are common in BHBs (e.g., Cygnus X-1, GX 339−4). Though QPO origins are often linked to Lense-Thirring precession or accretion-ejection instabilities, we cannot test these theories here, as our model fixes the disk's inner radius at ISCO.

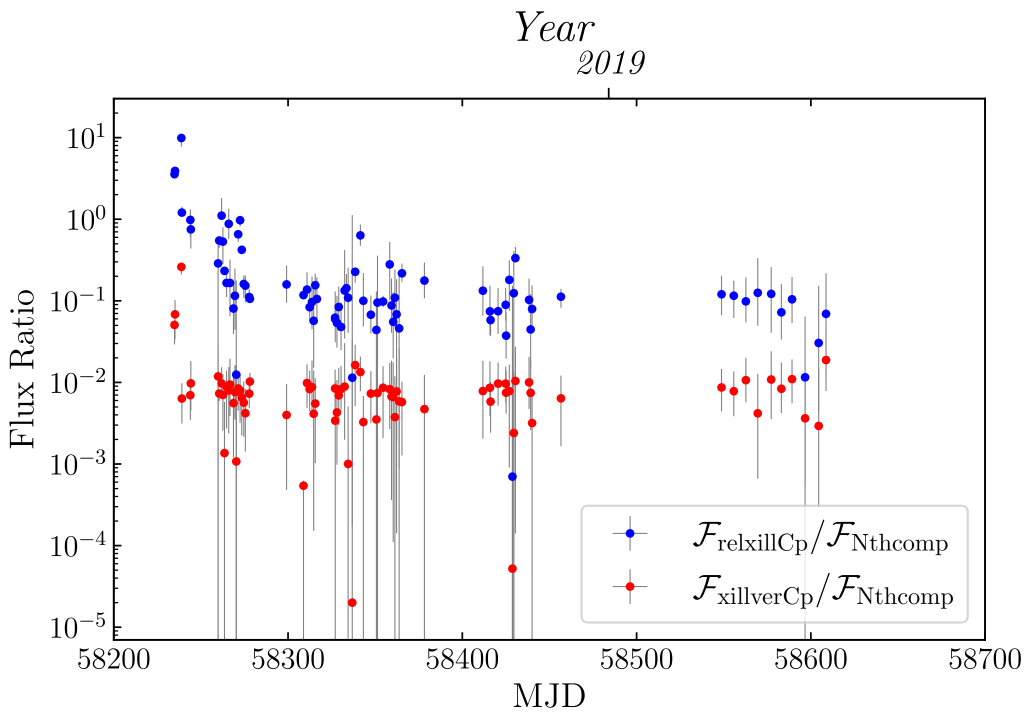

Figure 6.9: Evolution of the ratio of the unabsorbed flux of the incident Comptonization spectra and that of the relativistic and distant reflection components vs. time. The fluxes of `relxillCp`, which models the relativistic reflector, and those of `xillverCp`, which models the distant reflector, were corrected by the multiplicative model `nthratio`. $\mathcal{F}_{\rm relxillCp}/\mathcal{F}_{\rm Nthcomp}$ indicates the geometrical information of the accreting system. (Adopted from Zhou et al. [227])

The Ionization Degree and the Electron Density of the Accretion Disk

Ionization ($\log \xi$) affects the reflection spectrum, especially the Fe lines. Initially, $\log \xi$ values (2.7–3.0) resemble those from the soft state. After MJD 58238, spectra show two solution branches: (1) low $\log \xi \lesssim 2$ with stronger reflection; and (2) high $\log \xi \gtrsim 3$ with vanishing primary emission and extreme reflection fractions. Both branches fit statistically, but we discard the latter due to the presence of strong QPOs, which imply a non-negligible corona (Fig. 6.8).

From MJD 58238 onward, most observations favor low $\log \xi$, placing the Fe line at 6.4 keV, consistent with Fe I–Fe XVII [87], but differing from Koljonen & Hovatta [102] who found higher ionization. Electron density $\log N$ is poorly constrained, with a typical best-fit value of ∼18 (Fig. 6.6, panel f).

The Intensity of the Reflection Components

Assuming the corona dominates, we computed flux ratios of the reflection to the primary emission (Fig. 6.9). The distant reflection drops sharply in the first 10 days (MJD 58234–58244), likely due to self-obscuration by a thick inner disk. It then remains two orders of magnitude fainter. The relativistic reflection continues to decline until MJD 58280, eventually stabilizing at ∼10% of the primary flux.

The Ionized Absorption near the End of the Decay Phase (MJD 58548–58608)

In the final stage, we detect warm wind absorption in NICER spectra [102, 136]. Over 60 days, the absorption column density increases, while $\log \xi$ decreases from $\sim$4 to 3. Complex features near 6.4–6.7 keV emerge (Fig. 6.7).

Unlike typical soft-state winds (absent QPOs), these occur in a hard-intermediate state, with $\Gamma = 2.0$–2.4 and clear type-C QPOs. Using $N_{\rm e} = 10^{14}\,{\rm cm}^{-3}$, the inferred launching radius slightly increases (Fig. 6.7, panel *c*). However, this estimate is qualitative, as $N_{\rm e}$ depends on disk geometry [63]. The unabsorbed luminosity remains at $\sim$2% $L_{\rm Edd}$.

Though `zxipcf` assumes $\Gamma = 2$, and our spectra deviate slightly, this likely does not significantly bias our $\log \xi$ estimates. The uncertainties absorb such systematic effects.

6.3 Discussion

6.3.1 A Rarely Seen Warm Ionized Wind in the Hard-Intermediate State

Ionized disk winds in BHBs are mostly seen in soft states with high ionization ($\log \xi \geq 4$) [e.g., 134, 163]. Although some hard/hard-intermediate state detections exist [110, 182], they often involve high luminosity or depend on model assumptions [e.g., 214].

Our study confirms a warm ionized wind near the end of the hard decay in GRS 1915+105. The estimated launching radius remains stable under different density assumptions. The outflow velocities ($\geq 100\,{\rm km\,s}^{-1}$) far exceed any motion in the launching radius, suggesting a relatively stationary origin. The launching radii (10^3–$10^4\,r_{\rm g}$) are consistent with previous soft-state winds, implying a similar driving mechanism. The wind may later evolve into the cold absorbing medium observed in the obscured state.

6.3.2 The Interaction between the Corona and the Accretion Disk

Reflection-to-Incident flux ratios ($\mathcal{F}_{\rm relxillCp}/\mathcal{F}_{\rm Nthcomp}$ & $\mathcal{F}_{\rm xillverCp}/\mathcal{F}_{\rm Nthcomp}$) dropped sharply in early decay, indicating geometric changes in the accretion flow. The continued drop in the relativistic ratio suggests a receding corona or weakening interaction with the disk.

This deviates from typical hard-to-soft transitions, where reflection increases. Even though photon index and QPO frequency rose at the end of the decay, the reflection stayed weak—possibly due to a truncated disk or reduced returning radiation [44].

In the lamp-post geometry, the declining flux ratio indicates the corona is moving away from the disk. Alternatively, in horizontally extended corona models, this implies weakening disk-corona coupling, perhaps from a shrinking inner disk or reduced infall.

6.3.3 The Interplay between the Disk Winds and the Corona during and after the Decay

Jets and winds usually anti-correlate [156], but exceptions exist [145]. In GRS 1915+105, disk winds emerged late in the decay, while Type-C QPOs persisted, suggesting independent corona behavior.

Assuming the same wind-launching mechanism in both soft and decaying hard states leads to contradictions: the winds and radio jets coexisted, and inner disk radius evolution does not clearly trigger winds. Instead, we propose a delayed, outer-disk response to coronal changes—e.g., reduced jet power increases Compton heating, launching winds that extract angular momentum and cool the disk [21, 152]. This could accelerate the system's decay and promote obscuration.

Observations during the obscured state show Fe line variability linked to the brightness of the central source [155]. Both neutral and ionized Fe lines likely originate from different regions—disk surface and outflowing plasma, respectively—mirroring behavior in other high-inclination systems like V404 Cyg [98] and V4641 Sgr [180].

7 Polarimetric Measurements of 4U 1907+09 [225]

7.1 Results

7.1.1 Light Curves and Pulse Profiles

4U 1907+09 was observed twice between 2024 November 11–21, near periastron, during its brightest phases in the MAXI light curve (Fig. 4.3) [128]. The folded MAXI light curve after MJD 59000, based on in 't Zand et al. [91], is also shown with uncertainties.

Three brief flares, each lasting several hours and accounting for 30% of the total photons, were detected during the IXPE observations (marked in cyan in Fig. 4.3).

Pulse period and its derivative were derived using Z^2 statistics on 2–8 keV photons from both observations [28] (see Table 4.3). Corresponding pulse profiles and phaseograms over the 11-day span are shown in Fig. (7.1).

7.1.2 Polarimetric Analysis

We performed a polarimetric analysis of 4U 1907+09 using XSPEC, accounting for energy dispersion and spectral shape. Stokes I, Q, and U spectra from all three DUs were used to compute normalized Stokes parameters (q, u), PD, and PA following Kislat et al. [99]. All nine spectra were then jointly fitted.

The continuum was modeled with an absorbed power law using the form: `constant` × `tbabs` × `powerlaw` × `polconst`, where `polconst` assumes constant PD and PA. The model was applied to both phase-averaged and phase-resolved data. Results were cross-validated using the model-independent `pcube` method.

Phase-Averaged Analysis

We begin with a phase-averaged analysis over the full 2–8 keV range for both observations, with the results summarized in Table (7.1). Obs. 1 shows stronger polarization than Obs. 2, with phase-averaged PDs of $6.0 \pm 1.6\%$ and $2.2 \pm 1.6\%$, respectively. The corresponding PAs are $69° \pm 8°$ for Obs. 1 and $46° \pm 23°$ for Obs. 2. Additionally, we conducted a spectral-polarimetric analysis on the combined dataset from both observations, with the results summarized in the final column of Table (7.1). Assuming a source distance of $d \simeq 1.9$ kpc [8], we estimate the luminosity of 4U 1907+09 to be $L \simeq 2.5 \times 10^{35}$ erg/s.

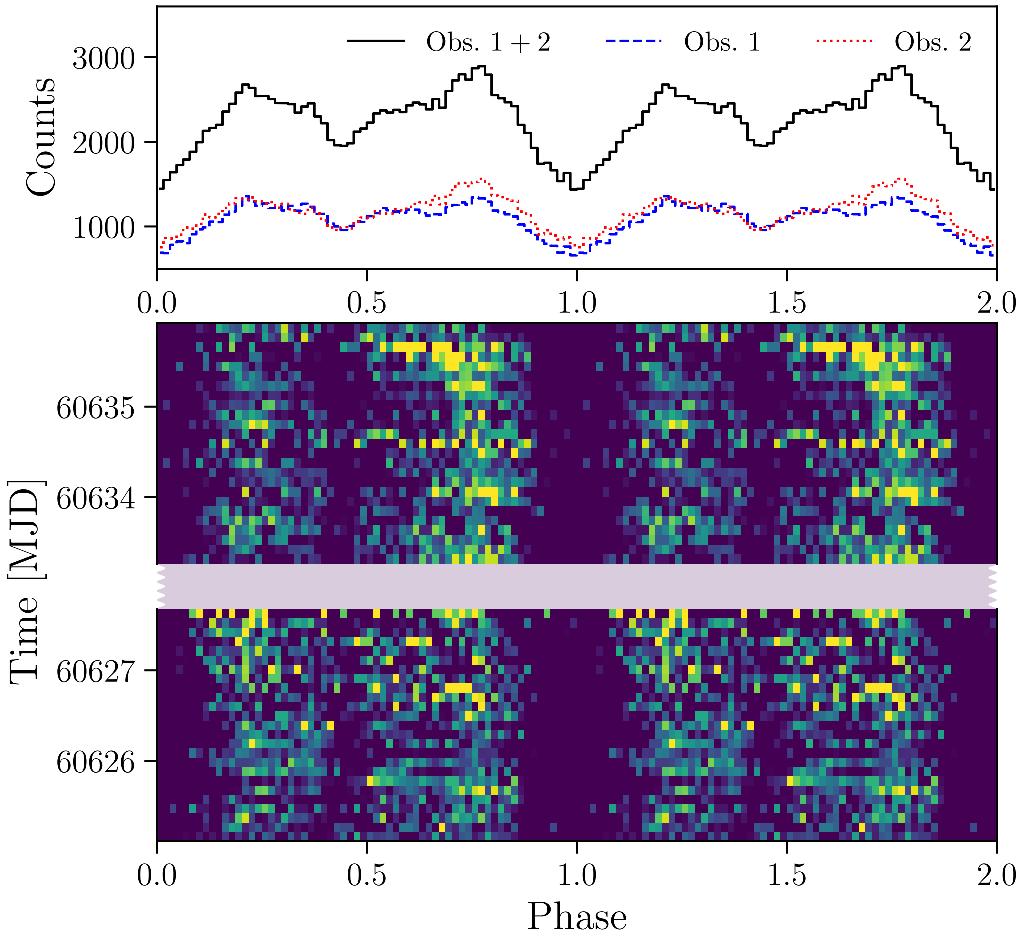

Figure 7.1: Pulse profiles of 4U 1907+09 during two IXPE observations and their phaseograms versus time. (Adopted from Zhou et al. [225])

Table 7.1: Spectral parameters for the best-fit model obtained from the phase-averaged spectro-polarimetric analysis with XSPEC for Obs. 1 and 2.

Component	Parameter	Unit	Obs. 1	Obs. 2	Obs. 1 & 2
`tbabs`	N_{H}	10^{22} cm^{-2}	4.86 ± 0.17	5.12 ± 0.17	4.99 ± 0.12
`powerlaw`	Γ		1.18 ± 0.04	1.27 ± 0.04	1.22 ± 0.03
`polconst`	PD	%	6.0 ± 1.6	2.2 ± 1.6	3.7 ± 1.1
	PA	deg	69 ± 8	46 ± 23	63 ± 9
`constant`	$\mathrm{const}_{\mathrm{DU2}}$		1.025 ± 0.010	1.027 ± 0.009	1.027 ± 0.007
	$\mathrm{const}_{\mathrm{DU3}}$		1.015 ± 0.010	0.995 ± 0.009	1.005 ± 0.007
	$\mathrm{Flux}_{2-8\,\mathrm{keV}}$ [a]	10^{-10} erg s^{-1} cm^{-2}	1.39 ± 0.01	1.47 ± 0.01	1.436 ± 0.009
	χ^2/d.o.f.		1133.1/1112	1201.0/1118	1295.9/1241

Notes. The uncertainties are given at the 68.3% (1σ) confidence level and were obtained using the `error` command in XSPEC with $\Delta\chi^2 = 1$ for one parameter of interest. [(a)] Observed (absorbed) flux in the 2–8 keV range.

Table 7.2: Polarimetric parameters in different energy bins for the two IXPE observations with XSPEC method.

	Obs. 1		Obs. 2		Obs. 1 & 2	
Energy (keV)	$\mathrm{PD_{XSPEC}}$ (%)	$\mathrm{PA_{XSPEC}}$ (deg)	$\mathrm{PD_{XSPEC}}$ (%)	$\mathrm{PA_{XSPEC}}$ (deg)	$\mathrm{PD_{XSPEC}}$ (%)	$\mathrm{PA_{XSPEC}}$ (deg)
2–3	7.1 ± 3.4	61 ± 14	3.8 ± 3.3	54 ± 30	5.4 ± 2.4	59 ± 13
3–4	$1.2^{+2.9}_{-1.2}$	$-55^{\dagger}$	4.1 ± 2.8	-47 ± 22	2.6 ± 2.0	-49 ± 26
4–5	12.9 ± 3.6	74 ± 8	6.6 ± 3.5	48 ± 16	8.5 ± 2.5	65 ± 8
5–6	6.8 ± 4.7	80 ± 22	$4.1^{+4.6}_{-4.1}$	$-39^{\dagger}$	$2.5^{+3.3}_{-2.5}$	$-78^{\dagger}$
6–8	13.1 ± 5.7	49 ± 13	17.0 ± 5.6	37 ± 10	13.4 ± 4.0	43 ± 9
2–8	6.0 ± 1.6	69 ± 8	2.2 ± 1.6	46 ± 23	3.7 ± 1.1	63 ± 9

Notes. The uncertainties computed using the `error` command are given at the 68.3% (1σ) confidence level ($\Delta\chi^2 = 1$ for one parameter of interest). $^{(\dagger)}$The PA cannot be confined within the 1σ confidence level; therefore, we present the most probable value instead.

We studied the energy dependence of the polarization properties of 4U 1907+09 by performing an energy-resolved polarimetric analysis, dividing the data into five energy bins. The fitting was done using XSPEC for the Stokes I spectra (2–8 keV) and excluding bins outside the interest range for Stokes Q and U spectra. The results are shown in Table (7.2). Similar outcomes were obtained using the model-independent `pcube` algorithm, as seen in Table (7.3).

Contrary to expectations, the PA was not energy-independent. A higher PD was observed in the 2–3, 4–5, and 6–8 keV bands with greater confidence during both IXPE observations. Polarimetric detections across energy bands also exhibited different PAs. The normalized Stokes parameters q and u for each energy band of the combined data set, shown in Fig. (7.2), highlight these polarization discrepancies.

A similar energy dependence of PA is seen in other XRPs. In VelaX-1, the PA shifts by approximately 90° between the 2–3 and 3–8 keV bands [60, 62], and in 4U 1538−52, the PA shifts by about 70° between the 2–3 and 4–8 keV bands [117].

We tested the null hypothesis that the PA does not depend on energy. Since PAs are not normally distributed, we used the probability density function (PDF) of PA, ψ, from Naghizadeh-Khouei & Clarke [150]:

$$G(\psi) = \frac{1}{\sqrt{\pi}} \left\{ \frac{1}{\sqrt{\pi}} + \eta \mathrm{e}^{\eta^2} \left[1 + \mathrm{erf}(\eta)\right] \right\} \mathrm{e}^{-p_0^2/2} \,, \tag{7.1}$$

where $p_0 = \mathrm{PD}/\mathrm{PD_{err}}$ is the measured PD in units of its error, and $\eta = p_0 \cos\left[2\left(\psi - \psi_0\right)\right]/\sqrt{2}$. We performed Monte Carlo simulations using the parameters from the XSPEC fit (Table 7.2), defining the Z-score as $Z = -\sum \log G(\psi)$. To simulate the Z-score distribution under the null hypothesis, we used the average PA (63°), PD (3.7%), and its uncertainty (1.1%) within the 2–8 keV range. The observed Z-score, based on the most probable values of ψ for each energy band, was calculated. The resulting p-value of 0.049 provides moderate evidence that PA depends on energy, with a statistical significance of 1.7σ.

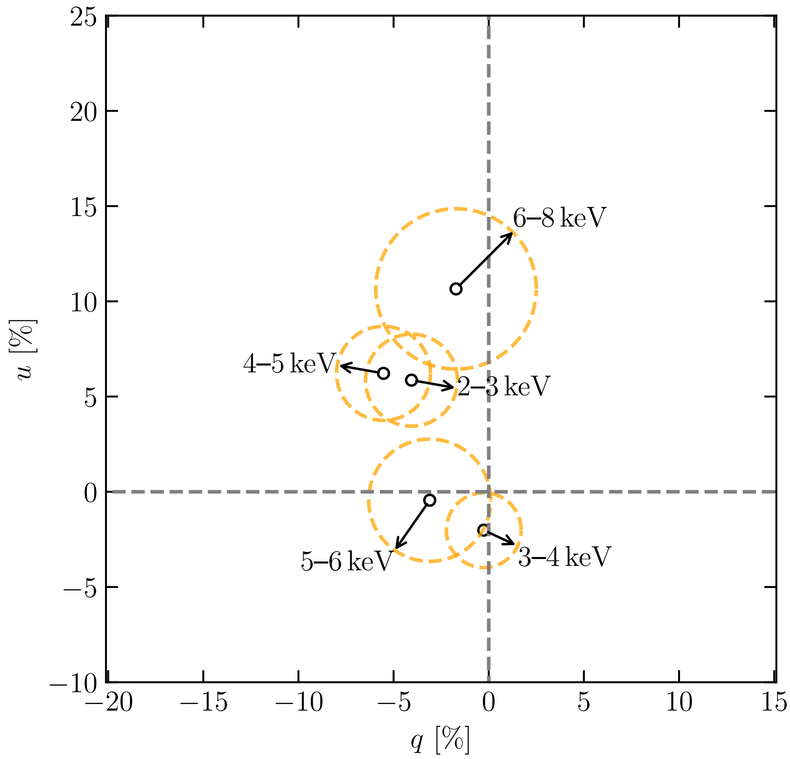

Figure 7.2: Energy dependence of the normalized Stokes parameters q and u for the phase-averaged data of the combined data set, obtained with the `pcube` algorithm. The 1σ contours are plotted as dashed circles around each best estimate. (Adopted from Zhou et al. [225])

Table 7.3: Polarimetric parameters in different energy bins for the two IXPE observations with `pcube` method.

	Obs. 1		Obs. 2		Obs. 1 & 2	
Energy (keV)	$PD_{\mathtt{pcube}}$ (%)	$PA_{\mathtt{pcube}}$ (deg)	$PD_{\mathtt{pcube}}$ (%)	$PA_{\mathtt{pcube}}$ (deg)	$PD_{\mathtt{pcube}}$ (%)	$PA_{\mathtt{pcube}}$ (deg)
2–3	10.1 ± 3.5	60 ± 10	4.5 ± 3.4	68 ± 21	7.1 ± 2.4	62 ± 10
3–4	$1.3^{+2.8}_{-1.3}$	$-43^{\dagger}$	2.7 ± 2.7	-51 ± 28	2.0 ± 2.0	-49 ± 28
4–5	13.3 ± 3.6	74 ± 8	5.5 ± 3.4	46 ± 18	8.3 ± 2.5	66 ± 9
5–6	6.9 ± 4.6	77 ± 19	$3.8^{+4.5}_{-3.8}$	$-46^{\dagger}$	$3.1^{+3.2}_{-3.1}$	$-86^{\dagger}$
6–8	9.0 ± 6.0	57 ± 19	13.0 ± 5.9	45 ± 13	10.8 ± 4.2	50 ± 11
2–8	7.2 ± 2.3	66 ± 9	3.7 ± 2.2	52 ± 17	5.2 ± 1.6	61 ± 9

Notes. The uncertainties are presented at the 1σ confidence level. $^{(\dagger)}$The PA cannot be confined within the 1σ confidence level; therefore, we present the most probable value instead.

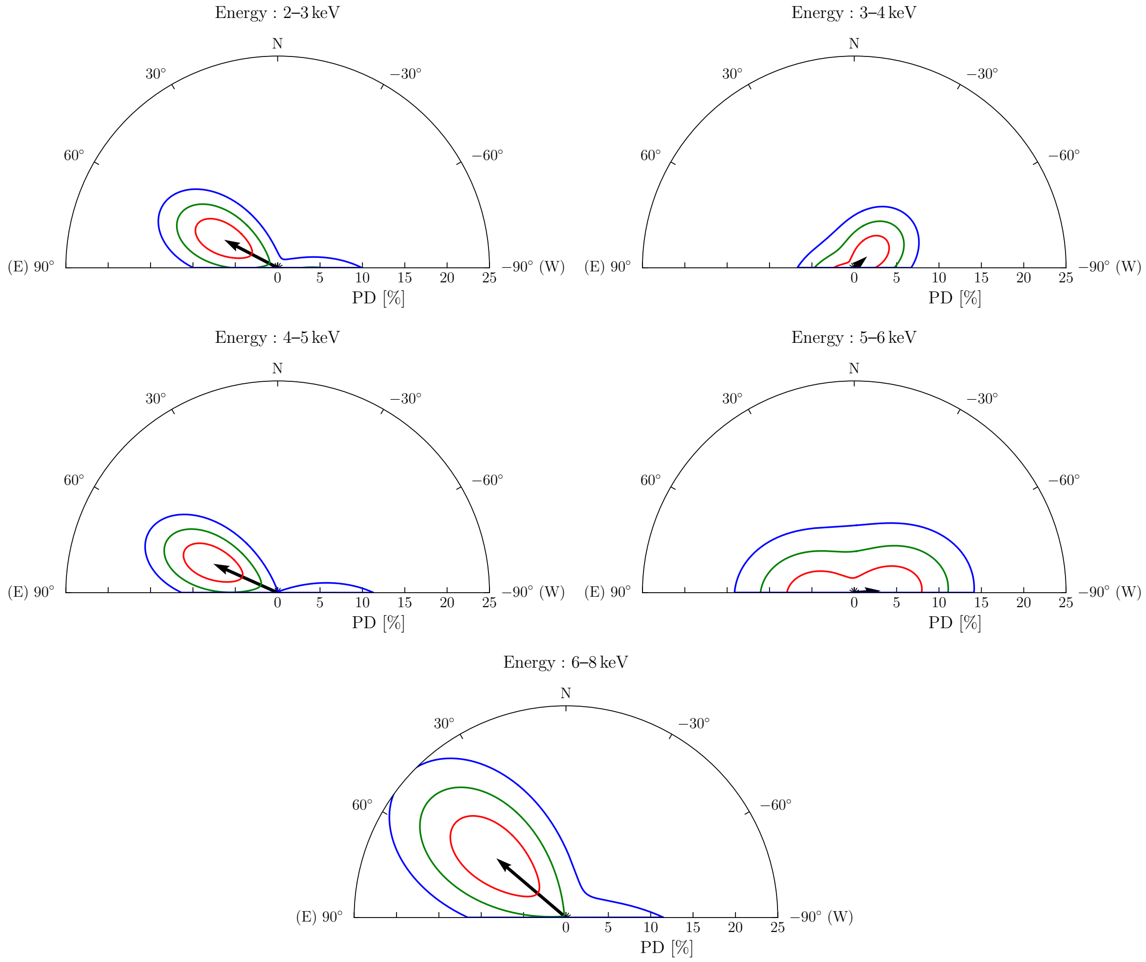

Figure 7.3: Polarization vectors of 4U 1907+09 across different energy bands derived from phase-averaged polarimetric analysis of the combined dataset using the `pcube` algorithm. Confidence contours at 68.3%, 95.45%, and 99.73% are displayed in red, green, and blue, respectively. (Adopted from Zhou et al. [225])

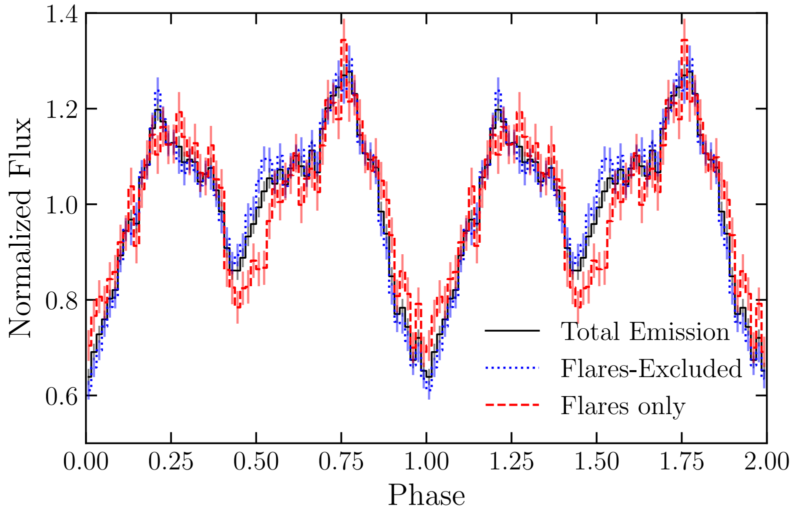

Figure 7.4: Pulse profiles of 4U 1907+09 from the combined IXPE observation with blue dotted, red dashed, and black solid lines representing the profiles for flares-excluded data, flare-only data, and total emission, respectively. (Adopted from Zhou et al. [225])

Phase-Resolved Analysis

Studying the phase-dependent properties of pulsars is important due to the change in their geometries with rotation. Using the ephemerides in Table (4.3), the phase of each photon event is calculated by

$$\phi = \frac{1}{P}(t - t_0) - \frac{1}{2}\frac{\dot{P}}{P^2}(t - t_0)^2 \, ,$$

where P is the pulse period, $\dot{P}$ is the period derivative, and t_0 is the reference time. The photons are divided into 8 uniform phase bins, and Stokes I, Q, and U spectra are generated for each bin.

We first apply the XSPEC method to the 2–8 keV range, and the results for the combined data set are shown in Table (7.4). While some phase bins show polarization detections below 1σ, the modulation of PA with pulse phase is still observable despite gaps in phase coverage.

Next, the `pcube` algorithm is applied to the phase-resolved data, with results shown in the last two columns of Table (7.4). The PDs from `pcube` are generally higher than those from XSPEC, and the PAs from both methods align when the respective PDs are significant.

Table 7.4: Spectral-polarimetric parameters in different pulse-phase bins for the combined data set, derived using XSPEC and PCUBE.

Phase	$N_{\rm H}$ (10^{22} cm^{-2})	Γ	PD$_{\rm XSPEC}$ (%)	PA$_{\rm XSPEC}$ (deg)	χ^2/d.o.f.	PD$_{\tt pcube}$ (%)	PA$_{\tt pcube}$ (deg)
0.0–0.15	$4.98^{+0.36}_{-0.35}$	1.37 ± 0.08	5.4 ± 3.3	-69 ± 19	$689.1/752$	7.9 ± 4.6	-86 ± 17
0.15–0.25	5.08 ± 0.37	1.04 ± 0.08	13.5 ± 3.3	71 ± 7	$825.6/758$	17.1 ± 4.7	60 ± 8
0.25–0.375	$4.32^{+0.33}_{-0.32}$	1.06 ± 0.07	4.1 ± 3.1	0 ± 24	$799.6/809$	$3.3^{+4.3}_{-3.3}$	$-29^{\dagger}$
0.375–0.5	6.09 ± 0.37	1.36 ± 0.08	$2.4^{+3.3}_{-2.4}$	$73^{\dagger}$	$838.9/776$	5.8 ± 4.7	67 ± 23
0.5–0.625	$4.74^{+0.34}_{-0.33}$	$1.06^{+0.08}_{-0.07}$	4.7 ± 3.1	44 ± 21	$828.1/806$	10.4 ± 4.4	40 ± 12
0.625–0.75	5.56 ± 0.32	1.13 ± 0.07	4.6 ± 3.0	61 ± 20	$825.4/845$	4.3 ± 4.1	73 ± 28
0.750–0.85	$4.59^{+0.36}_{-0.35}$	1.35 ± 0.08	4.1 ± 3.4	88 ± 28	$782.3/743$	$3.5^{+4.7}_{-3.5}$	$87^{\dagger}$
0.85–1.0	4.95 ± 0.35	$1.64^{+0.09}_{-0.08}$	7.1 ± 3.4	43 ± 14	$695.0/728$	8.3 ± 4.7	43 ± 16

Notes. The uncertainties in the spectral-polarimetric parameters, computed using the `error` command in XSPEC, are provided at the 68.3% (1σ) confidence level ($\Delta\chi^2 = 1$ for one parameter of interest). The right two columns give PD and PA estimated with the `pcube` algorithm and the uncertainties given at the 1σ confidence level. $^{(\dagger)}$The PA cannot be confined within the 1σ confidence level; therefore, we present the most probable value instead.

7.1.3 Flares and Their Impacts on Polarimetric Properties

The impact of flares on polarimetric detection remains unclear. To investigate, we analyzed flare and non-flare events separately.

First, we compare the pulse profiles during flare and non-flare periods, shown in Fig. (7.4). No significant differences are observed, suggesting that the accretion pulsar geometry remains stable during flares.

Next, we examine the Stokes parameters and PAs as functions of pulse phase and energy in Fig. (7.5). While uncertainties are larger during flares due to lower photon counts, the parameters remain consistent within their uncertainties.

Given that 4U 1907+09 is not particularly bright and photon counts during flares are insufficient, we conclude that the energy-dependent polarimetric properties are not influenced by the flares. Therefore, we include all emissions in the following analysis without distinguishing between flare and non-flare periods.

7.1.4 Energy-Dependent Polarimetric Properties in Different Pulse Phases

We observed energy-dependent polarimetric properties in the phase-averaged analysis and concluded in Sect. 7.1.3 that they are not due to flares. To explore the energy-dependent properties in each pulse phase, we divided photon events into eight phase bins and five energy bins (2–8 keV), then computed the PA and PD using the `pcube` algorithm. The results are shown in Fig. (7.6).

Due to limited photon counts, most PDs in the energy-phase bins fall below the minimum detectable polarization (MDP) at the 99% confidence level. However, PA evolution with energy is still noticeable in each phase bin. The most significant PA rotation occurs between the 4–5 keV and 5–6 keV bands in phase interval 0.25–0.375, with a $\sim 90^\circ$ difference. The PDs approach the MDP_{99}, suggesting a possible right-angle PA rotation within this phase. Protractor plots in Fig. (7.7) show the PAs are compatible only within the 3σ range.

7.2 Discussion

XRPs are prime targets for X-ray polarimetric studies, as the accretion of highly magnetized matter onto the magnetic poles of neutron stars (NSs) is expected to produce strong linear polarization. In such intense magnetic fields, vacuum birefringence causes the electric field vectors of emitted photons to align either parallel or perpendicular to the plane defined by the photon momentum and the local magnetic field [73, 74]. These are referred to as the ordinary (O) and extraordinary (X) modes, respectively. Below the cyclotron energy, the Compton scattering cross-section is significantly higher for O-mode photons than for X-mode, resulting in a predicted PD of up to 80% [32, 130].

However, most XRPs observed with IXPE show relatively low phase-averaged PDs [e.g., 60, 149, 195], with higher PDs typically emerging only in phase-resolved analyses. An exception is 4U1907+09, where polarization is weakly detected in most phase

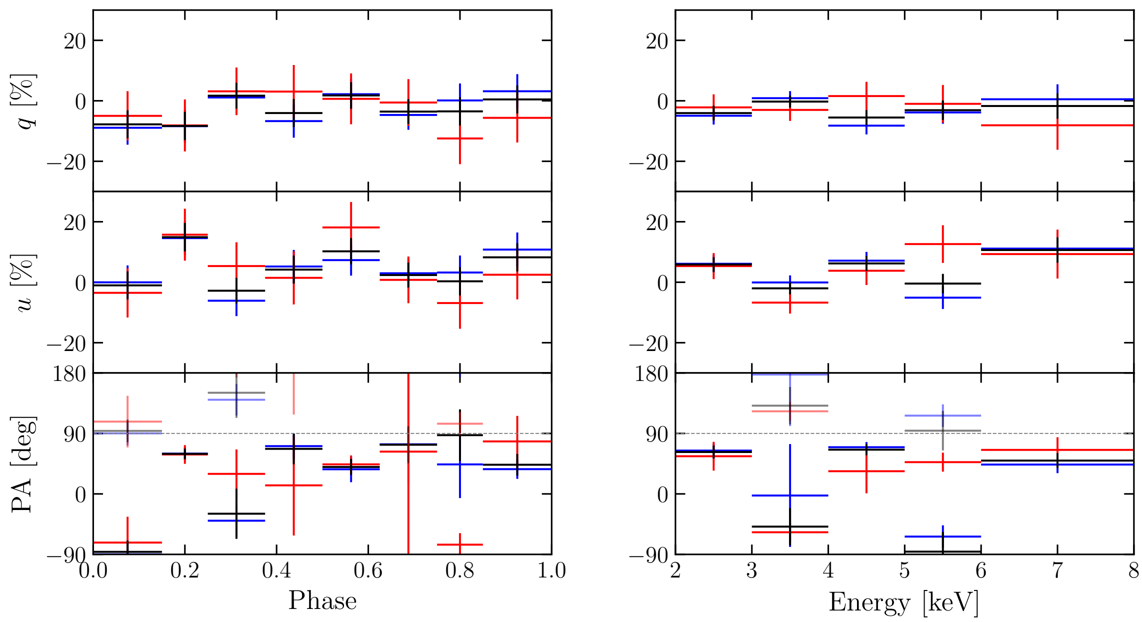

Figure 7.5: Normalized Stokes parameters and measured PAs as functions of pulse phase and energy from the combined IXPE observation, with blue, red, and black crosses representing the flares-excluded data, flare-only data, and total emission data, respectively. Some PAs are plotted twice with an added constant of 180° to illustrate the continuity of the PA with respect to phase and energy. (Adopted from Zhou et al. [225])

bins. Investigating the energy dependence of the PAs within individual phase bins moderately enhances the detection significance in some energy-phase regions (see Fig. 7.6), yet several bins still exhibit very low PD significance.

The phase-averaged analysis reveals a clear energy dependence of the PA, indicating that the rotating vector model (RVM)—which assumes the PA traces the magnetic field direction and is thus energy-independent—is not applicable for constraining the pulsar geometry in this case [130, 165, 169]. Additionally, the lack of a sharp PA transition at a specific energy rules out fitting the data with an energy-resolved RVM model [e.g., 62, 117].

This behavior may be explained by additional polarized components arising from reflection or scattering processes, which can interfere with the primary emission near the magnetic poles [see discussion in 195]. Energy-dependent polarization arising from such processes has been proposed by Forsblom et al. [62] and Loktev et al. [117]. In particular, Forsblom et al. [62] outlined two scenarios to account for energy-dependent PA variations: (1) the presence of a softer spectral component with a PA orthogonal to the dominant high-energy emission, which fades at higher energies; and (2) vacuum resonance effects, where polarization modes convert near the cyclotron energy, causing a 90° PA shift.

In our case, the sharp drop in PDs around 3–4 and 5–6 keV (Tables 7.2 and 7.3) is unlikely to be caused by an additional spectral component peaking only in these narrow bands. As for vacuum resonance, although it predicts an energy-independent PA at both low and high energies, this cannot be confirmed due to the limited photon statistics ($\sim$1.45 million photons in 2–8 keV) and the restricted energy band of IXPE. Moreover, a gradual PA variation with energy would suggest interference from an

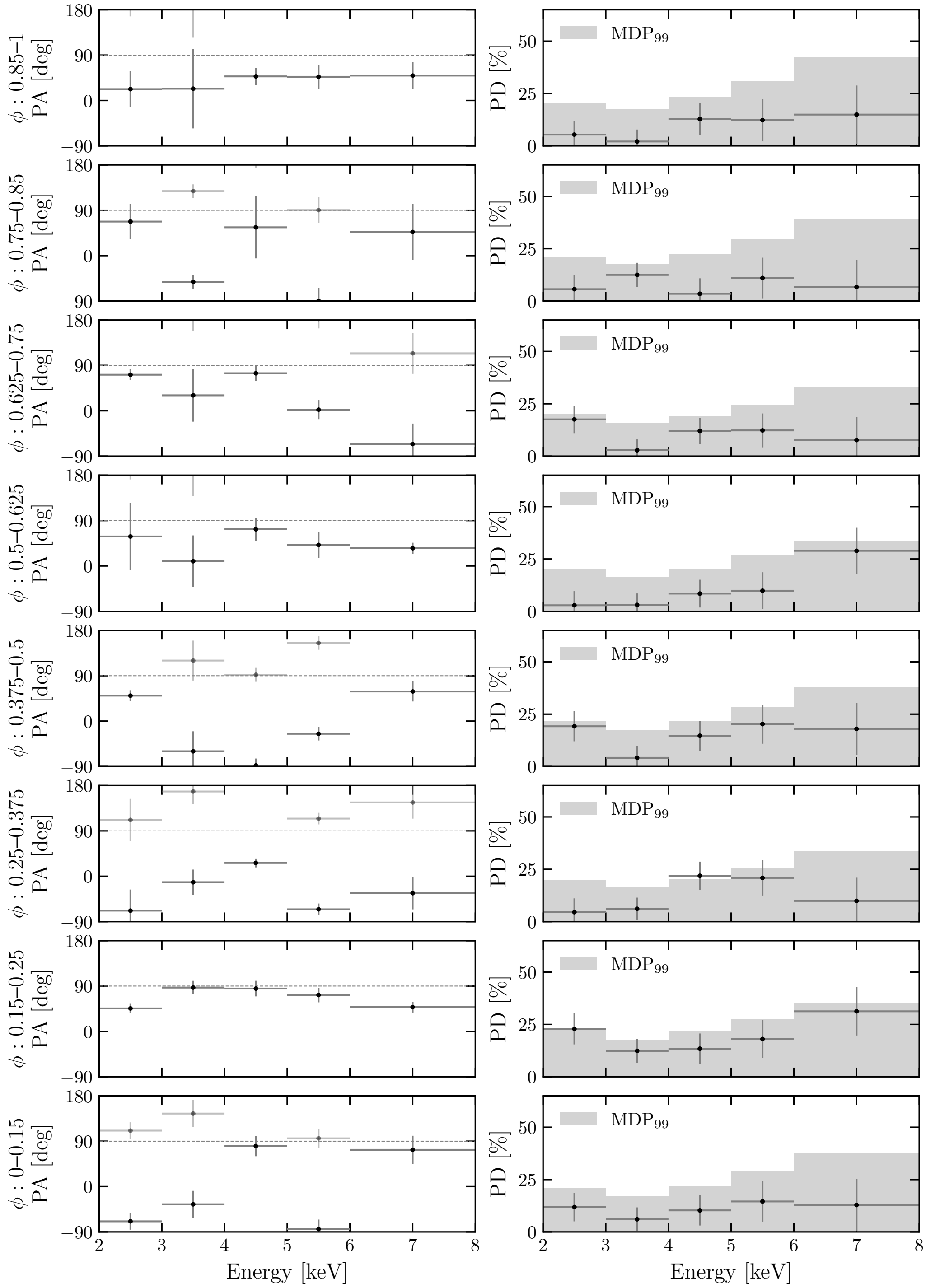

Figure 7.6: Energy-resolved polarization measurements of the combined data set across pulse phases. The left panels show the PA with 1σ uncertainties, while the right panels present the PD. Grey bars indicate the MDP_{99} value. Note that we plot the PA again with an added constant of 180° to illustrate the continuity of the PA versus energy. (Adopted from Zhou et al. [225])

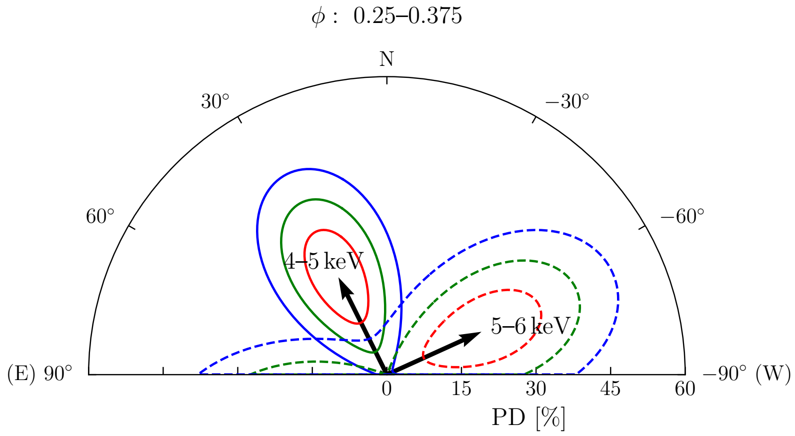

Figure 7.7: The protractor plot of the polarization measurement of the combined data set within the 4–5 keV band and the 5–6 keV band in pulse phase interval 0.25–0.375. (Adopted from Zhou et al. [225])

additional polarized component. Future observations with higher photon counts and broader energy coverage are needed to clarify the underlying polarization mechanisms.

8 Conclusions & Outlooks

This chapter is dedicated to presenting the main findings of Zhou et al. [226], Zhou et al. [227], and Zhou et al. [225].

8.1 Conclusions

8.1.1 Spectral-Timing Analysis of BHBs: Cygnus X-1 and GRS 1915+105

We performed a broadband spectral analysis of Cygnus X-1 using 145 exposures from the HXMT mission, applying a simple phenomenological model. Based on the best-fit results, we carried out energy-resolved timing analyses in the 1–150 keV range, which covers a broader energy band than the previous studies based on RXTE.

Our findings show that the strength of the reflection component increases as the source transitions from the hard to the soft state. We also interpret the relationship between the total rms variability and the soft photon index Γ_1, which depends on the spectral shape, the energy band under study, and especially on whether the disk emission dominates the spectrum.

During the hard-to-soft transition, we observe a clear evolution of the central frequencies of the variability components in the 1–10 Hz range as a function of Γ_1. This trend is traceable up to at least $\sim$90 keV. Once the transition is complete and the source reaches the soft state, the variability components disappear and are replaced by flicker noise in the power spectrum.

High-energy photons from the corona appear to be associated with the variability component with the highest central frequency, suggesting that these photons originate from regions very close to the BH. The intrinsic coherence of the signal helps distinguish between light curves in different spectral states, reflecting changes in the dominant emission mechanism (thermal vs. Comptonized). Additionally, we find that the averaged phase lag increases during the transition but drops sharply once the transition concludes.

For GRS 1915+105, we conducted a spectral-timing study using all NICER and Insight-HXMT observations prior to MJD 58617, before the source entered the obscured state. We constructed a broadband spectral model using simultaneous NICER and HXMT data, and used it in combination with high-cadence NICER observations to trace the source's evolution.

Before 2018, during a disk-dominated state, we consistently observed a highly ionized wind, revealed by the Fe XXVI Lyα line at 7 keV. The photon index Γ reached the upper bound of our model ($\sim$3.4), and the thermal emission strongly dominated the spectrum.

During the subsequent decay phase, which reflects a transition from partial hardening to an unusual obscured state, we identified a quasi-linear correlation between Γ and the main QPO frequency. As the decay progressed, the spectrum exhibited increasingly strong absorption features with a decreasing ionization degree, and clear type-C QPO features were present in the hard-intermediate state. The estimated launching radius of the warm ionized wind remained comparable to that in the soft state, suggesting that the same launching mechanism might operate in both spectral states.

At the onset of the decay phase, both relativistic and nonrelativistic reflection components were strong, but the relativistic component weakened by a factor of 10 within just 10 days, possibly due to diminishing self-obscuration. Over the next 30 days, the relativistic reflection continued to decline, while the nonrelativistic reflection remained stable. Midway through the decay, both components maintained their relative intensities, but the relativistic reflection began to show a decreasing trend as the warm wind reappeared.

This discrepancy is indicative of an unusual softening process, potentially signaling an increasing disk-corona separation (in the lamp-post geometry) or an expanding inner disk radius (in a returning radiation scenario). The evolving QPO frequency and photon index are tightly linked, and the reappearance of ionized winds suggests a slowing of accretion near the end of the decay.

8.1.2 Polarimetric Analysis of the Accretion-Powered Pulsar 4U 1907+09

The accretion-powered pulsar 4U 1907+09 was observed twice by IXPE between 2024 November 11 and 21, during its brightest periods near periastron. Our polarimetric analysis reveals notable differences between the two observations.

Observation 1 showed more significant polarization than Observation 2. The phase-averaged PD and PA were $6.0 \pm 1.6\%$ and $69^\circ \pm 8^\circ$, respectively, for Observation 1, compared to $2.2 \pm 1.6\%$ and $46^\circ \pm 23^\circ$ for Observation 2. When both data sets are combined, we find a PD of $3.7 \pm 1.1\%$ and a PA of $63^\circ \pm 9^\circ$.

Energy-dependent rotation of the PA is likely present in the phase-averaged polarimetric data, with a detection significance of 1.7σ. We observe potential PA shifts between adjacent energy bands within a single phase bin, which may partially explain the generally low-significance polarization detections.

We also investigated whether the three short flares detected by IXPE affect the pulsar's polarization properties. The results show that both the flare-excluded and flare-only data yield consistent polarimetric measurements. This suggests that the observed energy-dependent PA features are unlikely to be caused by these flares.

8.2 Outlook

Since completing my first paper, which focused on the X-ray properties of Cygnus X-1, I have been increasingly motivated to think beyond the immediate results and consider the broader direction of accretion studies in high-energy astrophysics. What is the next milestone in this field? What can we expect to discover, and how can we contribute meaningfully to uncovering the mechanisms that govern matter under extreme gravitational and magnetic conditions?

Although observational capabilities have advanced significantly—particularly in terms of spectral resolution, sensitivity, and energy coverage—observational high-energy astrophysics remains, at its core, a photon-starved science. Unlike radio or optical astronomy, where resolved imaging can reveal rich structural details, the study of compact objects in X-rays largely relies on indirect inference. Due to their small angular sizes and vast distances, even the brightest galactic BHs and NSs appear as point sources in the X-ray sky. As a result, our knowledge of these systems is largely reconstructed through careful analysis of their spectral energy distributions, timing properties, and, more recently, polarization signatures. Despite these constraints, such analyses have proven remarkably powerful. Still, they compel us to continually ask: how can we push further within these observational limits? What should the next steps be?

One of the most valuable observational opportunities in this regard is capturing a full state transition in an accreting BH or NS binary. While much has been learned from studies of the canonical hard and soft states, our understanding is primarily built on time-averaged observations during relatively stable intervals. Transitions themselves—especially the fast and unstable phases—are more rarely observed with sufficient cadence or exposure to resolve their detailed evolution. From current knowledge, we understand that the characteristic variability frequencies, such as LFQPOs, tend to increase as the X-ray spectrum softens during the transition from the hard to the soft state. In some well-sampled cases, the LFQPO frequency can increase up to $\sim$10 Hz. However, it remains an open question whether this trend continues to even higher frequencies during brief intermediate phases, or whether the QPOs disappear entirely, perhaps due to a disruption in the inner accretion flow or changes in the corona-disk coupling. In particular, it is unclear whether the disappearance of QPOs is abrupt or preceded by subtle changes in coherence, phase lag, or polarization—information that could point toward the physical mechanism responsible for their origin and termination. These unanswered questions make high-cadence, multi-wavelength observations during transitions critically important.

Equally important is the growing role of X-ray polarimetry, a technique that is finally coming of age with the recent launch of the IXPE, and with future missions such as eXTP on the horizon. Polarimetry offers an entirely new dimension for understanding the geometry and radiative mechanisms at play near compact objects. In particular, XRPs are excellent candidates for polarimetric studies due to their strong magnetic fields and well-defined pulse phases. As demonstrated in Sect. 7.1, XRPs can show energy-dependent PAs, potentially tracing the beaming geometry, the emission region shape, or magnetospheric scattering processes. However, the current interpretation of these results is hampered by statistical limitations—especially in phase-resolved and energy-resolved polarimetry, where the number of photons in each bin can be small.

At present, it is not yet clear whether the observed variation in PA is intrinsic to the source—suggesting a more complex magnetospheric structure or non-uniform emission pattern—or whether it results from insufficient exposure time, which limits our ability to constrain the PD and PA accurately in finer bins. Future observations with longer integration times, or coordinated multi-epoch campaigns, could help address this ambiguity. Furthermore, combining polarimetry with phase-resolved spectroscopy and timing analysis may open a path toward a more unified picture of emission processes in XRPs, including the structure of the accretion column, the role of cyclotron resonant scattering, and the angular dependence of the beam pattern.

Ultimately, the next advances in our understanding of accretion and high-energy emission will likely come not from a single observational breakthrough, but from the convergence of complementary techniques: spectral-timing-polarimetric analysis applied across different states, over a variety of compact object types, and on statistically robust datasets. My hope is to continue contributing to this effort, combining rigorous data analysis with physically motivated models to help illuminate the environments around some of the most extreme objects in our Galaxy.

A Published Article 1

A&A 666, A172 (2022)
https://doi.org/10.1051/0004-6361/202244240

Astronomy & Astrophysics

The spectral-timing analysis of Cygnus X-1 with Insight-HXMT

M. Zhou (周孟磊)[1], V. Grinberg[2], Q.-C. Bu (卜庆翠)[1], A. Santangelo[1], F. Cangemi[3], C. M. Diez[1], O. König[4], L. Ji (纪龙)[5], M. A. Nowak[6], K. Pottschmidt[7,8], J. Rodriguez[9], J. Wilms[4], S. Zhang (张澍)[10,11], J.-L. Qu (屈进禄)[10,11], and S.-N. Zhang (张双南)[10,11]

1 Institut für Astronomie und Astrophysik, Universität Tübingen, Sand 1, 72076 Tübingen, Germany
e-mail: menglei.zhou@astro.uni-tuebingen.de
2 European Space Agency (ESA), European Space Research and Technology Centre (ESTEC), Keplerlaan 1, 2201 AZ Noordwijk, The Netherlands
3 Laboratoire de Physique Nucléaire et des Hautes Énergies, Sorbonne Université, 4 Place Jussieu, 75005 Paris, France
4 Dr. Karl Remeis-Sternwarte and ECAP, Friedrich-Alexander-Universität Erlangen-Nürnberg, Sternwartstr. 7, 96049 Bamberg, Germany
5 School of Physics and Astronomy, Sun Yat-Sen University, 519082 Zhuhai, PR China
6 Physics Department, Washington University CB 1105, St Louis, MO 63130, USA
7 CRESST and Astroparticle Physics Laboratory, NASA Goddard Space Flight Center, Greenbelt, MD 20771, USA
8 Department of Physics and Center for Space Sciences and Technology, University of Maryland, Baltimore County, Baltimore, MD 21250, USA
9 Université Paris-Saclay, Université Paris Cité, CEA, CNRS, AIM de Paris-Saclay, 91191 Gif sur Yvette, France
10 Key Laboratory for Particle Astrophysics, Institute of High Energy Physics, Chinese Academy of Sciences, 100049 Beijing, PR China
11 University of Chinese Academy of Sciences, Chinese Academy of Sciences, 100049 Beijing, PR China

Received 10 June 2022 / Accepted 12 September 2022

ABSTRACT

Cygnus X-1, as the first discovered black hole binary, is a key source for understanding the mechanisms of state transitions and the scenarios of accretion in extreme gravity fields. We present a spectral-timing analysis of observations taken with the Insight–Hard X-ray Modulation Telescope (HXMT) mission, focusing on the spectral-state-dependent timing properties in the broad energy range of 1−150 keV, thus extending previous studies based on Rossi X-ray Timing Explorer (RXTE) to both lower and higher energies. Our main results are the following: (a) We successfully use a simple empirical model to fit all spectra, confirming that the reflection component is stronger in the soft state than in the hard state. (b) The evolution of the total fractional root mean square (rms) depends on the selected energy band and the spectral shape, which is a direct result of the evolution of the power spectral densities (PSDs). (c) In the hard/intermediate state, we see clear short-term variability features and a positive correlation between the central frequencies of the variability components and the soft photon index Γ_1, which we also see at energies above 15 keV. In the soft state, the power spectrum is instead dominated by red noise. These behaviors can be traced to at least 90 keV. (d) Finally, the coherence and the phase-lag spectra show different behaviors, depending on the different spectral shapes.

Key words. X-rays: binaries – accretion, accretion disks – X-rays: individuals: Cygnus X-1 – stars: black holes

1. Introduction

Black hole binaries (BHBs) are systems consisting of a black hole accreting material from a donor star (for a review on BHBs, see e.g., Remillard & McClintock 2006; Done et al. 2007; Dunn et al. 2010). The radiation produced by the accretion process is bright in the X-rays, exhibiting a rich phenomenology in both spectral and timing domains. Most BHBs are transient, and exhibit luminous outburts. Cygnus X-1 is one of the few persistent systems (Bowyer et al. 1965; Bolton 1972; Webster & Murdin 1972). Tananbaum et al. (1972) first reported a global change in the X-ray spectra of Cygnus X-1, with a simultaneous switching-on of the jet emission. It was later realized that this corresponded to a transition from the soft to the hard state.

The X-ray spectrum of the hard state is characterized by a (cut-off) power-law component with a photon index $\Gamma \lesssim 2.0$ and with weak or undetectable thermal black body emission from the accretion disk (e.g., Tomsick et al. 2008). The power-law emission is presumably produced via Comptonization by a hot ($kT_e \approx$ 100 keV) plasma (Haardt 1993; Dove et al. 1997; Zdziarski et al. 2003; Ibragimov et al. 2005). In contrast, the spectrum in the soft state is dominated by thermal emission with a characteristic temperature of several hundred electron volts (eV) and a steep power law with $\Gamma \gtrsim 2.7$. In between these two states, the intermediate state is defined, which exhibits spectral characteristics that are intermediate to the hard and the soft states but with distinct timing features. BHB transients spend most of their time in the quiescent state, which is extraordinarily faint and hard ($1.5 \lesssim \Gamma \lesssim 2.1$, see e.g., Plotkin et al. 2013). However, they usually trace the so-called q-track in the hardness–intensity diagram (HID) during the outburst, moving from the quiescent state, to the hard state, the intermediate state, and then the soft state (Homan et al. 2001; Fender et al. 2006).

Timing properties of BHBs also show distinct behaviors in different states (Wijnands & van der Klis 1999). In the hard and intermediate states, we see strong intrinsic variability with the central frequencies mostly located in the 0.1−10 Hz range, often referred to as low-frequency quasi-periodic oscillations (LFQPOs) if it is a narrow and prominent feature (see e.g., Done et al. 2007, and for a recent review see Ingram & Motta 2019). The variability is high (∼20% rms) in the hard state (Belloni 2010). The central frequencies of the variability components have been found to show a strong correlation with the spectral state (see Remillard & McClintock 2006, and the references therein). However, in the soft state, the power spectrum is dominated by the red noise with slope f^{-1} below 10 Hz and a cut-off tail at higher frequencies (e.g., Gilfanov et al. 2000; Axelsson et al. 2005). During the hard-to-intermediate transition, we often observe a continued growth of the averaged hard lags (i.e., the hard photons lag the soft photons) between two coherent energy bands (Cui et al. 1997a; Pottschmidt et al. 2000; Reig et al. 2018). The time-lags reach a maximum just before completing the transition to the soft state, and then drop to ∼0 s in the soft state (Böck et al. 2011; Grinberg et al. 2014; Altamirano & Méndez 2015).

The physics of the state transition is not yet fully understood. A widely used scenario to explain the state transition behaviors is the "truncated disk/hot inner flow model" (Ichimaru 1977; Narayan & Yi 1995; Narayan & McClintock 2008). The outer part of the disk is described by a standard optically thick accretion disk (Shakura & Sunyaev 1973), where the emission produced by the disk is modeled by the thermal black body radiation. The disk is truncated at some radius. The inner part is substituted by an optically thin hot flow, which corresponds to the "corona" that produces the nonthermal power-law emission (for a detailed review, see e.g., Done et al. 2007). The nature of the corona is also an open question, with some theories associating the corona with the base of a jet (Markoff et al. 2005). State transitions from hard to soft happen when the inner edge of the standard disk moves inward and the size of the optically thin hot flow shrinks. This model can partly explain the phenomena we observe during the state transition, but the observations support conflicting scenarios; on the one hand Gierliński & Done (2004), Penna et al. (2010), Steiner et al. (2010), Zhu et al. (2012), and Zdziarski et al. (2022), for example, support this scenario by obtaining large truncated radii in the hard state, with the truncated radii extending to the innermost stable circular orbits (ISCOs) when the transitions to the soft state are completed; on the other hand, this model is contested by other measurements of the inner edge of the disk, either by fitting the broadened iron Kα line (see e.g., García et al. 2015, 2019; Sridhar et al. 2020) or even the disk component itself (Miller et al. 2006; Rykoff et al. 2007; Reis et al. 2009, 2010; Reynolds et al. 2010).

Spectral-timing analysis might help to better understand the physics (and geometry) of state transitions. For instance, Axelsson et al. (2005) showed the evolution of the power spectra in different states of Cygnus X-1 and the correlation between two central frequencies of the variability component; Gierliński & Zdziarski (2005) showed the correlation between the total fractional root mean square (rms) and the photon energy spectra; Cassatella et al. (2012) simultaneously modeled the energy spectra and the frequency-dependent time-lags; and Arévalo & Uttley (2006) instead tried using a numerical implementation to reproduce the spectral-timing behaviors seen in BHBs.

In the present paper, we focus on Cygnus X-1, the first confirmed black hole candidate, with a supergiant O9.7 Iab donor star (HDE 226868). Using VLBA observations, Miller-Jones et al. (2021) recently estimated a black hole mass of $M_1 = (21.2 \pm 2.2)\,M_\odot$, a distance $D = 2.22^{+0.18}_{-0.17}$ kpc, and the mass of the donor star: $M_2 = 40.6^{+7.7}_{-7.1}\,M_\odot$. The compact object in Cygnus X-1 is a fast-rotating black hole, with a dimensionless spin parameter $a^* > 0.97$ (Fabian et al. 2012; Parker et al. 2015; Zhao et al. 2021, but see also e.g., Walton et al. 2016). Previous spectral-timing analyses on Cygnus X-1 based on the RXTE/PCA data (e.g., Pottschmidt et al. 2003; Shaposhnikov & Titarchuk 2006; Axelsson et al. 2006; Klein-Wolt & van der Klis 2008) studied the energy-independent evolution of the timing properties with different spectral shapes. Böck et al. (2011) and Grinberg et al. (2014) studied the energy-dependent timing behavior based on abundant X-ray data that covered all the states of Cygnus X-1 in the energy range up to ∼15 keV. In the present work, we extend previous studies, using wide-band data provided by the Insight–Hard X-ray Modulation Telescope (Insight–HXMT or HXMT) satellite, and exploring the spectral and temporal behaviors of Cygnus X-1 over a broader energy range, in particular covering energies above 15 keV where the contribution from reflection becomes important.

The remainder of this paper is structured as follows: in Sect. 2, we present the long-term behaviors of the source and an overview of the HXMT data we analyze in this paper. We show the results of the spectral analysis in Sect. 3, and the timing analysis extending to the 1−150 keV range in Sect. 4. We discuss the results of our timing analysis in Sect. 5, and devote particular attention to the accretion scenario in Sect. 6, which is important for understanding BHB systems but remains controversial. A summary and outlook are presented in Sect. 7.

Table 1. Start dates and end dates of the HXMT observations.

Proposal ID	Start date [a]	End date [a]
P0101315	2017-08-24 (57989)	2019-06-12 (58646)
P0201012	2019-07-11 (58675)	2020-04-27 (58966)
P0305079	2020-08-08 (59069)	2020-09-25 (59117)

Notes. [a] The date format is yyyy-mm-dd (MJD).

2. Observations and data

Insight–HXMT is China's first X-ray astronomical satellite launched on June 15, 2017 (Zhang et al. 2014, 2020). It has a broad energy band ranging nominally from 1 to around 250 keV, realized by three collimated telescopes: the Low-Energy (LE) telescope, whose energy range covers the 1−15 keV band (Chen et al. 2020); the Medium Energy (ME) telescope, covering 5−30 keV (Cao et al. 2020); and the High Energy (HE) telescope, covering the 25−250 keV band (Liu et al. 2020). In particular, the fast temporal response and large effective area of HXMT, even at higher energies, allow detailed spectral-timing studies above 15 keV.

We use three series of observations. The proposal IDs and the dates of observations are listed in Table 1. The duration of these observations is shown in Fig. 1, along with the light curves of Cygnus X-1 provided by two current all-sky monitors, MAXI (Matsuoka et al. 2009) and *Swift*-BAT (Barthelmy et al. 2005). The different states of the source are indicated by different colors determined according to Grinberg et al. (2013). We observe that Cygnus X-1 has been mostly in the soft state since 2018, but often moves between the hard and soft state.

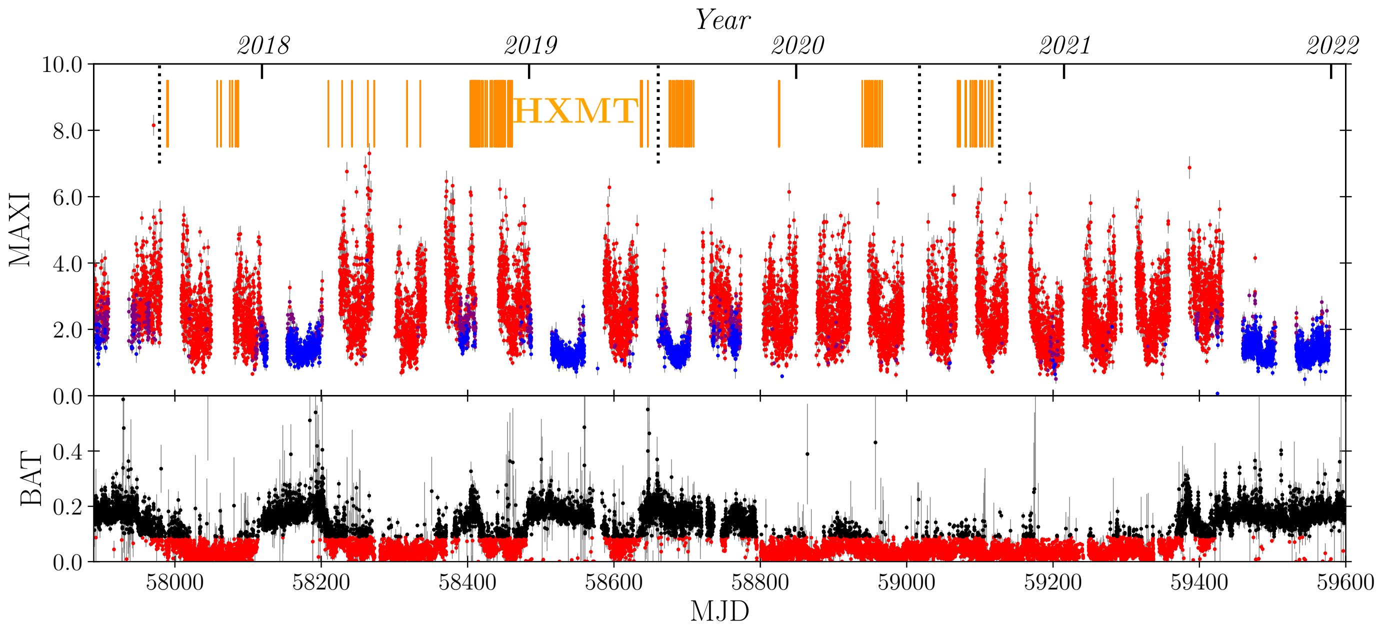

Fig. 1. Long-term behavior of Cygnus X-1 measured by all-sky monitors MAXI and *Swift*-BAT. We follow the same approaches of state definition proposed by Grinberg et al. (2013). *Upper panel*: the hard, intermediate, and soft states are denoted by blue, purple, and red points, respectively. *Lower panel*: the unclassified and soft states are plotted with black and red points, respectively. The duration of HXMT observations on Cygnus X-1 is shown in dark orange stripes at the top.

2.1. Data extraction

We use the pipeline based on Insight–HXMT Data Analysis Software (`HXMTDAS`) v2.04 along with the latest calibration database v2.05 to process the observational data. The good time intervals (GTIs) are selected according to the following criteria: an elevation angle (ELV) larger than 10°, a geometric cut-off rigidity (COR) larger than 8 GeV, an offset angle from the pointing direction (ANG_DIST) smaller than 0.04°, and at least 300 s before and after the South Atlantic Anomaly (SAA) passage. For the LE telescope, we adopt an additional criterion that the elevation angle for the bright Earth is larger than 30°. The individual detectors of the HXMT instruments have different fields of view (FoVs). Given that Cygnus X-1 is a bright source, we use photon events generated by the detectors with a small FoV for the following analysis.

In our analysis, we consider those GTIs that are covered by all three instruments and that are longer than the individual segment used for timing analysis, that is, longer than 16 s. In our timing analyses, we therefore used a total 145 exposures, for which we have obtained energy spectra. We use `ISIS 1.6.2` (Houck & Denicola 2000) – which allows access to the defined models in `Xspec` (Arnaud 1996) – to perform the spectral fitting. The energy bands for the spectral analyses are 2−10 keV for LE, 10−30 keV for ME, and 28−120 keV for HE. We use the tools `LEBKGMAP`, `MEBKGMAP`, and `HEBKGMAP` provided by the HXMT team to estimate the instrumental background (Liao et al. 2020a,b; Guo et al. 2020).

The light curves for timing analyses are generated by the corresponding event lists from the detectors with a small FoV directly, processed with `Stingray` (Bachetti et al. 2021; Huppenkothen et al. 2019a,b). The selected energy range is 1−10 keV for LE, 10−30 keV for ME, and 30−150 keV for HE. In order to study the energy-dependent properties, the energy range of LE was divided into four bands: 1−3 keV, 3−5 keV, 5−7 keV, and 7−10 keV; ME was divided into two bands: 10−20 keV and 20−30 keV; HE was divided into three bands: 30−50 keV, 50−90 keV, and 90v150 keV. In the following, whenever hardnesses are discussed, they are calculated using raw photon counts, not fluxes. The time resolution of those light curves is set to 2^{-9} s ≈2 ms. As we are using the fast Fourier transform for our calculations, we use segments with a length of $2^{13} \times \Delta t = 16$ s to calculate timing properties. The dead time of the LE telescope is negligible, and set to zero (Chen et al. 2020); the dead time of ME and HE are set to 200 µs and 2 µs, respectively (Cao et al. 2020; Liu et al. 2020). The power spectral densities (PSDs) are Poisson-noise and dead-time corrected according to Zhang et al. (1995). Thus, the Nyquist frequency for the light curves is $f_{\max} = 1/(2\Delta t) = 256$ Hz, and the lowest frequency we can access is $f_{\min} = 1/(n_{\rm bins}\Delta t) = 0.0625$ Hz.

2.2. Long-term source behavior

Different from the majority of the transient BHBs that trace the canonical `q`-track during the outburst, Cygnus X-1 is one of the only few known persistent BHBs, and is fed by the wind from its companion. It has been bright since its discovery, and often moves between the hard state and the soft state, without tracing any `q`-track (e.g., Wilms et al. 2006; Fender et al. 2006; Grinberg et al. 2013). Previous studies showed that Cygnus X-1 spends most of the time in the hard state and the soft state, which indicates that these two states are more stable than the intermediate state (see e.g., Grinberg et al. 2013; Meyer-Hofmeister et al. 2020). Prior to ∼2011, the source has spent most of the time in the hard state, with only occasional excursions toward the soft (Grinberg et al. 2013, 2014). Since then and within the life time of MAXI, it has mainly been in the soft state (Cangemi et al. 2021); the reason for this is not yet known.

Pottschmidt et al. (2003) report "failed transitions" frequently observed in Cygnus X-1: the source softens, but never reaches a proper soft state, instead eventually returning to the hard state. Similar failed transitions have also been

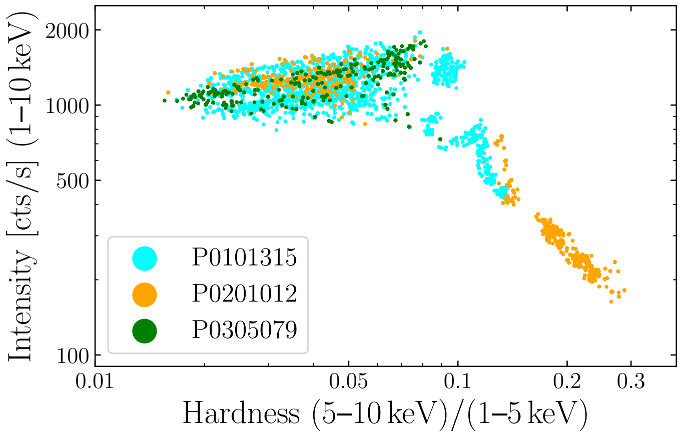

Fig. 2. HID of Cygnus X-1 using the data from three proposals: P0101315, P0201012, and P0305079, that are denoted by cyan, orange, and green, respectively. The intensity is defined by the photon count rate of LE ranging from 1 to 10 keV. We define the hardness as the ratio of the raw photon count rate between the 5−10 keV band and the 1−5 keV band. The time resolution is set to 60 s.

observed in transient BHBs (e.g., GX 339−4, see Fürst et al. 2015; García et al. 2019; and Swift J1753.5−0127, see Bu et al. 2019). Although enormous amounts of data have been collected over decades, the true mechanism of state transitions and the reason why BHBs maintain their stability particularly in the hard and soft states are still open questions.

Here we use the LE data of the three proposals in Table 1 to produce the HID for Cygnus X-1, as shown in Fig. 2. The data from proposals P0101315 and P0305079 cover the soft state and the intermediate state. However, the proposal P0201012 contains observations in the hard state, enabling us to compare source properties across all states.

3. Spectral analysis

3.1. Spectral modeling

For a spectral-timing study of numerous observation samples presented here, a reliable but simple characterization of the spectral shape is necessary. Former long-term spectral studies of Cygnus X-1 used a simple phenomenological model consisting of a broken power law modified by a high-energy cut-off and a disk component to fit the energy spectra (Wilms et al. 2006; Böck et al. 2011; Grinberg et al. 2014). We can write the model as:

$$\texttt{const}\times\texttt{tbabs}\times(\texttt{bknpower}\times\texttt{highecut}+\texttt{gaussian}+\texttt{diskbb}),$$

where `tbabs` calculates the photons absorbed by the interstellar medium, whose cross-sections are provided by Verner et al. (1996) and the element abundances are given by Wilms et al. (2000).

`Bknpower` × `highecut` empirically describes a continuum that dominates the spectrum in the hard X-ray band. `Bknpower` has three parameters except its normalization: Γ_1, the photon index of the soft band; Γ_2, the index of the hard band, and the breaking energy $E_{\rm break}$, in our case around 10 keV. We also included a Gaussian line in the fit in order to characterize the iron Kα line emission located at around 6.4 keV. Finally, we used `diskbb`, a multi-temperature disk model, to fit the thermal radiation from the accretion disk (Mitsuda et al. 1984; Makishima et al. 1986). Typical spectra for Cygnus X-1 are shown in Fig. 3. In the hard state, the disk component never dominates the spectrum. However, the thermal component plays a significant role at soft X-rays when the source is in the soft state.

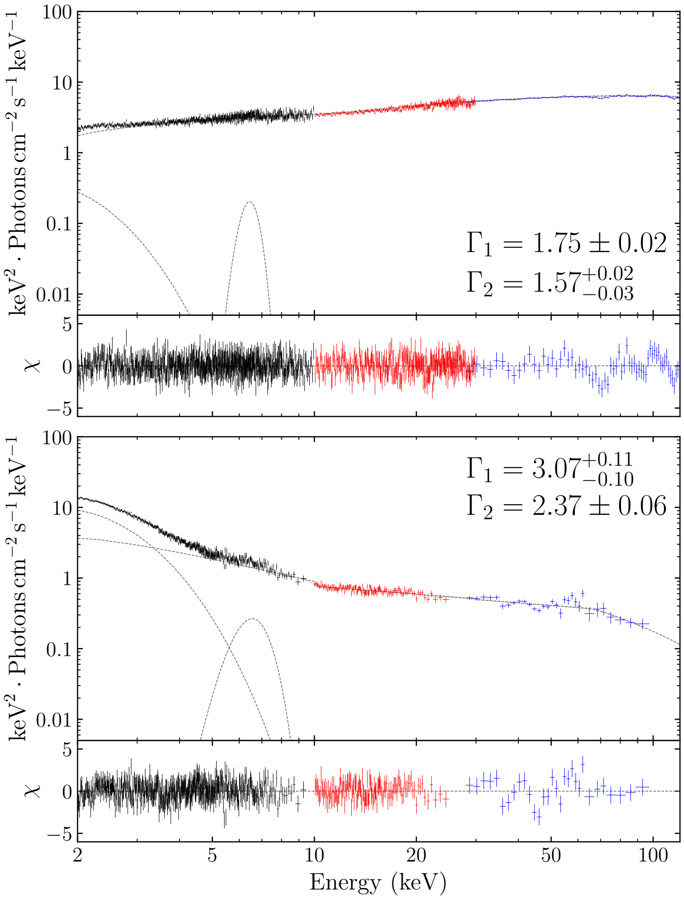

Fig. 3. Typical spectra of Cygnus X-1 with HXMT observations. *Upper panel*: a spectrum in the hard state (obs ID: P0201012171). The spectrum in the *lower panel*: is in the soft state (obs ID: P0101315057). Data from the LE, ME, and HE telescopes are denoted with black, red, and blue crosses, respectively. The power-law continuum, the thermal component, and the iron line emission are indicated with dashed lines.

For our study, this simple phenomenological modelization is sufficient to identify the different spectral component, but we note here that using a more sophisticated physical model to fit the spectra, involving more parameters and more complex assumptions, would be a worthwhile alternative (for a recent study using a physical model on Cygnus X-1 with the HXMT data, see e.g., Feng et al. 2022).

The data coming from all instruments are rebinned to a minimum signal-to-noise ratio of 10. Considering the accuracy of the current calibration and that Cygnus X-1 is a bright source, we adopt a systematic error of 0.5%, 0.5%, and 1.0% for LE, ME, and HE, respectively (Li et al. 2020; Kong et al. 2021). The peak energy of `gaussian` is fixed at 6.4 keV, and the column density $N_{\rm H}$ is fixed at the value of 7.1×10^{21} cm^{-2}, as given by the measurements of the HI4PI survey based on EBHIS and GASS (HI4PI Collaboration 2016). All the other parameters remain free.

While in general we expect $N_{\rm H}$ to be variable in Cygnus X-1, especially during the hard state (e.g., Grinberg et al. 2015; Hirsch et al. 2019; Lai et al. 2022), only a handful of our observations are in the hard state at the orbital phases where they could

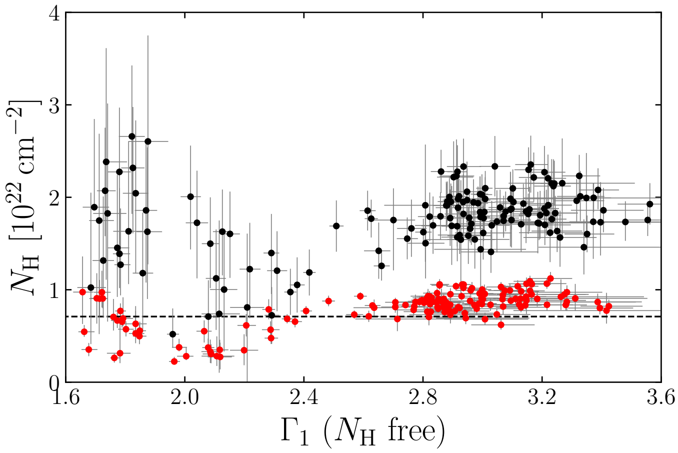

Fig. 4. Soft photon index Γ_1 of `bknpower` obtained by free column densities versus the obtained column densities N_H during the absorption. The black dots indicate the N_H obtained by the spectral fitting down to 2 keV; while the red dots indicate the N_H obtained down to 1.5 keV. The dashed line represents the value 7.1×10^{21} cm^{-2}, which is adopted during our spectral fitting.

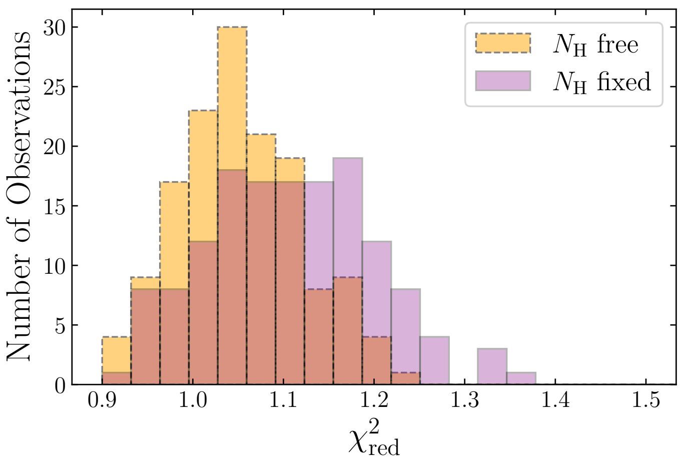

Fig. 5. Histogram of the reduced χ^2 over the best fits of the 145 spectra. Most of the χ^2_{red} with fixed column densities at 7.1×10^{21} cm^{-2} (in translucent purple) drop in the range 0.9−1.2, which suggests that the best fit is relatively satisfying. The bars in orange are the distribution of χ^2_{red} with free column densities.

be affected. In the soft state, the state in which Cygnus X-1 is found in most of our observations, the wind is expected to be highly ionized and thus would contribute little to the observed absorption. The N_H measurements obtained from our HXMT data if the absorption column density is left free to vary show trends that we interpret as systematic effects. In particular, in Fig. 4 (in black), we can see a clear increase in N_H for higher Γ_1, which we interpret as due to the strong contribution of the steep power law at low energy and the degeneracies between the power law, disk, and absorption contributions. This is particularly the case when the power law is steep and the contribution of the disk is strong, because the simple power-law model, which does not have a low-energy cut-off, extends below the energies of the putative seed photon contribution (i.e., the `diskbb` component) for the Comptonization component it is describing. Similar overestimation of N_H can also be seen in Böck et al. (2011) and Grinberg et al. (2015), for example, where the high N_H are associated with high uncertainties. We conduct an additional test by extending the lower limit of our spectra to 1.5 keV, taking advantage of the LE instrument response. We obtain better constraints on N_H, which are very close to the value suggested by the HI4PI survey (Fig. 4, in red). As this work does not focus on the contribution of the stellar wind but aims to obtain a satisfactory continuum description, we interpret this as confirming our choice to fix the N_H value, but caution that detailed disk and wind studies would require a careful consideration of possible calibration effects and model degeneracies.

Overall, we are able to obtain good fits for all our spectra as shown in Fig. 5, where we also show the quality of fits obtained when the column density is left free.

3.2. Discussion of spectral modeling

We first verify the validity of our spectral modeling by checking the correlations between the spectral hardness and soft photon index Γ_1, and between the ratio of unabsorbed energy flux directly from the thermal radiation (`diskbb`-model) over the total unabsorbed energy flux in the 2−5 keV range and Γ_1, as shown in the first two panels in Fig. 6. Both show the correlations expected for hard to soft transition.

We can now define the state of the source by the corresponding value of Γ_1: the hard state for $\Gamma_1 \leq 2.0$, the hard intermediate state for $2.0 < \Gamma_1 \leq 2.4$, the soft intermediate state for $2.4 < \Gamma_1 \leq 2.7$, and the soft state if $\Gamma_1 > 2.7$. Our choice is supported by the sudden change of the PSD shape in the 3−5 keV band and the intrinsic coherence in the 1−3 versus 3−5 keV band; see Sects. 5.2 and 5.3 for more details, as well as Grinberg et al. (2014).

The positive correlation between the intensity of the reflection – shown by the equivalent width of the iron Kα line – and the spectral parameter Γ_1 is presented in the bottom panel of Fig. 6. This result is consistent with the findings of Gilfanov et al. (1999), Ibragimov et al. (2005), Shaposhnikov & Titarchuk (2006), and Steiner et al. (2016) for example, all of whom used RXTE data for their analyses.

By studying Cygnus X-1, Shaposhnikov & Titarchuk (2006) propose that the corona may have a compact geometry in the intermediate and soft states. Based on observations of 29 stellar-mass BH candidates, Steiner et al. (2016) offer two interpretations. One agrees with Shaposhnikov & Titarchuk (2006) that the size of the corona shrinks when the state softens, and the other agrees with Petrucci et al. (2001), who discuss the Comptonization effect on the reflection component, stating that in the hard state, the iron line amplitude will be diluted by Compton scattering due to the higher optical depth of the corona.

The intensity of the reflection can be roughly quantified by the difference between the two photon indices as well, as the model combination `bknpower` × `highecut` with the breaking energy around 10 keV is capable of characterizing the Compton hump around 20−30 keV (Wilms et al. 2006). We present the correlations of two photon indices and the difference between them, $\Delta\Gamma$, in Fig. 7, and $\Delta\Gamma$ versus the equivalent widths of the iron lines in Fig. 8. Consistent with the apparent relationship between the equivalent width and Γ_1, we see a clear positive trend between $\Delta\Gamma$ and Γ_1. In addition, Fig. 8 shows that the two indicators of the reflectional strength are indeed positively correlated even in the soft state. We therefore conclude that in the soft state, the reflection is indeed stronger than in the hard state.

However, the correlation we observe between Γ_1 and Γ_2 shows a "bend" at $\Gamma_1 \approx 2.7$ as shown in the upper panel of Fig. 7. This is coincident with the onset of the soft state and fits where the uncertainties on the current steep power-law index are

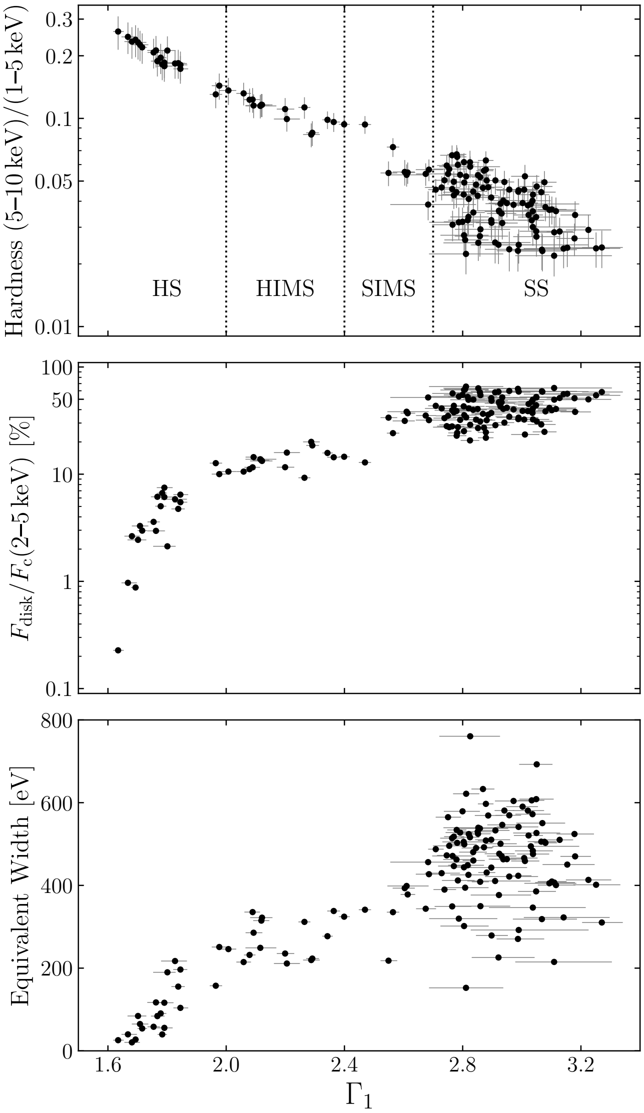

Fig. 6. Spectral evolution versus the soft photon index Γ_1. *Top panel*: correlations of the 5−10 keV/1−5 keV hardness versus Γ_1. We define the hard state (HS), the hard intermediate state (HIMS), the soft intermediate state (SIMS), and the soft state (SS) with Γ_1 values. *Middle panel*: ratio of unabsorbed energy flux of the disk components over the total energy flux versus Γ_1. *Bottom panel*: intensity of reflection that is denoted by the equivalent widths of the iron Kα lines, and is stronger in the soft state than in the harder state.

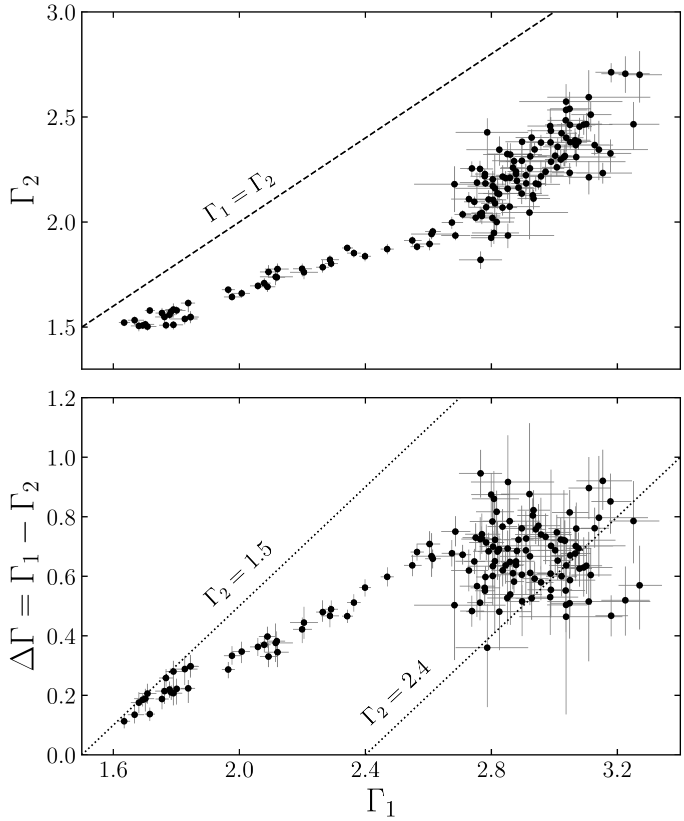

Fig. 7. *Upper panel*: soft photon index Γ_1 versus the hard photon index Γ_2 in model `bknpower`. The dashed line indicates that $\Gamma_1 = \Gamma_2$. *Lower panel*: the correlations between Γ_1 and the difference of two photon indices, defined by $\Delta\Gamma = \Gamma_1 - \Gamma_2$, are shown. The lines that are parallel to the dotted lines indicate a constant Γ_2.

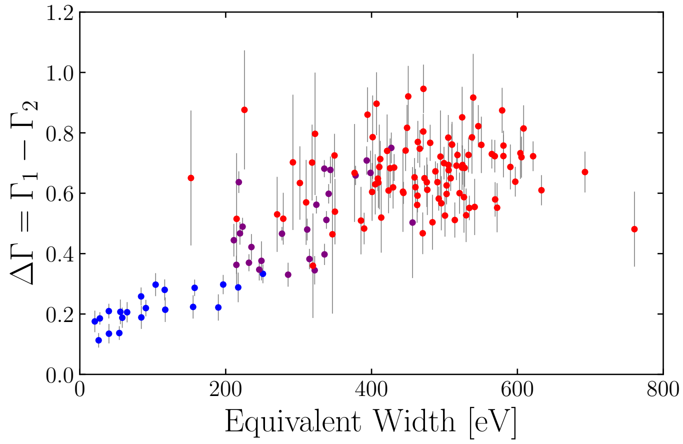

Fig. 8. The correlation of $\Delta\Gamma$ versus the equivalent widths of the iron Kα lines. The blue/purple/red points denote that the source is in the hard/intermediate/soft state, respectively.

larger. Similar trends were not observed by Wilms et al. (2006), who did not include a disk for their fits in the soft state, resulting in a poor description of the spectra below 6 keV. We check whether our choice to freeze N_H may lead to the observed bend in the correlation: We find that for Γ_1 (N_H fixed) $\gtrsim 2.7$, an evident deviation between the Γ_1s with fixed and free N_H appears (see Fig. 9). Still, the bend in the correlation appears even for free N_H, meaning that it is not purely an artifact of the choice of parameter space for our model.

4. Energy-resolved variability properties

4.1. Power spectra and the fractional rms

Power spectra (also power spectral densities, or PSDs), are the first-order products of the discrete Fourier transform performed on a time series, and their calculations are discussed in detail by Nowak et al. (1999), for example; see their Sect. 2. The power spectra are calculated in units of rms fluctuations scaled to the mean count rate (Belloni & Hasinger 1990a; Miyamoto et al. 1991). This normalization is often employed, as it is convenient to compare the power spectra from different states or even different sources, because the variance that each frequency contributes is independent of the averaged photon count rate. The

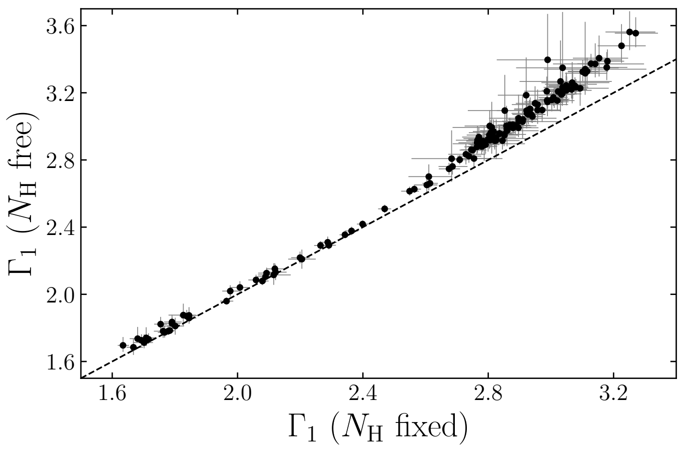

Fig. 9. The soft photon index Γ_1 of `bknpower` obtained by fixed $N_H = 7.1 \times 10^{21}\,cm^{-2}$ and free N_H. The dashed line indicates that Γ_1 (N_H fixed) = Γ_1 (N_H fixed).

total fractional rms is the integral of the PSDs over all available frequencies, which in our case is 0.0625−256 Hz.

In some of the energy bands considered for our analysis, the background photons contribute significantly. Especially in the soft state, they dominate in the hard X-ray bands and need to be taken into account. We therefore adopt a background correction for the fractional rms (Belloni & Hasinger 1990b; Bu et al. 2015):

$$\text{rms} = \sqrt{\sum P \cdot \Delta f} \left(\frac{S+B}{S}\right), \quad (1)$$

where P is the noise-subtracted power normalized according to Miyamoto et al. (1991), and S and B are the averaged photon count rates from the source and the background, respectively. This background correction adds a factor $(S + B)/S$ – the value of which is always greater than 1 – to the raw rms values. This implies the assumption that the background is intrinsically invariant and therefore does not contribute to the total variability. As expected, this assumption is not true when background noise dominates the data, and will lead to the overestimation of the fractional rms, because the background noise has its own intrinsic variability as well.

Figure 10 shows the correlations of different estimates of total rms with spectral shape as represented by Γ_1 for all instruments and energy ranges under consideration. To present the effect of the employed background correction, we additionally show the inverse of the correction factor, $[(S + B)/S]^{-1} = S/(S + B)$. For $S/(S + B)$ close to 1, most of the photons come from the source, and therefore the corrected rms is almost equal to the raw rms. The corrected rms is higher than the raw rms when $S/(S+B) < 1$. As some of the data with a high Γ_1 are very noisy, we use smooth curves calculated through simple interpolation between data points to present the macroscopic trends between the total rms and Γ_1.

4.2. Evolution of the power spectral density with spectral shape

We follow the approach of Böck et al. (2011) and Grinberg et al. (2014) to visualize the whole power spectra by color maps in Γ_1-f_i-space. The values of Γ_1 are obtained from the best fits from Sect. 3, where $\Gamma_{1,\min} = 1.63$ and $\Gamma_{1,\max} = 3.27$. The grid of Γ_1 is defined linearly by constant steps of $\Delta\Gamma_1 = 0.1$ between the two limits. The power spectra from different observations will be averaged if their Γ_1 belongs to the same bin of the grid. The frequencies f are rebinned logarithmically between 0.0625 Hz and 256 Hz, with an equally spaced grid in logarithmic scale $df/f = 0.15$. The evolution of the PSD shape versus Γ_1 is shown in Fig. 11.

The PSDs shown in Fig. 11 have not been corrected by Eq. (1), and therefore the integral over all frequencies corresponds to the uncorrected rms shown in Fig. 10. We can also see that the strength of the variability from HE bands is weaker than that from ME bands. The main reason is that the background photons that significantly contribute to the harder X-ray bands will elevate the detected count rate, which leads to underestimation of the strength of the intrinsic variability of the source. To clearly show the evolution of the variability above 30 keV, we rescale the color map of HE bands; see Fig. 12.

Figures A.1–A.3 show the averaged PSD shapes versus Γ_1 for all the three instruments. We note that ME and HE bands are both dominated by background photons when Cygnus X-1 is in the extreme soft state. The flux in those bands is weak, and the uncertainties of the Fourier signals at high frequency bands are large. In this case, those PSDs should not be considered as physical.

4.3. Coherence function and phase-lags

The coherence, as well as the phase-lags, are the products of Fourier transform between two simultaneous light-curve series. Usually we study these quantities between two different energy bands, to identify the lost phase-related information when we compute the moduli of the products of Fourier transform. The intrinsic coherence function, $\gamma^2(f)$, is defined by Vaughan & Nowak (1997), where the auxiliary quantity n^2 defined in Eq. (4) by Vaughan & Nowak (1997) is the expectation of the noise contribution.

The coherence function itself is a frequency-dependent measurement of the linear correlation between two simultaneous time series. In principle, the coherence function ranges from 0 to 1, where 0 means no coherence and 1 means perfect linear coherence. But when considering the noise correction, we possibly obtain a coherence of greater than 1 or even negative. A negative coherence can merely emerge if the noise dominates one of the power spectra. In this case, the negative coherence there does not make sense. However, a coherence of greater than 1 may be seen even when the signals at that frequency are well measured. This is due to the fact that the auxiliary quantity n^2 cannot be estimated well when there are insufficient segments, or when the signals from two bands correlate extraordinarily strongly. Therefore, a coherence of higher than 1 still means good linear correlation between the two light curves and is not considered problematic in the following parts of the analysis.

We follow the same recipe to present the coherence function in Γ_1-f_i-space, as shown on the left-hand side of Fig. 13. Similarly to Figs. 11 and 12, we use a thermal color map to visualize the coherence, where brighter colors represent better coherence, and dimmer colors represent poorer coherence. We can see a clear envelope located at ∼10 Hz in each panel on the left-hand side of Fig. 13, and above ∼10 Hz, the noise-subtracted power densities are close to zero and the coherence fluctuates violently.

The three panels in the first column of Fig. 13 are the coherence functions of the softest band (1−3 keV) versus the other harder bands (3−5 keV, 5−7 keV, and 7−10 keV). In the hard state and the hard intermediate state, where $1.6 \leq \Gamma_1 \lesssim 2.4$, the coherence function in the 1−3 keV versus 3−5 keV band is

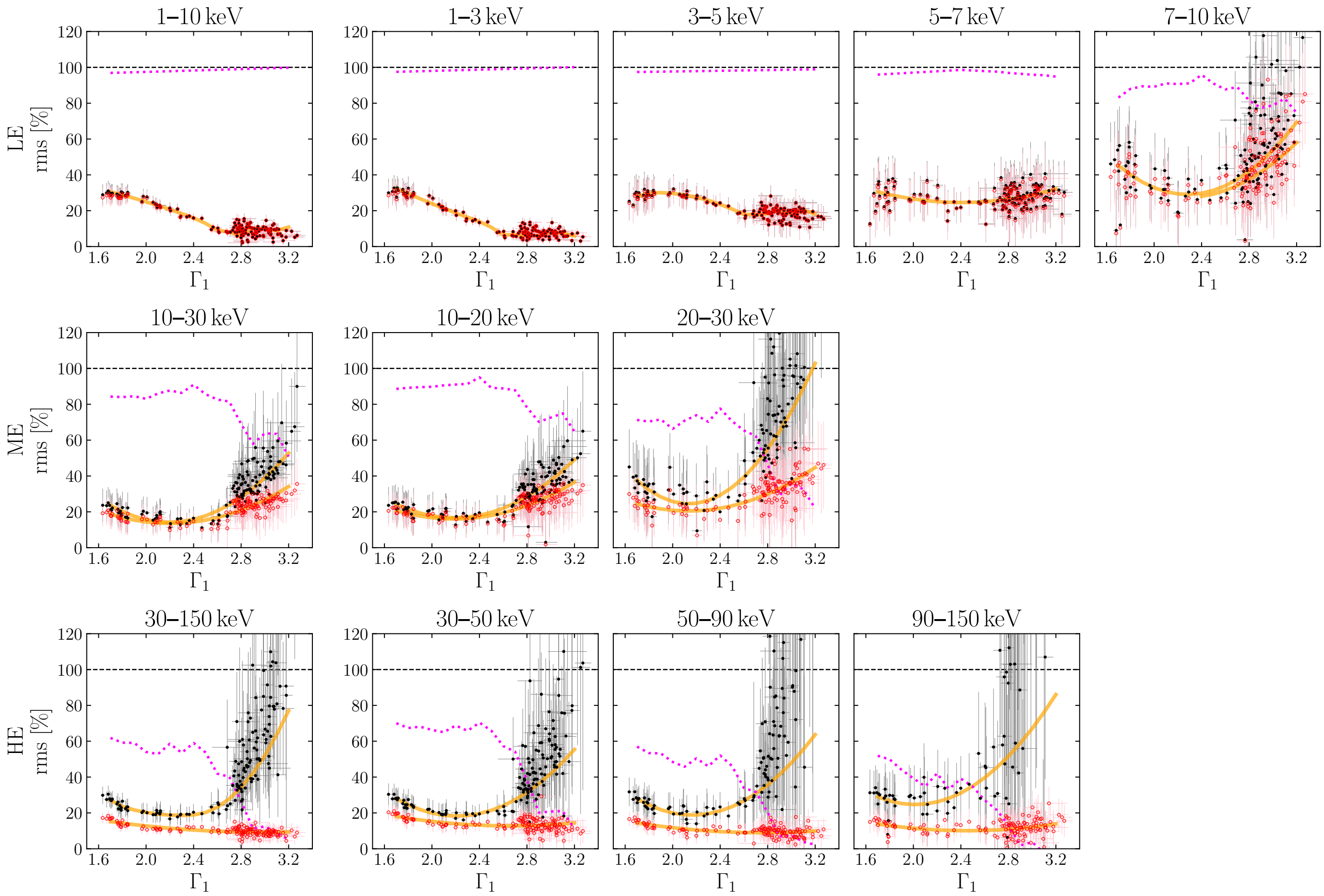

Fig. 10. Correlations between the soft photon index Γ_1 and the fractional rms from all the instruments on HXMT. The red circles are the raw rms without the correction of Eq. (1), and the black dots are the corrected total rms according to Eq. (1). The magenta dotted lines denote the signal-to-background ratio $S/(S+B)$. The orange solid lines show the trends of the corrected and uncorrected total rms when varying Γ_1.

quite close to 1. But in the soft intermediate state and the soft state, where $2.4 \lesssim \Gamma_1 \lesssim 3.3$, the loss of coherence emerges at low frequencies. A similar loss of coherence can also be found in the 1−3 keV versus 5−7 keV band and the 1−3 keV versus 7−10 keV band. The loss of coherence in the soft/intermediate state in these bands is due to the fact that the dominant spectral component in the 1−3 keV band has changed during the state transition. In the hard state, where $\Gamma_1 \leq 2.0$, the 1−3 keV band is dominated by the power-law emission. But in the soft state, where $\Gamma_1 \gtrsim 2.7$, the thermal emission from the disk becomes dominant. As expected, and as the dominant emission comes from spatially distinct regions, we observe a loss of coherence.

When the two energy bands are both power-law dominated, the loss of coherence in the soft state disappears, which can be seen in the remaining three panels on the left-hand side of Fig. 13. We obtain the best coherence for nearly all Γ_1 values in 3−5 keV versus 5−7 keV band.

On the right-hand side of Fig. 13, we show the frequency-dependent phase-lags between different energy bands of LE, but using a different color map. Hard lags are denoted in red, while soft lags are denoted in blue. For ME and HE data, the coherence and the phase-lags are noisier and cannot be visualized using this approach. Instead, we show the averaged coherence function and the averaged phase-lags taken over the frequency band and Γ_1 band. Inspired by the coherence evolution in 1−3 keV versus 3−5 keV band, we divide the soft photon index Γ_1 into five sub-bands: 1.6−2.0, 2.0−2.4, 2.4−2.7, 2.7−3.0, and 3.0−3.3, consistent with the state definitions in Sect. 3.2. We first rebin the raw coherence and phase-lag spectra to a logarithmically spaced frequency grid with $df/f = 0.15$, and average the coherence and the phase-lag in the 0.0625−6 Hz frequency range in each Γ_1 band. Here, we correct any coherence greater than 1 (mostly seen in the HE data) to simply 1 in order to cancel the effect of strong correlation when averaging. The results are shown in Figs. 14 and 15.

5. Discussion of the timing properties

5.1. The total fractional rms

We show both corrected and uncorrected rms in Fig. 10 in order to underline the differences between them. For LE, the signal-to-background ratio is higher than 75%, and the differences between the two rms estimates can be ignored, as clearly seen in the upper row of Fig. 10. However, when a non-negligible fraction of photons comes from the background, they inevitably smear the power spectrum and the rms. In order to obtain the true trends of total rms using the available data, our assumption can be stated as follows: (1) The raw rms is true if the background has the same intrinsic variability as the source; (2) the corrected rms is true if the background rate is intrinsically invariant and does not contribute to the total variability at all; and (3) the true value should lie between the two extreme cases above: the background has its own intrinsic variability, but in all

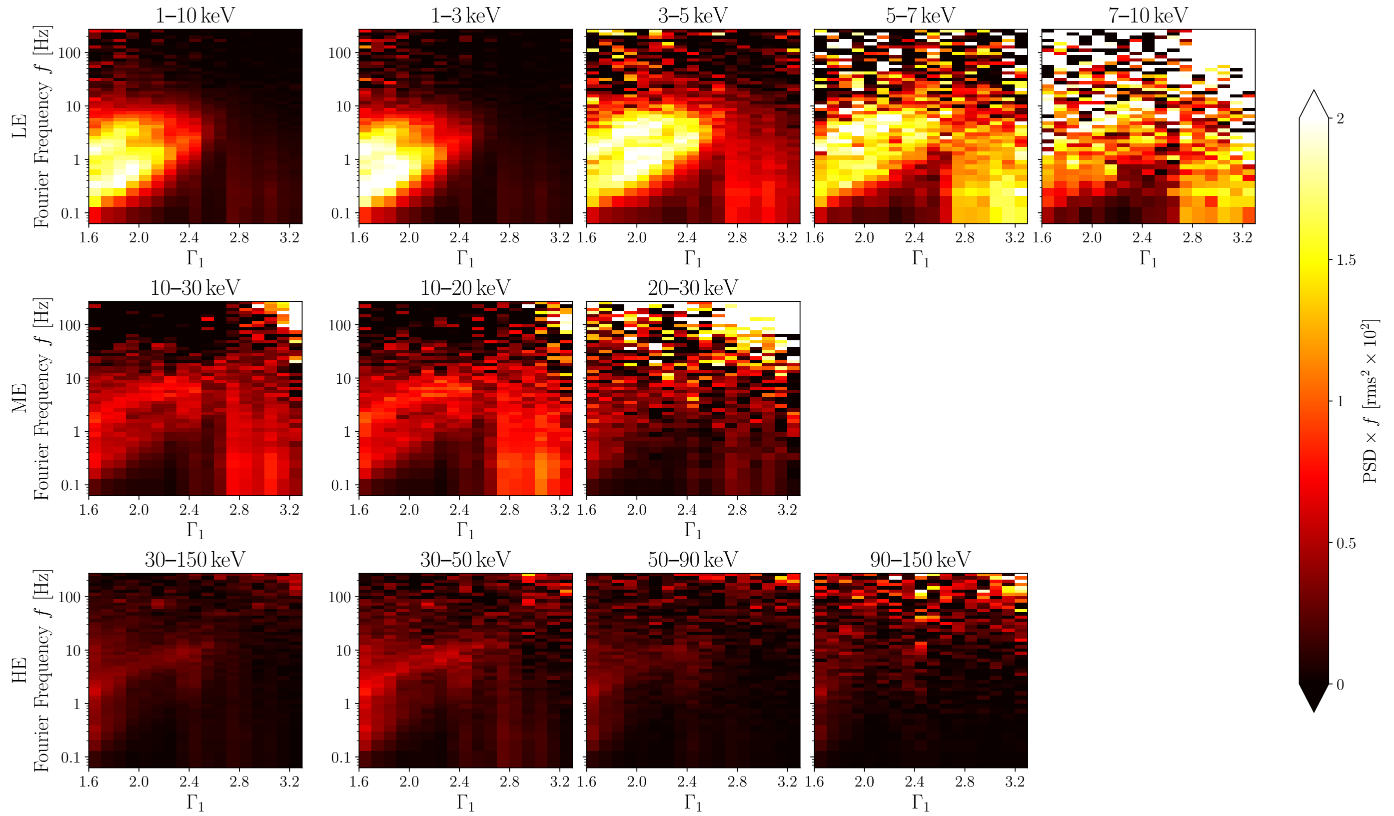

Fig. 11. Evolution of PSDs versus the soft photon index Γ_1 from different energy bands provided by all instruments on HXMT. The color scale represents the average value of PSD(f_i) × f_i at individual frequencies f_i. Please note that the PSD values in these plots have not been corrected by Eq. (1) in order to avoid the covering effect due to the high signal-to-background ratio.

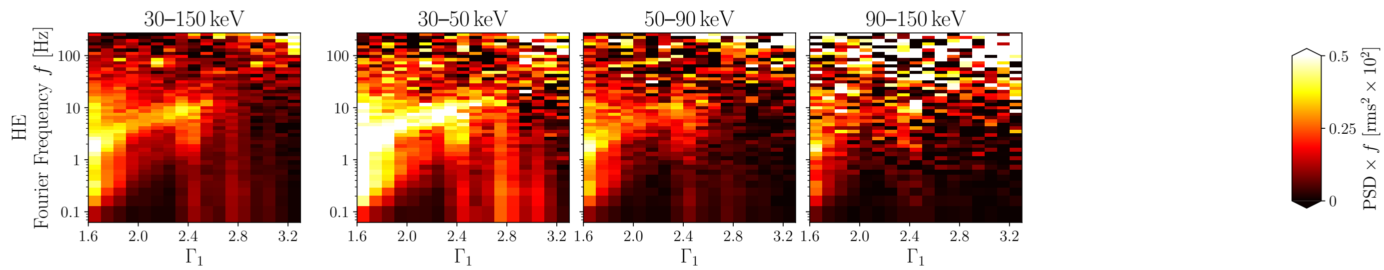

Fig. 12. Same as the last row of Fig. 11, but with a different color scale in order to illustrate the evolution of the variability component more clearly.

cases, the variability from the source dominates. Therefore, the true total rms should be between the two trends (denoted by the two orange solid lines) in all panels in Fig. 10. Along with the improved quality of the data, the two curves that represent the two extreme cases become closer, and the uncertainty range of the true trend is smaller.

As shown in Fig. 10, the macroscopic positive trends between the total rms and Γ_1 in hard X-ray bands in the soft state challenge the well-known statement that, due to the domination of the thermal emission in the soft state, the total rms is much lower than that in the hard state (e.g., Belloni et al. 2005; Heil et al. 2015). We note that this statement is only true when the soft X-ray band – that is dominated by thermal photons in the soft state – is contained (e.g., 1–3 keV band or 1–10 keV band). The exact reason for this is discussed in Sect. 5.2. For other, harder bands, where Comptonized photons dominate even in the soft state, indeed we see a slightly negative trend when $\Gamma_1 \lesssim 2.7$, and a positive trend when $\Gamma_1 \gtrsim 2.7$.

The total rms works as an integral of the PSDs over all available frequencies. Different fractional rms values doubtlessly tell us that the properties of the source radiation are different, but even with a flat correlation of rms-Γ_1, such as that shown in the 5.0–7.0 keV band in Fig. 10, the timing properties in soft and hard states are still quite different. These properties can be revealed by the PSD evolution with spectral shape, which is presented and discussed in Sects. 4.2 and 5.2.

5.2. Evolution of the PSD

Our work extends the previous RXTE-based analysis, which covered the 2.1–15 keV range (Böck et al. 2011; Grinberg et al. 2014), to both lower and higher energies. Our maps therefore allow us to better trace both the variability of the disk that contributes to the lowest energies and the variability of the high-energy part of the power law.

In Fig. 11, we see a clear boundary at $\Gamma_1 \simeq 2.7$. Before this boundary, there are at least two pronounced variability

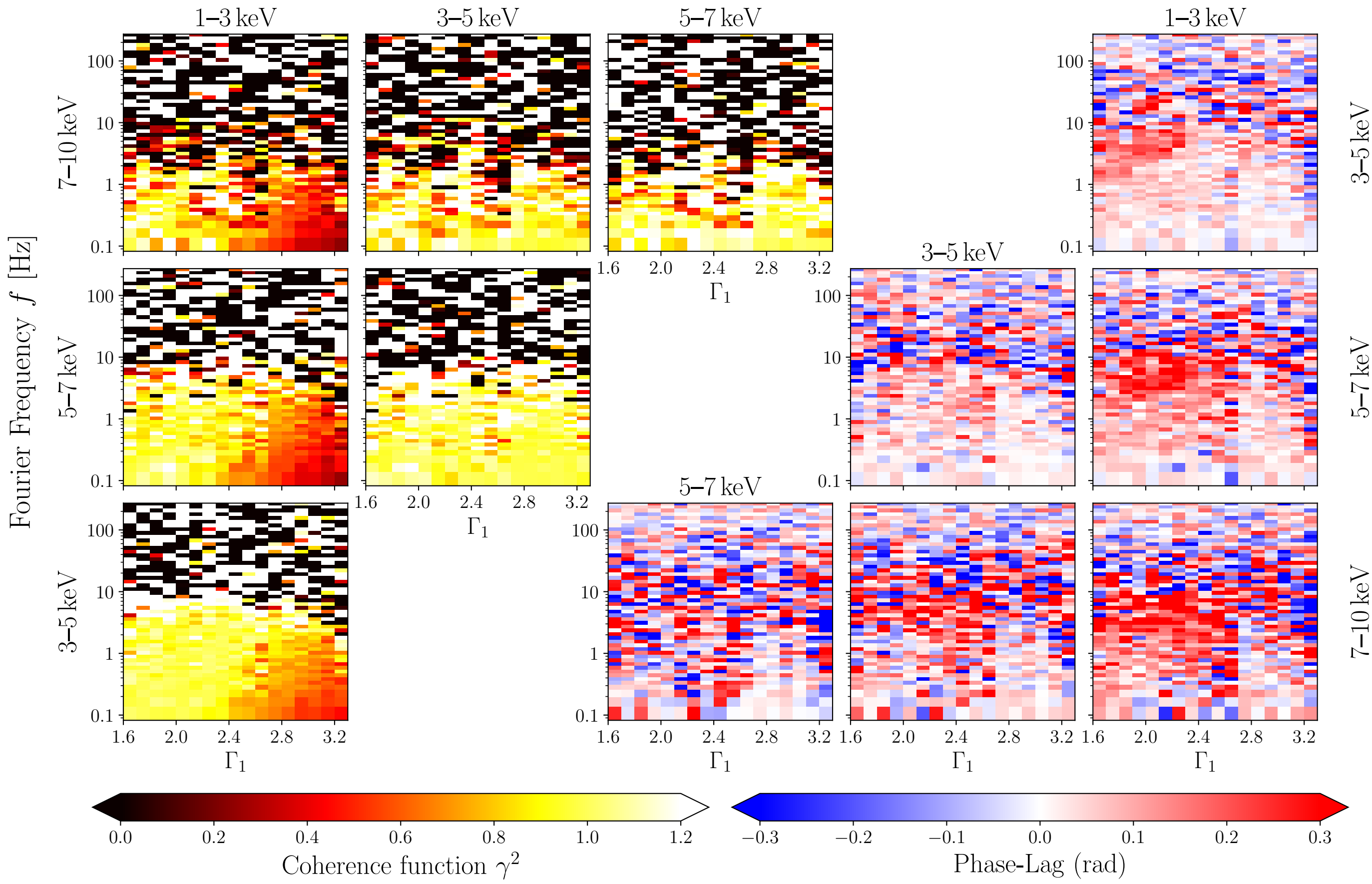

Fig. 13. Evolution of the coherence function γ^2 and the phase-lags versus the soft photon index Γ_1 between different energy bands of the LE telescope.

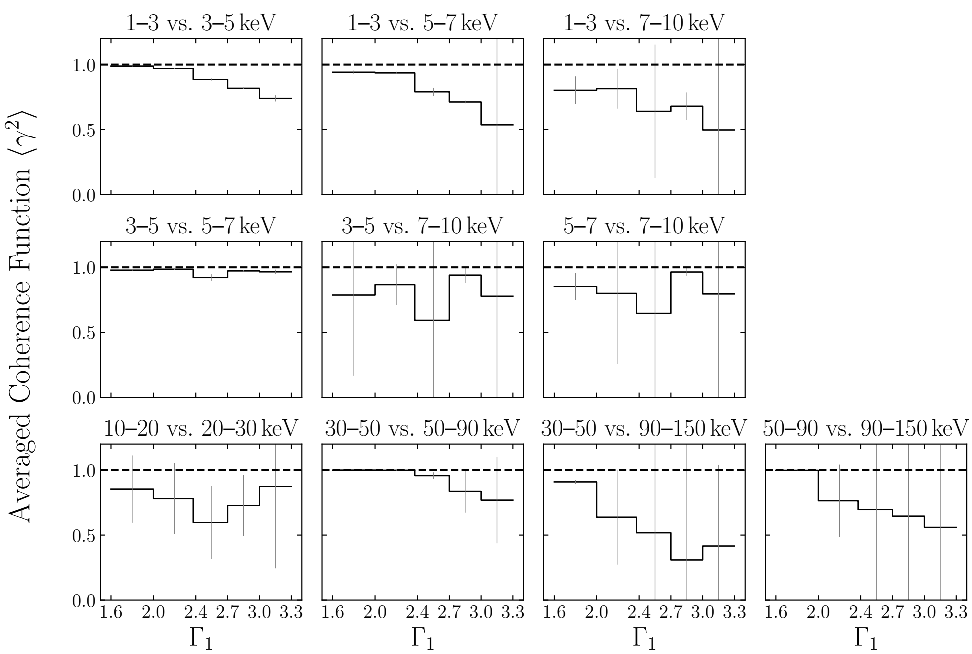

Fig. 14. Evolution of the coherence $\langle\gamma^2\rangle$ averaged over the 0.0625−6 Hz frequency range versus the states (classified by the soft photon index Γ_1) between different energy bands.

components in the 1−10 Hz range. Their frequency increases when the source softens.

The central frequencies are approximately independent of the energy bands (for similar results recently obtained for other BHBs, see e.g., Ma et al. 2021). The power spectra of Cygnus X-1 in the hard and intermediate states are comparatively smooth and without narrow features (see e.g., Axelsson et al. 2005, 2006; Rapisarda et al. 2017). While we acknowledge that there is some confusion in the literature, with the broad variability components having been referred to as quasi-periodic oscillations (QPOs) in

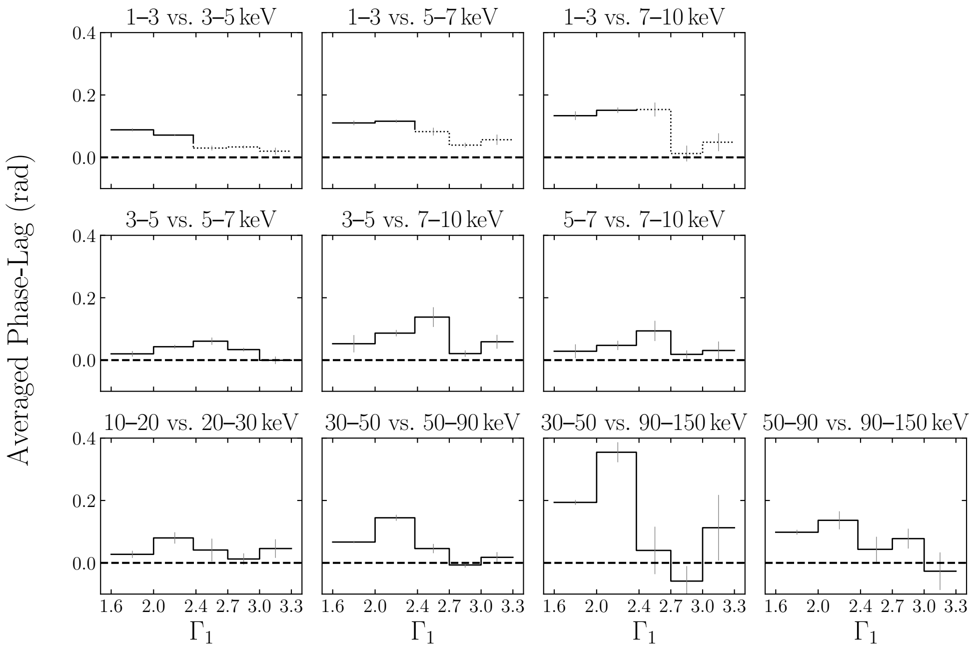

Fig. 15. Similar to Fig. 14, but with the evolution of the average phase-lag versus the states (classified by the soft photon index Γ_1). In the first three panels, the average phase-lags with $\Gamma_1 \geq 2.4$ are denoted by dotted lines, as we know that the loss of coherence is due to the different emission origins.

past analyses (Gilfanov et al. 1999; Shaposhnikov & Titarchuk 2006), the behavior of the observed variability components does not agree with the established definition of LFQPOs (see e.g., Ingram & Motta 2019).

Following Grinberg et al. (2014), we label the variability component with a lower central frequency as "Component 1" and that with a higher central frequency as "Component 2". We can see a gradual growth of the strength of Component 2, but Component 1 fades when the X-ray bands become harder. The Component 2 becomes dominant above ~10 keV. Here, we can, for the first time, trace this behavior above ~15 keV.

We are able to trace the variability components, especially Component 2, in the hard state and their increasing frequency with an increasing Γ_1 to at least the 50−90 keV range. This is especially clearly visible in Fig. 12 where we rescale the map colors to account for the overall low variability detected in the HE instrument.

The maps in the 90−150 keV range do not show a clear pattern. This band is especially interesting since the spectral cutoff in the hard intermediate state is around ~150 keV (Wilms et al. 2006, and our fits in this analysis), with a polarized hard tail present above these energies (Laurent et al. 2011; Jourdain et al. 2012; Rodriguez et al. 2015; Cangemi et al. 2021). To enhance the signal, we calculate the average PSDs for four states defined by Γ_1 values, the hard state ($\Gamma_1 \leq 2.0$), the hard intermediate state ($2.0 < \Gamma_1 \leq 2.4$), the soft intermediate state ($2.4 < \Gamma_1 \leq 2.7$), and the soft state ($\Gamma_1 > 2.7$) (see Fig. 16). However, the power spectra in the 90−150 keV band are still too noisy to allow firm conclusions to be drawn. Nevertheless, we do see an overall decrease in variability, in agreement with previous results using INTEGRAL/SPI (Cabanac et al. 2011).

In the prior studies of Cygnus X-1, the variability components seen in the hard and intermediate states can be well modeled by usually two Lorentzians with different central frequencies (Nowak 2000). Consistent with for example Cui et al. (1997a), Gilfanov et al. (1999), Pottschmidt et al. (2003), Axelsson et al. (2006), Shaposhnikov & Titarchuk (2006), and Böck et al. (2011), who studied the evolution of the behavior of these components, we find that their central frequencies increase as the source softens. The strength of components in the 1−10 Hz band directly determines the total fractional rms that is shown in Fig. 10. For those bands above 3 keV, the total rms slightly drops during the hard-to-intermediate transition, where $1.6 \lesssim \Gamma_1 \lesssim 2.7$. But the variability in the 1−3 keV band is additionally influenced by the thermal photons from the accretion disk. The thermal photons that present red-noise spectra in the PSDs make the variability of the smooth components fade more quickly than the harder bands. This is the exact reason why we see a continuously decreasing value of the total rms only in the 1−3 keV band or the 1−10 keV band during the softening of the state.

When the source continues its transition to the soft state, crossing the boundary of $\Gamma_1 \simeq 2.7$, the power spectrum of hard X-ray bands suddenly changes to a red-noise spectrum with a slope of f^{-1} below 10 Hz. A similar behavior of the PSD evolution was also reported by Grinberg et al. (2014) at energies up to 15 keV and is traced here for the first time at higher energies, where the power law is the dominating spectral component even in the soft state. The sudden change of the PSD shape at $\Gamma_1 \simeq 2.7$ is the reason why the total rms has a positive tail versus Γ_1 in the hard X-ray bands.

In the soft state of Cygnus X-1, with $\Gamma_1 \gtrsim 2.7$, the PSD shape shows a red-noise spectrum with a slope of f^{-1} below 10 Hz (see e.g., Cui et al. 1997a,b; Gilfanov et al. 2000; Churazov et al. 2001; Pottschmidt et al. 2003; Axelsson et al. 2005; Grinberg et al. 2014). Cui et al. (1997a) and Churazov et al. (2001) also state that the red-noise variability becomes stronger when our focused energy range moves to the harder X-ray bands. This is confirmed by the higher total rms shown by the positive tails of the trends of the corrected rms in Fig. 10 and the brightness of the PSD shapes in Fig. 11.

5.3. The coherence function and the phase-lags

Figure 14 shows that, in the soft state where $\Gamma_1 \geq 2.7$, the HE data ($\geq$ 30 keV) and the LE data involving the 1−3 keV band tend to have poorer coherence than those with lower Γ_1s. The loss of coherence in LE data is interpreted by the domination of

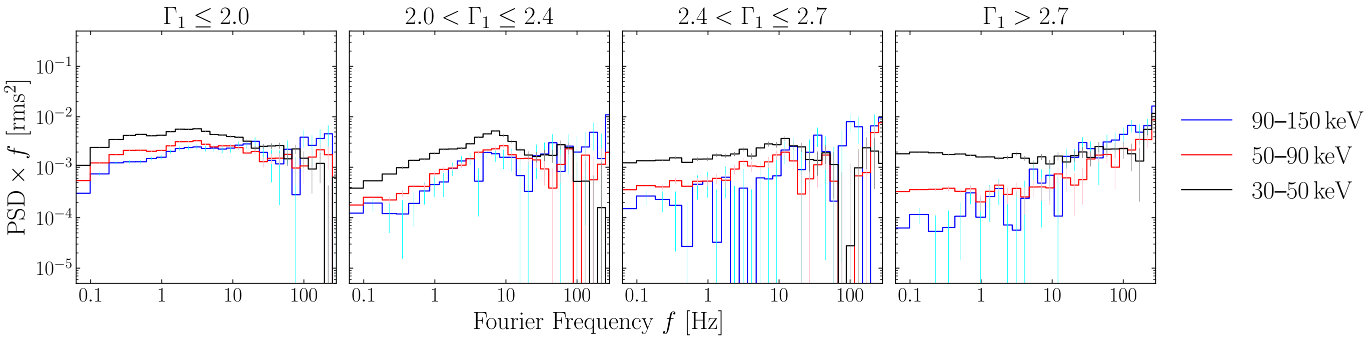

Fig. 16. Average power spectra calculated from light curves obtained from the HE instrument in different energy bands in four different Γ_1 ranges. The PSDs for the 30−50 keV band, 50−90 keV band, and 90−150 keV band are denoted with black, red, and blue lines, respectively. The PSDs are rebinned to $\mathrm{d}f/f = 0.3$.

the thermal photons from the disk in the 1−3 keV band. But the loss in HE data is mainly due to the low signal-to-background ratio when $\Gamma_1 \geq 2.7$. Here we note that Grinberg et al. (2014) do not find similar loss of coherence due to the thermal photons with RXTE/PCA data, as the lower limit of their softest energy band is 2.1 keV, which in our case is 1.0 keV. In order to check this supposition, we also extract the event lists from LE for photons of 2.1−4.5 keV and compute the coherence involving this new energy band. We do not see evident loss of coherence in the soft state. This fact indicates that the thermal photons may dominate the 1−3 keV band, but cannot dominate the 2.1−4.5 keV band in the soft state of Cygnus X-1.

In addition, in those bands where the coherence can be well measured, we can see a coherence decrease where $2.4 \lesssim \Gamma_1 \lesssim 2.7$. Grinberg et al. (2014) report a similar loss of coherence when $2.35 \lesssim \Gamma_1 \lesssim 2.65$ based on an analysis of the RXTE/PCA data for Cygnus X-1. The origin of the loss of coherence in this soft intermediate state has not been ascertained. Considering that the jet emission in this state becomes weak and unstable or even hardly detectable (e.g., Fender et al. 2004; Böck et al. 2011; Corbel et al. 2013), the loss of coherence is highly possibly connected with the unstable jet base.

As the different origins of the emission in the 1−3 keV band in the hard and the soft state are confirmed by previous spectral and timing analyses, we denote those phase-lags where $\Gamma_1 \geq 2.4$ with dotted lines in Fig. 15, and do not discuss them further, because there the quality of the linear coherence between two light curves is poor.

Figure 13 shows that the dominant hard lags contribute from the 1−10 Hz band when Cygnus X-1 is in the intermediate state. In the hard state, hard lags tend to be generated at slightly lower frequencies, in comparison with those in the intermediate state. This consistency of the central frequencies of the variability components and the dominant contribution of the frequency-dependent phase-lags indicates that the lags of the hard photons are likely related to the variability components. However, the phase-lags in the soft state in general stochastically fluctuate around zero, resulting in a sudden drop in the average phase-lags when $\Gamma_1 > 2.7$, which is shown in Fig. 15.

Most of the average phase-lags in Fig. 15 are positive, which means that in our data, the hard photons usually lag the soft photons. Similar hard lags observed on Cygnus X-1 are also reported; for example, by Cui et al. (1997a), Nowak et al. (1999), Pottschmidt et al. (2003), Böck et al. (2011), and Grinberg et al. (2014).

We are particularly interested in the average phase-lags between the adjacent energy bands (e.g., 3−5 keV vs. 5−7 keV band or 10−20 keV vs. 20−30 keV band), because the phase-lags between the nonadjacent bands can be estimated by summing the phase-lags between the adjacent bands in one 2π period if the coherence remains good. From the 3−5 keV vs. 5−7 keV band, the 5−7 keV vs. 7−10 keV band, and the 10−20 keV vs. 20−30 keV band in Fig. 15, we see that the average phase-lags in the 0.0625−6 Hz band always increase as the state softens, where Γ_1 transitions from 1.6 to 2.7. But when Γ_1 continues to increase, the average phase-lags will decrease. In our work, the maximum lags are observed in the soft intermediate state, where $2.4 \lesssim \Gamma_1 \lesssim 2.7$. Grinberg et al. (2014) reported the lag evolution with RXTE/PCA data on Cygnus X-1, with their maximum values consistently at $\Gamma \simeq 2.65$, but using the form of time-lags, suggesting that the geometry of the corona shows a sudden change, which was indicated by the sudden change of the PSD shape as well.

Intriguingly, this positive correlation between the average phase-lags and Γ_1 no longer holds in the 1−3 keV vs. 3−5 keV band, when the source transitions from the hard to hard intermediate state, where $1.6 \lesssim \Gamma_1 \lesssim 2.4$, as shown in Figs. 13 and 15. Figure 13 indicates that the dominant hard lags are contributed from the hard and hard intermediate states, within the frequency band of the variability components. In Fig. 15 we can see that the phase-lags decrease slightly as Γ_1 increases. The coherence there is good and the measured phase-lags are accurate. This phenomenon may suggest that in the hard state, although both the 1−3 keV band and the 3−5 keV band are both dominated by power-law photons, the 1−3 keV band is more likely to be dominated by the seed photons, which are possibly produced by the thermal black-body radiation of the accretion disk or the synchrotron radiation in the jet base; while the 3−5 keV band is dominated by the Comptonized photons up-scattered from the seed photons in softer X-ray bands.

6. Variability properties of Cygnus X-1 in a larger context

So far, we have discussed the individual variability properties of Cygnus X-1 (Sects. 5.1–5.3). We now discuss our results in the context of mechanisms of state transition, the disk-corona model, and the plausible scenarios of accretion in BHB systems.

6.1. Comparison with the behaviors of other BHBs

Cygnus X-1 is a persistently luminous BHB fed by the wind of its companion. However, the majority of BHBs are transient. Although we expect similar accretion scenarios for both kinds of system, it is still meaningful to compare the phenomenology observed for Cygnus X-1 with other known BHBs.

The total fractional rms, which is the integral of PSDs over all frequencies, decreases as the state softens (Belloni et al. 2005). This is also observed in transient and other persistent BHBs (e.g., Remillard & McClintock 2006). However, as discussed in Sect. 5.1, we should always outline the chosen energy band when defining the total rms, as different energy bands give different trends.

The evolution of the power spectra during state transitions has been reported in other BHBs, such as GX 339−4 (Zdziarski et al. 2004; Motta et al. 2011; Shui et al. 2021), GRS 1915+105 (Soleri et al. 2008; Ueda et al. 2009), XTE J1550−564 (Sobczak et al. 2000; Rodriguez et al. 2004; Rao et al. 2010), 4U 1630−47 (Tomsick & Kaaret 2000), and Swift J1753.5−0127 (Soleri et al. 2013; Bu et al. 2019). Most of the transient BHBs show narrow features in their power spectra, classified into type A, B, and C LFQPOs by their central frequencies, time-lags, and the quality factor (Casella et al. 2005; Motta et al. 2015). The central frequencies of the LFQPO components rise when the state of the BHB softens, and drop when returning back to the hard state (Vignarca et al. 2003). Sobczak et al. (2000) also reported an exception, GRO J1655−40, which shows a negative correlation of the central frequency of the 14−28 Hz LFQPO versus the power-law index, but a positive correlation with the disk flux, during a transition from very high state to the usual soft state. However, Motta et al. (2012) confirmed that the central frequencies of the LFQPO components still increase during the hard-to-soft transition. We note here that the transition from the very high state to the soft may not follow the regulation we talk about, and GRO J1655−40 is also special, as the HFQPO component and more than two LFQPO components can be observed (Strohmayer 2001; Belloni et al. 2012).

When those sources complete their transition from the hard state to the soft state, their power spectra with narrow or smooth peaks will be substituted by a red-noise power spectra with f^{-1} slope (see e.g., Miyamoto et al. 1994; Remillard & McClintock 2006; Ueda et al. 2009; Klein-Wolt & van der Klis 2008; Mao & Yu 2021), although Cygnus X-1 generally shows a higher overall variability than transients in the the soft state (e.g., Heil et al. 2015).

Fewer studies have addressed the higher order timing properties (the coherence function and phase/time-lag). Reig et al. (2018) report the growth of the hard lag of eight BHBs when the sources undergo a hard-to-intermediate transition. Altamirano & Méndez (2015) additionally find a sudden decrease in the averaged phase-lag at the transition point between the intermediate state and the soft state in GX 339−4, which is consistent with Grinberg et al. (2014) and our results.

6.2. Current models to describe timing properties

All the timing studies presented and discussed in Sects. 4 and 5 conclude that the variability components are strongly correlated with the mechanism of the transition between the hard and the soft state. Therefore, interpretation of their origin is crucial in order to reveal the accretion scenario.

Böck et al. (2011) reported a fast state transition in Cygnus X-1 within less than 2.5 h, but with their available data, they could only reach the soft intermediate state with $\Gamma_1 < 2.7$. The sudden change in the PSD from distinct variability components to red-noise spectrum has not been observed.

The variability components seen in the PSDs of Cygnus X-1 are smooth, with a quality factor $Q \lesssim 1$ modeled by two Lorentzian curves (e.g., Böck et al. 2011). Therefore, the models developed for the LFQPOs – for example, the Lense-Thirring precession (Bardeen & Petterson 1975) or the accretion-ejection instability (Tagger & Pellat 1999) – are not suitable in our case. Besides, even for the narrow LFQPOs commonly seen in other transient BHBs, we do not yet have a satisfying physical model that can consistently explain the spectral and timing behaviors (see Ingram & Motta 2019 for a recent review).

Among those models, a large fraction of them assume a truncated disk and hot inner flow geometry. In this scenario, the hard-to-soft transition happens when the truncation radius between the standard disk and the hot accretion flow decreases, which means an increasing characteristic frequency for all variabilities. Fruitful developments have been made by applying this scenario. For instance, Ingram et al. (2009) consider the precession of a hot flow inside a truncated disk, which is able to explain why the observed maximum frequency is almost constant for all BHBs. Ingram & Done (2011) further include the effect of the local fluctuations in the mass accretion rate in the model, which can reproduce the PSD shapes that are commonly seen in real data. Recently, Kawamura et al. (2022) considered propagating mass accretion rate fluctuations to map the *NICER* data of MAXI J1820−070, and were able in this way to explain the observed two-hump power spectra and the lag-frequency spectrum, supporting the idea that the disk is truncated at a few tens of a gravitational radius.

While, in practice, the inner edge of the accretion disk is usually measured by spectral fitting, some obtained results challenge this truncated-disk scenario in the hard state, both via the iron line method (e.g., García et al. 2015; Buisson et al. 2019; Sridhar et al. 2020; Wang et al. 2021) and the continuum fitting method (e.g., Miller et al. 2006; Reis et al. 2009, 2010), suggesting that even for the hard state, the inner edge of the disk should be close to the ISCO. A recent spectral study of Cygnus X-1 with a physical model set carried out by Feng et al. (2022) uses two fixed spin and inclination values suggested by Zhao et al. (2021), concluding that with these two parameter settings, there is no strong correlation between the state and the inner radius of the disk. If, as indicated by these results, the true mechanism of state transition between the hard and soft states is independent of the inner edge of the disk, then the evolution of the typical frequencies of variability components in the hard and intermediate states as observed here cannot be explained by a change in the inner disk radius or a precession motion of a flow that changes in size. At this stage, we are inclined to consider the variability component as a geometrical effect originating from the corona, but examining each model quantitatively with our data is beyond the scope of this paper.

In the soft state, the power spectrum is dominated by red noise for all energy bands. The shapes of the PSD are similar, except for the normalization of the f^{-1} power law. A plausible explanation is that the Comptonization process is completely triggered by the thermal photons, indicating that the initial structure of the corona is destroyed; hence the disappearance of characteristic frequencies of the power law emission, which is presented by variability components in the hard and intermediate states. The broadband noise seen in the power spectrum can be well explained by the fluctuation propagation model (e.g., Lyubarskii 1997; Arévalo & Uttley 2006).

6.3. The geometry of the corona during the state transitions

In order to probe the corona geometry, we first need to empirically explain why the intensity of the reflection component is stronger in the soft state than in the hard state. We partly adopt the interpretation of both Petrucci et al. (2001) and Shaposhnikov & Titarchuk (2006): when the state softens from hard to intermediate, the spatial size of the corona shrinks, and the corona may move closer to the accretion center. This geometrical configuration also matches the apparent phenomenon that the disk component gradually dominates the soft X-ray bands during the process of state softening. Based on a different technique, the reverberation lag model, Kara et al. (2019) arrive at similar conclusions (but also see e.g., Wang et al. 2021).

In the hard state, a corona with a higher optical depth can cover the central part of the accretion system, absorbing most of the seed photons and Comptonizing them to produce a power-law emission. According to Petrucci et al. (2001), the reflection component is highly likely to be Comptonized by the large corona as well. Therefore, the reflection feature will be diluted and the measured intensity of the reflection will decrease. When the state softens to an intermediate state, the corona becomes smaller, and then part of the seed photons can escape to infinity without being Comptonized. In the soft state with a red-noise-like PSD shape, the corona may shrink to a relatively small size, allowing most of the thermal photons escape to infinity, while it only captures and Comptonizes a few seed photons to a power-law shape.

The sudden change of the PSD shape and the sudden drop in the phase-lag might even support the idea that the shrinking corona is split into pieces at this stage, then losing its intrinsic frequency (Esin 1997; Done et al. 2007). Instead, the emission from these pieces is sustained by the seed photons, as their PSD shapes become consistent. Rapid fluctuations of the equivalent width of the iron Kα line, or a difference between two photon indices $\Delta\Gamma$, when $\Gamma_1 \gtrsim 2.7$ – which are both compatible with our results, as shown in Figs. 6 and 7 – would support this scenario, although the large uncertainties that we see on $\Delta\Gamma$ prevent us from firmly concluding that such fluctuations exist. A small-sized corona in the soft state, located at slightly different regions around the accreting center, can possibly produce large differences in the reflection strength. But for a larger corona with higher covering fraction in the hard and intermediate states, such evolution is much smoother.

7. Summary and outlook

In this paper, we use a simple phenomenological model to perform a broadband spectral analysis of Cygnus X-1 with 145 available exposures provided by the HXMT mission. With the best fits obtained, we then perform an energy-resolved timing analysis in the range between 1 and 150 keV, covering a larger energy range than most previous analyses. We list the most interesting results of our analysis below:

1. The spectral analysis confirms that the reflection strength becomes higher when the state transitions from hard to soft.
2. We offer an explanation as to the trends between the total rms and the soft photon index Γ_1. The trends depend on the spectral shape and the studied energy band, and especially on whether the disk emission dominates the spectrum.
3. During the hard-to-soft transition, we see a clear evolution of the central frequencies of the variability components in the 1–10 Hz range with Γ_1. In particular, we are able to trace this behavior up to at least ~90 keV. When the source has fully transitioned to the soft state, the variability component is substituted by the red noise in the power spectrum.
4. The high-energy photons from the corona are likely associated with the variability component with a higher central frequency, suggesting that they are produced from a region very close to the black hole.
5. The intrinsic coherence can be used to distinguish between the light curves from different states, as the dominant photons are produced via different mechanisms (thermal emission or Comptonization).
6. The averaged phase-lag increases during the hard-to-soft transition, but it quickly drops when the transition finishes.

With quasi-simultaneous radio and X-ray monitoring, we may further answer the question of disk–jet coupling; that is, whether the sudden change of the PSD shape and the recovery of the coherence when $\Gamma \simeq 2.7$ is due to the switching off of the jet emission.

Acknowledgements. M.Z. would like to thank the support from China Scholarship Council (CSC 202006100027). This research has made use of NASA's Astrophysics Data System Bibliographic Services. This research also made use of ISIS functions (isisscripts http://www.sternwarte.uni-erlangen.de/isis/) provided by ECAP/Remeis observatory and MIT. This work made use of data from the Insight-HXMT mission, a project funded by China National Space Administration (CNSA) and the Chinese Academy of Sciences (CAS). J.R. acknowledges partial funding from the French space agency (CNES), and the French programme national des hautes énergies. Z.S. is supported by the National Key R&D Program of China (2021YFA0718500), the National Natural Science Foundation of China under grants U1838201, U1838202. The material is based upon work supported by NASA under award number 80GSFC21M0002 (CRESST II).

References

Altamirano, D., & Méndez, M. 2015, MNRAS, 449, 4027
Arévalo, P., & Uttley, P. 2006, MNRAS, 367, 801
Arnaud, K. A. 1996, in Astronomical Data Analysis Software and Systems V, eds. G. H. Jacoby, & J. Barnes, ASP Conf. Ser., 101, 17
Axelsson, M., Borgonovo, L., & Larsson, S. 2005, A&A, 438, 999
Axelsson, M., Borgonovo, L., & Larsson, S. 2006, A&A, 452, 975
Bachetti, M., Huppenkothen, D., Khan, U., et al. 2021, https://doi.org/10.5281/zenodo.4881255
Bardeen, J. M., & Petterson, J. A. 1975, ApJ, 195, L65
Barthelmy, S. D., Barbier, L. M., Cummings, J. R., et al. 2005, Space Sci. Rev., 120, 143
Belloni, T. M. 2010, in Lecture Notes in Physics (Berlin: Springer-Verlag), 794, 53
Belloni, T., & Hasinger, G. 1990a, A&A, 227, L33
Belloni, T., & Hasinger, G. 1990b, A&A, 230, 103
Belloni, T., Homan, J., Casella, P., et al. 2005, A&A, 440, 207
Belloni, T. M., Sanna, A., & Méndez, M. 2012, MNRAS, 426, 1701
Böck, M., Grinberg, V., Pottschmidt, K., et al. 2011, A&A, 533, A8
Bolton, C. T. 1972, Nature, 235, 271
Bowyer, S., Byram, E. T., Chubb, T. A., & Friedman, H. 1965, Science, 147, 394
Bu, Q.-C., Chen, L., Li, Z.-S., et al. 2015, ApJ, 799, 2
Bu, Q.-C., Tao, L., Lu, Y., et al. 2019, MNRAS, 487, 1439
Buisson, D. J. K., Fabian, A. C., Barret, D., et al. 2019, MNRAS, 490, 1350
Cabanac, C., Roques, J.-P., & Jourdain, E. 2011, ApJ, 739, 58
Cangemi, F., Beuchert, T., Siegert, T., et al. 2021, A&A, 650, A93
Cao, X., Jiang, W., Meng, B., et al. 2020, Sci. China Phys. Mech. Astron., 63, 249504
Casella, P., Belloni, T., & Stella, L. 2005, ApJ, 629, 403
Cassatella, P., Uttley, P., Wilms, J., & Poutanen, J. 2012, MNRAS, 422, 2407
Chen, Y., Cui, W., Li, W., et al. 2020, Sci. China Phys. Mech. Astron., 63, 249505
Churazov, E., Gilfanov, M., & Revnivtsev, M. 2001, MNRAS, 321, 759
Corbel, S., Coriat, M., Brocksopp, C., et al. 2013, MNRAS, 428, 2500
Cui, W., Zhang, S. N., Focke, W., & Swank, J. H. 1997a, ApJ, 484, 383
Cui, W., Heindl, W. A., Rothschild, R. E., et al. 1997b, ApJ, 474, L57
Done, C., Gierliński, M., & Kubota, A. 2007, A&ARv, 15, 1
Dove, J. B., Wilms, J., Maisack, M., & Begelman, M. C. 1997, ApJ, 487, 759
Dunn, R. J. H., Fender, R. P., Körding, E. G., Belloni, T., & Cabanac, C. 2010, MNRAS, 403, 61

Esin, A. A. 1997, ApJ, 482, 400
Fabian, A. C., Wilkins, D. R., Miller, J. M., et al. 2012, MNRAS, 424, 217
Fender, R. P., Belloni, T. M., & Gallo, E. 2004, MNRAS, 355, 1105
Fender, R. P., Stirling, A. M., Spencer, R. E., et al. 2006, MNRAS, 369, 603
Feng, M. Z., Kong, L. D., Wang, P. J., et al. 2022, ApJ, 934, 47
Fürst, F., Nowak, M. A., Tomsick, J. A., et al. 2015, ApJ, 808, 122
García, J. A., Steiner, J. F., McClintock, J. E., et al. 2015, ApJ, 813, 84
García, J. A., Tomsick, J. A., Sridhar, N., et al. 2019, ApJ, 885, 48
Gierliński, M., & Done, C. 2004, MNRAS, 347, 885
Gierliński, M., & Zdziarski, A. A. 2005, MNRAS, 363, 1349
Gilfanov, M., Churazov, E., & Revnivtsev, M. 1999, A&A, 352, 182
Gilfanov, M., Churazov, E., & Revnivtsev, M. 2000, MNRAS, 316, 923
Grinberg, V., Hell, N., Pottschmidt, K., et al. 2013, A&A, 554, A88
Grinberg, V., Pottschmidt, K., Böck, M., et al. 2014, A&A, 565, A1
Grinberg, V., Leutenegger, M. A., Hell, N., et al. 2015, A&A, 576, A117
Guo, C.-C., Liao, J.-Y., Zhang, S., et al. 2020, J. High Energy Astrophys., 27, 44
Haardt, F. 1993, ApJ, 413, 680
Heil, L. M., Uttley, P., & Klein-Wolt, M. 2015, MNRAS, 448, 3339
HI4PI Collaboration (Ben Bekhti, N., et al.) 2016, A&A, 594, A116
Hirsch, M., Hell, N., Grinberg, V., et al. 2019, A&A, 626, A64
Homan, J., Wijnands, R., van der Klis, M., et al. 2001, ApJS, 132, 377
Houck, J. C., & Denicola, L. A. 2000, in Astronomical Data Analysis Software and Systems IX, eds. N. Manset, C. Veillet, & D. Crabtree, ASP Conf. Ser., 216, 591
Huppenkothen, D., Bachetti, M., Stevens, A., et al. 2019a, J. Open Sour. Softw., 4, 1393
Huppenkothen, D., Bachetti, M., Stevens, A. L., et al. 2019b, ApJ, 881, 39
Ibragimov, A., Poutanen, J., Gilfanov, M., Zdziarski, A. A., & Shrader, C. R. 2005, MNRAS, 362, 1435
Ichimaru, S. 1977, ApJ, 214, 840
Ingram, A., & Done, C. 2011, MNRAS, 415, 2323
Ingram, A. R., & Motta, S. E. 2019, New Astron. Rev., 85, 101524
Ingram, A., Done, C., & Fragile, P. C. 2009, MNRAS, 397, L101
Jourdain, E., Roques, J. P., Chauvin, M., & Clark, D. J. 2012, ApJ, 761, 27
Kara, E., Steiner, J. F., Fabian, A. C., et al. 2019, Nature, 565, 198
Kawamura, T., Axelsson, M., Done, C., & Takahashi, T. 2022, MNRAS, 511, 536
Klein-Wolt, M., & van der Klis, M. 2008, ApJ, 675, 1407
Kong, L. D., Zhang, S., Ji, L., et al. 2021, ApJ, 917, L38
Lai, E. V., De Marco, B., Zdziarski, A. A., et al. 2022, MNRAS, 512, 2671
Laurent, P., Rodriguez, J., Wilms, J., et al. 2011, Science, 332, 438
Li, X., Li, X., Tan, Y., et al. 2020, J. High Energy Astrophys., 27, 64
Liao, J.-Y., Zhang, S., Chen, Y., et al. 2020a, J. High Energy Astrophys., 27, 24
Liao, J.-Y., Zhang, S., Lu, X.-F., et al. 2020b, J. High Energy Astrophys., 27, 14
Liu, C., Zhang, Y., Li, X., et al. 2020, Sci. China Phys. Mech. Astron., 63, 249503
Lyubarskii, Y. E. 1997, MNRAS, 292, 679
Ma, X., Tao, L., Zhang, S.-N., et al. 2021, Nat. Astron., 5, 94
Makishima, K., Maejima, Y., Mitsuda, K., et al. 1986, ApJ, 308, 635
Mao, D.-M., & Yu, W.-F. 2021, Res. Astron. Astrophys., 21, 170
Markoff, S., Nowak, M. A., & Wilms, J. 2005, ApJ, 635, 1203
Matsuoka, M., Kawasaki, K., Ueno, S., et al. 2009, PASJ, 61, 999
Meyer-Hofmeister, E., Liu, B. F., Qiao, E., & Taam, R. E. 2020, A&A, 637, A66
Miller, J. M., Homan, J., Steeghs, D., et al. 2006, ApJ, 653, 525
Miller-Jones, J. C. A., Bahramian, A., Orosz, J. A., et al. 2021, Science, 371, 1046
Mitsuda, K., Inoue, H., Koyama, K., et al. 1984, PASJ, 36, 741
Miyamoto, S., Kimura, K., Kitamoto, S., Dotani, T., & Ebisawa, K. 1991, ApJ, 383, 784
Miyamoto, S., Kitamoto, S., Iga, S., Hayashida, K., & Terada, K. 1994, ApJ, 435, 398
Motta, S., Muñoz-Darias, T., Casella, P., Belloni, T., & Homan, J. 2011, MNRAS, 418, 2292
Motta, S., Homan, J., Muñoz Darias, T., et al. 2012, MNRAS, 427, 595
Motta, S. E., Casella, P., Henze, M., et al. 2015, MNRAS, 447, 2059
Narayan, R., & McClintock, J. E. 2008, New Astron. Rev., 51, 733
Narayan, R., & Yi, I. 1995, ApJ, 452, 710
Nowak, M. A. 2000, MNRAS, 318, 361
Nowak, M. A., Vaughan, B. A., Wilms, J., Dove, J. B., & Begelman, M. C. 1999, ApJ, 510, 874
Parker, M. L., Tomsick, J. A., Miller, J. M., et al. 2015, ApJ, 808, 9
Penna, R. F., McKinney, J. C., Narayan, R., et al. 2010, MNRAS, 408, 752
Petrucci, P. O., Merloni, A., Fabian, A., Haardt, F., & Gallo, E. 2001, MNRAS, 328, 501
Plotkin, R. M., Gallo, E., & Jonker, P. G. 2013, ApJ, 773, 59
Pottschmidt, K., Wilms, J., Nowak, M. A., et al. 2000, A&A, 357, L17
Pottschmidt, K., Wilms, J., Nowak, M. A., et al. 2003, A&A, 407, 1039
Rao, F., Belloni, T., Stella, L., Zhang, S. N., & Li, T. 2010, ApJ, 714, 1065
Rapisarda, S., Ingram, A., & van der Klis, M. 2017, MNRAS, 472, 3821
Reig, P., Kylafis, N. D., Papadakis, I. E., & Costado, M. T. 2018, MNRAS, 473, 4644
Reis, R. C., Miller, J. M., & Fabian, A. C. 2009, MNRAS, 395, L52
Reis, R. C., Fabian, A. C., & Miller, J. M. 2010, MNRAS, 402, 836
Remillard, R. A., & McClintock, J. E. 2006, ARA&A, 44, 49
Reynolds, M. T., Miller, J. M., Homan, J., & Miniutti, G. 2010, ApJ, 709, 358
Rodriguez, J., Corbel, S., Kalemci, E., Tomsick, J. A., & Tagger, M. 2004, ApJ, 612, 1018
Rodriguez, J., Grinberg, V., Laurent, P., et al. 2015, ApJ, 807, 17
Rykoff, E. S., Miller, J. M., Steeghs, D., & Torres, M. A. P. 2007, ApJ, 666, 1129
Shakura, N. I., & Sunyaev, R. A. 1973, A&A, 24, 337
Shaposhnikov, N., & Titarchuk, L. 2006, ApJ, 643, 1098
Shui, Q. C., Yin, H. X., Zhang, S., et al. 2021, MNRAS, 508, 287
Sobczak, G. J., McClintock, J. E., Remillard, R. A., et al. 2000, ApJ, 531, 537
Soleri, P., Belloni, T., & Casella, P. 2008, MNRAS, 383, 1089
Soleri, P., Muñoz-Darias, T., Motta, S., et al. 2013, MNRAS, 429, 1244
Sridhar, N., García, J. A., Steiner, J. F., et al. 2020, ApJ, 890, 53
Steiner, J. F., McClintock, J. E., Remillard, R. A., et al. 2010, ApJ, 718, L117
Steiner, J. F., Remillard, R. A., García, J. A., & McClintock, J. E. 2016, ApJ, 829, L22
Strohmayer, T. E. 2001, ApJ, 552, L49
Tagger, M., & Pellat, R. 1999, A&A, 349, 1003
Tananbaum, H., Gursky, H., Kellogg, E., Giacconi, R., & Jones, C. 1972, ApJ, 177, L5
Tomsick, J. A., & Kaaret, P. 2000, ApJ, 537, 448
Tomsick, J. A., Kalemci, E., Kaaret, P., et al. 2008, ApJ, 680, 593
Ueda, Y., Yamaoka, K., & Remillard, R. 2009, ApJ, 695, 888
Vaughan, B. A., & Nowak, M. A. 1997, ApJ, 474, L43
Verner, D. A., Ferland, G. J., Korista, K. T., & Yakovlev, D. G. 1996, ApJ, 465, 487
Vignarca, F., Migliari, S., Belloni, T., Psaltis, D., & van der Klis, M. 2003, A&A, 397, 729
Walton, D. J., Tomsick, J. A., Madsen, K. K., et al. 2016, ApJ, 826, 87
Wang, J., Mastroserio, G., Kara, E., et al. 2021, ApJ, 910, L3
Webster, B. L., & Murdin, P. 1972, Nature, 235, 37
Wijnands, R., & van der Klis, M. 1999, ApJ, 514, 939
Wilms, J., Allen, A., & McCray, R. 2000, ApJ, 542, 914
Wilms, J., Nowak, M. A., Pottschmidt, K., Pooley, G. G., & Fritz, S. 2006, A&A, 447, 245
Zdziarski, A. A., Lubiński, P., Gilfanov, M., & Revnivtsev, M. 2003, MNRAS, 342, 355
Zdziarski, A. A., Gierliński, M., Mikołajewska, J., et al. 2004, MNRAS, 351, 791
Zdziarski, A. A., You, B., Szanecki, M., Li, X.-B., & Ge, M. 2022, ApJ, 928, 11
Zhang, W., Jahoda, K., Swank, J. H., Morgan, E. H., & Giles, A. B. 1995, ApJ, 449, 930
Zhang, S., Lu, F. J., Zhang, S. N., & Li, T. P. 2014, in Space Telescopes and Instrumentation 2014: Ultraviolet to Gamma Ray, eds. T. Takahashi, J. W. A. den Herder, & M. Bautz, SPIE Conf. Ser., 9144, 914421
Zhang, S.-N., Li, T., Lu, F., et al. 2020, Sci. China Phys. Mech. Astron., 63, 249502
Zhao, X., Gou, L., Dong, Y., et al. 2021, ApJ, 908, 117
Zhu, Y., Davis, S. W., Narayan, R., et al. 2012, MNRAS, 424, 2504

Appendix A: Overview of the average PSDs at different spectral shapes

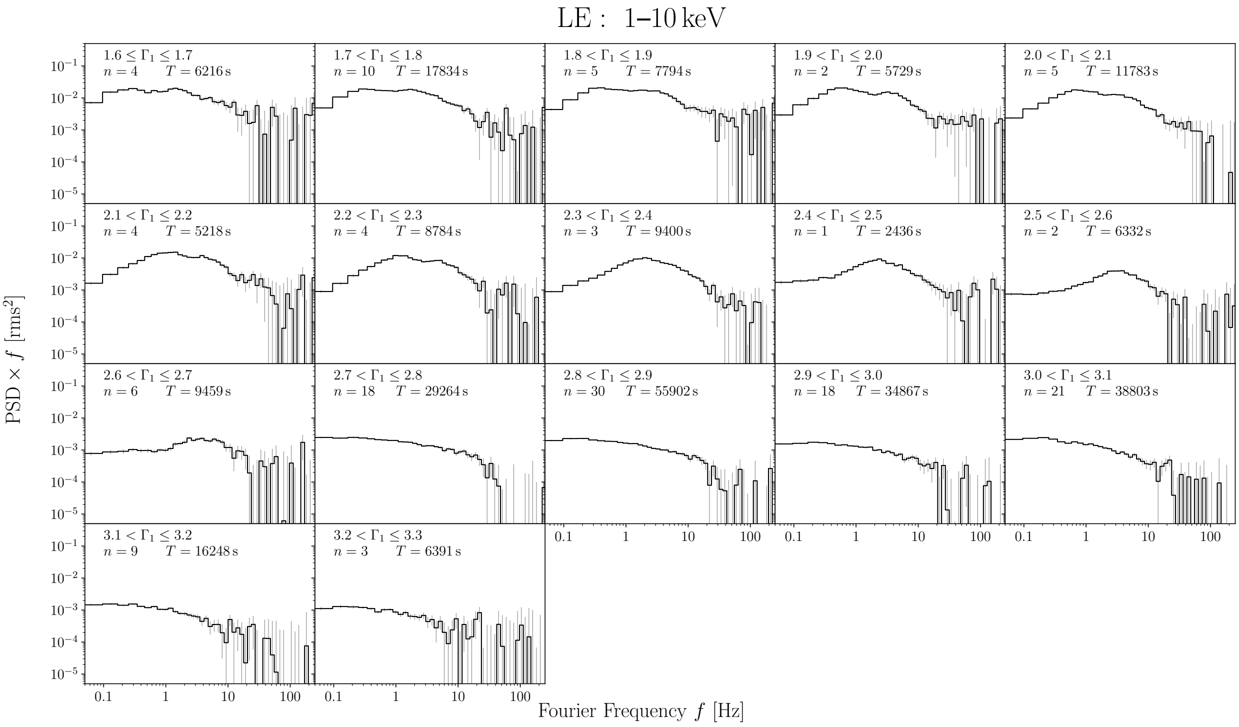

Fig. A.1. Average PSDs of 1−10 keV band (LE) in different spectral states. Each PSD is the average of all n PSDs falling within the given Γ_1 interval. We also denote the total exposure time T in GTIs for each Γ_1 interval.

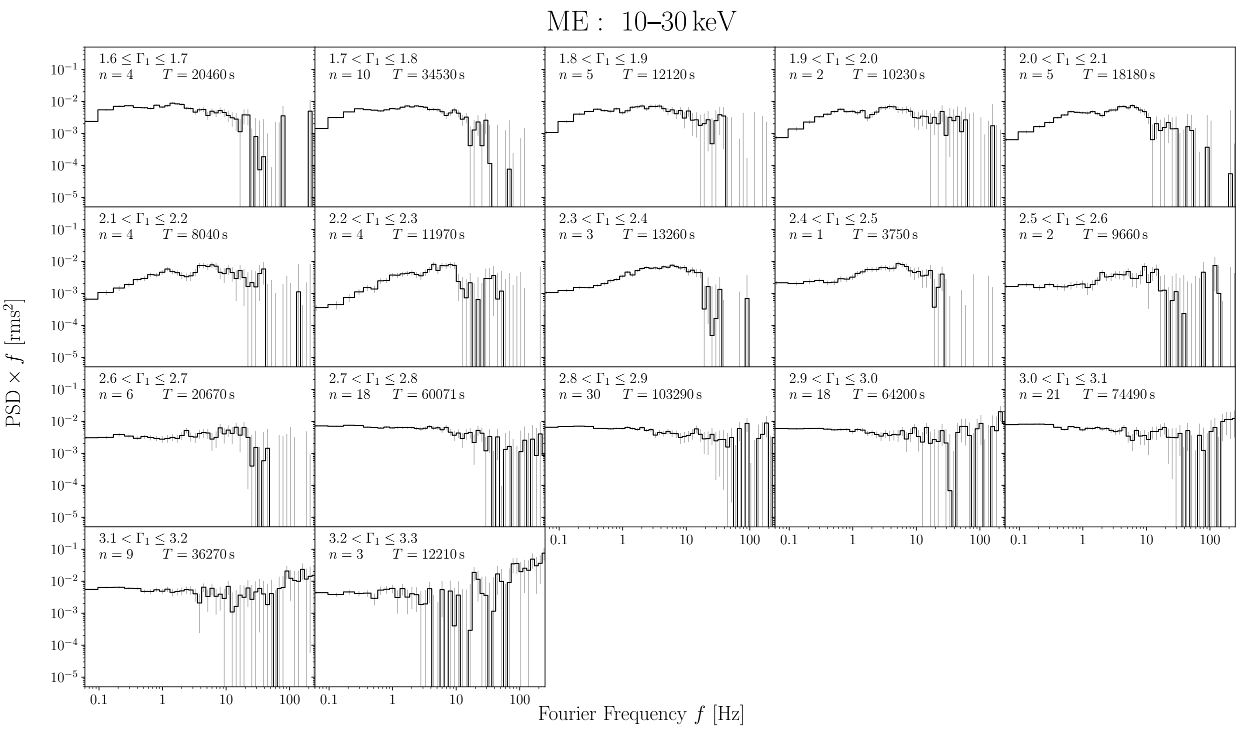

Fig. A.2. Similar to Fig. A.1, but for 10−30 keV band (ME).

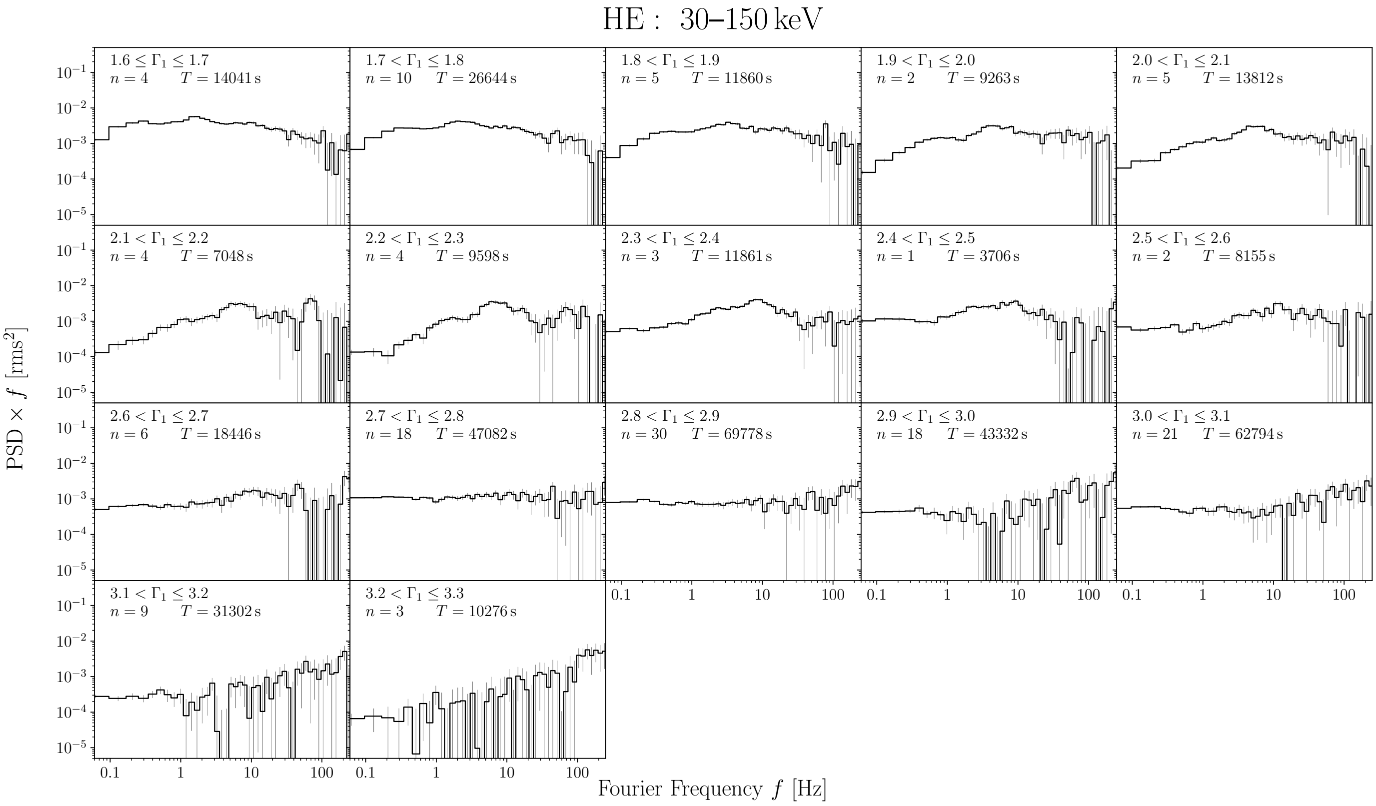

Fig. A.3. Similar to Figs. A.1 and A.2, but for 30−150 keV band (HE).

B Published Article 2

A&A, 694, A104 (2025)
https://doi.org/10.1051/0004-6361/202451558

Astronomy & Astrophysics

Dimming GRS 1915+105 observed with NICER and Insight–HXMT

M. Zhou[1,⋆], V. Grinberg[2], A. Santangelo[1], C. Bambi[3,4], Q. Bu[5], C. M. Diez[6], L. Kong[1], J. F. Steiner[7], and Y. Tuo[1]

[1] Institut für Astronomie und Astrophysik, Universität Tübingen, Sand 1, 72076 Tübingen, Germany
[2] European Space Agency (ESA), European Space Research and Technology Centre (ESTEC), Keplerlaan 1, 2201 AZ Noordwijk, The Netherlands
[3] Center for Astronomy and Astrophysics, Center for Field Theory and Particle Physics, and Department of Physics, Fudan University, Shanghai 200438, China
[4] School of Natural Sciences and Humanities, New Uzbekistan University, Tashkent 100007, Uzbekistan
[5] Institute of Astrophysics, Central China Normal University, Wuhan 430079, China
[6] European Space Astronomy Centre (ESAC), Camino Bajo del Castillo s/n, Villanueva de la Cañada 28692, Madrid, Spain
[7] Harvard-Smithsonian Center for Astrophysics, 60 Garden Street, Cambridge, MA 02138, USA

Received 18 July 2024 / Accepted 1 January 2025

ABSTRACT

The black hole X-ray binary GRS 1915+105 was bright for 26 years since its discovery and is well known for its disk instabilities, quasi-periodic oscillations, and disk wind signatures. We report a long-term spectral-timing tracing of this source from mid-2017 until the onset of the so-called obscured state based on the complete data from the Neutron Star Interior Composition Explorer (NICER) and the Insight–Hard X-ray Modulation Telescope (HXMT), whose hard coverage decisively informs the modeling at lower energies. In the soft state predating 2018, we observed highly ionized winds. However, in the hard state shortly before transitioning into the obscured state on May 14, 2019 (MJD 58617), the winds exhibited a discernible reduction in ionization degree ($\log \xi$), which decreased from above 4 to approximately 3. Our analysis involves the measurement of the frequencies of the quasi-periodic oscillations and the estimation of the properties of the ionized winds and the intensities of different spectral components through spectroscopy during the decay phase. We studied the origin of these infrequently observed warm outflows in the hard state. The launching radius of the winds in the hard decay phase is similar to that in the soft state, which indicates that the launching mechanism of these winds likely is the same in both states. The presence of the ionized winds is preferentially dependent on the periphery of the accretion disk, but it is not directly related to the corona activities in the center of the binary system.

Key words. accretion, accretion disks – stars: black holes – X-rays: binaries – X-rays: individuals: GRS 1915+105

1. Introduction

Black hole binaries (BHBs) consist of a black hole and a donor star companion (for a review on BH binaries, see e.g. Remillard & McClintock 2006, and the references therein). The black hole (BH) accretes matter from its companion star. The accretion process leads to the release of intense radiation and outflows that can be observed across the electromagnetic spectrum. GRS 1915+105 is a particularly interesting BHB. First discovered by the Gamma-Ray Astronomical Telescope/Wide Angle Telescope for Cosmic Hard X-rays (GRANAT/WATCH) all-sky monitor in 1992 (Castro-Tirado et al. 1992, 1994), GRS 1915+105 has been well studied since. The captivating phenomena of this source, such as the exhibition of apparently superluminal radio jets (Mirabel & Rodríguez 1994), rarely seen high-frequency quasi-periodic oscillation (HFQPO) features in the timing domain (Morgan et al. 1997), the highly ionized winds generated from the accretion disk (Lee et al. 2002; Ueda et al. 2009), and the characteristic patterns of its light curves that can be classified into at least 14 different classes (Belloni et al. 2000; Klein-Wolt et al. 2002; Hannikainen et al. 2005; Zoghbi et al. 2016; Athulya et al. 2022; Shi et al. 2023), all make GRS 1915+105 valuable and important for our understanding of astrophysical processes such as accretion and the outflow formation, including the jet ejection and disk winds.

Unlike other transient X-ray binaries that brighten and fade during weeks or months (e.g., Remillard et al. 1999; Homan et al. 2001; Williams et al. 2020), GRS 1915+105 was consistently bright for 26 years since its discovery and was thought to be a quasi-persistent source. However, its luminosity unexpectedly underwent an exponential decay in early 2018 (Negoro et al. 2018). During this flux decline, the source also showed prominent and narrow low-frequency quasi-periodic oscillation (LFQPO) features (Koljonen & Hovatta 2021). It was then thought that GRS 1915+105 had nearly completed its 26-year-long outburst and entered its quiescent state. In April 2019 (~MJD 58600), the source became dimmer during a pre-flare dip (Homan et al. 2019). A few days later, short flares lasting for hours were observed in the radio and X-ray band (Motta et al. 2019, 2021; Koljonen et al. 2019), but they had an even lower average X-ray flux. The LFQPO features within 1−10 Hz were either halted or became undetectable synchronously. However, during a 60-day rebrightening phase in mid-2021, strong QPO features with an unprecedentedly low frequency ($f_{\rm QPO} \simeq$ 0.2 Hz) were discovered (Kong et al. 2024). Intriguingly, despite the rapid luminosity decay measured in X-rays, the radio

⋆ Corresponding author;
menglei.zhou@astro.uni-tuebingen.de

observations suggest that GRS 1915+105 has remained active in the accretion process after mid-2019.

Generally, the physics of the state transition of BHBs is not fully understood. Empirically, a typical outburst observed in a BHB can form a q-track in its hardness-intensity diagram (HID) (Homan et al. 2001; Fender et al. 2006). During the hard state in which the (cutoff) power-law emission dominates in X-rays, jet emission is observed in radio and infrared bands, and LFQPOs in the timing domain often emerge. In contrast, in the soft state when thermal radiation becomes primary, the jet typically becomes either weak and unstable or undetectable, with a power spectrum dominated by flicker noise. The central frequencies of the LFQPOs are found to have a negative correlation with the spectral hardness up to at least 90 keV (e.g., Zdziarski et al. 2004; Soleri et al. 2008; Zhou et al. 2022). As an ingredient involved in the accretion process, ionized disk winds are thought to play an important role during the state transition and are preferentially discovered in the soft state, where the jet emission is usually quenched (Neilsen & Lee 2009; Ponti et al. 2012). The state-dependent anticorrelation between the disk winds and the jets indicates that the disk winds may work as an alternative mode to eject matters. Previous studies have shown that GRS 1915+105 displays prominent blueshifted ionization absorption features, for instance, the Fe XXV Heα line and the Fe XXVI Lyα line, which are located at 6.7 keV and 7 keV, respectively (Ueda et al. 2009; Miller et al. 2016; Neilsen et al. 2018).

It is still unclear which mechanism drives the ionized absorption outflow. It can be generated by radiation pressure if the luminosity of the source approaches the Eddington limit (Proga & Kallman 2002; Higginbottom & Proga 2015), by thermal pressure when the gas of the disk atmosphere is irradiated by the energetic photons from the inner part of the accretion disk (Begelman et al. 1983; Woods et al. 1996; Done et al. 2018), or by magnetic pressure given the strong magnetic field close to the BH (Fukumura et al. 2017). Additionally, the partial concealment of cold dense absorption detected in some BHBs may also arise from an internal obscured clump that failed to escape from the strong gravitational field (Miller et al. 2020). The presence of the obscured clump, which exhibits fast absorption variabilities that can be seen in BHBs (see e.g., Motta et al. 2017a,b; Koljonen & Tomsick 2020; Balakrishnan et al. 2021) and active galactic nuclei (AGNs) (e.g., Matt et al. 2003), provides significant diagnostic information for understanding how accretion behaves within the full range of BH masses from a few $M_\odot$ to $10^9\ M_\odot$.

We focus on the period just before GRS 1915+105 entered the obscured state and use all the public data that were observed between MJD 57932 (June 8, 2017) and MJD 58608 (May 5, 2019). The data were obtained from the archive of X-ray Timing Instrument (XTI) of the Neutron Star Interior Composition Explorer (NICER; Gendreau et al. 2016) and Insight–Hard X-ray Modulation Telescope (Insight–HXMT or HXMT; Zhang et al. 2014, 2020). We perform a spectral-timing analysis based on these data by tracing the evolution of key parameters and probing their correlations using the simultaneous broadband coverage by both instruments, in particular, the high-energy coverage afforded by HXMT where available, to also inform the single-instrument fits. The results contribute to our understanding of the physics of the accretion process and the mechanisms behind the state transitions of transient BHBs. The remainder of this paper is structured as follows: In Sect. 2 we present the long-term behaviors of the source and an overview of the data we analyze in this paper. The spectral-timing analysis is detailed in Sect. 3 and the results are presented in Sect. 4. We discuss the results of our analysis in Sect. 5. A summary and outlook are presented in Sect. 6.

2. Observations and data reduction

The long-term behavior of GRS 1915+105 since 2017 is shown in Fig. 1. The light curve monitored by MAXI (Matsuoka et al. 2009) indicates that this source was consistently active before 2018, but then underwent a transition from an exponential decay to a linear decay until the beginning of May 2019 (we followed the state definitions of Koljonen & Hovatta 2021). After this, the source became extraordinarily faint, and its flux was reduced by a factor of 10. It exhibited three month-long flares and several short flares that only lasted a few hours in the X-ray band (see e.g., Neilsen et al. 2020; Kong et al. 2021), but it remained particularly active in the radio band (Motta et al. 2021). The abundant observations focusing on GRS 1915+105 by NICER and HXMT allowed us to closely trace the evolution of this source after 2017. We are particularly interested in the observations before the source entered the purely obscured state, and we used all the available NICER and HXMT data before MJD 58617.

The NICER and the HXMT both produce essential spectral-timing data. The XTI of NICER consists of an aligned collection of 56 X-ray concentrator optics and silicon drift-detector pairs that extend to a softer X-ray band (0.25−10 keV) with a time-tagging resolution of ∼100 nanoseconds. HXMT instead has a broader energy band that nominally ranges from 2 to around 250 keV, which is realized by three collimated telescopes: the Low-Energy (LE) telescope, whose energy range covers the 1−15 keV band (Chen et al. 2020); the Medium Energy (ME) telescope, covering 5−30 keV (Cao et al. 2020); and the High Energy (HE) telescope, covering the 25−250 keV band (Liu et al. 2020). In particular, the fast temporal response and large effective area of HXMT at higher energies allowed us to conduct spectral-timing studies above 15 keV, and in particular, to better constrain the continuum spectral models by providing high-energy leverage on the spectral shape. We present the details of the data processing in the following subsections.

2.1. NICER data

We processed all NICER data using the tools provided in `HEASOFT` v6.32.1 and the calibration database `xti20221001`. The cleaned event lists are produced by the standard `nicerl2` task, including calibration and filtering steps. To minimize the background effects, we applied a custom set of selection criteria to identify good time intervals (GTIs) based on standard NICER screening criteria: an overshoot rate lower than 10 cts per FPM (`FPM_OVERONLY_COUNT` < 10), an undershoot rate lower than 200 cts per FPM (`FPM_UNDERONLY_COUNT` < 200), and a geomagnetic cutoff-rigidity greater than 2 GeV (`COR_SAX` > 2). The photons registered by the noisy detectors (`DET_ID = 14,34,43,54`) were also omitted (e.g., Bogdanov et al. 2019). Finally, we extracted the spectra and light curves within our selected GTIs with `nicerl3-spect` and `nicerl3-lc`. The background spectrum was estimated with model `3C50` (Remillard et al. 2022). The energy band for the spectral analyses is 0.4−10 keV.

2.2. HXMT data

For the HXMT data, we used the pipeline based on the Insight–HXMT Data Analysis Software (`HXMTDAS`) v2.05 and the calibration database v2.06. The GTIs were selected according

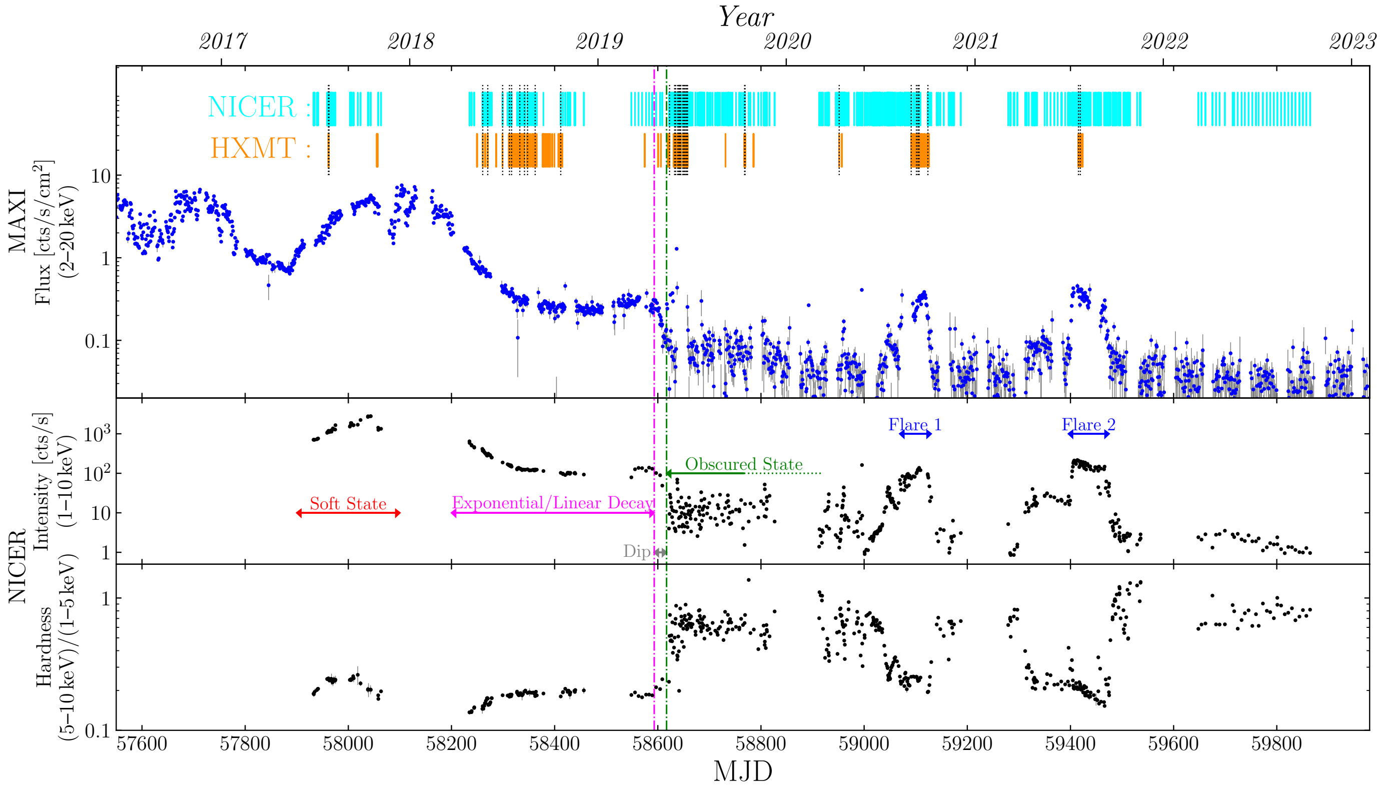

Fig. 1. Long-term behavior of GRS 1915+105 monitored by MAXI and NICER. Top panel: Daily flux measured by MAXI in the 2−20 keV band. The duration of NICER and Insight–HXMT observations is shown at the top with cyan and dark orange stripes. The dotted black lines denote the available quasi-simultaneous observations by two instruments. Middle panel: Intensity of GRS 1915+105, defined by the raw photon count rate registered in the 1−10 keV band of NICER. The spectral states are classified with spectral-timing features and denoted with arrows. More details can be found in the literature. Bottom panel: Hardness of the spectra, defined by the raw count rate between the 5−10 keV band and the 1−5 keV band of NICER. The vertical dash-dotted magenta line (~MJD 58593) represents the start point of the pre-flare dip, and the dash-dotted green line (~MJD 58617) marks the passing of this source into the obscured state.

to the following criteria: an elevation angle larger than 10° (`ELV` > `10`), a geomagnetic cut-off rigidity higher than 8 GeV (`COR` > `8`), an offset angle from the pointing direction smaller than 0.04° (`ANG_DIST` < 0.04), and at least 300 seconds before and after the South Atlantic Anomaly passage (`T_SAA` ≧ `300 &&` `TN_SAA` ≧ `300`). We adopted an additional criterion for the LE telescope: the elevation angle for the bright Earth must be larger than 30°. Since the individual detectors of the HXMT instruments have different fields of view (FoVs), we selected photon events that were registered by detectors with a small FoV for the following analysis.

The energy bands for the spectral analyses were 2−10 keV for LE, 10−30 keV for ME, and 28−90 keV for HE. We additionally ignored photons within the 21−24 keV band of the ME telescope to avoid detecting the silver K-shell fluorescent lines produced by the material of the instrument (Li et al. 2020). We used the tools `LEBKGMAP` (Liao et al. 2020a), `MEBKGMAP` (Guo et al. 2020), and `HEBKGMAP` (Liao et al. 2020b) that are provided by the HXMT team to estimate the instrumental background.

2.3. Joint fitting with NICER and HXMT data

NICER has a large effective area in the soft X-ray band (~1900 cm^2, peaking at 1.5 keV), which makes it well suited for probing absorption characteristics, while HXMT covers a wider energy range up to roughly 250 keV, which enables a good constraint on the slope of the continuum. We exploited the combination of the two X-ray missions where simultaneous data are available and used the results to inform models where the coverage exist only below 10 keV. This allowed an improved modeling and better model constraints. A total of 20 joint spectra are available before the obscured state of GRS 1915+105 (see the top panel in Fig. 1). Seven of these occurred before 2018 (in the soft state) and 13 during the exponential and linear decay, during which the spectra are relatively hard. We optimized our modeling by conducting a joint fitting, which helped us to rule out unsound parameters and obtain better constraints on various theories. We used NICER/XTI and HXMT/ME together to extend our spectra to higher energies for observations prior to 2018, as HXMT/HE is predominantly affected by background. During the decay phase, we combined the spectra from NICER/XTI, HXMT/ME, and HXMT/HE.

3. Spectral-timing analysis

We used `ISIS` v1.6.2 (Houck & Denicola 2000), which allowed us access to the defined models in `Xspec` (Arnaud 1996), to perform the spectral-timing fitting.

3.1. Timing analysis

All the light curves obtained from both NICER and HXMT were directly generated from the corresponding screened event lists and were processed with `Stingray` (Bachetti et al. 2021; Huppenkothen et al. 2019a,b). The selected energy range for

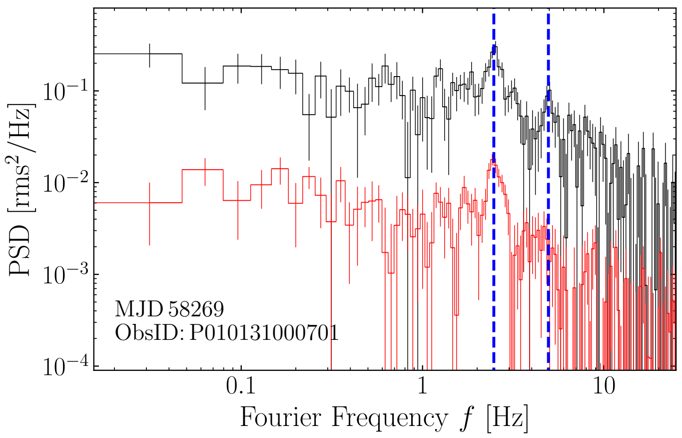

Fig. 2. Typical PSDs simultaneously observed with HXMT/LE (in black) and HXMT/ME (in red). The PSDs of LE are multiplied by a constant of 20 to avoid overlapping in the figure. The central frequencies of the main QPO and its first harmonic are 2.47 Hz and 4.94 Hz, respectively, as indicated by two dashed blue lines.

NICER/XTI is 1−10 keV. The time resolution (Δt) of these light curves was set to 2^{-9} s $\approx$ 2 ms. The power spectrum densities (PSDs) were computed using segments with a length of $2^{14} \times \Delta t = 32$ s. Thus, the Nyquist frequency for these PSDs is $f_{\rm max} = 1/(2\Delta t) = 256$ Hz, and the lowest frequency we were able to access is $f_{\rm min} = 1/(n_{\rm bins}\Delta t) = 0.03125$ Hz. The frequencies f were rebinned logarithmically between $f_{\rm min}$ and $f_{\rm max}$, with an equally spaced grid in logarithmic scale $\mathrm{d}f/f = 0.03$. The expectations of the white noise were reduced according to Zhang et al. (1995). We omitted the data above 30 Hz since they are dominated by Poisson noise.

The spectral states of GRS 1915+105 can clearly be classified by the timing properties. Before 2018, GRS 1915+105 was in a spectrally soft state, and its light curve is predominantly categorized as class λ (Belloni et al. 2000; Neilsen et al. 2018). The flicker noise dominated the power spectrum, without unambiguous LFQPO features in the 1−10 Hz band. From the end of April 2018 to the end of April 2019, the power spectra exhibited at least two prominent LFQPO features whose central frequencies were in the 1−10 Hz range. At the end of the decay phase, the power spectra were dominated by Poisson noise since MJD 58621 (May 18, 2019), marking the onset of the obscured state. During the year before the onset of the obscured state, we additionally examined the data from HXMT/LE and HXMT/ME. We found that the central frequencies of the LFQPO components are consistent in these simultaneous observations (see, e.g., Fig. 2), even though the PSDs produced by HXMT are noisier than those of NICER because HXMT has stronger background effects. The QPOs thus clearly extend above 10 keV, that is, in a range that is dominated by the continuum with no disk contribution.

We modeled the NICER spectra because they are less affected by noise. To do this, we chose an empirical model consisting of two Lorentzian functions with central frequencies fixed at zero to characterize the noise continuum (Nowak 2000). The combination of these two Lorentzians is appropriate for flicker and flat-top noise with a high-frequency cutoff. The LFQPO signals were captured by three additional Lorentzian functions with free central frequencies. Two typical fits with this model are shown in Fig. 3. We obtained a relatively good fit for most of our power spectra. The most significant Lorentzian signal with a lower frequency is identified as the main QPO component, and the second with a higher frequency is recognized as the first harmonic. We show their central frequencies along with their posterior uncertainties versus time in Fig. 4, and the correlation between these two components is plotted in the upper panel of Fig. 6. Our findings suggest that there is always a 2:1 relation between the central frequencies of two QPO components, which measures LFQPO frequencies more soundly. While we occasionally observe a third QPO component, there are no clear patterns in its appearance concerning the former two prominent QPO features.

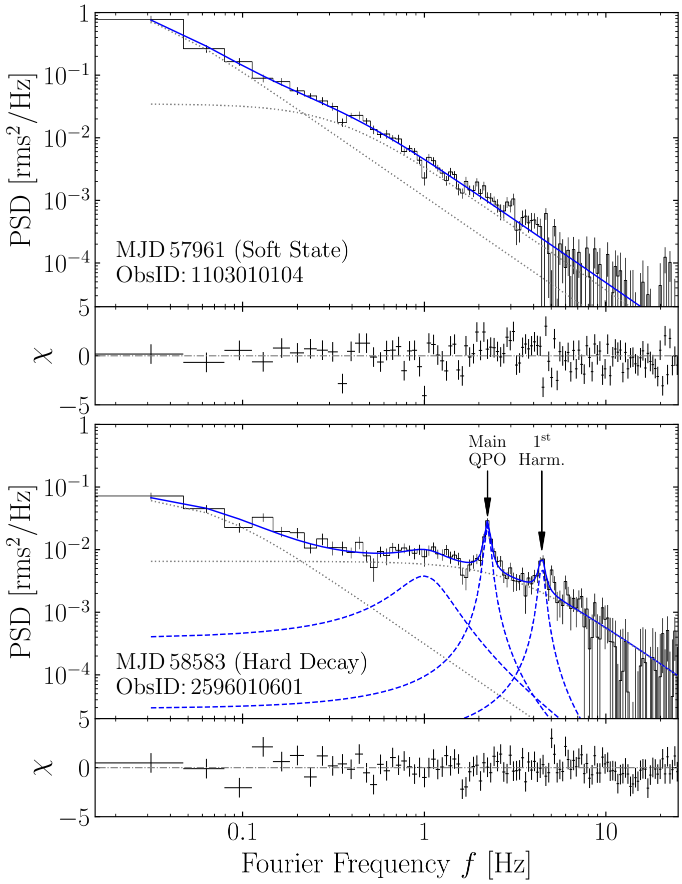

Fig. 3. Two typical power spectra produced by NICER data in the soft (upper panel) and hard state during the decay phase (lower panel) with their best-fit models. The Lorentzians with a central frequency at zero are indicated with dotted gray lines, and the Lorentzians with a nonvanishing central frequency are indicated with dashed blue lines. As the best-fit model, the sums of all the Lorentzians are denoted with solid blue lines. The measured central frequencies of the main QPO and the first harmonic in the hard state are $2.23^{+0.18}_{-0.19}$ Hz and $4.44^{+0.05}_{-0.06}$ Hz, respectively.

3.2. Spectral analysis

We adopted a systematic error of 0.5% and 1.0% for HXMT/ME and HXMT/HE, respectively (Li et al. 2020), and of 1.5% for NICER/XTI[1]. All the spectra were grouped using the optimal binning method detailed in Kaastra & Bleeker (2016), and we ensured that there were 30 photon counts per bin at least.

[1] https://heasarc.gsfc.nasa.gov/docs/nicer/analysis_threads/cal-recommend/

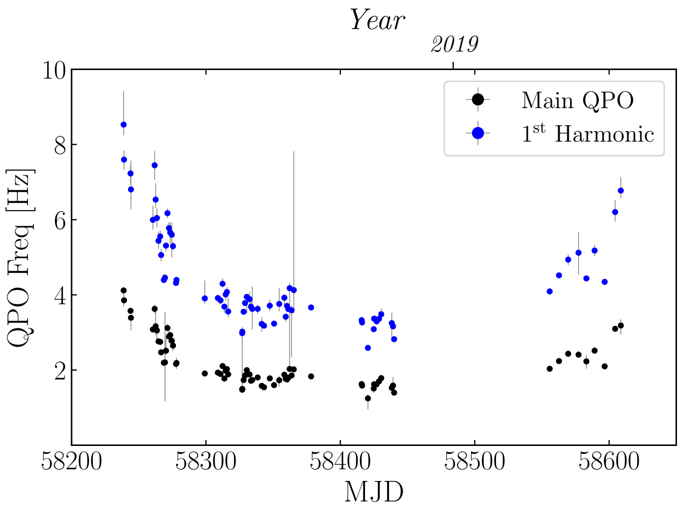

Fig. 4. Evolution of the QPO frequencies vs. time during the exponential and linear decay.

3.2.1. Preliminary modeling for NICER only

We first tried to fit the NICER spectra with a simple continuum of the Comptonization emission produced by the corona (Nthcomp; Zdziarski et al. 1996; Życki et al. 1999), multiplied by the Galactic absorption model TBabs to characterize the photoelectric absorption by the interstellar medium (ISM). The cross sections were provided by Verner et al. (1996) and the element abundances were given by Wilms et al. (2000). The multitemperature thermal radiation generated from the accretion disk (diskbb; Mitsuda et al. 1984; Makishima et al. 1986) was further included in our model in the soft state. Typical residuals are presented in the upper panel of Fig. 5. These exploratory fits are usually poor, with high reduced χ^2s, but we obtained a well-constrained estimate of the photon index of the continuum. The correlation of the main QPO frequencies and the measured photon index Γ is shown in blue in the lower panel of Fig. 6. A quasi-linear trend between these two parameters is observed even with this preliminary model.

In the soft state, we detected absorption at ∼7 keV, which we identified with Fe XXVI Lyα. The observed Fe Kα emission line is broadened.

During the decay phase, we detected a narrow emission feature below 7 keV. This feature plays a major role in shaping the whole iron-line region of the spectrum. If this narrow iron line is produced by the accretion disk and models the region with a single relativistic reflection model, the inferred inclination angle of the system is smaller than 30° (see, e.g., Table 4 in Shreeram & Ingram 2020), which contradicts known constraints for the inclination of GRS 1915+105 to be in the order of $i \simeq 60°$ (e.g., Reid et al. 2014; Fender et al. 1999). When the inclination angle in our model is constrained to 60°, the iron-line region, in particular, the narrow component, cannot be well modeled. Therefore, we conclude that an additional component, a distant reflector, is necessary, and the observed complexity of the iron-line region is an interplay of the broad relativistic and narrow distant components.

In addition to the narrow iron line, one unsolved feature remains in the residual plots: a suspected additional Si edge at ∼1.84 keV. This additional Si edge was discussed, for example, by Lee et al. (2002), Martocchia et al. (2006), and Koljonen & Hovatta (2021), and it can likely be attributed to

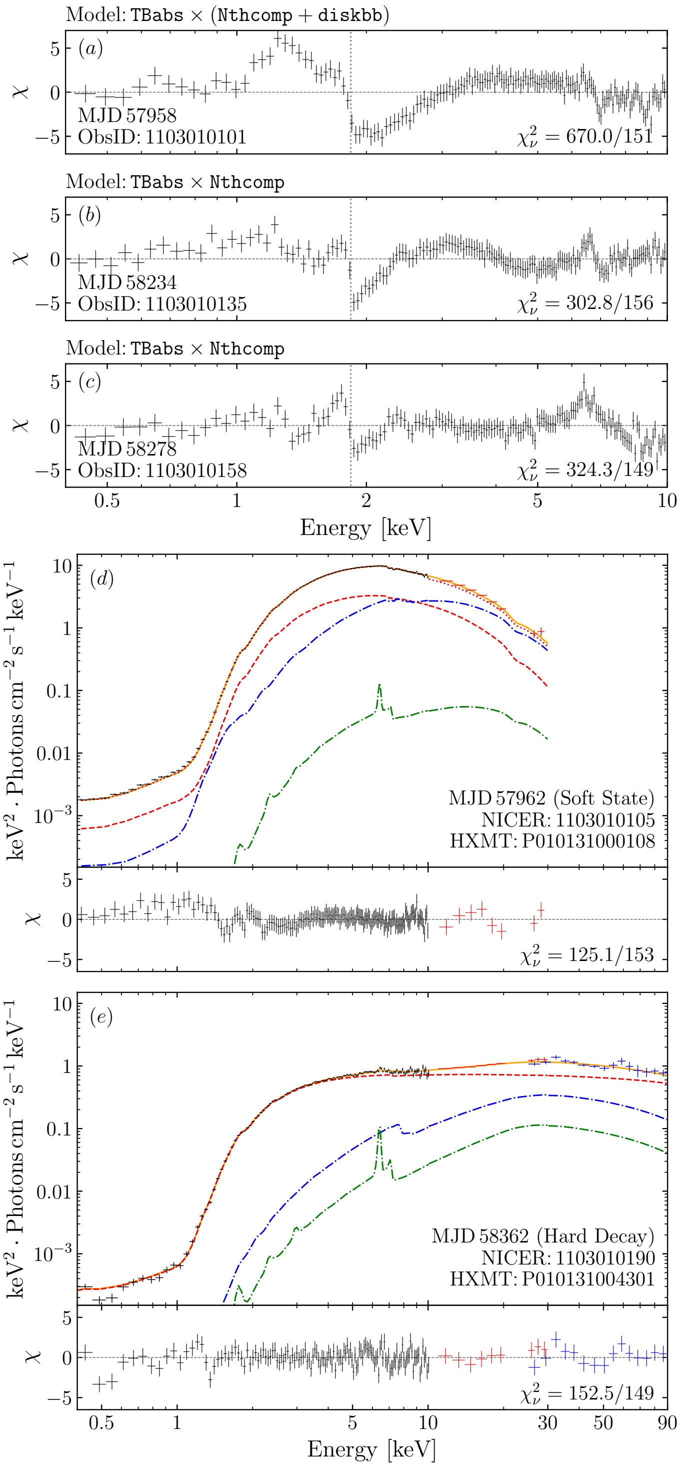

Fig. 5. The residuals and the spectral composition diagrams for different states. From (a) to (c): Residuals for the preliminary modeling to fit the NICER observation during the soft state (MJD 57958) at the beginning and the middle of the decay phase (MJD 58234 and 58278). An additional silicon absorption edge (1.84 keV, denoted by the dotted line) and a narrow iron Kα line with a cutoff energy lower than 7 keV are plotted as well. From (d) to (e): Two typical merged unfolded spectra of GRS 1915+105 in different states, fit by the physical model illustrated in Eq. (1). Different spectral components, i.e., the power-law continuum, the relativistic reflection component from the accretion disk, and the nonrelativistic reflection component from a distant reflector, are shown with the dashed red line, the dash-dotted blue line, and the dash-dotted line line, respectively. See the text for detailed information.

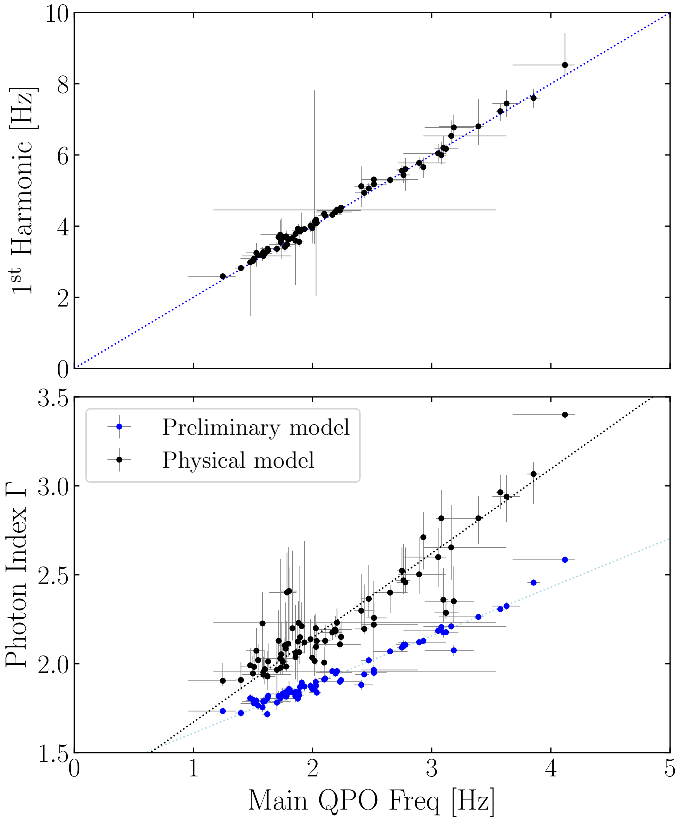

Fig. 6. Upper panel: Correlation between the main QPO frequency and the first harmonic. The dotted blue line indicates the double relation. Lower panel: Correlation between the main QPO frequency and the measured photon index Γ with the preliminary model and an improved physical model described in Sects. 3.2.1 and 3.2.2, respectively. The dotted lines show the best fits assuming a linear model.

calibration issues. To consider this additional absorption edge, we added an `edge` model whose threshold energy was fixed at 1.84 keV, which we multiplied throughout the entire model.

We thus had a simple phenomenological model for GRS 1915+105 in the soft and hard states. However, more interesting information on the accretion system can be extracted from the spectra with an improved physical model. We introduce an improved model for spectral fitting in the next section, where we use the NICER and HXMT data to constrain the broadband shape of the continuum.

3.2.2. An improved physical model for a simultaneous fit

We started the joint fitting with the NICER and HXMT data to construct an improved physical model for the soft state before 2018 and the dimming phase after 2018 of GRS 1915+105. The energy coverage is broader when both instruments are used, and some key parameters such as the photon index Γ and the intensity of the reflection component can be better constrained by the joint modeling.

Based on the results provided by our preliminary fitting in Sect. 3.2.1, we used the Comptonization continuum multiplied by the neutral absorption model `TBabs`. We considered an additional Si absorption edge and a nonrelativistic reflection component as our initial improvement. We chose `xillverCp` to characterize this distant reflector (García et al. 2013).

With the distant reflector, we still had to consider the effect of the accretion disk. We used the fully relativistic reflection model `relxillCp` (from the `relxill` v2.3 package) to model the reflection produced on the accretion disk (García et al. 2014; Dauser et al. 2014). The indices of the emissivity profile $q_{\rm in}$ and $q_{\rm out}$ were fixed at 3, assuming a flat spacetime. The BH spin a_* was fixed at 0.98 (Miller et al. 2013; Reid et al. 2014) and the inclination angle was fixed at 60° (Reid et al. 2014; Fender et al. 1999). We froze $R_{\rm in}$ at the innermost stable circular orbit (ISCO). The outer radius of the disk was fixed at 400 $r_{\rm g}$, which can be considered sufficiently large. The indices of the power law Γ and the temperatures of the electrons $kT_{\rm e}$ in `relxillCp` and `xillverCp` were linked together with the parameters in the `Nthcomp` model because we assumed that the incident spectrum for the two reflectors is the same. The elemental abundance of the iron $A_{\rm Fe}$ in the two reflection models were tied, and we first allowed it to vary between 0.5 and 2 in units of solar abundance. The ionization degrees $\log\xi$ and the electron densities $\log N$ in `relxillCp` and `xillverCp` were left free because we cannot assume the properties of the reflectors at this stage. We set `refl_frac = -1` in the two reflection models, so that only the reflection fraction of the `relxillCp` and `xillverCp` was taken into account. Since both `relxillCp` and `xillverCp` were calculated with the inner temperature of the seed photons produced by the disk fixed at 0.01 keV, we used a multiplicative table model `nthratio`[2] to correct their slope in the low-energy band.

We selected the table model `zxipcf` to characterize the ionization absorption lines, and it provided a rough estimate of the ionization degree (Reeves et al. 2008). We note that `zxipcf` was calculated based on `XSTAR` (Kallman et al. 2004), whose elemental abundances were given by Grevesse et al. (1996) and are different from Wilms et al. (2000). In addition, the absorption features were calculated with a given ionization degree $\log\xi$ with the assumption that the source has an initial power-law spectrum of $\Gamma = 2$. This means that when the spectrum strongly deviates from a $\Gamma = 2$ power law, the estimated ionization parameter is unreliable, especially when the ionization parameter is required for further physical calculations. Nevertheless, considering all these caveats, this model was still our best choice because it is fast and universal for absorption from cold to hot plasma. We fixed the covering fraction of `zxipcf` at one and froze the redshift factor at zero, as the wind velocity cannot be constrained well due to the gain calibration of NICER.

In `Xspec` parlance, the full model we used in the following spectral analysis can be written as

$$\texttt{TBabs} \times \texttt{edge} \times \texttt{zxipcf} \times (\texttt{Nthcomp} + \texttt{diskbb} + \texttt{nthratio} \times (\texttt{relxillCp} + \texttt{xillverCp})). \quad (1)$$

We note that the spectra show no strong ionized absorption features in 2018 when the source was in the decay phase. Therefore, we omitted the `zxipcf` component in Eq. (1).

The NICER-only observations were previously analyzed by Koljonen & Hovatta (2021). Our model was developed using the HMXT data to constrain the continuum above 10 keV, and while it is similar to the one employed in Koljonen & Hovatta (2021), it shows several differences. First, we opted for `TBabs` combined with an additional Si edge to minimize the impact of the absorption model on the slope of the continuum. We incorporated emission lines from various elements using `xillverCp` and accounted for the absorption lines with `zxipcf` to accurately

[2] https://github.com/garciafederico/nthratio

estimate the ionization degree and the flux ratios of the different spectral components. Finally, we employed `nthratio` to adjust the slopes of the reflection components to ensure consistency with the incident spectrum.

We show examples of the joint results that fit this optimized modeling in panels d and e in Fig. 5. We obtained better fit statistics than with the preliminary model, and almost all features in the residuals vanished. The fits show that the iron abundance A_{Fe} and the electron density $\log N$ in `xillverCp` cannot be constrained in most of our observations, and we therefore later fixed A_{Fe} to the solar value and set $\log N$ to 15. The ionization degree of `xillverCp` was also fixed at the lowest value ($\log \xi = 0$) as a cold distant reflector was assumed.

3.2.3. NICER-only modeling

The joint fit shows that the obtained temperature of the electrons kT_e reaches the upper limit of the allowed range (150 keV) in the decay phase. While in the soft state, the kT_e cannot be constrained even when the HXMT data are included. We let the electron temperature free when we fit the data before 2018. As mentioned before, we omitted the ionized absorption `zxipcf` for the observations from MJD 58200 to MJD 58500. Therefore, we only considered the ionized absorption for the observations in the soft state (before 2018) and at the end of the decay phase (after 2019). The thermal emission from the disk, the `diskbb` component, was omitted during the decay phase because the spectral fits suggested that the thermal emission was not necessary.

For most of our observations, no simultaneous NICER and HXMT data are available. We based the fits of the NICER-only data on the model developed above for the broader NICER + HXMT energy range with the following adaptations: We fixed the kT_e at 150 keV in the hard decay phase, but we let it free in the soft state. The iron abundance A_{Fe} and the electron density $\log N$ of the distant reflector were fixed at the solar value and 15, respectively. The ionization degree $\log \xi$ of `xillverCp` was fixed at zero. The results of our fitting based on the NICER data are reported in Fig. 7.

4. Results

4.1. Before 2018

GRS 1915+105 was in the soft state, where thermal emission dominated the spectrum. The column densities N_H of the absorption caused by the ISM is steadily measured at $(5.7 \pm 0.1) \times 10^{22}\,\mathrm{cm^{-2}}$. The Comptonization exhibits photon indices approaching the upper limit of our model ($\Gamma \simeq 3.4$), and the inner temperatures T_{in} of the accretion disk are approximately 1 keV, which is higher than those during the decay phase (see panels a, c, and d of Fig. 7). The electron temperatures kT_e are poorly constrained in the soft state, with a lower limit established at 5 keV. The accretion disk is highly ionized, and the ionization degree $\log \xi$ is always greater than 3.

Our estimated T_{in}, which is $\simeq$1 keV, is lower than previous studies (e.g., Neilsen et al. 2018 obtained a T_{in} of 1.65–2.15 keV based on the same NICER data). The reason likely is the lower estimate of the column density of the ISM absorption with our modeling.

The ionized absorption feature is detected in all the NICER observations before 2018. The material is highly ionized with an ionization degree ($\log \xi$) greater than 4. The dips produced by the ionized absorption shown in the spectra are mostly the Fe XXVI Lyα line at 7 keV (see panel a of Fig. 5). The column densities of the absorption are poorly constrained as the winds are highly ionized.

We used the formula $R_{launch} \leq \sqrt{L/(N_e \cdot \xi)}$ to estimate the upper limit of the launching radius of the winds, where L is the unabsorbed luminosity of the source (Tarter et al. 1969). The unabsorbed luminosity of the source continued at $\sim(18 \pm 8)\%\,L_{Edd}$ in the soft state before 2018. The electron number density N_e of the winds is typically quoted as $10^{14}\,\mathrm{cm^{-3}}$ (following the method described in Sect. 4 of Neilsen et al. 2020). The estimated launching radius with the fixed electron density is 10^3–$10^4\,r_g$ and shows a significant negative correlation with the ionization degree. The results are shown in Fig. 8. No strong correlation between R_{launch} and the disk inner temperature T_{in} is observed.

4.2. During the decay phase

With the modeling described in Sect. 3.2, we obtained results from the spectral analysis by focusing on the exponential and linear decay phase. The behaviors of the source can be traced via the evolution of the key parameters.

4.2.1. The QPO-Γ correlation

We have illustrated the correlation between QPO-Γ and a preliminary model in Fig. 6. In the same figure, we also presented their correlation with the improved physical model (Eq. 1) shown in black. The uncertainties of the newly estimated Γ are larger as the model becomes more complex and has more degrees of freedom. We note that the new Γ values are consistently higher than those measured with the preliminary model because the prominent iron-line feature is absorbed in a continuum produced by the reflection process of an incident Comptonization spectrum, which causes the slope of the primary emission to become steeper. The quasi-linear correlation between the main frequency of the QPOs and the photon index is still maintained.

The evolution of the LFQPO central frequencies in Fig. 4 suggests that GRS 1915+105 begins in an intermediate state, transitions to a harder state after MJD 58200, and returns to a hard-intermediate state at the end of the decay phase. The photon index Γ of the Comptonization is mostly consistent with such a canonical state transition behavior. Although the strongly ionized winds are detected at the end of the decay phase, the photon index values increase simultaneously with the frequencies of the QPOs. This phenomenon indicates that the corona behaves independently from the ionized disk winds. Instead, the QPO frequencies are strongly related to the corona.

The general quasi-linear correlation between the main QPO frequency and the photon index Γ of the power-law component is commonly seen in most BHBs, for instance, Cyg X-1, GX 339−4, and 4U 1630−47 (see e.g., Tomsick & Kaaret 2000; Zdziarski et al. 2004; Motta et al. 2011; Böck et al. 2011; Grinberg et al. 2014; Zhou et al. 2022). Although theories have been proposed to physically explain the origin of QPOs, for example, the Lense-Thirring precession (Bardeen & Petterson 1975; Ingram et al. 2009; Ingram & Done 2011) or the accretion-ejection instability (Tagger & Pellat 1999), many of which assumed a truncated disk with hot flows inside, we cannot verify these theories by our results owing to the fixed inner radius of the accretion disk at ISCO in our model.

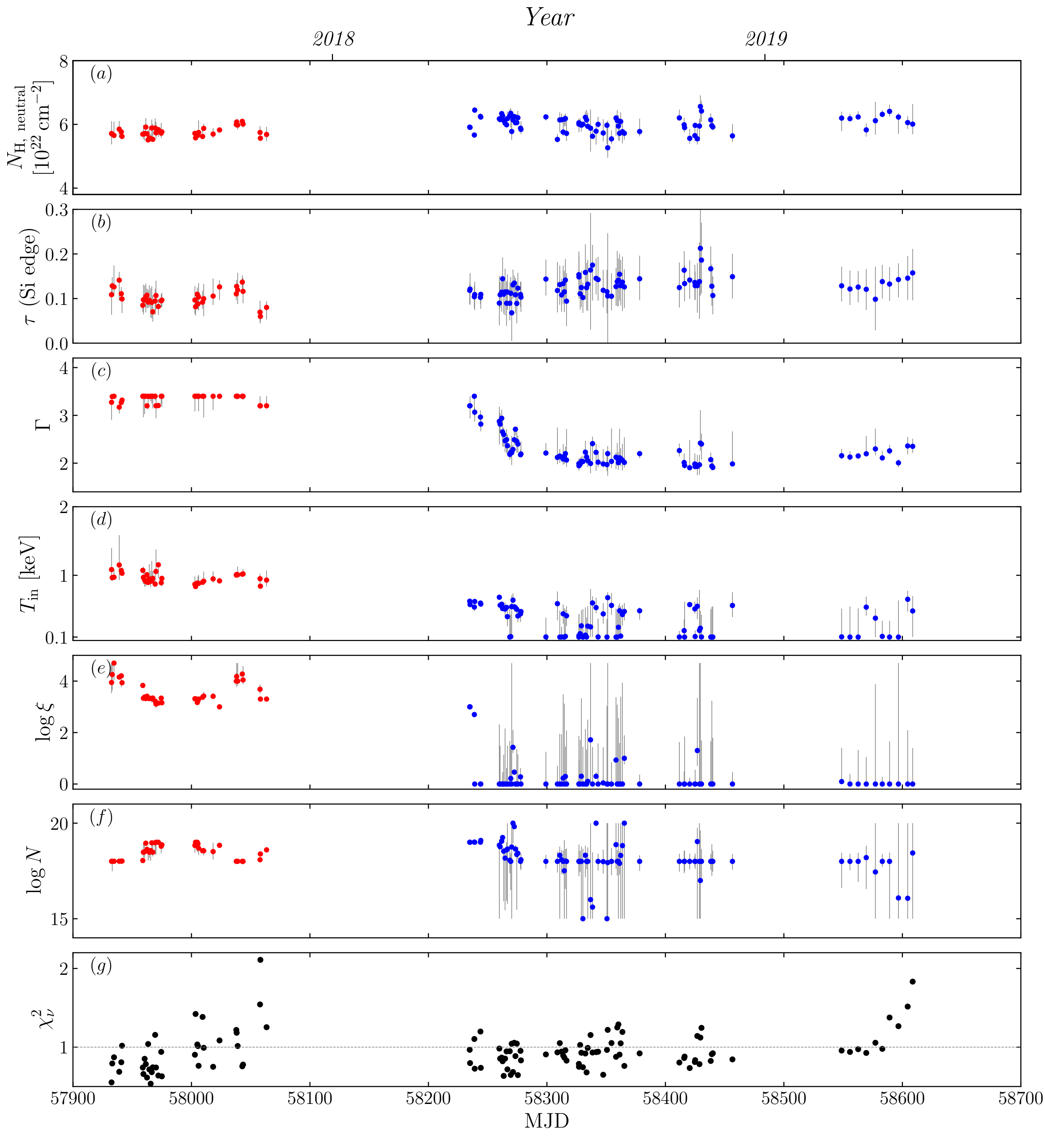

Fig. 7. Evolution of the key parameters measured via the spectral analysis as a function of time. The panels show (from a to g) the equivalent hydrogen column N_{H} of the neutral absorption, the optical depth τ of the additional silicon edge, the photon index Γ, the temperature at the inner edge of the disk T_{in}, the ionization degree $\log\xi$ of the accretion disk, the logarithmic number density of electrons of the accretion disk $\log N$, and the reduced chi-squares χ^2_ν of the best-fits. The red and blue dots denote parameters obtained in the soft state and hard decay phase, respectively.

4.2.2. The ionization degree and the electron density of the accretion disk

Generally speaking, the influence of the ionization degree acting on the spectrum is complex. Different types of ions can produce large numbers of emission lines depending on the abundance of ions. These emission lines are broadened by the general relativistic effects, and the reflection spectrum is partly smoothed in the soft X-ray band. However, the iron emission lines at 6−7 keV are usually not strongly affected by other emission lines because iron is more abundant than other heavier elements. The ionization degree can be precisely measured with a

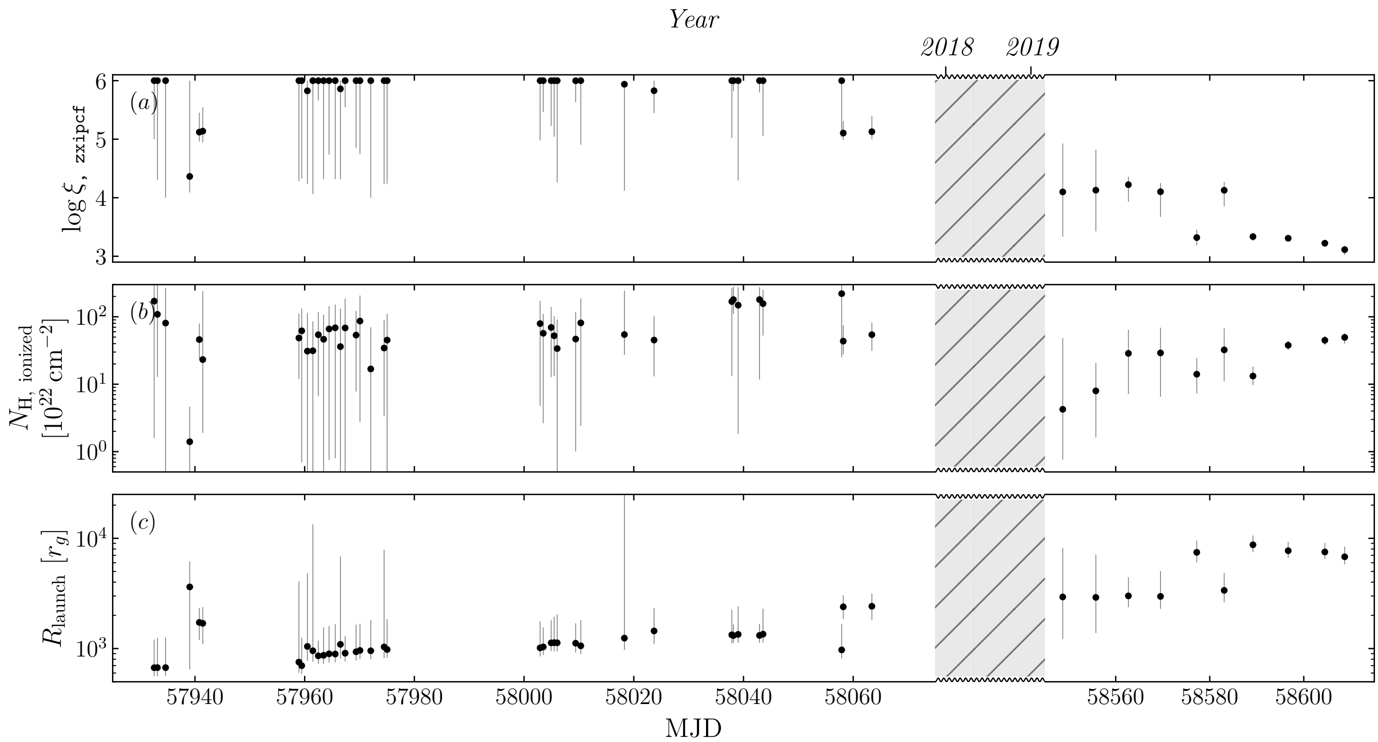

Fig. 8. Evolution of the ionized wind absorption feature in the soft state and near the end of the decay phase. We omit the period from MJD 58075 to 58545 as there is no strong evidence of an ionized absorption within this period. Panel a: Ionization degree of the ionized absorption. Panel b: Column density of the ionized absorption. Panel c: Inferred launching radius of the ionized winds vs. time given a typical number density of the winds of 10^{14} cm^{-3}.

clear cutoff energy of the iron-line shape and a fixed inclination angle.

At the beginning of the decay phase, the ionization degree ($\log \xi$) is in the range of 2.7–3.0, close to the values we observed in the soft state. However, shortly after the start of the decay phase (since MJD 58238), two branches of potential solutions with distinct ionization degrees and comparable statistical significance based on the spectral analysis develop. One example is shown in Fig. 9. One possible solution branch has very low ionization degrees ($\log \xi \leq 2$), with the relative intensities of the relativistic reflection component divided by those of the primary emission from the corona being higher. The other branch typically exhibits a high ionization degree ($3 \leq \log \xi \leq 4$), but the fluxes from the primary emission tend to vanish in most of the spectra, causing the reflection fraction to approach an extremely high value, significantly greater than 10. Neither branch is universally superior to the other in a statistical sense. The strong degeneracy between the ionization degree and the relative intensity of spectral components arises from the asymptotic convergence between the reflection spectrum and the incident spectrum at high ionization degrees, where the material becomes transparent to X-ray photons. Statistically, both branches should be retained. However, the strong LFQPO features observed in the time domain indicate that the primary emission from the corona should not be too weak. Therefore, we decided to discard the branch of solutions with vanishing primary emission.

Since MJD 58238, the ionization degree ($\log \xi$) of the relativistic reflection component is constrained at low values for the majority of the observations (see panel e in Fig. 7), suggesting that the iron line is more likely located at 6.4 keV in the rest frame of the accretion disk (the iron ions are in the form of Fe I–Fe XVII; see House 1969). This result differs from the estimation

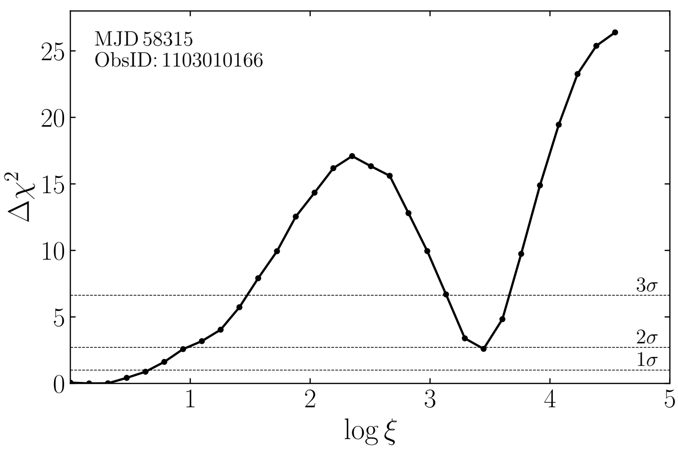

Fig. 9. $\Delta\chi^2$ fitting statistics of an example spectrum in the decay phase, plotted vs. different values of the ionization degree $\log \xi$ of the relativistic reflection component `relxillCp`. The sample points are shown as black dots and are connected by solid lines. There are two local minima in this plot, with distinct ionization degrees. We discarded the solution with higher $\log \xi$ because it resulted in a vanishing primary emission originating from the corona.

in Koljonen & Hovatta (2021), who obtained relatively high ionization degrees ($\log \xi \geq 3.5$).

The logarithmic electron densities $\log N$ of the accretion disk cannot be well constrained for most of the observations during the decay phase. We obtained a mean value of $\log N \simeq 18$ from the best fits (see panel f of Fig. 7).

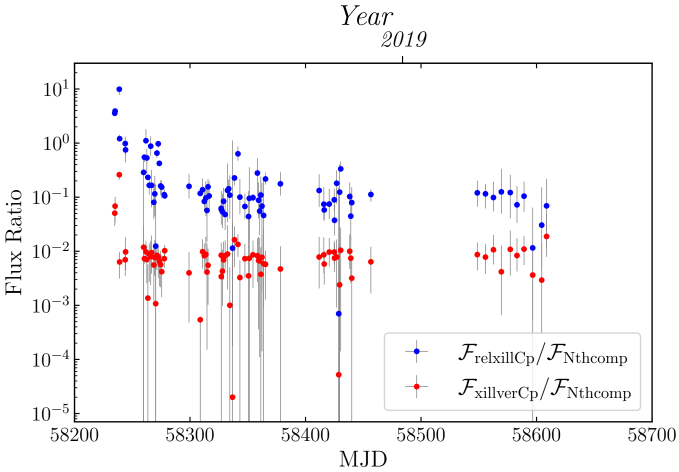

Fig. 10. Evolution of the ratio of the unabsorbed flux of the incident Comptonization spectra and that of the relativistic and distant reflection components vs. time. The fluxes of `relxillCp`, which models the relativistic reflector, and those of `xillverCp`, which models the distant reflector, were corrected by the multiplicative model `nthratio` (see Sect. 3.2.2). $\mathcal{F}_{\rm relxillCp}/\mathcal{F}_{\rm Nthcomp}$ indicates the geometrical information of the accreting system.

4.2.3. The intensity of the reflection components

Assuming that the emission from the corona is dominant and discarding the branch of solutions with higher $\log\xi$ values, we computed the intensity of each spectral component in our modeling in Eq. (1). The flux ratios of the (non-)relativistic reflection components and the incident primary emission with its 1σ uncertainties were computed, and the results are shown in Fig. 10.

We first find that the flux ratio $\mathcal{F}_{\rm xillverCp}/\mathcal{F}_{\rm Nthcomp}$ drops rapidly within the first ten days of the decay phase (MJD 58234–58244) and then steadily remains weaker by two orders of magnitude than the primary emission for the remaining time. When we assume that the distant reflector remains stable over a ten-day period, the sudden drop in the flux ratio $\mathcal{F}_{\rm xillverCp}/\mathcal{F}_{\rm Nthcomp}$ is likely due to the self-obscuration of the source, that is, the radiation from the accretion center was impeded by the thickness of the inner accretion disk. In contrast, the flux ratio $\mathcal{F}_{\rm relxillCp}/\mathcal{F}_{\rm Nthcomp}$ continues to decrease after the self-obscuration period, and this decline lasted until MJD 58280 and finally reached approximately one-tenth of the primary emission. It maintained this relative strength until the end of the decay phase.

4.2.4. The ionized absorption near the end of the decay phase (MJD 58548–58608)

The emission generated by GRS 1915+105 underwent a warmly ionized wind absorption near the end of the linear decay (Miller et al. 2020; Koljonen & Hovatta 2021). With the quasi-weekly NICER observations between MJD 58548 and MJD 58608, we measured the column densities and the ionization degrees of the wind absorption. The results with their 2σ uncertainties are presented in the right part of Fig. 8.

We observe a gradually strengthening absorption column with a slowly decreasing ionization degree $\log\xi$ from ~4 to 3 within 60 days. In the last few observations, the complex features between 6.4 keV and 6.7 keV produced by the warm ionized absorber are detected. Highly ionized winds are usually observed in the soft state without QPO features in the time domain (Ponti et al. 2012). However, GRS 1915+105 exhibited strong evidence of a hard-intermediate state at the end of the decay phase, with intermediate Γ values ($2.0 \le \Gamma \le 2.4$) and clear type-C QPO signals.

Similar to Sect. 4.1, the launching radius of the wind was calculated with a fixed electron density of 10^{14} cm^{-3}. We thus observe a slightly increasing launching radius with relatively large uncertainties during the end of the decay phase (see panel c of Fig. 8) with this fixed electron density. However, we note that the number density of the wind is highly dependent on the radius and polar angle of the disk (Fukumura et al. 2017). Thus, the estimation of the launching radius of the wind here is a qualitative response to the ionization degree, as the unabsorbed luminosity of the source maintains ~2% $L_{\rm Edd}$ during the end of the decay phase.

We note that although the model `zxipcf` characterizing the ionized absorption was computed with an incident power-law spectrum of $\Gamma = 2$, which may cause a deviation when estimating the ionization degree as the incident spectrum is not a pure power-law with $\Gamma = 2$, the estimated ionization degree $\log\xi$ is not expected to deviate much from the physical value in our study. The uncertainties of $\log\xi$ absorb the systematic errors made by the incident spectrum due to the highly ionized plasma outflowing in the soft state, and the Γ values do not strongly deviate from 2 at the end of the decay phase.

5. Discussion

5.1. A rarely seen warm ionized wind in the hard-intermediate state

Since the discovery of the disk winds, the majority of the confirmed ionized wind cases detected in the iron band were found in the soft state of the BHBs and with a high ionization degree ($\log\xi \ge 4$) (see e.g., Miller et al. 2006a,b; Kubota et al. 2007; Neilsen & Lee 2009; Ponti et al. 2012). Although there are several reports on the ionized absorption observed in the hard or hard-intermediate state, some of the detections depend on the choice of the reflection models (Xu et al. 2018; Wang et al. 2021). Lee et al. (2002) reported a highly ionized wind ($\log\xi \simeq 4.15$) in GRS 1915+105 when the source was in the hard χ state, but the unabsorbed luminosity of the source reached ~40% $L_{\rm Edd}$ at that time. It is natural to produce a highly ionized wind with such a high luminosity. Shidatsu et al. (2013) detected a warmly ionized wind in the hard state of MAXI J1305−704, with an ionization degree of $\log\xi \sim 2$.

The behaviors of the absorber are dependent on the assumptions. With a variable electron density by assuming that the thickness of the wind ΔR is comparable to the launching radius $R_{\rm launch}$, the electron density $N_{\rm e}$ can be estimated by $N_{\rm e} = N_{\rm H}/\Delta R \sim N_{\rm H}/R_{\rm launch}$. Therefore, $R_{\rm launch} \sim L/(N_{\rm H}\cdot\xi)$. The mean value of the estimated $N_{\rm e}$ at the end of the decay is about 10^{13} cm^{-3}, which does not result in a change in $R_{\rm launch}$ by more than one order of magnitude. With a constant $N_{\rm e}$ of 10^{14} cm^{-3}, the estimated $R_{\rm launch}$ of the absorber instead shows a potentially extremely slow outward movement with an upper-limit speed of $\dot{R}_{\rm launch} \simeq 0.02$ km s^{-1}. Compared with the velocity of the wind itself ($v \ge 10^2$ km s^{-1}; see Miller et al. 2020), the motion of the launching radius is negligible.

The estimated launching radii of the winds in GRS 1915+105 during the soft state before 2018 and at the end of the decay phase in 2019 are both in the range of 10^3–10^4 $r_{\rm g}$, which suggests that the launching mechanism of the outflow likely was the same. Although the obscuration of this source after May 2019 was attributed to local absorption (Neilsen et al. 2020; Balakrishnan et al. 2021), the cause of the decay before the obscuration is different. The neutral absorption $N_{\rm H,\,neutral}$ maintains $6 \times 10^{22}\,{\rm cm}^{-2}$ throughout the decay and shows no significant enhancement until the onset of the obscured state. The cold matter seen in the obscured state likely originates from the outflow that formed near the end of the decay.

5.2. The interaction between the corona and the accretion disk

In Sect. 4.2.3 we presented the intensity analysis of the primary emission and the (non-)relativistic reflection components (see Fig. 10). The ratio $\mathcal{F}_{\rm relxillCp}/\mathcal{F}_{\rm Nthcomp}$ and $\mathcal{F}_{\rm xillverCp}/\mathcal{F}_{\rm Nthcomp}$ may unveil the geometrical information of the accreting system.

$\mathcal{F}_{\rm relxillCp}/\mathcal{F}_{\rm Nthcomp}$ and $\mathcal{F}_{\rm xillverCp}/\mathcal{F}_{\rm Nthcomp}$ dropped to one-tenth of their original values during the first 10 days of the decay phase (MJD 58234–58244). These drastic decreases were likely produced by the fading of the self-obscuration of the accreting system. $\mathcal{F}_{\rm xillverCp}/\mathcal{F}_{\rm Nthcomp}$ remained at 10^{-2} after the 10-day period, but $\mathcal{F}_{\rm relxillCp}/\mathcal{F}_{\rm Nthcomp}$ continued to decrease from 10^{0} to 10^{-1} in the following 30 days (MJD 58245–58275). The decrease observed solely in $\mathcal{F}_{\rm relxillCp}/\mathcal{F}_{\rm Nthcomp}$ was likely associated with the geometrical changes in the accreting system during an intermediate-to-hard transition.

The reflection component in BHBs becomes stronger in general when the spectrum is softer because the Comptonization in soft states is weaker (Steiner et al. 2016). Therefore, the ratio $\mathcal{F}_{\rm relxillCp}/\mathcal{F}_{\rm Nthcomp}$ is assumed to become smaller in the intermediate-to-hard transition and vice versa. Although the states exhibited by GRS 1915+105 are generally not strictly the canonical hard or soft states during an outburst, it can still undergo transitions that are considered part of the canonical state evolution due to the long-term instability of the corona. Similar incomplete transitions have also been found in other persistent sources, for example, in Cyg X-1 (Zhou et al. 2022). The reduced flux ratio at the beginning of the decay phase aligns with this expectation. We expect to observe an increase in this ratio at the end of the decay phase if the latter transition is normal because the photon indices Γ and the frequencies of the QPO increase then. However, the flux ratio remained low and even exhibited a decreasing trend until the end of the decay phase, which suggests that the transition near the end of the decay phase is different from a normal softening state transition.

In the context of the lamp-post model, in which the corona is simplified as a point-like source above the disk, the two ratios can easily be interpreted as signals of the distances between the corona and two different reflectors. An increasing ratio means a closer distance, and vice versa. The evolution of $\mathcal{F}_{\rm relxillCp}/\mathcal{F}_{\rm Nthcomp}$ suggests that the corona consistently recedes from the accretion disk in this scenario. However, recent polarization results indicate that the primary photon emitter could be parallel to the accretion disk rather than a source perpendicular to the accretion disk (Krawczynski et al. 2022; Veledina et al. 2023; however, see e.g., Dexter & Begelman 2024 for a different interpretation). In this scenario, the ratio $\mathcal{F}_{\rm relxillCp}/\mathcal{F}_{\rm Nthcomp}$ works as an indicator of the strength of the interaction between the corona and the standard accretion disk. In the normal hard state, the optical depth of the corona is higher, which causes more photons to be scattered and dilutes the initial relativistic effects of the disk photons (Petrucci et al. 2001). In contrast, the source exhibits a weak interaction at the end of the decay phase. This odd phenomenon might be attributed to the changed geometry of the accretion system, for instance, a relatively shrinking standard disk due to the lack of infalling material. Returning radiation can also play an important role in producing reflection components (Mirzaev et al. 2024). The photons emitted from the inner part of the disk have a higher probability of arriving at the surface of the accretion disk and re-irradiating the disk again (Dauser et al. 2022). An increasing inner radius of the disk during this period can weaken the irradiation from the returning radiation and thus reduce the flux of the relativistic reflection component.

5.3. The interplay between the disk winds and the corona during and after the decay

The physical mechanisms in the accretion process of BHBs are still debated, but we benefit from observational evidence to gradually disentangle the puzzle of accretion. The jets and disk winds usually exhibit mutually exclusive interplay within a normal outburst (Neilsen & Lee 2009; Ponti et al. 2012), although exceptions exist (Miller et al. 2006b; Kalemci et al. 2016; Homan et al. 2016; Motta et al. 2021). The behaviors of the jet are considered to be closely related to the corona (see e.g., Markoff et al. 2005).

In GRS 1915+105, we have confirmed that the source underwent a partially hardening-to-softening transition during the decay phase, where the ionized wind absorption features merely appeared near the end of the decay. Type-C QPOs were detected throughout the decay phase, and their frequencies were strongly correlated to the photon indices of the Comptonization component. The spectral-timing behaviors of the corona seem to be independent from the emergence of the ionized disk outflow.

When we assume that the disk winds that were observed in the soft state and the hard decay phase share the same launching mechanism, irreconcilable contradictions will arise when the appearance of the disk wind is forcibly linked with the vanishing of the jet or the softening of the spectrum. The radio emission and the disk wind clearly coexist at the end of the decay phase (Motta et al. 2021). It is not very feasible either to connect the appearance of disk winds with the movement of $r_{\rm in}$, the inner radius of the disk, as $r_{\rm in}$ approaches the ISCO in the soft state but increases in the scenario of returning radiation. However, considering that the launching position of the wind is far from the binary center, we suggest a potential hysteretic interaction between the corona and the periphery of the accretion disk. Typically, suppressed jets release less energy into the environment, and more energy is directed toward Compton heating, which accelerates the winds (Narayan & Yi 1995; Merloni & Fabian 2002). These winds carry angular momentum away, which slows the mass inflow down and promotes faster thermal equilibrium in the inner regions of the accretion disk (Blandford & Begelman 1999). However, during the decay phase of GRS 1915+105, winds driven by a relatively low luminosity would further decelerate the infalling matter, which would lead to a more rapid fading of the accretion system and eventually to the emergence of the obscured state.

Neilsen et al. (2020) reported a fast flare observed in the obscured state of GRS 1915+105. Fe XXVI Lyα and Fe XXV Heα lines were detected in emission before the flare and in absorption when the count rate increased, indicating that the highly ionized outflow always existed during the focused observation: Absorption lines are visible when a strong central source back-lights the medium, and emission lines emerge when the central source becomes faint. In periods with a lower count rate, three prominent emission lines (quasi-neutral Fe Kα line at 6.4 keV, Fe XXV Heα line at 6.7 keV, and Fe XXVI Lyα at 7 keV) were observed

(Miller et al. 2020; Koljonen & Hovatta 2021) in the Fe band. The origins of the three lines are different, as the quasi-neutral Fe lines come from the cooling area of the accretion disk and the ionized Fe lines come from the highly ionized plasma that flows out of the disk. The emergence of three Fe emission lines is not unique to GRS 1915+105 and was found in other systems such as V404 Cygni (King et al. 2015) and V4641 Sgr (Shaw et al. 2022), which are well-known for their high inclination and variable local obscuration (Koljonen & Tomsick 2020).

6. Conclusions

We have conducted a spectral-timing analysis of GRS 1915+105, for which we used all available NICER and Insight-HXMT data before MJD 58617, when the source entered the obscured state. In particular, we used simultaneous NICER and HXMT data to develop a model that described the broadband spectrum of the source, and we used this model with the higher-cadence NICER data to trace the evolution of the source.

In the disk-dominated state before 2018, we consistently observed a highly ionized wind with the detection of the Fe XXVI Lyα line at 7 keV. The photon index approached the upper limit of our model ($\Gamma \simeq 3.4$), and the intensity of the thermal radiation dominated the spectrum.

During the decay phase, which corresponds to a spectral transition from a partially hardening process to an unusual obscuring process, we found a quasi-linear correlation between the photon index Γ and the frequency of the main QPO with an empirical model and an improved physical model. At the end of the decay phase, the spectrum showed strong absorption features with a decreasing ionization degree when the source was in the hard-intermediate state, with clear type-C QPO features. The estimated launching radius of this warmly ionized outflow appears to be on the same order of magnitude as that in the soft state. This indicates that the launching mechanism of the winds is likely the same in the soft and hard states near the end of the decay.

At the beginning of the decay phase, the relative intensity of the relativistic and nonrelativistic reflection components was strong, but it weakened by a factor of 10 within 10 days, possibly due to the vanishing self-obscuration in the accreting system. The relativistic reflection component continued to weaken over the next 30 days, while the nonrelativistic reflection component remained steady. The two reflection components maintained their relative strengths in the middle of the decay phase. However, the relativistic component even showed a potentially decreasing trend as warmly ionized winds appeared near the end of the decay. This discrepancy corresponds to an unusual softening process that either indicates an increasing distance between the disk and the corona (in the context of the lamp-post model) or a rising inner radius of the disk (in the context of returning radiation). The QPO frequencies and photon index are strongly interdependent, and the launch of ionized winds further slowed the accreting of the infalling matter down.

Acknowledgements. M. Z. would like to thank the support from the China Scholarship Council (CSC 202006100027). This research has made use of NASA's Astrophysics Data System Bibliographic Services. This research also made use of ISIS functions (isisscripts http://www.sternwarte.uni-erlangen.de/isis/) provided by ECAP/Remeis observatory and MIT. This work made use of data from the Insight–HXMT mission, a project funded by the China National Space Administration (CNSA) and the Chinese Academy of Sciences (CAS). L. D. Kong is grateful for the financial support provided by the Sino-German (CSC-DAAD) Postdoc Scholarship Program (57607866).

References

Arnaud, K. A. 1996, ASP Conf. Ser., 101, 17
Athulya, M. P., Radhika, D., Agrawal, V. K., et al. 2022, MNRAS, 510, 3019
Bachetti, M., Huppenkothen, D., Khan, U., et al. 2021, https://doi.org/10.5281/zenodo.4881255
Balakrishnan, M., Miller, J. M., Reynolds, M. T., et al. 2021, ApJ, 909, 41
Bardeen, J. M., & Petterson, J. A. 1975, ApJ, 195, L65
Begelman, M. C., McKee, C. F., & Shields, G. A. 1983, ApJ, 271, 70
Belloni, T., Klein-Wolt, M., Méndez, M., van der Klis, M., & van Paradijs, J. 2000, A&A, 355, 271
Blandford, R. D., & Begelman, M. C. 1999, MNRAS, 303, L1
Böck, M., Grinberg, V., Pottschmidt, K., et al. 2011, A&A, 533, A8
Bogdanov, S., Guillot, S., Ray, P. S., et al. 2019, ApJ, 887, L25
Cao, X., Jiang, W., Meng, B., et al. 2020, Sci. China Phys. Mech. Astron., 63, 249504
Castro-Tirado, A. J., Brandt, S., & Lund, N. 1992, IAU Circ., 5590, 2
Castro-Tirado, A. J., Brandt, S., Lund, N., et al. 1994, ApJS, 92, 469
Chen, Y., Cui, W., Li, W., et al. 2020, Sci. China Phys. Mech. Astron., 63, 249505
Dauser, T., Garcia, J., Parker, M. L., Fabian, A. C., & Wilms, J. 2014, MNRAS, 444, L100
Dauser, T., García, J. A., Joyce, A., et al. 2022, MNRAS, 514, 3965
Dexter, J., & Begelman, M. C. 2024, MNRAS, 528, L157
Done, C., Tomaru, R., & Takahashi, T. 2018, MNRAS, 473, 838
Fender, R. P., Garrington, S. T., McKay, D. J., et al. 1999, MNRAS, 304, 865
Fender, R. P., Stirling, A. M., Spencer, R. E., et al. 2006, MNRAS, 369, 603
Fukumura, K., Kazanas, D., Shrader, C., et al. 2017, Nat. Astron., 1, 0062
García, J., Dauser, T., Reynolds, C. S., et al. 2013, ApJ, 768, 146
García, J., Dauser, T., Lohfink, A., et al. 2014, ApJ, 782, 76
Gendreau, K. C., Arzoumanian, Z., Adkins, P. W., et al. 2016, SPIE Conf. Ser., 9905, 99051H
Grevesse, N., Noels, A., Sauval, A., Holt, S., & Sonneborn, G. 1996, ASP Conf. Ser., 99, 117
Grinberg, V., Pottschmidt, K., Böck, M., et al. 2014, A&A, 565, A1
Guo, C.-C., Liao, J.-Y., Zhang, S., et al. 2020, J. High Energy Astrophys., 27, 44
Hannikainen, D. C., Rodriguez, J., Vilhu, O., et al. 2005, A&A, 435, 995
Higginbottom, N., & Proga, D. 2015, ApJ, 807, 107
Homan, J., Wijnands, R., van der Klis, M., et al. 2001, ApJS, 132, 377
Homan, J., Neilsen, J., Allen, J. L., et al. 2016, ApJ, 830, L5
Homan, J., Neilsen, J., Steiner, J., et al. 2019, ATel, 12742, 1
Houck, J. C., & Denicola, L. A. 2000, ASP Conf. Ser., 216, 591
House, L. L. 1969, ApJS, 18, 21
Huppenkothen, D., Bachetti, M., Stevens, A., et al. 2019a, J. Open Source Softw., 4, 1393
Huppenkothen, D., Bachetti, M., Stevens, A. L., et al. 2019b, ApJ, 881, 39
Ingram, A., & Done, C. 2011, MNRAS, 415, 2323
Ingram, A., Done, C., & Fragile, P. C. 2009, MNRAS, 397, L101
Kaastra, J. S., & Bleeker, J. A. M. 2016, A&A, 587, A151
Kalemci, E., Begelman, M. C., Maccarone, T. J., et al. 2016, MNRAS, 463, 615
Kallman, T. R., Palmeri, P., Bautista, M. A., Mendoza, C., & Krolik, J. H. 2004, ApJS, 155, 675
King, A. L., Miller, J. M., Raymond, J., Reynolds, M. T., & Morningstar, W. 2015, ApJ, 813, L37
Klein-Wolt, M., Fender, R. P., Pooley, G. G., et al. 2002, MNRAS, 331, 745
Koljonen, K. I. I., & Hovatta, T. 2021, A&A, 647, A173
Koljonen, K. I. I., & Tomsick, J. A. 2020, A&A, 639, A13
Koljonen, K., Vera, R., Lahteenmaki, A., & Tornikoski, M. 2019, ATel, 12839, 1
Kong, L. D., Zhang, S., Chen, Y. P., et al. 2021, ApJ, 906, L2
Kong, L.-D., Ji, L., Santangelo, A., et al. 2024, A&A, 686, A211
Krawczynski, H., Muleri, F., Dovčiak, M., et al. 2022, Science, 378, 650
Kubota, A., Dotani, T., Cottam, J., et al. 2007, PASJ, 59, 185
Lee, J. C., Reynolds, C. S., Remillard, R., et al. 2002, ApJ, 567, 1102
Li, X., Li, X., Tan, Y., et al. 2020, J. High Energy Astrophys., 27, 64
Liao, J.-Y., Zhang, S., Chen, Y., et al. 2020a, J. High Energy Astrophys., 27, 24
Liao, J.-Y., Zhang, S., Lu, X.-F., et al. 2020b, J. High Energy Astrophys., 27, 14
Liu, C., Zhang, Y., Li, X., et al. 2020, Sci. China Phys. Mech. Astron., 63, 249503
Makishima, K., Maejima, Y., Mitsuda, K., et al. 1986, ApJ, 308, 635
Markoff, S., Nowak, M. A., & Wilms, J. 2005, ApJ, 635, 1203
Martocchia, A., Matt, G., Belloni, T., et al. 2006, A&A, 448, 677
Matsuoka, M., Kawasaki, K., Ueno, S., et al. 2009, PASJ, 61, 999
Matt, G., Guainazzi, M., & Maiolino, R. 2003, MNRAS, 342, 422
Merloni, A., & Fabian, A. C. 2002, MNRAS, 332, 165
Miller, J. M., Raymond, J., Fabian, A., et al. 2006a, Nature, 441, 953
Miller, J. M., Raymond, J., Homan, J., et al. 2006b, ApJ, 646, 394
Miller, J. M., Parker, M. L., Fuerst, F., et al. 2013, ApJ, 775, L45
Miller, J. M., Raymond, J., Fabian, A. C., et al. 2016, ApJ, 821, L9
Miller, J. M., Zoghbi, A., Raymond, J., et al. 2020, ApJ, 904, 30
Mirabel, I. F., & Rodríguez, L. F. 1994, Nature, 371, 46

Mirzaev, T., Riaz, S., Abdikamalov, A. B., et al. 2024, ApJ, 965, 66
Mitsuda, K., Inoue, H., Koyama, K., et al. 1984, PASJ, 36, 741
Morgan, E. H., Remillard, R. A., & Greiner, J. 1997, ApJ, 482, 993
Motta, S., Muñoz-Darias, T., Casella, P., Belloni, T., & Homan, J. 2011, MNRAS, 418, 2292
Motta, S. E., Kajava, J. J. E., Sánchez-Fernández, C., et al. 2017a, MNRAS, 471, 1797
Motta, S. E., Kajava, J. J. E., Sánchez-Fernández, C., Giustini, M., & Kuulkers, E. 2017b, MNRAS, 468, 981
Motta, S., Williams, D., Fender, R., et al. 2019, ATel, 12773, 1
Motta, S. E., Kajava, J. J. E., Giustini, M., et al. 2021, MNRAS, 503, 152
Narayan, R., & Yi, I. 1995, ApJ, 444, 231
Negoro, H., Tachibana, Y., Kawai, N., et al. 2018, ATel, 11828, 1
Neilsen, J., & Lee, J. C. 2009, Nature, 458, 481
Neilsen, J., Cackett, E., Remillard, R. A., et al. 2018, ApJ, 860, L19
Neilsen, J., Homan, J., Steiner, J. F., et al. 2020, ApJ, 902, 152
Nowak, M. A. 2000, MNRAS, 318, 361
Petrucci, P. O., Merloni, A., Fabian, A., Haardt, F., & Gallo, E. 2001, MNRAS, 328, 501
Ponti, G., Fender, R. P., Begelman, M. C., et al. 2012, MNRAS, 422, L11
Proga, D., & Kallman, T. R. 2002, ApJ, 565, 455
Reeves, J., Done, C., Pounds, K., et al. 2008, MNRAS, 385, L108
Reid, M. J., McClintock, J. E., Steiner, J. F., et al. 2014, ApJ, 796, 2
Remillard, R. A., & McClintock, J. E. 2006, ARA&A, 44, 49
Remillard, R. A., Morgan, E. H., McClintock, J. E., Bailyn, C. D., & Orosz, J. A. 1999, ApJ, 522, 397
Remillard, R. A., Loewenstein, M., Steiner, J. F., et al. 2022, AJ, 163, 130
Shaw, A. W., Miller, J. M., Grinberg, V., et al. 2022, MNRAS, 516, 124
Shi, Z., Wu, Q., Yan, Z., Lyu, B., & Liu, H. 2023, MNRAS, 525, 1431
Shidatsu, M., Ueda, Y., Nakahira, S., et al. 2013, ApJ, 779, 26
Shreeram, S., & Ingram, A. 2020, MNRAS, 492, 405
Soleri, P., Belloni, T., & Casella, P. 2008, MNRAS, 383, 1089
Steiner, J. F., Remillard, R. A., García, J. A., & McClintock, J. E. 2016, ApJ, 829, L22
Tagger, M., & Pellat, R. 1999, A&A, 349, 1003
Tarter, C. B., Tucker, W. H., & Salpeter, E. E. 1969, ApJ, 156, 943
Tomsick, J. A., & Kaaret, P. 2000, ApJ, 537, 448
Ueda, Y., Yamaoka, K., & Remillard, R. 2009, ApJ, 695, 888
Veledina, A., Muleri, F., Dovčiak, M., et al. 2023, ApJ, 958, L16
Verner, D. A., Ferland, G. J., Korista, K. T., & Yakovlev, D. G. 1996, ApJ, 465, 487
Wang, Y., Ji, L., García, J. A., et al. 2021, ApJ, 906, 11
Williams, D. R. A., Motta, S. E., Fender, R., et al. 2020, MNRAS, 491, L29
Wilms, J., Allen, A., & McCray, R. 2000, ApJ, 542, 914
Woods, D. T., Klein, R. I., Castor, J. I., McKee, C. F., & Bell, J. B. 1996, ApJ, 461, 767
Xu, Y., Harrison, F. A., Kennea, J. A., et al. 2018, ApJ, 865, 18
Zdziarski, A. A., Johnson, W. N., & Magdziarz, P. 1996, MNRAS, 283, 193
Zdziarski, A. A., Gierliński, M., Mikołajewska, J., et al. 2004, MNRAS, 351, 791
Zhang, W., Jahoda, K., Swank, J. H., Morgan, E. H., & Giles, A. B. 1995, ApJ, 449, 930
Zhang, S., Lu, F. J., Zhang, S. N., & Li, T. P. 2014, SPIE Conf. Ser., 9144, 914421
Zhang, S.-N., Li, T., Lu, F., et al. 2020, Sci. China Phys. Mech. Astron., 63, 249502
Zhou, M., Grinberg, V., Bu, Q. C., et al. 2022, A&A, 666, A172
Zoghbi, A., Miller, J. M., King, A. L., et al. 2016, ApJ, 833, 165
Życki, P. T., Done, C., & Smith, D. A. 1999, MNRAS, 309, 561

C Submitted Article 3 (Accepted)

Astronomy & Astrophysics manuscript no. output
July 29, 2025

Probing the polarized emission from the accretion-powered pulsar 4U 1907+09 with IXPE

Menglei Zhou[1], Lorenzo Ducci[1,2], Honghui Liu[1], Sergey S. Tsygankov[3], Sofia V. Forsblom[3], Alexander A. Mushtukov[4], Valery F. Suleimanov[1], Juri Poutanen[3], Pengju Wang[1], Alessandro Di Marco[5], Victor Doroshenko[1], Fabio La Monaca[5,6], Vladislav Loktev[3,7], Alexander Salganik[3], and Andrea Santangelo[1]

[1] Institut für Astronomie und Astrophysik, Universität Tübingen, Sand 1, D-72076 Tübingen, Germany
e-mail: menglei.zhou@astro.uni-tuebingen.de
[2] ISDC Data Center for Astrophysics, Université de Genève, 16 chemin d'Écogia, 1290 Versoix, Switzerland
[3] Department of Physics and Astronomy, 20014 University of Turku, Finland
[4] Astrophysics, Department of Physics, University of Oxford, Denys Wilkinson Building, Keble Road, Oxford OX1 3RH, UK
[5] INAF Istituto di Astrofisica e Planetologia Spaziali, Via del Fosso del Cavaliere 100, 00133 Roma, Italy
[6] Dipartimento di Fisica, Università degli Studi di Roma "Tor Vergata", Via della Ricerca Scientifica 1, 00133 Roma, Italy
[7] Department of Physics, P.O. Box 64, 00014 University of Helsinki, Finland

– / –

ABSTRACT

We present observations of the accretion-powered X-ray pulsar 4U 1907+09 conducted with the Imaging X-ray Polarimetry Explorer, which has delivered the first high-quality polarization measurements of this source. 4U 1907+09 was observed twice during its brightest periods, close to the periastron. We observe a stronger polarization in the first observation, with a phase-averaged polarization degree (PD) of 6.0 ± 1.6% and a polarization angle (PA) of 69° ± 8°. The second observation provides weaker constraints on the polarimetric properties, PD=2.2 ± 1.6% and PA=46° ± 23°, as determined from the spectro-polarimetric analysis. Combining the data from the two observations results in PD=3.7 ± 1.1% and PA=63° ± 9°. We detect an energy-dependent PA in the phase-averaged analyses with a significance of 1.7 σ. In the phase-resolved analyses, we observe a potential PA rotation of approximately 90° between adjacent energy bands (4–5 and 5–6 keV) within the single phase bin of 0.25–0.375. We also investigate the influence of short flares on the polarization properties of this source. The results suggest that flares do not significantly affect the energy-phase-dependent PA, implying that the pulsar's geometry remains stable during flare events.

Key words. accretion, accretion disks – magnetic fields – polarization – pulsars: individual: 4U 1907+09 – stars: neutron – X-rays: binaries

1. Introduction

High-mass X-ray binaries (HMXBs) comprise a compact object that accretes matter from a massive companion star. In HMXB systems with strongly magnetized neutron stars (NSs), the accretion flow is interrupted by the NS's magnetosphere at a distance of approximately 10^8–10^9 cm (Lamb et al. 1973; Elsner & Lamb 1977). The accreted matter is then channeled along magnetic field lines onto the NS's surface, where its gravitational potential energy is released. Depending on the accretion rate, the accretion process can generate hot spots or extended accretion columns at the magnetic poles. Due to the misalignment between the magnetic poles and the spin axis, the system emits pulsed X-rays, manifesting as an X-ray pulsar (XRP; see, e.g., Mushtukov & Tsygankov 2024 for a recent review). XRPs serve as natural laboratories for studying the extreme conditions where matter, light, and magnetic fields interact in ways unattainable in terrestrial labs.

The phase-dependent characteristics of pulsed X-ray emission in XRPs are determined by the geometry of the emission region, the orientation of the pulsar relative to the observer, and the intricacies of radiative transfer processes in the presence of an intense magnetic field. Despite this understanding, a comprehensive theoretical framework capable of fully describing these properties is lacking. One of the primary challenges is the uncertainty surrounding the fundamental geometric configuration of XRPs.

Polarimetric observations provide a means to address this uncertainty, by enabling the determination of key geometric parameters, such as the inclination of the pulsar's spin axis with respect to the line of sight and the magnetic obliquity. They also offer the potential to distinguish between different emission region geometries.

The NS's extreme magnetic field significantly influences X-ray emission polarization from XRPs by modifying the Compton scattering cross sections. Under favorable orientations, photon scattering in such a highly magnetized plasma is predicted to result in a substantial degree of polarization, reaching up to 80% (Meszaros et al. 1988; Caiazzo & Heyl 2021). As shown by Meszaros et al. (1988), the linear polarization of X-rays is highly sensitive to the geometry of the emission region and exhibits variability with energy and pulse phase. Consequently, phase-resolved polarimetry serves as a critical tool for constraining the system's viewing geometry and for differentiating between competing radiation models.

The Imaging X-ray Polarimetry Explorer (IXPE) is the first mission dedicated to imaging X-ray polarimetry, enabling the detection of linear X-ray polarization in numerous astrophysical

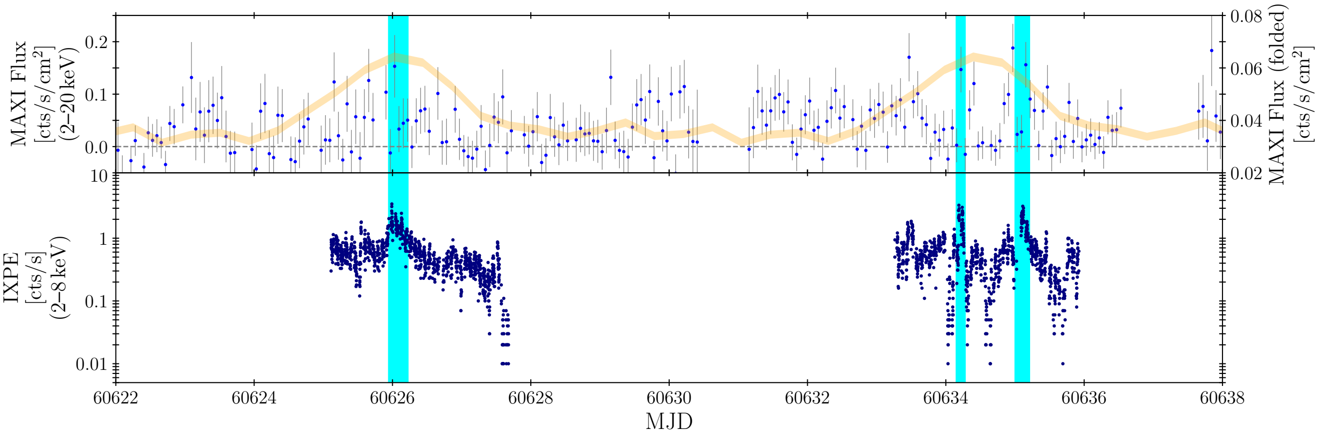

Fig. 1. X-ray light curve of 4U 1907+09. Upper panel: Light curve in the 2–20 keV band as observed by MAXI near the IXPE observations. We also present the folded orbital light curve for MAXI data after MJD 59000 based on the ephemerides from in 't Zand et al. (1998), displayed in light orange, with its width representing flux uncertainties. Note that the folded orbital light curve uses the right-hand axis to emphasize its shape. Lower panel: Combined light curve of 4U 1907+09 from all three DUs of IXPE, with a time resolution of 100 s. The duration of the three flares observed by IXPE is indicated by cyan stripes.

X-ray sources, including XRPs (see Poutanen et al. 2024 for a review). Most studied pulsars show no significant dependence of the polarization angle (PA) on energy, with Vela X-1 and 4U 1538−52 being the only known exceptions (Forsblom et al. 2023; Loktev et al. 2025). However, they exhibit a polarization degree (PD) that is significantly lower than any theoretical predictions.

The source reported in this work, 4U 1907+09, was first detected in the third Uhuru survey (Giacconi et al. 1971; Forman et al. 1978) and subsequently confirmed as an HMXB with an O-type supergiant donor star (van Kerkwijk et al. 1989; Cox et al. 2005; Nespoli et al. 2008). It hosts a pulsar with a spin period of ∼ 437.5 s (Makishima et al. 1984) orbiting a highly reddened companion in an eccentric orbit ($e \simeq 0.28$) with a period of ≃ 8.3753 d (Marshall & Ricketts 1980; in 't Zand et al. 1998). Cox et al. (2005) estimated a lower limit on the distance (d) of 5 kpc, while Nespoli et al. (2008) reported $d \simeq 2.8$ kpc. More recently, Bailer-Jones et al. (2021) derived $d \simeq 1.9$ kpc using *Gaia* Early Data Release 3.

The broadband X-ray spectrum of 4U 1907+09 can be modeled by an absorbed power law with a high energy cutoff (Ferrigno et al. 2022). The cyclotron resonance scattering feature (CRSF) at 17–19 keV, along with its harmonic at approximately 38 keV, has been reported by Mihara (1995), Cusumano et al. (2000), and Tobrej et al. (2023). Moreover, Tobrej et al. (2023) report an absorption line feature at ∼8 keV, which might be produced by the Kβ transition of Fe xxv. Based on the presence of the CRSF, the magnetic field strength of 4U 1907+09 is estimated to be 2×10^{12} G (see, e.g., Hemphill et al. 2013; Varun et al. 2019, and references therein). However, the CRSFs were not detected in *Rossi* X-ray Timing Explorer or *Suzaku* data (in 't Zand et al. 1998; Fürst et al. 2012). As a highly magnetized NS, the compact object in 4U 1907+09 exhibits a complex pulse profile that depends on both energy and luminosity (Mukerjee et al. 2001; Rivers et al. 2010; Şahiner et al. 2012).

IXPE observations, supported by high-quality data, have provided the first robust detection of the polarization properties of 4U 1907+09. The remainder of this paper is structured as follows: In Sect. 2 we present the long-term behaviors of the source and an overview of the data we analyzed. The results are presented in Sect. 3. We discuss the results of our analysis in Sect. 4. A summary and outlook are presented in Sect. 5.

Table 1. Orbital parameters for 4U 1907+09 (adopted from in 't Zand et al. 1998).

Parameter	Value	Unit
Orbital period	$8.3753^{+0.0003}_{-0.0002}$	d
$T_{\pi/2}$	$50134.76^{+0.16}_{-0.20}$	MJD
$a_X \sin i$	83 ± 4	light-sec
Longitude of periastron	330 ± 20	deg
Eccentricity	$0.28^{+0.10}_{-0.14}$	

Table 2. Pulsar ephemerides for Obs. 1 and 2 of 4U 1907+09 with IXPE.

Parameter	Obs. 1	Obs. 2
Start [MJD]	60625.1	60633.3
End [MJD]	60627.7	60635.9
Exposure [ks]	117.9	118.0
t_0 [MJD]	60625.1139919[a]	
Pulse period [s]	$443.73^{+0.03}_{-0.01}$	
Pulse period derivative [10^{-8} s s^{-1}]	5^{+3}_{-6}	

Notes. [(a)] The reported reference time (t_0) defines the zero phases of the pulse profiles (see Fig. 2).

2. Observations and data reduction

IXPE is a joint mission of NASA and the Italian Space Agency launched by a Falcon 9 rocket on 2021 December 9, intending to provide imaging polarimetry over the 2–8 keV energy range (Weisskopf et al. 2022). IXPE consists of three identical grazing incidence telescopes. Each telescope comprises an X-ray mirror assembly and a polarization-sensitive detector unit (DU) equipped with a gas-pixel detector (Soffitta et al. 2021; Baldini et al. 2021). In addition to recording the sky coordinates, arrival time, and energy of each photon, the system also measures the scattering direction of the photo-electron, thereby enabling polarimetric analysis.

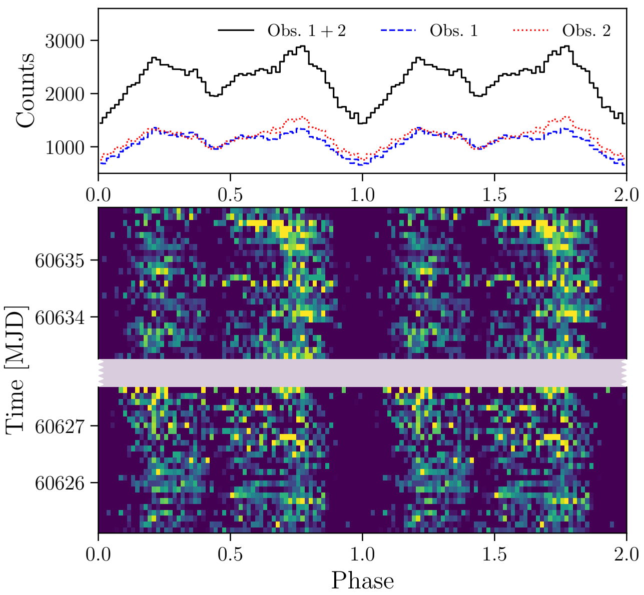

Fig. 2. Pulse profiles of 4U 1907+09 during two IXPE observations and their phaseograms versus time.

IXPE observed 4U 1907+09 twice, 2024 November 11–13 and 19–21 (hereafter Obs. 1 and 2) with total effective exposures of 117.9 ks and 118.0 ks, respectively, during the brightest period near the periastron (see the upper panel of Fig. 1). Its light curve in the 2–8 keV energy range from the IXPE observatory is shown in the lower panel of Fig. 1. The data have been processed using the IXPEOBSSIM package (version 31.0.3, Baldini et al. 2022) with calibration files from the calibration database released on 2024 July 1. Before the analysis, position offset corrections and energy calibration were applied. Source photons are extracted from a circular region with a radius of $R_{\rm src} = 70''$, centered on the source position. The background region is defined as an annular area centered on the source, with an inner radius of $R_{\rm in} = 120''$ and an outer radius of $R_{\rm out} = 240''$. The source photon flux in the 2–8 keV band is ~ 0.6 cps when combining all the three DUs, while the average background count rate in the same band is estimated at 0.001 cps arcmin^{-2} per DU. Thus, the background is not subtracted when using the `pcube` algorithm provided by the IXPEOBSSIM team (Di Marco et al. 2023). However, the background effect is accounted for in the spectro-polarimetric analysis conducted with XSPEC. We performed the unweighted analysis approach, following the methodology described in Di Marco et al. (2022).

Event arrival times were corrected to the Solar System barycenter using the `barycorr` tool from the FTOOLS package. To account for the effects of binary orbital motion, additional corrections were applied using the orbital ephemerides provided by in 't Zand et al. (1998) extrapolated to the IXPE observation epoch (see Table 1).

The pulse period (P) and its first derivative ($\dot{P}$) are independently determined by collecting photon events from both observations using Z^2 statistics. The obtained spin parameters and pulse epochs are listed in Table 2. This method naturally ensures alignment of the pulse profiles over long periods, as shown in Fig. 2. The zero point of the pulse profile is defined at the phase corresponding to the minimum count value.

The Stokes I, Q, and U spectra from all three DUs are produced via the unweighted `PHA1`, `PHA1Q`, and `PHA1U` algorithms provided in the `xpbin` tool in the IXPEOBSSIM package. Later, the I, Q, and U spectra are re-binned to ensure at least 30 counts per energy channel, with consistent energy binning applied across all spectra. The spectra are simultaneously fitted using the XSPEC package (version 12.14.0, Arnaud 1996) and IXPE response matrices (ixpe:obssim20240701:v13). Fits are performed using χ^2 statistics, and uncertainties are reported at the 68.3% confidence level (1σ) unless otherwise specified.

We also employed the `pcube` method provided by the IXPEOBSSIM package to perform a model-independent polarimetric analysis. This method disregards the full energy response matrix but accounts for energy dependence by weighting individual photon contributions. All photons detected within the selected time interval and energy band are used to compute the Stokes parameters through weighted summation (see Eq. 11 in Baldini et al. 2022).

3. Results

3.1. Light curves and pulse profiles

4U 1907+09 was observed two separate times in the period 2024 November 11–21, corresponding to the brightest periods close to the periastron as seen in the light curve (see the upper panel of Fig. 1) measured by MAXI[1] (Matsuoka et al. 2009). Three short flares, each lasting several hours, were captured during the IXPE observations, as indicated by the cyan stripes in Fig. 1. The fraction of photons obtained during the flares accounts for approximately 30% of the total number of photons.

The pulse period and pulse period derivative are measured simultaneously by maximizing the Z^2 statistics using all the photon events recorded within the 2–8 keV band in both observations (Buccheri et al. 1983). The determined values can be found in Table 2. The resulting pulse profiles for the observations of 4U 1907+09 in the 2–8 keV energy band are shown in Fig. 2 together with the phaseograms, which display the evolution of the pulse profiles over 11 days.

The energy-resolved pulse profiles are generated using IXPE data, with the results shown in Fig. 3. No significant evolution in the shape of the pulse profiles is observed between 3 and 6 keV. In the softer energy band, the profiles may be influenced by absorption from the stellar wind or interstellar medium, while the harder energy band is characterized by reduced photon counts due to the instrument's lower effective area.

3.2. Polarimetric analysis

The exploratory polarimetric analysis of 4U 1907+09 is performed with XSPEC, fully considering the energy dispersion and the spectral shape. We first generated the Stokes I, Q, and U spectra from all three DUs. We then computed the normalized Stokes parameters $q = Q/I$, $u = U/I$, the PD using the equation PD$=\sqrt{q^2 + u^2}$, and the PA using PA$=\frac{1}{2}\arctan(u/q)$ measured from north to east counterclockwise on the sky (Kislat et al. 2015). Later, we fitted all nine spectra simultaneously with XSPEC.

The spectral continuum of the source can be modeled well by an absorbed power law with a high-energy cutoff (see, e.g., Fritz et al. 2006; Hemphill et al. 2013; Tobrej et al. 2023). Given the sensitivity of IXPE in the soft X-ray bands, we adopted a simple phenomenological model:

$$\texttt{constant} \times \texttt{tbabs} \times \texttt{powerlaw} \times \texttt{polconst}\,,$$

[1] http://maxi.riken.jp/

Table 3. Spectral parameters for the best-fit model obtained from the phase-averaged spectro-polarimetric analysis with XSPEC for Obs. 1 and 2.

Component	Parameter	Unit	Obs. 1	Obs. 2	Obs. 1 & 2
tbabs	N_H	10^{22} cm^{-2}	4.86 ± 0.17	5.12 ± 0.17	4.99 ± 0.12
powerlaw	Γ		1.18 ± 0.04	1.27 ± 0.04	1.22 ± 0.03
polconst	PD	%	6.0 ± 1.6	2.2 ± 1.6	3.7 ± 1.1
	PA	deg	69 ± 8	46 ± 23	63 ± 9
constant	$\mathrm{const_{DU2}}$		1.025 ± 0.010	1.027 ± 0.009	1.027 ± 0.007
	$\mathrm{const_{DU3}}$		1.015 ± 0.010	0.995 ± 0.009	1.005 ± 0.007
	$\mathrm{Flux}_{2-8\,\mathrm{keV}}{}^{a}$	10^{-10} erg s^{-1} cm^{-2}	1.39 ± 0.01	1.47 ± 0.01	1.436 ± 0.009
	χ^2/d.o.f.		1133.1/1112	1201.0/1118	1295.9/1241

Notes. The uncertainties are given at the 68.3% (1σ) confidence level and were obtained using the `error` command in XSPEC with $\Delta\chi^2 = 1$ for one parameter of interest. $^{(a)}$ Observed (absorbed) flux in the 2–8 keV range.

Table 4. Polarimetric parameters in different energy bins for the two IXPE observations derived using the XSPEC method.

	Obs. 1		Obs. 2		Obs. 1 & 2	
Energy (keV)	$\mathrm{PD_{XSPEC}}$ (%)	$\mathrm{PA_{XSPEC}}$ (deg)	$\mathrm{PD_{XSPEC}}$ (%)	$\mathrm{PA_{XSPEC}}$ (deg)	$\mathrm{PD_{XSPEC}}$ (%)	$\mathrm{PA_{XSPEC}}$ (deg)
2–3	7.1 ± 3.4	61 ± 14	3.8 ± 3.3	54 ± 30	5.4 ± 2.4	59 ± 13
3–4	$1.2^{+2.9}_{-1.2}$	$-55^{\dagger}$	4.1 ± 2.8	−47 ± 22	2.6 ± 2.0	−49 ± 26
4–5	12.9 ± 3.6	74 ± 8	6.6 ± 3.5	48 ± 16	8.5 ± 2.5	65 ± 8
5–6	6.8 ± 4.7	80 ± 22	$4.1^{+4.6}_{-4.1}$	$-39^{\dagger}$	$2.5^{+3.3}_{-2.5}$	$-78^{\dagger}$
6–8	13.1 ± 5.7	49 ± 13	17.0 ± 5.6	37 ± 10	13.4 ± 4.0	43 ± 9
2–8	6.0 ± 1.6	69 ± 8	2.2 ± 1.6	46 ± 23	3.7 ± 1.1	63 ± 9

Notes. The uncertainties computed using the `error` command are given at the 68.3% (1σ) confidence level ($\Delta\chi^2 = 1$ for one parameter of interest). $^{(\dagger)}$ The PA cannot be confined within the 1σ confidence level; therefore, we present the most probable value instead.

Table 5. Polarimetric parameters in different energy bins for the two IXPE observations derived using the `pcube` method.

	Obs. 1		Obs. 2		Obs. 1 & 2	
Energy (keV)	$\mathrm{PD_{pcube}}$ (%)	$\mathrm{PA_{pcube}}$ (deg)	$\mathrm{PD_{pcube}}$ (%)	$\mathrm{PA_{pcube}}$ (deg)	$\mathrm{PD_{pcube}}$ (%)	$\mathrm{PA_{pcube}}$ (deg)
2–3	10.1 ± 3.5	60 ± 10	4.5 ± 3.4	68 ± 21	7.1 ± 2.4	62 ± 10
3–4	$1.3^{+2.8}_{-1.3}$	$-43^{\dagger}$	2.7 ± 2.7	−51 ± 28	2.0 ± 2.0	−49 ± 28
4–5	13.3 ± 3.6	74 ± 8	5.5 ± 3.4	46 ± 18	8.3 ± 2.5	66 ± 9
5–6	6.9 ± 4.6	77 ± 19	$3.8^{+4.5}_{-3.8}$	$-46^{\dagger}$	$3.1^{+3.2}_{-3.1}$	$-86^{\dagger}$
6–8	9.0 ± 6.0	57 ± 19	13.0 ± 5.9	45 ± 13	10.8 ± 4.2	50 ± 11
2–8	7.2 ± 2.3	66 ± 9	3.7 ± 2.2	52 ± 17	5.2 ± 1.6	61 ± 9

Notes. The uncertainties are presented at the 1σ confidence level.$^{(\dagger)}$ The PA cannot be confined within the 1σ confidence level; therefore, we present the most probable value instead.

where `constant` accounts for the cross-calibration among three DUs, with the value for DU1 fixed at unity. The galactic absorption model `tbabs` characterizes the photoelectric absorption by the interstellar medium. The cross sections are provided by Verner et al. (1996) and the element abundances are given by Wilms et al. (2000). We used `polconst` as the polarization model, which assumes an energy-independent PD and PA. This model is applied to both the phase-averaged and phase-resolved analysis. The model-independent `pcube` method was subsequently adopted as a reference for the results obtained with XSPEC, as the two methods are expected to yield similar outcomes.

3.2.1. Phase-averaged analysis

We began with a phase-averaged analysis in the full 2–8 keV band for both observations, with the results summarized in Table 3. Obs. 1 exhibits stronger polarization than Obs. 2, with phase-averaged PD of 6.0 ± 1.6% and 2.2 ± 1.6%, respectively. The corresponding PAs are 69° ± 8° for Obs. 1 and 46° ± 23° for Obs. 2. We also performed a spectro-polarimetric analysis on the combined dataset from the two observations, with the results summarized in the last column of Table 3. Assuming a source distance of $d \simeq 1.9$ kpc (Bailer-Jones et al. 2021), we estimate the luminosity of 4U 1907+09 to be $L \simeq 2.5 \times 10^{35}$ erg s^{-1}.

Next, we studied the energy dependence of the polarization properties of 4U 1907+09 by performing an energy-resolved polarimetric analysis on each observation, dividing the data into five energy bins (2–3, 3–4, 4–5, 5–6, and 6–8 keV). We performed the fitting with XSPEC, using all energy bins within 2–8 keV for the Stokes I spectra while excluding bins outside the interested energy range for the Stokes Q and U spectra. The results are shown in Table 4. We also conducted the polarimetric

Table 6. Spectro-polarimetric parameters in different pulse-phase bins for the combined dataset, derived using XSPEC and `pcube`.

Phase	N_H (10^{22} cm^{-2})	Γ	PD$_{XSPEC}$ (%)	PA$_{XSPEC}$ (deg)	χ^2/d.o.f.	PD$_{pcube}$ (%)	PA$_{pcube}$ (deg)
0.0–0.15	$4.98^{+0.36}_{-0.35}$	1.37 ± 0.08	5.4 ± 3.3	-69 ± 19	689.1/752	7.9 ± 4.6	-86 ± 17
0.15–0.25	5.08 ± 0.37	1.04 ± 0.08	13.5 ± 3.3	71 ± 7	825.6/758	17.1 ± 4.7	60 ± 8
0.25–0.375	$4.32^{+0.33}_{-0.32}$	1.06 ± 0.07	4.1 ± 3.1	0 ± 24	799.6/809	$3.3^{+4.3}_{-3.3}$	$-29^{\dagger}$
0.375–0.5	6.09 ± 0.37	1.36 ± 0.08	$2.4^{+3.3}_{-2.4}$	$73^{\dagger}$	838.9/776	5.8 ± 4.7	67 ± 23
0.5–0.625	$4.74^{+0.34}_{-0.33}$	$1.06^{+0.08}_{-0.07}$	4.7 ± 3.1	44 ± 21	828.1/806	10.4 ± 4.4	40 ± 12
0.625–0.75	5.56 ± 0.32	1.13 ± 0.07	4.6 ± 3.0	61 ± 20	825.4/845	4.3 ± 4.1	73 ± 28
0.750–0.85	$4.59^{+0.36}_{-0.35}$	1.35 ± 0.08	4.1 ± 3.4	88 ± 28	782.3/743	$3.5^{+4.7}_{-3.5}$	$87^{\dagger}$
0.85–1.0	4.95 ± 0.35	$1.64^{+0.09}_{-0.08}$	7.1 ± 3.4	43 ± 14	695.0/728	8.3 ± 4.7	43 ± 16

Notes. The uncertainties in the spectro-polarimetric parameters, computed using the `error` command in XSPEC, are provided at the 68.3% (1σ) confidence level ($\Delta\chi^2 = 1$ for one parameter of interest). The right two columns give PDs and PAs estimated with the `pcube` algorithm and the uncertainties given at the 1σ confidence level.$^{(\dagger)}$ The PA cannot be confined within the 1σ confidence level; therefore, we presented the most probable value instead.

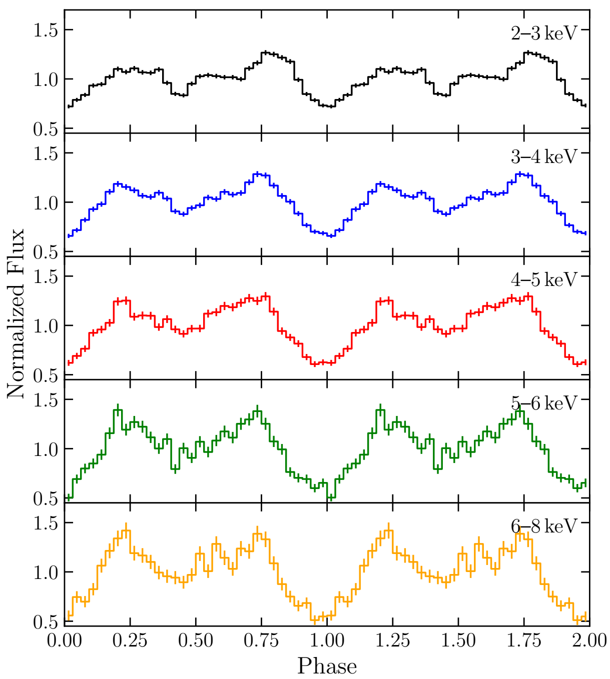

Fig. 3. Pulse profiles of 4U 1907+09 in different energy bands for the combined dataset (Obs. 1 and 2). The pulse profile fluxes are normalized such that their mean values are unity.

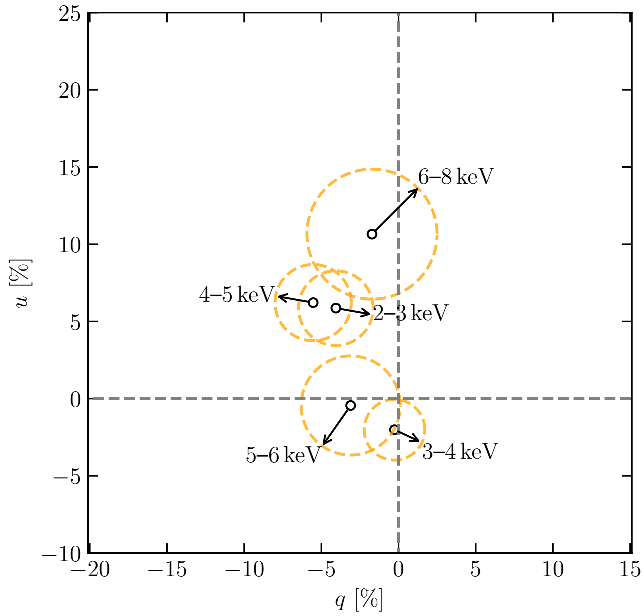

Fig. 4. Energy dependence of the normalized Stokes parameters q and u for the phase-averaged data of the combined dataset (Obs. 1 and 2), obtained with the `pcube` algorithm. The 1σ contours are plotted as dashed circles around each best estimate.

analysis with the model-independent `pcube` algorithm, with the results shown in Table 5, demonstrating similar outcomes.

Contrary to the expectation that the PA is independent of energy, we observed a larger PD with greater confidence in the 2–3, 4–5, and 6–8 keV bands during the two IXPE observations. Furthermore, polarimetric detections in different energy bands exhibit distinct PAs. The normalized Stokes parameters q and u for each energy band of the combined dataset, as shown in Fig. 4, further highlight the polarization discrepancies across energy bands.

The energy dependence of the PA is also observed in other XRPs. In Vela X-1, the PA differs by approximately 90° between the 2–3 and 3–8 keV bands (Forsblom et al. 2023, 2025). Similarly, in 4U 1538−52, the PA exhibits a shift of about 70° between the 2–3 and 4–8 keV bands (Loktev et al. 2025).

We then tested the null hypothesis that the PA does not depend on energy. Since PAs are not normally distributed, we adopted the probability density function of the PA, ψ, as derived by Naghizadeh-Khouei & Clarke (1993):

$$G(\psi) = \frac{1}{\sqrt{\pi}} \left\{ \frac{1}{\sqrt{\pi}} + \eta e^{\eta^2} \left[1 + \mathrm{erf}(\eta)\right] \right\} e^{-p_0^2/2},$$

where $p_0 = \mathrm{PD}/\mathrm{PD}_{\mathrm{err}}$ is the measured PD in units of its error, $\eta = p_0 \cos\left[2\left(\psi - \psi_0\right)\right] / \sqrt{2}$, and ψ_0 is the expectation value of the PA. Here, erf denotes the error function. To evaluate the statistical significance, we employed the parameters obtained from the XSPEC fit (see Table 4) to perform Monte Carlo simulations. We defined the statistical test quantity, the Z-score, as $Z = -\sum \log G(\psi)$. To simulate the probability distribution of the Z-score under the null hypothesis, we used the average PA (63°), PD (3.7%) and its uncertainty (1.1%) within the 2–8 keV range. The observed Z-score is calculated using the most probable values of ψ of the individual energy bands, with p_0 determined based on the corresponding PDs and their positive uncertainties, and setting $\psi_0 = 63°$. Our analysis yields a p-value of

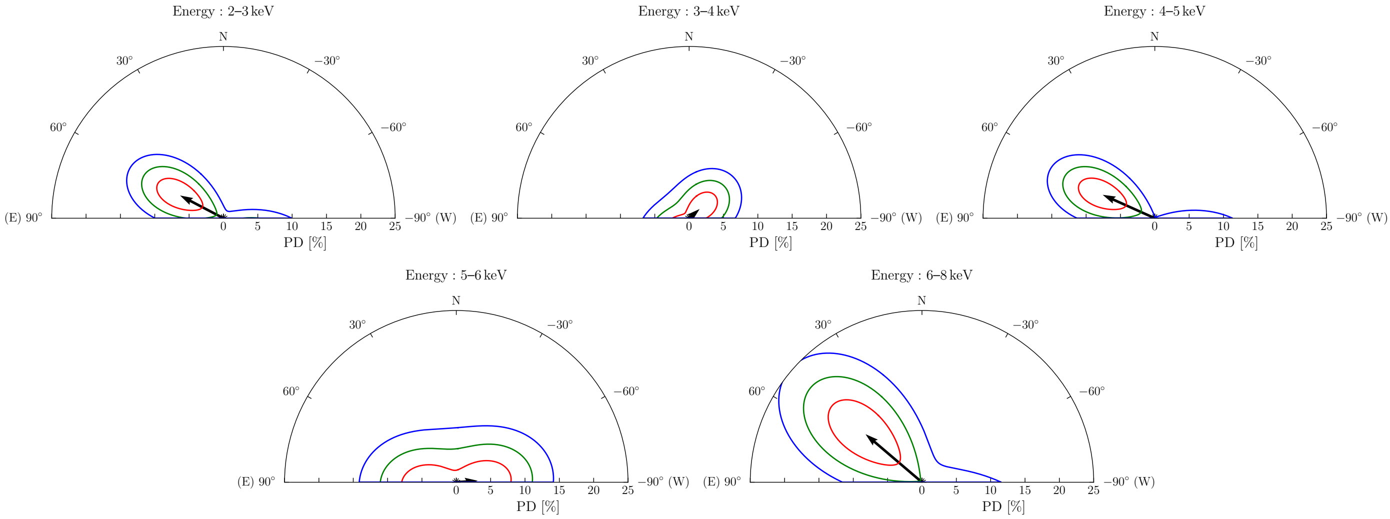

Fig. 5. Polarization vectors of 4U 1907+09 across different energy bands derived from the phase-averaged polarimetric analysis of the combined dataset using the `pcube` algorithm. Confidence contours at 68.3%, 95.45%, and 99.73% are displayed in red, green, and blue, respectively.

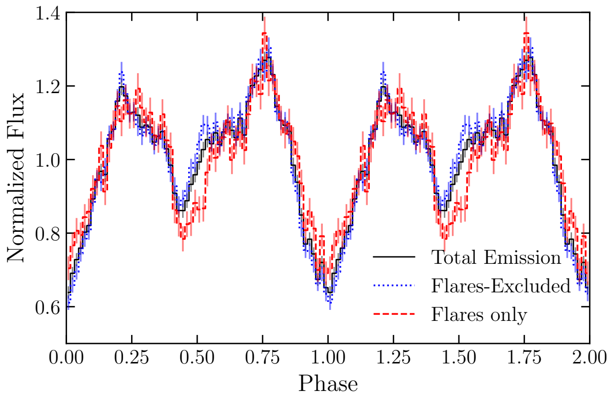

Fig. 6. Pulse profiles of 4U 1907+09 from the combined IXPE observation. Dotted blue, dashed red, and solid black lines represent the profiles for flares-excluded data, flare-only data, and total emission, respectively. The pulse profile fluxes are normalized such that their mean values are unity.

0.049 to reject the null hypothesis, corresponding to a statistical significance of 1.7 σ. This result suggests tentative evidence that the PA depends on the energy.

3.2.2. Phase-resolved analysis

Studying the phase-dependent properties of pulsars is crucial, as their geometries change with rotation. Applying the ephemerides in Table 2, the phase of each photon event can be determined by

$$\phi = \frac{1}{P}(t - t_0) - \frac{1}{2}\frac{\dot{P}}{P^2}(t - t_0)^2 ,$$

in which P is the pulse period and $\dot{P}$ is the pulse period derivative at a reference time t_0, which also defines the zero phase. The photons are divided into eight phase bins, selected to ensure that each bin contains approximately the same number of photon counts. For each phase bin, we generated the Stokes I, Q, and U spectra, as described in Sect. 2.

We first applied the XSPEC method to each phase bin, focusing on the 2–8 keV energy range. The results of the combined dataset are presented in Table 6. Although a few phase bins show polarization detections with a significance level below 1σ, the modulation of the PA with pulse phase remains detectable despite the gaps in phase coverage.

The `pcube` algorithm is subsequently applied to the phase-resolved data, with the results shown in the last two columns of Table 6. The PDs obtained using the `pcube` method are generally higher than those derived with XSPEC, while the PAs from both methods are typically well aligned when the respective PDs are significant.

3.3. Flares and their impacts on polarimetric properties

To date, the impact of flares on polarimetric detection remains unclear. To investigate this influence, we analyzed the events detected during the flares separately from those detected outside of the flares.

We first examined the pulse profiles during the flare and non-flare periods. The results, along with a comparison to the pulse profile of the total emission, are shown in Fig. 6. The pulse profiles exhibit subtle differences, suggesting that the geometry of the accreting pulsar undergoes slight changes during flares.

We then investigated the behavior of the Stokes parameters as functions of pulse phase and energy. The normalized Stokes parameters q, u, and the derived PAs across different phase and energy intervals are presented in Fig. 7. The uncertainties of these parameters during flares are larger due to the lower photon counts in the flare periods. However, the parameters are consistent within their respective uncertainties.

Given that 4U 1907+09 is not particularly bright and the photon counts during flares are insufficient, we conclude that the energy-dependent polarimetric properties are not a result of the flares. In fact, flares have minimal impact on the observed polarimetric properties. Therefore, in the following analysis, we include all emissions from the source without distinguishing between flares and non-flares.

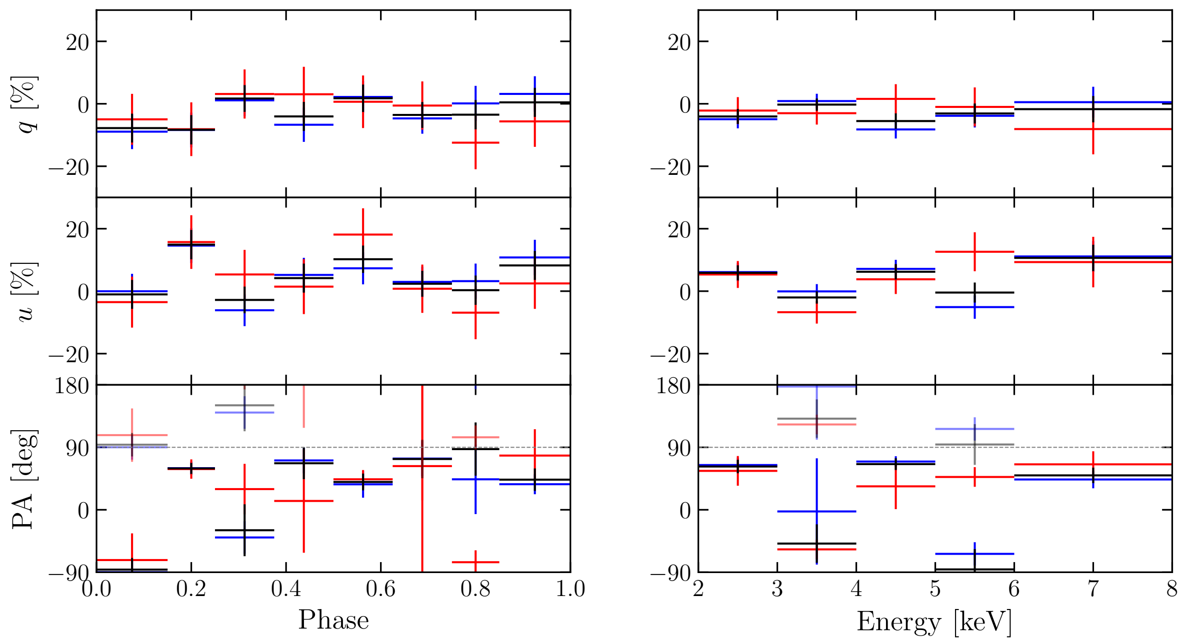

Fig. 7. Normalized Stokes parameters and measured PAs as functions of pulse phase and energy from the combined IXPE observation. Blue, red, and black crosses represent the flares-excluded data, flare-only data, and total emission data, respectively. Some PAs are plotted twice with an added constant of 180° to illustrate the continuity of the PA with respect to phase and energy.

3.4. Energy-dependent polarimetric properties in different pulse phases

We have observed energy-dependent polarimetric properties in the phase-averaged analysis, and in Sect. 3.3 we concluded that they are unlikely to be produced by flares. It is then necessary to examine the energy-dependent polarimetric properties in each pulse phase. Accordingly, we divided the phase-tagged photon events into eight phase bins, as in Table 6, and into five energy bins covering the 2–8 keV range, following Tables 4 and 5. The `pcube` algorithm was then used to compute the PA and PD in each energy-phase bin. The results are shown in Fig. 8.

Due to the limited photon counts, most PDs in the energy-phase bins do not exceed the minimum detectable polarization at the 99% confidence level (MDP_{99}). Nonetheless, the evolution of the PA with energy is still observable in each phase bin. The most notable detection of a PA rotation between adjacent energy bands within a single phase bin occurs in the phase interval 0.25–0.375. In this interval, the PA of photons in the 4–5 keV and 5–6 keV energy bands differs by approximately 90°. Their PDs marginally reach the MDP_{99}, suggesting a "probable" right-angle rotation of the PA between these energy bands within this phase interval. Protractor plots illustrating the PAs with their 1σ, 2σ, and 3σ uncertainties are shown in Fig. 9, where the PAs are compatible only within the 3σ range. It is worth noting that in Vela X-1, a PA shift of $\sim 90°$ between two energy bands is also detected within a single phase bin (Forsblom et al. 2025).

4. Discussion

X-ray Pulsars are considered prime candidates for X-ray polarimetric analysis, as the highly magnetized matter accreting onto the magnetic poles of the NS can naturally generate a high PD due to the birefringence of the medium in such a strong magnetic field. The oscillations of the electric field of the emitted photons are expected to align either parallel or perpendicular to the plane formed by the photon momentum and the local magnetic field (Gnedin & Pavlov 1974; Gnedin et al. 1978). These modes are referred to as the ordinary (O) and extraordinary (X), respectively. The Compton scattering cross section below the cyclotron energy for the O-mode radiation is much higher than that for the X-mode (Lai & Ho 2003), predicting a high PD up to 80% (Meszaros et al. 1988; Caiazzo & Heyl 2021).

Nevertheless, most XRPs observed by IXPE exhibit low phase-averaged PDs (see, e.g., Tsygankov et al. 2022; Mushtukov et al. 2023; Forsblom et al. 2023), with higher PDs emerging in phase-resolved analyses. This trend does not fully hold for 4U 1907+09, where polarization is weakly detected in most phase bins. Further examination of the energy dependence of the PA within individual phase bins partially enhances the significance of polarization detection in some energy-phase bins, as shown in Fig. 8. However, some energy-phase bins still exhibit extremely low PD significance.

Because the measured PAs exhibit energy dependence in the phase-averaged analysis, the rotating vector model (RVM; Radhakrishnan & Cooke 1969; Meszaros et al. 1988; Poutanen 2020), which assumes that the PA aligns with the local magnetic field and is therefore energy-independent, is not suitable for constraining the pulsar's geometry. Furthermore, the absence of a distinct PA transition at any specific energy further precludes the application of an energy-resolved RVM fit (e.g., Forsblom et al. 2025; Loktev et al. 2025).

Various accretion processes involving reflection and scattering can introduce additional polarized components that tangle with the emission produced near the magnetic poles (see the discussion in Tsygankov et al. 2022). Consequently, it is natural to consider an energy-dependent polarized component as a potential explanation for the unusual energy dependence of the PA. This idea has been explored by Forsblom et al. (2025) and Loktev et al. (2025). Specifically, Forsblom et al. (2025) propose two possible mechanisms for the observed PA variation with energy. The first involves a spectral component that diminishes at higher energies and generally has a PA orthogonal to that of the dominant high-energy component. The second in-

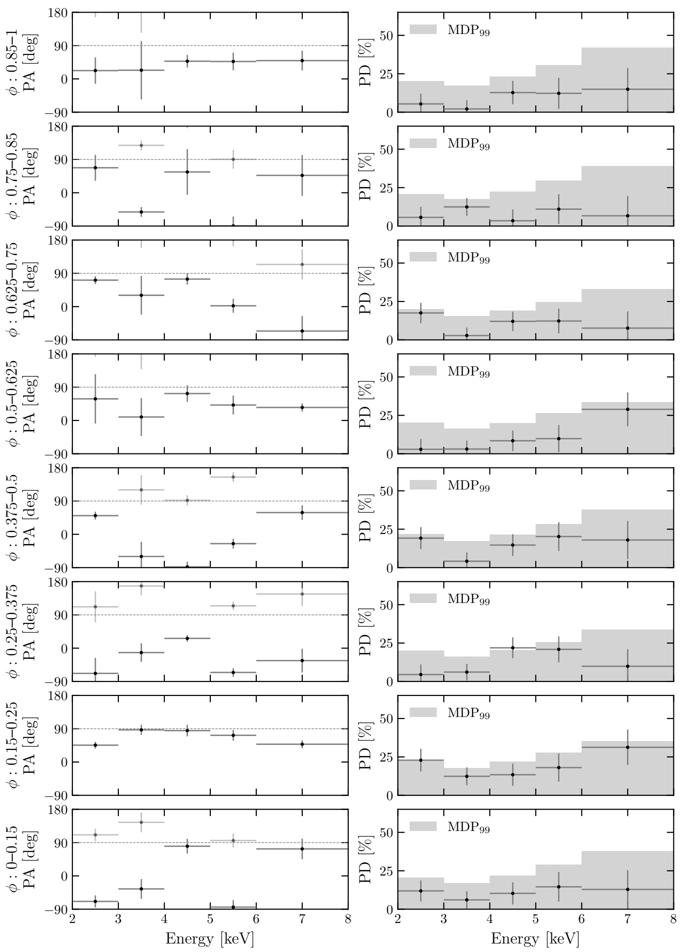

Fig. 8. Energy-resolved polarization measurements of the combined dataset across pulse phases. Left: PAs with 1σ uncertainties. Right: PDs. Gray bars indicate the MDP$_{99}$ value. Note that we again plot the PAs with an added constant of 180° to illustrate the continuity of the PAs versus energy.

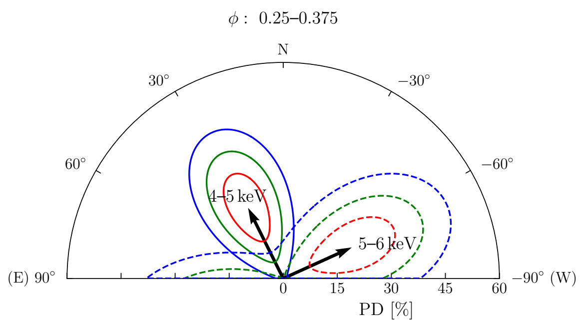

Fig. 9. Protractor plot of the polarization measurement of the combined dataset within the 4–5 keV band and the 5–6 keV band in the pulse phase interval 0.25–0.375.

vokes vacuum resonance, in which one polarization mode converts into another near the cyclotron line energy, resulting in a 90° shift in the PA. Given the results shown in Tables 4 and 5, it is difficult to envision a spectral component that is extraordinarily strong specifically in the 3–4 and 5–6 keV bands, thereby causing the observed drop in PDs. Regarding the second mechanism, it predicts an energy-independent PA at both low and high energies. However, this prediction cannot be confirmed due to the limited photon statistics ($\simeq$ 1.45 million photons within the 2–8 keV band for the combined dataset) and the restricted energy coverage of IXPE. Furthermore, if a gradual shift in the PA with energy is observed, it would indicate the presence of an additional polarized component. More robust results are expected from future observations with improved photon statistics and broader energy coverage.

5. Summary

4U 1907+09 was observed by IXPE twice during the period 2024 November 11–21, during its brightest periods close to the periastron. We summarize the results of the polarimetric analysis of 4U 1907+09 as follows:

1. A more significant polarization is detected in Obs. 1 than in Obs. 2, with phase-averaged PD and PA values of 6.0 ± 1.6% and 69°±8° for Obs. 1 and 2.2±1.6% and 46°±23° for Obs. 2. The combined dataset from the two observations yields a PD of 3.7 ± 1.1% and a PA of 63° ± 9°.
2. An energy-dependent PA is likely observed in the phase-averaged polarimetric analyses with a significance of 1.7 σ, partially explaining the generally insignificant polarization detections. Specifically, we detect a probable rotation of the PA between adjacent energy bands within one single phase bin.
3. We further examined whether the three brief flares detected by IXPE significantly affect the pulsar's polarization. Our analysis concludes that the polarimetric properties are similar in the flare-excluded and flare-only data, suggesting that the observed energy-dependent PAs are unlikely due to the flares.

Acknowledgements. The Imaging X-ray Polarimetry Explorer (IXPE) is a joint US and Italian mission. The US contribution is supported by the National Aeronautics and Space Administration (NASA) and led and managed by its Marshall Space Flight Center (MSFC), with industry partner Ball Aerospace (contract NNM15AA18C). The Italian contribution is supported by the Italian Space Agency (Agenzia Spaziale Italiana, ASI) through contract ASI-OHBI-2022-13-I.0, agreements ASI-INAF-2022-19-HH.0 and ASI-INFN-2017.13-H0, and its Space Science Data Center (SSDC) with agreements ASI-INAF-2022-14-HH.0 and ASI-INFN 2021-43-HH.0, and by the Istituto Nazionale di Astrofisica (INAF) and the Istituto Nazionale di Fisica Nucleare (INFN) in Italy. This research used data products provided by the IXPE Team (MSFC, SSDC, INAF, and INFN) and distributed with additional software tools by the High-Energy Astrophysics Science Archive Research Center (HEASARC), at NASA Goddard Space Flight Center (GSFC). This research has been supported by the Deutsche Forschungsgemeinschaft (DFG) grants 549824807 (LD) and WE 1312/59-1 (VFS), Vilho, Yrjö, and Kalle Väisälä foundation (SVF), and the UKRI Stephen Hawking fellowship (AAM). ASal acknowledges funding from the EDUFI Fellowship and Jenny and Antti Wihuri Foundation. ADM and FLM are partially supported by MAECI with grant CN24GR08 "GRBAXP: Guangxi-Rome Bilateral Agreement for X-ray Polarimetry in Astrophysics".

References

Arnaud, K. A. 1996, in ASP Conf. Ser., Vol. 101, Astronomical Data Analysis Software and Systems V, ed. G. H. Jacoby & J. Barnes (San Francisco: Astron. Soc. Pac.), 17

Bailer-Jones, C. A. L., Rybizki, J., Fouesneau, M., Demleitner, M., & Andrae, R. 2021, AJ, 161, 147

Baldini, L., Barbanera, M., Bellazzini, R., et al. 2021, Astroparticle Physics, 133, 102628

Baldini, L., Bucciantini, N., Lalla, N. D., et al. 2022, SoftwareX, 19, 101194

Buccheri, R., Bennett, K., Bignami, G. F., et al. 1983, A&A, 128, 245

Caiazzo, I., & Heyl, J. 2021, MNRAS, 501, 109

Cox, N. L. J., Kaper, L., & Mokiem, M. R. 2005, A&A, 436, 661

Şahiner, Ş., Inam, S. Ç., & Baykal, A. 2012, MNRAS, 421, 2079

Cusumano, G., di Salvo, T., Burderi, L., et al. 2000, Advances in Space Research, 25, 409

Di Marco, A., Costa, E., Muleri, F., et al. 2022, AJ, 163, 170

Di Marco, A., Soffitta, P., Costa, E., et al. 2023, AJ, 165, 143
Elsner, R. F., & Lamb, F. K. 1977, ApJ, 215, 897
Ferrigno, C., Bozzo, E., & Romano, P. 2022, A&A, 664, A99
Forman, W., Jones, C., Cominsky, L., et al. 1978, ApJS, 38, 357
Forsblom, S. V., Tsygankov, S. S., Suleimanov, V. F., Mushtukov, A. A., & Poutanen, J. 2025, A&A, 696, A224
Forsblom, S. V., Poutanen, J., Tsygankov, S. S., et al. 2023, ApJ, 947, L20
Fritz, S., Kreykenbohm, I., Wilms, J., et al. 2006, A&A, 458, 885
Fürst, F., Pottschmidt, K., Kreykenbohm, I., et al. 2012, A&A, 547, A2
Giacconi, R., Kellogg, E., Gorenstein, P., Gursky, H., & Tananbaum, H. 1971, ApJ, 165, L27
Gnedin, Y. N., & Pavlov, G. G. 1974, Soviet Journal of Experimental and Theoretical Physics, 38, 903
Gnedin, Y. N., Pavlov, G. G., & Shibanov, Y. A. 1978, Soviet Astronomy Letters, 4, 117
Hemphill, P. B., Rothschild, R. E., Caballero, I., et al. 2013, ApJ, 777, 61
in 't Zand, J. J. M., Baykal, A., & Strohmayer, T. E. 1998, ApJ, 496, 386
Kislat, F., Clark, B., Beilicke, M., & Krawczynski, H. 2015, Astroparticle Physics, 68, 45
Lai, D., & Ho, W. C. 2003, Phys. Rev. Lett., 91, 071101
Lamb, F. K., Pethick, C. J., & Pines, D. 1973, ApJ, 184, 271
Loktev, V., Forsblom, S. V., Tsygankov, S. S., et al. 2025, A&A, 698, A22
Makishima, K., Kawai, N., Koyama, K., et al. 1984, PASJ, 36, 679
Marshall, N., & Ricketts, M. J. 1980, MNRAS, 193, 7P
Matsuoka, M., Kawasaki, K., Ueno, S., et al. 2009, PASJ, 61, 999
Meszaros, P., Novick, R., Szentgyorgyi, A., Chanan, G. A., & Weisskopf, M. C. 1988, ApJ, 324, 1056
Mihara, T. 1995, PhD thesis, University of Tokyo
Mukerjee, K., Agrawal, P. C., Paul, B., et al. 2001, ApJ, 548, 368
Mushtukov, A., & Tsygankov, S. 2024, Accreting strongly magnetised neutron stars: X-ray Pulsars, ed. C. Bambi & A. Santangelo (Singapore: Springer), 4105
Mushtukov, A. A., Tsygankov, S. S., Poutanen, J., et al. 2023, MNRAS, 524, 2004
Naghizadeh-Khouei, J., & Clarke, D. 1993, A&A, 274, 968
Nespoli, E., Fabregat, J., & Mennickent, R. E. 2008, A&A, 486, 911
Poutanen, J. 2020, A&A, 641, A166
Poutanen, J., Tsygankov, S. S., & Forsblom, S. V. 2024, Galaxies, 12, 46
Radhakrishnan, V., & Cooke, D. J. 1969, Astrophys. Lett., 3, 225
Rivers, E., Markowitz, A., Pottschmidt, K., et al. 2010, ApJ, 709, 179
Soffitta, P., Baldini, L., Bellazzini, R., et al. 2021, AJ, 162, 208
Tobrej, M., Rai, B., Ghising, M., Tamang, R., & Paul, B. C. 2023, MNRAS, 518, 4861
Tsygankov, S. S., Doroshenko, V., Poutanen, J., et al. 2022, ApJ, 941, L14
van Kerkwijk, M. H., van Oijen, J. G. J., & van den Heuvel, E. P. J. 1989, A&A, 209, 173
Varun, Pradhan, P., Maitra, C., Raichur, H., & Paul, B. 2019, ApJ, 880, 61
Verner, D. A., Ferland, G. J., Korista, K. T., & Yakovlev, D. G. 1996, ApJ, 465, 487
Weisskopf, M. C., Soffitta, P., Baldini, L., et al. 2022, JATIS, 8, 026002
Wilms, J., Allen, A., & McCray, R. 2000, ApJ, 542, 914

Bibliography

[1] 2017, National Science Review, 4, 934

[2] Altamirano, D. & Méndez, M. 2015, MNRAS, 449, 4027

[3] Arnaud, K., Smith, R., & Siemiginowska, A. 2011, Handbook of X-ray Astronomy

[4] Arnaud, K. A. 1996, in Astronomical Society of the Pacific Conference Series, Vol. 101, Astronomical Data Analysis Software and Systems V, ed. G. H. Jacoby & J. Barnes, 17

[5] Athulya, M. P., Radhika, D., Agrawal, V. K., et al. 2022, MNRAS, 510, 3019

[6] Axelsson, M., Borgonovo, L., & Larsson, S. 2006, A&A, 452, 975

[7] Bachetti, M., Huppenkothen, D., Khan, U., et al. 2021, StingraySoftware/stingray: Version 0.3

[8] Bailer-Jones, C. A. L., Rybizki, J., Fouesneau, M., Demleitner, M., & Andrae, R. 2021, AJ, 161, 147

[9] Balakrishnan, M., Miller, J. M., Reynolds, M. T., et al. 2021, ApJ, 909, 41

[10] Bambi, C. 2017, Black Holes: A Laboratory for Testing Strong Gravity

[11] Bambi, C. 2017, Reviews of Modern Physics, 89, 025001

[12] Bambi, C. & Santangelo, A. 2024, Handbook of X-ray and Gamma-ray Astrophysics

[13] Bardeen, J. M. & Petterson, J. A. 1975, ApJL, 195, L65

[14] Bardeen, J. M., Press, W. H., & Teukolsky, S. A. 1972, ApJ, 178, 347

[15] Becker, P. A. & Wolff, M. T. 2007, ApJ, 654, 435

[16] Beer, M. E. & Podsiadlowski, P. 2002, MNRAS, 331, 351

[17] Begelman, M. C., McKee, C. F., & Shields, G. A. 1983, ApJ, 271, 70

[18] Belloni, T. & Hasinger, G. 1990, A&A, 227, L33

[19] Belloni, T., Homan, J., Casella, P., et al. 2005, A&A, 440, 207

[20] Belloni, T., Klein-Wolt, M., Méndez, M., van der Klis, M., & van Paradijs, J. 2000, A&A, 355, 271

[21] Blandford, R. D. & Begelman, M. C. 1999, MNRAS, 303, L1

[22] Blandford, R. D. & Znajek, R. L. 1977, MNRAS, 179, 433

[23] Böck, M., Grinberg, V., Pottschmidt, K., et al. 2011, A&A, 533, A8

[24] Bogdanov, S., Guillot, S., Ray, P. S., et al. 2019, ApJL, 887, L25

[25] Bolton, C. T. 1972, Nature, 235, 271

[26] Borghese, A. & Coti Zelati, F. 2025, arXiv e-prints, arXiv:2502.17652

[27] Bowyer, S., Byram, E. T., Chubb, T. A., & Friedman, H. 1965, Science, 147, 394

[28] Buccheri, R., Bennett, K., Bignami, G. F., et al. 1983, A&A, 128, 245

[29] Bucciantini, N., Ferrazzoli, R., Bachetti, M., et al. 2023, Nature Astronomy, 7, 602

[30] Cabanac, C., Roques, J.-P., & Jourdain, E. 2011, ApJ, 739, 58

[31] Cai, C., Xiong, S. L., Li, C. K., et al. 2021, MNRAS, 508, 3910

[32] Caiazzo, I. & Heyl, J. 2021, MNRAS, 501, 109

[33] Cangemi, F., Beuchert, T., Siegert, T., et al. 2021, A&A, 650, A93

[34] Cao, X., Jiang, W., Meng, B., et al. 2020, Science China Physics, Mechanics, and Astronomy, 63, 249504

[35] Castro-Tirado, A. J., Brandt, S., & Lund, N. 1992, IAU Circ., 5590, 2

[36] Castro-Tirado, A. J., Brandt, S., Lund, N., et al. 1994, ApJS, 92, 469

[37] Chen, Y., Cui, W., Li, W., et al. 2020, Science China Physics, Mechanics, and Astronomy, 63, 249505

[38] Churazov, E., Gilfanov, M., & Revnivtsev, M. 2001, MNRAS, 321, 759

[39] Coburn, W., Heindl, W. A., Rothschild, R. E., et al. 2002, ApJ, 580, 394

[40] Corbel, S., Coriat, M., Brocksopp, C., et al. 2013, MNRAS, 428, 2500

[41] Cox, N. L. J., Kaper, L., & Mokiem, M. R. 2005, A&A, 436, 661

[42] Cui, W., Zhang, S. N., Focke, W., & Swank, J. H. 1997, ApJ, 484, 383

[43] Cusumano, G., di Salvo, T., Burderi, L., et al. 2000, Advances in Space Research, 25, 409

[44] Dauser, T., García, J. A., Joyce, A., et al. 2022, MNRAS, 514, 3965

[45] Dauser, T., Wilms, J., Reynolds, C. S., & Brenneman, L. W. 2010, MNRAS, 409, 1534

[46] Done, C., Gierliński, M., & Kubota, A. 2007, A&ARV, 15, 1

[47] Done, C., Tomaru, R., & Takahashi, T. 2018, MNRAS, 473, 838

[48] Doroshenko, V., Poutanen, J., Heyl, J., et al. 2023, A&A, 677, A57

[49] Doroshenko, V., Poutanen, J., Tsygankov, S. S., et al. 2022, Nature Astronomy, 6, 1433

[50] Elsner, R. F. & Lamb, F. K. 1977, ApJ, 215, 897

[51] Esin, A. A. 1997, ApJ, 482, 400

[52] Fabian, A. C., Iwasawa, K., Reynolds, C. S., & Young, A. J. 2000, The Publications of the Astronomical Society of the Pacific, 112, 1145

[53] Fabian, A. C., Wilkins, D. R., Miller, J. M., et al. 2012, MNRAS, 424, 217

[54] Fender, R. P., Belloni, T. M., & Gallo, E. 2004, MNRAS, 355, 1105

[55] Fender, R. P., Garrington, S. T., McKay, D. J., et al. 1999, MNRAS, 304, 865

[56] Fender, R. P., Homan, J., & Belloni, T. M. 2009, MNRAS, 396, 1370

[57] Fender, R. P., Stirling, A. M., Spencer, R. E., et al. 2006, MNRAS, 369, 603

[58] Ferrigno, C., Bozzo, E., & Romano, P. 2022, A&A, 664, A99

[59] Forman, W., Jones, C., Cominsky, L., et al. 1978, ApJS, 38, 357

[60] Forsblom, S. V., Poutanen, J., Tsygankov, S. S., et al. 2023, ApJL, 947, L20

[61] Forsblom, S. V., Tsygankov, S. S., Poutanen, J., et al. 2024, A&A, 691, A216

[62] Forsblom, S. V., Tsygankov, S. S., Suleimanov, V. F., Mushtukov, A. A., & Poutanen, J. 2025, A&A, 696, A224

[63] Fukumura, K., Kazanas, D., Shrader, C., et al. 2017, Nature Astronomy, 1, 0062

[64] García, J., Dauser, T., Reynolds, C. S., et al. 2013, ApJ, 768, 146

[65] García, J. & Kallman, T. R. 2010, ApJ, 718, 695

[66] García, J. A., Steiner, J. F., McClintock, J. E., et al. 2015, ApJ, 813, 84

[67] García, J. A., Tomsick, J. A., Sridhar, N., et al. 2019, ApJ, 885, 48

[68] Gendreau, K. C., Arzoumanian, Z., Adkins, P. W., et al. 2016, in Society of Photo-Optical Instrumentation Engineers (SPIE) Conference Series, Vol. 9905, Space Telescopes and Instrumentation 2016: Ultraviolet to Gamma Ray, ed. J.-W. A. den Herder, T. Takahashi, & M. Bautz, 99051H

[69] Ghez, A. M., Salim, S., Hornstein, S. D., et al. 2005, ApJ, 620, 744

[70] Giacconi, R., Kellogg, E., Gorenstein, P., Gursky, H., & Tananbaum, H. 1971, ApJL, 165, L27

[71] Gierliński, M. & Done, C. 2004, MNRAS, 347, 885

[72] Gilfanov, M., Churazov, E., & Revnivtsev, M. 1999, A&A, 352, 182

[73] Gnedin, Y. N. & Pavlov, G. G. 1974, Soviet Journal of Experimental and Theoretical Physics, 38, 903

[74] Gnedin, Y. N., Pavlov, G. G., & Shibanov, Y. A. 1978, Soviet Astronomy Letters, 4, 117

[75] Grinberg, V., Hell, N., Pottschmidt, K., et al. 2013, A&A, 554, A88

[76] Grinberg, V., Pottschmidt, K., Böck, M., et al. 2014, A&A, 565, A1

[77] Guo, C.-C., Liao, J.-Y., Zhang, S., et al. 2020, Journal of High Energy Astrophysics, 27, 44

[78] Hannikainen, D. C., Rodriguez, J., Vilhu, O., et al. 2005, A&A, 435, 995

[79] Heger, A., Fryer, C. L., Woosley, S. E., Langer, N., & Hartmann, D. H. 2003, ApJ, 591, 288

[80] Heil, L. M., Uttley, P., & Klein-Wolt, M. 2015, MNRAS, 448, 3339

[81] Hemphill, P. B., Rothschild, R. E., Caballero, I., et al. 2013, ApJ, 777, 61

[82] Heyl, J., Doroshenko, V., González-Caniulef, D., et al. 2024, Nature Astronomy, 8, 1047

[83] HI4PI Collaboration, Ben Bekhti, N., Flöer, L., et al. 2016, A&A, 594, A116

[84] Higginbottom, N. & Proga, D. 2015, ApJ, 807, 107

[85] Homan, J., Wijnands, R., van der Klis, M., et al. 2001, ApJS, 132, 377

[86] Houck, J. C. & Denicola, L. A. 2000, in Astronomical Society of the Pacific Conference Series, Vol. 216, Astronomical Data Analysis Software and Systems IX, ed. N. Manset, C. Veillet, & D. Crabtree, 591

[87] House, L. L. 1969, ApJS, 18, 21

[88] Huppenkothen, D., Bachetti, M., Stevens, A., et al. 2019, The Journal of Open Source Software, 4, 1393

[89] Huppenkothen, D., Bachetti, M., Stevens, A. L., et al. 2019, ApJ, 881, 39

[90] Ichimaru, S. 1977, ApJ, 214, 840

[91] in 't Zand, J. J. M., Baykal, A., & Strohmayer, T. E. 1998, ApJ, 496, 386

[92] Ingram, A. R. & Motta, S. E. 2019, New Astron. Rev., 85, 101524

[93] Jiang, J. 2024, Galaxies, 12, 80

[94] Jourdain, E., Roques, J. P., Chauvin, M., & Clark, D. J. 2012, ApJ, 761, 27

[95] Kaastra, J. S. & Bleeker, J. A. M. 2016, A&A, 587, A151

[96] Kalogera, V. & Baym, G. 1996, ApJL, 470, L61

[97] Karttunen, H., Krüger, P., Oja, H., Poutanen, M., & Donner, K. J., eds. 2007, Fundamental Astronomy

[98] King, A. L., Miller, J. M., Raymond, J., Reynolds, M. T., & Morningstar, W. 2015, ApJL, 813, L37

[99] Kislat, F., Clark, B., Beilicke, M., & Krawczynski, H. 2015, Astroparticle Physics, 68, 45

[100] Klein-Wolt, M., Fender, R. P., Pooley, G. G., et al. 2002, MNRAS, 331, 745

[101] Koljonen, K., Vera, R., Lahteenmaki, A., & Tornikoski, M. 2019, ATel, 12839, 1

[102] Koljonen, K. I. I. & Hovatta, T. 2021, A&A, 647, A173

[103] Koljonen, K. I. I. & Tomsick, J. A. 2020, A&A, 639, A13

[104] Kong, L.-D., Ji, L., Santangelo, A., et al. 2024, A&A, 686, A211

[105] Kong, L. D., Zhang, S., Ji, L., et al. 2021, ApJL, 917, L38

[106] Krawczynski, H., Muleri, F., Dovčiak, M., et al. 2022, Science, 378, 650

[107] Lamb, F. K., Pethick, C. J., & Pines, D. 1973, ApJ, 184, 271

[108] Laurent, P., Rodriguez, J., Wilms, J., et al. 2011, Science, 332, 438

[109] Leahy, D. A., Darbro, W., Elsner, R. F., et al. 1983, ApJ, 266, 160

[110] Lee, J. C., Reynolds, C. S., Remillard, R., et al. 2002, ApJ, 567, 1102

[111] Li, L.-X., Zimmerman, E. R., Narayan, R., & McClintock, J. E. 2005, ApJS, 157, 335

[112] Li, X., Li, X., Tan, Y., et al. 2020, Journal of High Energy Astrophysics, 27, 64

[113] Liao, J.-Y., Zhang, S., Chen, Y., et al. 2020, Journal of High Energy Astrophysics, 27, 24

[114] Liao, J.-Y., Zhang, S., Lu, X.-F., et al. 2020, Journal of High Energy Astrophysics, 27, 14

[115] Lightman, A. P. & White, T. R. 1988, ApJ, 335, 57

[116] Liu, C., Zhang, Y., Li, X., et al. 2020, Science China Physics, Mechanics, and Astronomy, 63, 249503

[117] Loktev, V., Forsblom, S. V., Tsygankov, S. S., et al. 2025, A&A, 698, A22

[118] Longair, M. S. 2011, High Energy Astrophysics

[119] Lyubarskii, Y. E. 1997, MNRAS, 292, 679

[120] Ma, X., Tao, L., Zhang, S.-N., et al. 2021, Nature Astronomy, 5, 94

[121] Makishima, K., Kawai, N., Koyama, K., et al. 1984, PASJ, 36, 679

[122] Makishima, K., Maejima, Y., Mitsuda, K., et al. 1986, ApJ, 308, 635

[123] Malacaria, C., Heyl, J., Doroshenko, V., et al. 2023, A&A, 675, A29

[124] Manchester, R. N., Hobbs, G. B., Teoh, A., & Hobbs, M. 2005, AJ, 129, 1993

[125] Marshall, H. L., Ng, M., Rogantini, D., et al. 2022, ApJ, 940, 70

[126] Marshall, N. & Ricketts, M. J. 1980, MNRAS, 193, 7P

[127] Martocchia, A., Matt, G., Belloni, T., et al. 2006, A&A, 448, 677

[128] Matsuoka, M., Kawasaki, K., Ueno, S., et al. 2009, PASJ, 61, 999

[129] Matt, G., Guainazzi, M., & Maiolino, R. 2003, MNRAS, 342, 422

[130] Meszaros, P., Novick, R., Szentgyorgyi, A., Chanan, G. A., & Weisskopf, M. C. 1988, ApJ, 324, 1056

[131] Meyer-Hofmeister, E., Liu, B. F., Qiao, E., & Taam, R. E. 2020, A&A, 637, A66

[132] Mihara, T. 1995, PhD thesis, University of Tokyo

[133] Miller, J. M., Parker, M. L., Fuerst, F., et al. 2013, ApJL, 775, L45

[134] Miller, J. M., Raymond, J., Fabian, A., et al. 2006, Nature, 441, 953

[135] Miller, J. M., Raymond, J., Fabian, A. C., et al. 2016, ApJL, 821, L9

[136] Miller, J. M., Zoghbi, A., Raymond, J., et al. 2020, ApJ, 904, 30

[137] Miller-Jones, J. C. A., Bahramian, A., Orosz, J. A., et al. 2021, Science, 371, 1046

[138] Mirabel, I. F. & Rodríguez, L. F. 1994, Nature, 371, 46

[139] Mitsuda, K., Inoue, H., Koyama, K., et al. 1984, PASJ, 36, 741

[140] Miyamoto, S., Kimura, K., Kitamoto, S., Dotani, T., & Ebisawa, K. 1991, ApJ, 383, 784

[141] Miyamoto, S., Kitamoto, S., Iga, S., Negoro, H., & Terada, K. 1992, ApJL, 391, L21

[142] Morgan, E. H., Remillard, R. A., & Greiner, J. 1997, ApJ, 482, 993

[143] Motta, S., Muñoz-Darias, T., Casella, P., Belloni, T., & Homan, J. 2011, MNRAS, 418, 2292

[144] Motta, S., Williams, D., Fender, R., et al. 2019, ATel, 12773, 1

[145] Motta, S. E., Kajava, J. J. E., Giustini, M., et al. 2021, MNRAS, 503, 152

[146] Motta, S. E., Kajava, J. J. E., Sánchez-Fernández, C., et al. 2017, MNRAS, 471, 1797

[147] Motta, S. E., Kajava, J. J. E., Sánchez-Fernández, C., Giustini, M., & Kuulkers, E. 2017, MNRAS, 468, 981

[148] Mushtukov, A. & Tsygankov, S. 2023, in Handbook of X-ray and Gamma-ray Astrophysics, 138

[149] Mushtukov, A. A., Tsygankov, S. S., Poutanen, J., et al. 2023, MNRAS, 524, 2004

[150] Naghizadeh-Khouei, J. & Clarke, D. 1993, A&A, 274, 968

[151] Narayan, R. & McClintock, J. E. 2008, New Astron. Rev., 51, 733

[152] Narayan, R. & Yi, I. 1995, ApJ, 444, 231

[153] Negoro, H., Tachibana, Y., Kawai, N., et al. 2018, ATel, 11828, 1

[154] Neilsen, J., Cackett, E., Remillard, R. A., et al. 2018, ApJL, 860, L19

[155] Neilsen, J., Homan, J., Steiner, J. F., et al. 2020, ApJ, 902, 152

[156] Neilsen, J. & Lee, J. C. 2009, Nature, 458, 481

[157] Nespoli, E., Fabregat, J., & Mennickent, R. E. 2008, A&A, 486, 911

[158] Nowak, M. A. 2000, MNRAS, 318, 361

[159] Nowak, M. A., Vaughan, B. A., Wilms, J., Dove, J. B., & Begelman, M. C. 1999, ApJ, 510, 874

[160] Parker, M. L., Tomsick, J. A., Miller, J. M., et al. 2015, ApJ, 808, 9

[161] Penna, R. F., McKinney, J. C., Narayan, R., et al. 2010, MNRAS, 408, 752

[162] Petrucci, P. O., Merloni, A., Fabian, A., Haardt, F., & Gallo, E. 2001, MNRAS, 328, 501

[163] Ponti, G., Fender, R. P., Begelman, M. C., et al. 2012, MNRAS, 422, L11

[164] Pottschmidt, K., Wilms, J., Nowak, M. A., et al. 2003, A&A, 407, 1039

[165] Poutanen, J. 2020, A&A, 641, A166

[166] Poutanen, J., Tsygankov, S. S., Doroshenko, V., et al. 2024, A&A, 691, A123

[167] Poutanen, J., Tsygankov, S. S., & Forsblom, S. V. 2024, Galaxies, 12, 46

[168] Proga, D. & Kallman, T. R. 2002, ApJ, 565, 455

[169] Radhakrishnan, V. & Cooke, D. J. 1969, Astrophys. Lett., 3, 225

[170] Reid, M. J., McClintock, J. E., Steiner, J. F., et al. 2014, ApJ, 796, 2

[171] Reig, P. 2011, Astrophysics and Space Science, 332, 1

[172] Reig, P., Kylafis, N. D., Papadakis, I. E., & Costado, M. T. 2018, MNRAS, 473, 4644

[173] Remillard, R. A. & McClintock, J. E. 2006, ARA&A, 44, 49

[174] Reynolds, C. S. 2021, ARA&A, 59, 117

[175] Rezzolla, L., Pizzochero, P., Jones, D. I., Rea, N., & Vidaña, I., eds. 2018, Astrophysics and Space Science Library, Vol. 457, The Physics and Astrophysics of Neutron Stars

[176] Rodriguez, J., Grinberg, V., Laurent, P., et al. 2015, ApJ, 807, 17

[177] Ross, R. R. & Fabian, A. C. 2005, MNRAS, 358, 211

[178] Shahbaz, T., Ringwald, F. A., Bunn, J. C., et al. 1994, MNRAS, 271, L10

[179] Shaposhnikov, N. & Titarchuk, L. 2006, ApJ, 643, 1098

[180] Shaw, A. W., Miller, J. M., Grinberg, V., et al. 2022, MNRAS, 516, 124

[181] Shi, Z., Wu, Q., Yan, Z., Lyu, B., & Liu, H. 2023, MNRAS, 525, 1431

[182] Shidatsu, M., Ueda, Y., Nakahira, S., et al. 2013, ApJ, 779, 26

[183] Soleri, P., Belloni, T., & Casella, P. 2008, MNRAS, 383, 1089

[184] Sridhar, N., García, J. A., Steiner, J. F., et al. 2020, ApJ, 890, 53

[185] Steiner, J. F., McClintock, J. E., Remillard, R. A., et al. 2010, ApJL, 718, L117

[186] Steiner, J. F., Remillard, R. A., García, J. A., & McClintock, J. E. 2016, ApJL, 829, L22

[187] Suleimanov, V. F., Forsblom, S. V., Tsygankov, S. S., et al. 2023, A&A, 678, A119

[188] Tagger, M. & Pellat, R. 1999, A&A, 349, 1003

[189] Tananbaum, H., Gursky, H., Kellogg, E., Giacconi, R., & Jones, C. 1972, ApJL, 177, L5

[190] Tarter, C. B., Tucker, W. H., & Salpeter, E. E. 1969, ApJ, 156, 943

[191] Tobrej, M., Rai, B., Ghising, M., Tamang, R., & Paul, B. C. 2023, MNRAS, 518, 4861

[192] Tomsick, J. A., Kalemci, E., Kaaret, P., et al. 2008, ApJ, 680, 593

[193] Torrejón, J. M., Schulz, N. S., Nowak, M. A., & Kallman, T. R. 2010, ApJ, 715, 947

[194] Tsygankov, S. S., Doroshenko, V., Mushtukov, A. A., et al. 2023, A&A, 675, A48

[195] Tsygankov, S. S., Doroshenko, V., Poutanen, J., et al. 2022, ApJL, 941, L14

[196] Ueda, Y., Yamaoka, K., & Remillard, R. 2009, ApJ, 695, 888

[197] van den Heuvel, E. P. J. 2009, in Astrophysics and Space Science Library, Vol. 359, Physics of Relativistic Objects in Compact Binaries: From Birth to Coalescence, ed. M. Colpi, P. Casella, V. Gorini, U. Moschella, & A. Possenti, 125

[198] van der Klis, M. 1989, in NATO Advanced Study Institute (ASI) Series C, Vol. 262, Timing Neutron Stars, ed. H. Ögelman & E. P. J. van den Heuvel, 27

[199] van Kerkwijk, M. H., van Oijen, J. G. J., & van den Heuvel, E. P. J. 1989, A&A, 209, 173

[200] Varun, Pradhan, P., Maitra, C., Raichur, H., & Paul, B. 2019, ApJ, 880, 61

[201] Vaughan, B. A. & Nowak, M. A. 1997, ApJL, 474, L43

[202] Verner, D. A., Ferland, G. J., Korista, K. T., & Yakovlev, D. G. 1996, ApJ, 465, 487

[203] Vignarca, F., Migliari, S., Belloni, T., Psaltis, D., & van der Klis, M. 2003, A&A, 397, 729

[204] Walton, D. J., Tomsick, J. A., Madsen, K. K., et al. 2016, ApJ, 826, 87

[205] Wang, J., Kara, E., Lucchini, M., et al. 2022, ApJ, 930, 18

[206] Webster, B. L. & Murdin, P. 1972, Nature, 235, 37

[207] Weisskopf, M. C., Ramsey, B., O'Dell, S., et al. 2016, in Society of Photo-Optical Instrumentation Engineers (SPIE) Conference Series, Vol. 9905, Space Telescopes and Instrumentation 2016: Ultraviolet to Gamma Ray, ed. J.-W. A. den Herder, T. Takahashi, & M. Bautz, 990517

[208] Weisskopf, M. C., Soffitta, P., Baldini, L., et al. 2022, Journal of Astronomical Telescopes, Instruments, and Systems, 8, 026002

[209] Wijnands, R. & van der Klis, M. 1999, ApJ, 514, 939

[210] Wilms, J., Allen, A., & McCray, R. 2000, ApJ, 542, 914

[211] Wilms, J., Nowak, M. A., Pottschmidt, K., Pooley, G. G., & Fritz, S. 2006, A&A, 447, 245

[212] Woods, D. T., Klein, R. I., Castor, J. I., McKee, C. F., & Bell, J. B. 1996, ApJ, 461, 767

[213] Woosley, S. & Janka, T. 2005, Nature Physics, 1, 147

[214] Xu, Y., Harrison, F. A., Kennea, J. A., et al. 2018, ApJ, 865, 18

[215] Yilmaz, A., Svoboda, J., Grinberg, V., et al. 2023, MNRAS, 525, 1288

[216] Zdziarski, A. A., Gierliński, M., Mikołajewska, J., et al. 2004, MNRAS, 351, 791

[217] Zdziarski, A. A., Johnson, W. N., & Magdziarz, P. 1996, MNRAS, 283, 193

[218] Zdziarski, A. A., Ziółkowski, J., & Mikołajewska, J. 2019, MNRAS, 488, 1026

[219] Zhang, S., Lu, F. J., Zhang, S. N., & Li, T. P. 2014, in Society of Photo-Optical Instrumentation Engineers (SPIE) Conference Series, Vol. 9144, Space Telescopes and Instrumentation 2014: Ultraviolet to Gamma Ray, ed. T. Takahashi, J.-W. A. den Herder, & M. Bautz, 914421

[220] Zhang, S. N., Cui, W., & Chen, W. 1997, ApJL, 482, L155

[221] Zhang, S.-N., Li, T., Lu, F., et al. 2020, Science China Physics, Mechanics, and Astronomy, 63, 249502

[222] Zhang, W., Jahoda, K., Swank, J. H., Morgan, E. H., & Giles, A. B. 1995, ApJ, 449, 930

[223] Zhao, Q. C., Li, H. C., Tao, L., et al. 2024, MNRAS, 531, 3935

[224] Zhao, X., Gou, L., Dong, Y., et al. 2021, ApJ, 908, 117

[225] Zhou, M., Ducci, L., Liu, H., et al. 2025, arXiv e-prints, arXiv:2507.17873

[226] Zhou, M., Grinberg, V., Bu, Q. C., et al. 2022, A&A, 666, A172

[227] Zhou, M., Grinberg, V., Santangelo, A., et al. 2025, A&A, 694, A104

[228] Zoghbi, A., Miller, J. M., King, A. L., et al. 2016, ApJ, 833, 165

Acknowledgments

It has been over four years since I arrived in Tübingen, this lovely town with its historic and distinguished University. These four years have meant far more to me than simply earning a doctoral degree; they represent a cherished period of my life, filled with supportive supervisors, wonderful colleagues, and the experience of a vibrant and diverse lifestyle. I am deeply grateful to all those who have accompanied me along the way.

First and foremost, I owe my deepest thanks to my supervisors, Dr. Victoria Grinberg and Prof. Dr. Andrea Santangelo. Their patience, encouragement, and unwavering support in my work have been a source of strength during my entire Ph.D. life. When I first arrived in Tübingen, the city was gripped by the pandemic, and fear of infection was widespread. I was also anxious about studying and living in a non-English-speaking foreign country. It was truly my good fortune to have you as my supervisors. Even though we did not meet every day, I could always feel your kindness and encouragement in every conversation we had, and I drew energy from your support.

I would also like to express my gratitude to the senior members of our institute: Dr. Gerd Pühlhofer, Dr. Chris Tenzer, Dr. Denys Malyshev, and our secretary, Frau Sabine Lauer. Although administrative matters can sometimes be tedious, working alongside you has brought me genuine joy. Our conversations were always a pleasure.

To Dr. Lorenzo Ducci, my roommate for over four years: it has been a pleasure to share an office with you and to have countless enjoyable conversations.

I am also thankful to the former members of our institute, Prof. Qingcui Bu, Prof. Long Ji, and Dr. Victor Doroshenko. It has been a pleasure working with you, and I have learned much from our collaborations.

My sincere thanks go to my Chinese colleagues at the institute: Dr. Honghui Liu, Dr. Youli Tuo, Dr. Lingda Kong, Dr. Pengju Wang, and Dr. Qi Liu, as well as the Ph.D. students who matriculated around the same time with me: Xiaohang Dai, Hao Xiong, Yujia Du, and Xianqi Wang (soon to be doctors themselves!). Many of you have become dear friends, enriching my life in Germany. I will fondly remember our lively dinner parties and board game nights, filled with loud conversations and laughter.

I am deeply grateful to my girlfriend, Frau Xuefeng Yang, who has shaped my life in Tübingen in so many ways. She transformed me from a free-spirited wanderer into someone who takes responsibility not only for himself but also for others. She has made my life better, and I am determined to do the same for her.

To my friends in Tübingen (Shuning Xia, Ying Xu, Pengfei Liu, Gaopeng Li, Jingyun Ding, Qingjun Jiang, Ying Zhang, . . .), in China, and around the world—let's keep in touch! I will always cherish our friendship, and you will always hold an important

place in my heart.

Last, but certainly not least, I would like to express my gratitude to my parents. Pursuing a doctoral degree abroad has inevitably meant being apart for extended periods, often missing out on important family moments and daily life together. Yet, despite the distance, you have always stood by me, supporting my decisions with quiet strength and unwavering love. Your patience, trust, and encouragement have been a constant source of motivation throughout this journey. I am profoundly grateful for everything you have done, and I promise to carry forward that same spirit of unconditional love and support when raising my own children in the future.

As I close this chapter, I carry with me not only the knowledge gained, but also the gratitude that shaped it. Here's to the next journey, wherever it may lead.

Menglei Zhou
Tübingen, 1st May, 2025

List of Publications

During my doctoral studies in Tübingen

As the leading author

1) Zhou, M., Ducci, L., Liu, H., Tsygankov, S., Forsblom, S., ... & Santangelo, A. (2025). *Probing the polarized emission from the accretion-powered pulsar 4U 1907+09 with IXPE.* (Accepted for publication in A&A)

2) Zhou, M., Grinberg, V., Santangelo, A., Bambi, C., Bu, Q., ... & Tuo, Y. (2025). *Dimming GRS 1915+105 observed with NICER and Insight–HXMT*. A&A, 694, A104.

3) Zhou, M., Grinberg, V., Bu, Q., Santangelo, A., Cangemi, F., ... & Zhang, S.-N. (2022). *The spectral-timing analysis of Cygnus X-1 with Insight-HXMT*. A&A, 666, A172.

As the co-author

1) Abalo, L., Kretschmar, P., Fürst, F., Diez, C. M., El Mellah, I., Grinberg, V., Guainazzi, M., Martínez-Núñez, S., Manousakis, A., Amato, R., Zhou, M. & Beijersbergen, M. W. (2024). *Variable structures in the stellar wind of the HMXB Vela X-1.* A&A, 692, A188

2) Dai, X., Kong, L., Ji, L., Zhou, M., Shui, Q., Wang, P., Zhang, Shu & Santangelo, A. (2024). *Unveiling the rebrightening mechanism of GRS 1915+105: Insights from a change in the quasi-periodic oscillations and from a wind analysis*. A&A, 692, A117

3) Kong, L., Ji, L., Santangelo, A., Zhou, M. and Shui, Q. & Zhang, Shu. (2024). *Likely detection of magnetic field related LFQPO in the soft X-ray rebrightening of GRS 1915+105.* A&A, 686, A211

4) Yorgancioglu, E. S., Bu, Q. C., Santangelo, A., Tao, L., Davis, S. W., Vahdat, A., Kong, L. D., Piraino, S., Zhou, M. & Zhang, S. N. (2023). *Spin measurement of 4U 1543-47 with Insight-HXMT and NICER from its 2021 outburst. A test of accretion disk models at high luminosities.* A&A, 677, A79

5) Diez, C. M., Grinberg, V., Fürst, F., El Mellah, I., Zhou, M., Santangelo, A., Martínez-Núñez, S., Amato, R., Hell, N. & Kretschmar, P. (2023). *Observing the onset of the accretion wake in Vela X-1.* A&A, 674, A147

Before my doctoral studies

1) Zhou, M., Abdikamalov, A. B., Ayzenberg, D., Bambi, C., Grinberg, V., & Tripathi, A. (2020). *Thermal spectra of thin accretion discs of finite thickness around Kerr black holes.* MNRAS, 496(1), 497-503.

2) Abdikamalov, A. B., Ayzenberg, D., Bambi, C., Dauser, T., Garcia, J. A., ... & Zhou, M. (2020). *Testing the Kerr black hole hypothesis using X-ray reflection spectroscopy and a thin disk model with finite thickness.* ApJ, 899(1), 80.

3) Zhou, M., Ayzenberg, D., Bambi, C., & Nampalliwar, S. (2020). *Modeling uncertainties in x-ray reflection spectroscopy measurements. I. Impact of higher order disk images.* PRD, 101(4), 043010.

4) Zhou, M., Abdikamalov, A. B., Ayzenberg, D., Bambi, C., Liu, H., & Nampalliwar, S. (2019). *XSPEC model for testing the Kerr black hole hypothesis using the continuum-fitting method.* PRD, 99(10), 104031.

5) Zhou, M., Cao, Z., Abdikamalov, A., Ayzenberg, D., Bambi, C., ... & Nampalliwar, S. (2018). *Testing conformal gravity with the supermassive black hole in 1H 0707−495.* PRD, 98(2), 024007.

6) Zhou, M., Bambi, C., Herdeiro, C. A., & Radu, E. (2017). *Iron Kα line of Kerr black holes with Proca hair.* PRD, 95(10), 104035.

7) Zhou, M., Cardenas-Avendano, A., Bambi, C., Kleihaus, B., & Kunz, J. (2016). *Search for astrophysical rotating Ellis wormholes with X-ray reflection spectroscopy.* PRD, 94(2), 024036.